BURSA TECHNICAL UNIVERSITY

JISE

JOURNAL OF INNOVATIVE SCIENCE AND ENGINEERING

Volume: **9** Issue: **1** Year: **2025** ISSN: **2602-4217**

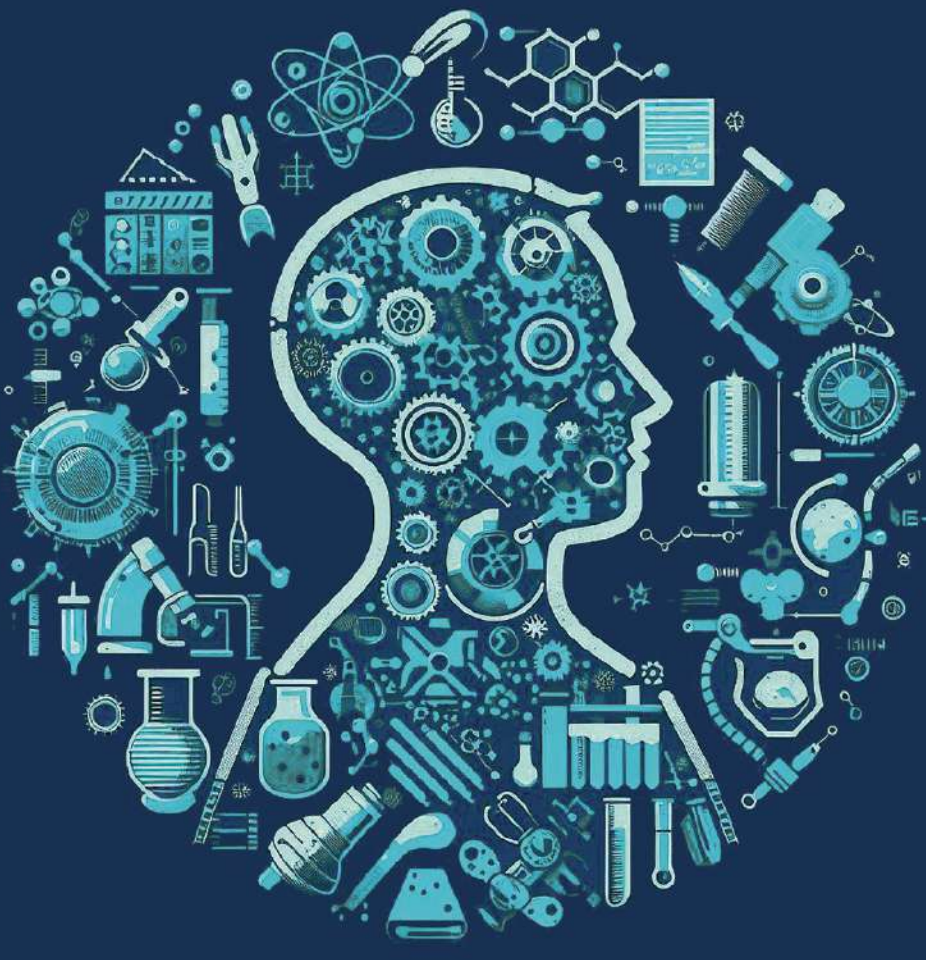

http://jise.btu.edu.tr/en

Aircraft Recognition Based on CNN Using Satellite Images

Meriç GENÇ[1] ,Yıldıray YALMAN[2*]

[1] *Department of Electrical and Electronics Engineering, Piri Reis University, 34940, İstanbul, Türkiye*

[2] *Department of Computer Engineering, Piri Reis University, 34940, Istanbul, Türkiye*

ARTICLE INFO

Received Date: 3/08/2024
Accepted Date: 24/11/2024

Cite this paper as:
Genc M. and Yalman Y. (2025). *Aircraft Recognition Based on CNN Using Satellite Images.*Journal of Innovative Science and Engineering. 9(1): 1-14

*Corresponding author: Yıldıray Yalman
E-mail:yyalman@pirireis.edu.tr

Keywords:
VGG16
VGG19
Convolutional Neural Networks
Aircraft Recognition
Visual Recognition

ABSTRACT

This study investigates the use of Convolutional Neural Networks (CNN), particularly the VGG16 and VGG19 architectures, for aircraft recognition with satellite-derived image data. Deep learning, especially multi-layer neural networks, addresses significant limitations in artificial intelligence, allowing advanced models to achieve high accuracy in complex tasks like aircraft recognition. The MTARSI dataset is exclusively used to evaluate these models. Motivated by the importance of accurate aircraft recognition in civil aviation, military security, and emergency interventions, this study aims to develop a CNN-based aircraft recognition system. Experimental results show that VGG19 outperforms VGG16, achieving an accuracy of 89.29% compared to 82.67% for VGG16. These findings highlight VGG19's advantage over traditional methods and underscore its potential in future military aircraft recognition systems.

1. Introduction

In today's rapidly digitizing world, technological tools that were once exclusive to defense systems have found effective applications in military aircraft recognition, particularly using satellite imagery and deep learning algorithms. The advancement of technology, coupled with the efficient use of deep learning techniques, has enabled the use of images and videos for a range of tasks, such as computer vision studies, which address crucial issues including national security, traffic management, and agricultural health monitoring.

The development of artificial intelligence, especially in the domain of computer vision, has significantly increased the demand for more efficient and effective vision systems. As artificial intelligence evolves, it has led to the creation of more sophisticated tools for a variety of tasks, such as object recognition, behavioral analysis, and scene understanding. Research in AI and deep learning, particularly focusing on applying these technologies for the benefit of humanity and simplifying daily life, has been particularly successful in high-demand tasks such as surveillance and object detection, which require intense focus. These innovations have not only ensured more efficient use of human resources but also minimized human errors and negligence in critical tasks. In recent years, researchers have focused on enhancing the capabilities of deep learning algorithms. Notably, deep learning architectures such as VGG16 and VGG19 have demonstrated impressive success in image recognition and classification tasks. These models, with their deep architectures comprising multiple layers, are highly effective in learning complex image features and improving performance in challenging classification problems.

This study aims to evaluate the performance of VGG16 and VGG19 architectures for military aircraft classification using the MTARSI dataset. The MTARSI dataset contains high-resolution images of military aircraft taken from various angles, making it an ideal resource for identifying different aircraft types and models. In this research, object recognition and classification tasks were performed by using VGG16 and VGG19 models, starting from pre-trained weights and fine-tuned transfer learning techniques. Preprocessing steps, including resizing and normalization, were applied to the dataset images before training. On the other hand, the aim of this study is to investigate the effectiveness of the VGG16 and VGG19 architectures in military aircraft classification using satellite imagery. By analyzing the performance of these models, we aim to demonstrate the potential of deep learning methods in improving the accuracy and efficiency of military aircraft classification systems.

The application of artificial intelligence (AI) and deep learning algorithms in the defense industry has led to significant advancements, particularly in areas such as military aircraft recognition using satellite imagery. In recent years, the focus has shifted towards using satellite images and remote sensing data to improve aircraft classification systems. Traditional image recognition methods, such as SIFT (Scale-Invariant Feature Transform) combined with Bag of Words (BOW), and HOG (Histogram of Oriented Gradients) with Support Vector Machines (SVM), have been widely used for this purpose. While these methods have provided some success, they are often computationally expensive and are sensitive to changes in image resolution and viewing angles. These techniques also struggle with distinguishing between similar-looking objects, which makes the task of recognizing military aircraft particularly challenging.

With the rapid development of deep learning methods, particularly Convolutional Neural Networks (CNNs), new solutions have emerged to improve classification tasks. CNN architectures like VGG16 and VGG19, known for their ability to learn complex image features, have shown remarkable performance in various computer vision tasks, including object classification, scene recognition, and more. These deep learning models can process large volumes of data and automatically extract important features from images without requiring hand-crafted feature engineering.

Recent studies have demonstrated the effectiveness of CNNs, particularly VGG architectures, in the classification of military aircraft from satellite imagery. For instance, Chen et al. [1] proposed a Region Locating Network (RLN) to improve the Faster R-CNN framework. This RLN strategy is designed to identify regions, such as runway and apron areas, where aircraft are typically located. They used a dataset of 265 images from 12 different airports, totaling over 6,000 annotated aircraft, to train the model. Their approach achieved a detection accuracy of 53.64%. To enhance the training dataset, they applied data augmentation techniques, including flipping the images horizontally and vertically.

Luo and Shi [2] addressed the problem of efficient aircraft localization in remote sensing images using a simple yet effective object proposal method. Their approach involved generating a small set of bounding boxes likely to contain the objects of interest (in this case, aircraft) and applying HOG features with an SVM classifier for detection. The model achieved an 80% detection accuracy on test data from 20 airport images collected from Google Earth, with image sizes ranging from 1000 × 1000 to 2000 × 2000.

Another related study, by Zhang et al. [3], explored the integration of traditional computer vision methods with deep learning to improve the accuracy of aircraft recognition. The researchers combined SIFT features with a CNN classifier, resulting in a notable improvement in the accuracy of aircraft detection in satellite images. They also introduced a novel data augmentation method that generated realistic synthetic images to increase the variety of the training dataset, further boosting the model’s performance.

These advancements in deep learning and computer vision have significantly contributed to the improvement of military aircraft recognition systems, enhancing both the accuracy and efficiency of such tasks. By utilizing pre-trained deep learning models and transfer learning, these systems can be further fine-tuned to achieve better results, especially in highly specialized fields like defense and national security.

In conclusion, the integration of artificial intelligence and deep learning algorithms has revolutionized the defense industry and various other industrial applications. Projects that explore and implement such technologies are paving the way for future advancements, contributing to a safer and more efficient world. The success of models like VGG16 and VGG19 in military aircraft classification demonstrates the potential of deep learning methods in enhancing national security and defense systems, reducing human error, and improving operational efficiency.

2. Convolutional Neural Networks (CNN)

Convolutional Neural Networks (CNN) are a type of Multi-Layer Perceptron (MLP), characterized by multi-layered detectors. Cells in the visual center are divided into subregions to encompass the entire image, with simple cells focusing on edge-like features, and complex cells having broader receptors concentrating on the entire visual field. The CNN algorithm, an advanced neural network, is inspired by the visual center of animals. The mathematical convolution operation here can be thought of as a neuron's response to stimuli within its receptive field [3,4,5]. CNN consists of one or more convolutional layers, a subsampling layer, and one or more fully connected layers, similar to a standard multi-layer neural network, following that [6]. The LeNet architecture, introduced by Yann LeCun in 1988 and illustrated in Figure 1, underwent continuous improvements until the late 1990s [7]. Within the LeNet network, the lower layers consist of consecutively placed convolution and maximum pooling layers, while the subsequent upper layers align with the structure of fully connected traditional Multi-Layer Perceptron (MLP). Convolutional Neural Network (CNN) algorithms have diverse applications across various domains, such as image and audio processing, natural language processing (NLP), and biomedical research. Notably, CNN has excelled in the field of image processing, achieving state-of-the-art results. In a study focusing on the MNIST dataset, Cireşan has significantly reduced the error rate by using CNN [8]. Another investigation by Cireşan and colleagues, involving the MNIST and NORB datasets, showcased the rapid learning capabilities of CNN, surpassing conventional methods [9].

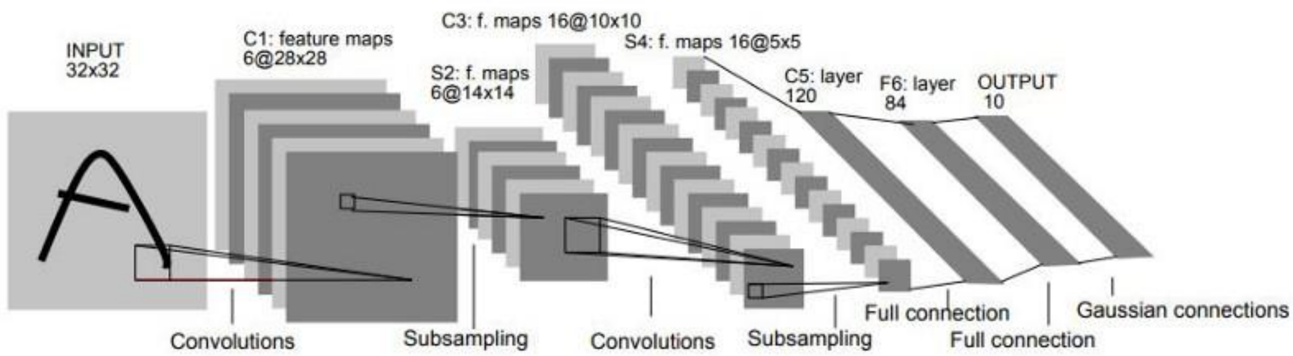

Figure 1: Demographics of the study participants.

In 2014, top-ranking teams in the ImageNet Competition, dealing with millions of images and hundreds of object classes in object classification and detection, employed modified versions of CNN algorithms. A subsequent study in 2015 highlighted CNN's ability to capture faces at wide angles, including upside-down faces. The network underwent training on a database comprising 200,000 images with faces at various angles and orientations, along with an additional 20 million images without faces [10].

The evolution and success of CNN algorithms, demonstrated through these studies, underscore their versatility and effectiveness across a spectrum of applications, contributing significantly to advancements in image processing and related fields.

CNN models have shown versatility beyond image processing and can be applied to various NLP problems. Exceptional results were achieved in semantic parsing [11], query generation [12], sentence modeling [13], classification [14], and prediction problems [13]. CNN algorithms have also been employed in drug discovery. AtomNet, developed by Atomwise in 2015, was the first deep neural network designed for drug design. Trained on 3D representations of chemical reactions, the system was used to discover new biomolecules for diseases such as Ebola and sclerosis [16].

2.1. Visual Geometry Group

The Visual Geometry Group (VGG) is a research group at the University of Oxford, and VGG represents a series of deep learning models developed by this group. VGG models, particularly the ones used for image classification tasks on large datasets like ImageNet, have achieved high accuracy. A distinctive feature of VGG models is their deep architecture in convolutional neural networks (CNN). For example, the VGG16 model has a 16-layer structure, consisting of 13 convolutional layers and 3 fully connected layers. This depth allows the model to effectively learn complex features.

VGG models use convolutional layers to identify different features in an image. These convolutional layers enable the model to understand the patterns in the image by creating feature maps. VGG models trained on extensive datasets often offer the ability to use their pre-trained weights for transfer learning or fine-tuning. This feature allows for a quick and effective start in new tasks. VGG models have shown significant success in various computer vision tasks, such as image classification, object detection, and localization. Their impressive performance in ImageNet competitions highlights the impact of VGG in both industry and research domains.

The VGG, or Visual Geometry Group, represents a typical design for a deep Convolutional Neural Network (CNN) characterized by numerous layers. The term “deep” refers to the significant layer count, with VGG-16 or VGG-19 having 16 or 19 convolutional layers, respectively. The VGG architecture serves as the foundation for constructing innovative models for object identification. As a deep neural network, VGGNet surpasses benchmarks across various tasks and datasets beyond ImageNet. It continues to be one of the most employed architectures for image recognition in use today. Figure 2 shows the VGG architecture structure.

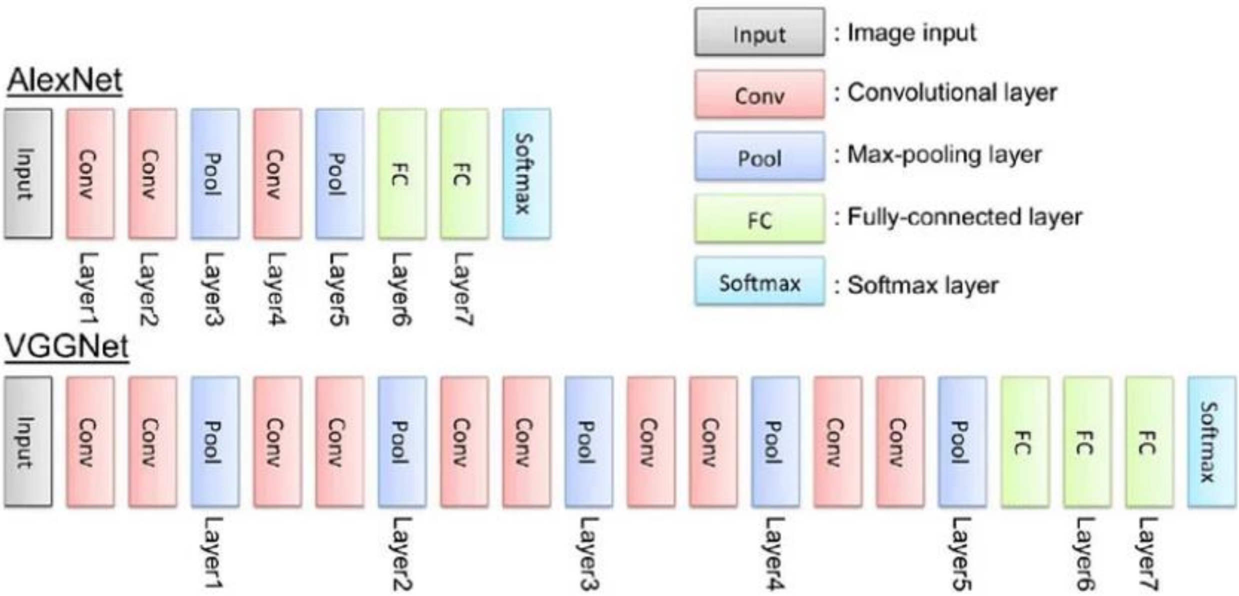

Figure 2: VGG architectures.

2.2.1. VGG 16

The convolutional neural network model known as VGG, or VGGNet, specifically with 16 layers, is commonly referred to as VGG16. This model was developed by A. Zisserman and K. Simonyan at the University of Oxford. The research paper titled “Very Deep Convolutional Networks for Large-Scale Image Recognition” presents the model released by these researchers.

The VGG16 model attains a top-5 test accuracy of approximately 92.7 percent on ImageNet. ImageNet, a dataset comprising over 14 million photos across nearly 1000 categories, served as the testing ground. VGG16 emerged as one of the most favored models during ILSVRC2014. Its superior performance over AlexNet is attributed to the substitution of multiple 3x3 kernel-sized filters for larger ones. The training process for the VGG16 model spanned several weeks, utilizing Nvidia Titan Black GPUs.

With 16 layers, VGGNet-16 excels in classifying images into 1000 distinct object categories, including items like keyboards, animals, pencils, mice, etc., as mentioned earlier. The model accommodates images with a resolution of 224 by 224 pixels. Figure 3 shows the VGG16 architecture structure.

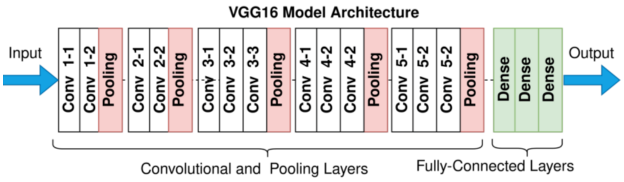

Figure 3: VGG16 architecture.

2.2.2. VGG 19

The VGG19 model, also known as VGGNet-19, follows the same fundamental concept as the VGG16 model, except it features 19 layers. The numbers “16” and “19” correspond to the model’s weight layers, specifically the convolutional layers. In contrast to VGG16, VGG19 incorporates three additional convolutional layers.

3. Dataset Preparation

In this experimental study, the choice of utilizing the Multi-type Aircraft of Remote Sensing Images (MTARSI) dataset over traditional datasets like Pascal VOC, MS COCO, CIFAR, ImageNet, and MNIST stems from several critical considerations, elucidating the rationale behind the selection of specific aircraft types, namely “A-10”, “B-52”, “C-21”, and “F-22”. Additionally, example photos can be seen in Figures 4, 5, 6, and 7.

The MTARSI dataset offers a unique advantage due to its specialized focus on remote sensing images of various aircraft types, specifically curated from Google Earth satellite imagery. With a total of 9,385 meticulously collected images, spanning 20 distinct aircraft types across 36 airports, MTARSI represents a comprehensive and diverse collection that presents a rich landscape for training and validating object recognition and detection models.

The decision to narrow down the selection to “A-10”, “B-52”, “C-21”, “F22” aircraft types is founded upon the availability of a substantial number of images for these specific categories within the MTARSI dataset. By focusing on these aircraft types, which are well-represented within the dataset, the study aims to ensure a robust and extensive training and validation process.

Figure 4: A-10 aircraft.

Furthermore, the careful curation and labeling of each image by seven specialists in the field of remote sensing image interpretation underscore the high quality and reliability of the MTARSI dataset. This meticulous labeling process enhances the credibility and accuracy of the dataset, mitigating potential ambiguities or inconsistencies in object annotations.

Figure 5: B-52 aircraft.

Moreover, the selection of these specific aircraft types aligns with the objectives of the study, which may prioritize certain types of aircraft based on their prevalence, significance, or relevance to specific applications or domains. For instance, “A-10”, “B-52”, “C-21”, and “F22” aircraft types may hold particular importance in military or aviation-related contexts, thereby justifying their inclusion in the experimental investigation.

By leveraging the MTARSI dataset and focusing on these specific aircraft types, the study aims to contribute valuable insights and advancements to the field of object recognition and detection, particularly in the domain of remote sensing imagery analysis. This targeted approach not only harnesses the richness and diversity of the dataset but also ensures the relevance and applicability of the findings to real-world scenarios and applications.

The table provided outlines the distribution of data samples across the “Train”, “Validation” and “Test” sets for each of the selected aircraft types: “A-10”, “B-52”, “C-21”, “F-22”. These values play a crucial role in ensuring the efficacy and reliability of the experimental study conducted by using the MTARSI dataset.

Figure 6: C-21 aircraft.

The Train set comprises the largest portion of data samples and is utilized for training the deep learning models. The aircraft types and their numbers in the “training” set are as follows: 324 for “A-10”, 432 for “B-52”, 392 for “C-21”, 672 for “F-22”. This distribution ensures that the models have access to a substantial amount of training data, facilitating the learning process and enabling them to capture diverse patterns and characteristics associated with each aircraft type.

Figure 7: F-22 aircraft.

Following the training phase, the Validation set is employed to fine-tune model parameters and monitor performance during training iterations. The Validation set contains a smaller subset of data samples compared to the Train set, serving as an independent evaluation mechanism to gauge the generalization capabilities of the models. The aircraft types and their numbers in the “validation” set are as follows: 59 for “A-10”, 55 for “B-52”, 49 for “C-21”, 84 for “F-22”.

Finally, the Test set is utilized to assess the overall performance and generalization ability of the trained models on unseen data. The Test set is crucial for evaluating the models’ effectiveness in accurately recognizing and detecting aircraft types under real-world conditions. The aircraft types and their numbers in the “test” set are as follows: 59 for “A-10”, 55 for “B-52”, 49 for “C-21”, 84 for “F-22”.

Overall, this meticulous partitioning of data into Train, Validation, and Test sets ensures a rigorous and systematic evaluation of the deep learning models trained on the MTARSI dataset. By leveraging these carefully curated datasets, the study aims to achieve robust and reliable results in the domain of object recognition and detection for remote sensing images of various aircraft types.

4. The Proposed Aircraft Recognition Approach

In this study, a project was conducted for the recognition of military aircraft using VGG16 and VGG19 models. The MTARSI dataset was utilized throughout the project, following several stages as depicted in Figure 8. These stages comprise two main phases: “data preparation”, “training and testing”.

The initial stage, data preparation, involves several steps. First, the MTARSI dataset was thoroughly examined to ensure its suitability for training Convolutional Neural Networks (CNNs) for aircraft recognition. Relevant data were extracted from the dataset, focusing on obtaining a representative sample of images for various aircraft classes. The extracted data were then categorized into different classes of aircraft to facilitate supervised learning, which is crucial for training the CNN models to differentiate between various types of aircraft. Finally, the data were divided into three subsets: training data (80%), validation data (10%), and test data (10%). Training data was used to train the CNN models, validation data to validate the model during training and adjust hyperparameters, and test data to evaluate the final performance of the trained model.

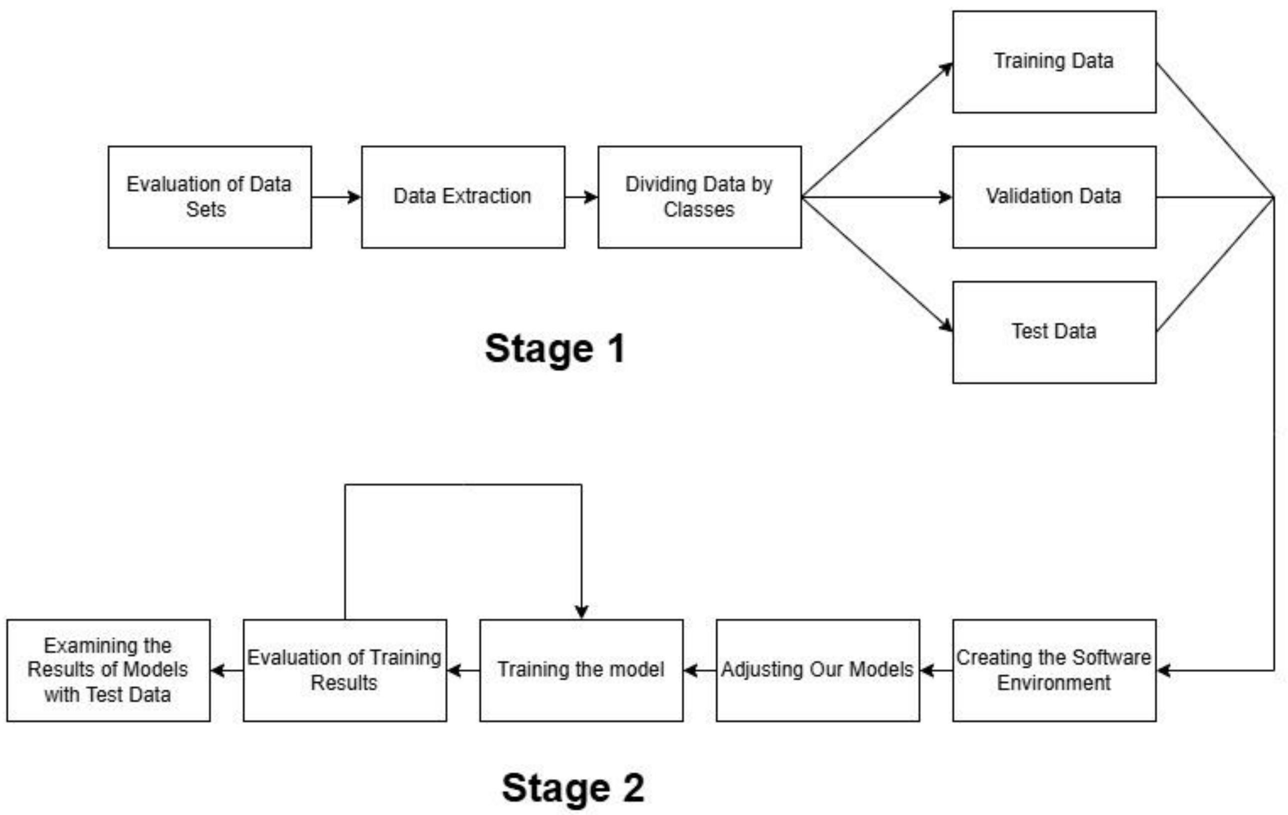

Figure 8: Flowchart of the proposed aircraft recognition approach.

The second stage, model training and testing, encompasses several sub steps. A suitable software environment was set up, including the installation of necessary libraries and frameworks such as TensorFlow and Keras. Initial parameters for the VGG16 and VGG19 models were set, and to prevent overfitting, the maximum epoch value was set to 10. The models were then trained by using the training data, which involved feeding the images into the models and optimizing the parameters through backpropagation. The performance of the models was evaluated by using the validation data, monitoring metrics such as accuracy and loss, and necessary adjustments were made to the models. Based on the evaluation results, parameters were fine-tuned, and the models were re-trained to improve the performance. Finally, the models were tested by using the test data, generating a confusion matrix and calculating test accuracy to assess the overall performance of the models.

The final trained models were evaluated by using the test data. The confusion matrix provided insights into the classification performance across different aircraft classes, and the test accuracy metric helped in quantifying the overall effectiveness of the models. The results indicated that both VGG16 and VGG19 models were successful in recognizing military aircraft with high accuracy, demonstrating the potential of CNNs in satellite image analysis for aircraft recognition.

In conclusion, the presented method successfully implemented VGG16 and VGG19 models for the recognition of military aircraft using satellite images from the MTARSI dataset. Through a structured approach involving data preparation, model training, and testing the models were optimized, and they demonstrated robust performance. Future work could explore the integration of additional data augmentation techniques and the use of other advanced CNN architectures to further enhance recognition accuracy.

5. Experimental Results and Discussions

In this study, deep learning models, specifically VGG-16 and VGG-19, were trained on the MTARSI dataset to classify aircraft images. The VGG-16 model demonstrated excellent performance, achieving an accuracy of 99.31% on the training set and 96.35% on the validation set (Figure 9). These results reflect both a strong fit to the training data and a robust generalization capability, indicating that the VGG-16 model successfully learned to classify images from the MTARSI dataset. However, given the widespread use of these architectures in similar studies, it is essential to explore novel modifications or techniques that could further differentiate the approach and improve its performance beyond the existing methods.

In comparison, the VGG-19 model, with its deeper architecture, also demonstrates excellent performance. Achieving a training accuracy of 99.62% and a validation accuracy of 98.96% (Figure 9), VGG-19 shows a strong fit to the training data and robust generalization to unseen data. While the VGG-19 model provides slightly higher accuracy than VGG-16, the marginal performance increase raises questions about the trade-off between model complexity and computational resources. The added depth of VGG-19 allows for more complex feature extraction, but future studies should investigate whether this increase in accuracy is substantial enough to justify the higher computational cost associated with deeper architectures.

These findings demonstrate that both VGG-16 and VGG-19 architectures can be effectively utilized for aircraft classification on the MTARSI dataset, each offering distinct advantages. While VGG-16 is more computationally efficient, with fewer layers and faster training times, VGG-19's deeper architecture enables more nuanced feature extraction, which could improve classification accuracy in more complex tasks. However, given the extensive use of these architectures in similar studies, future work could explore modifications, such as incorporating advanced regularization techniques or hybrid models, to further enhance the performance of these networks, particularly in specialized image datasets like MTARSI.

In recent years, deep learning models have revolutionized the field of computer vision, achieving unprecedented performance across a wide array of tasks. The Visual Geometry Group (VGG) architecture family has become one of the most influential approaches for image classification, delivering remarkable results on benchmark datasets such as ImageNet. Despite the success of VGG models in standard applications, there is an ongoing need to innovate and optimize these architectures for specific domains, such as satellite imagery or specialized datasets like MTARSI. Exploring modifications, such as layer-wise fine-tuning or novel data augmentation strategies, could further enhance their performance and applicability.

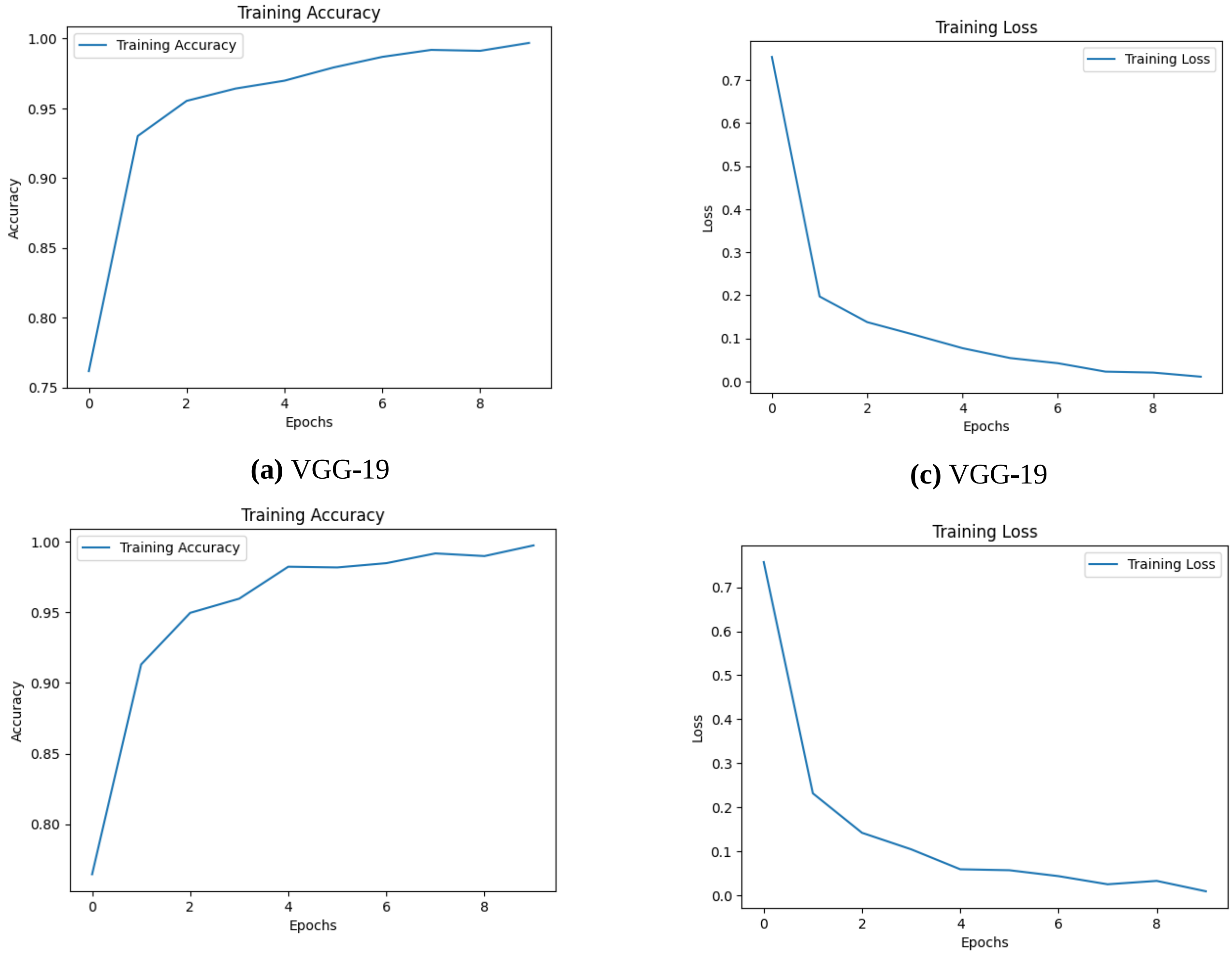

(a) VGG-19

(c) VGG-19

(b) VGG-16

(d) VGG-16

Figure 9: Training accuracy and Training loss for VGG-16 and VGG-19.

On a separate test dataset, VGG-19 achieved an accuracy of 85.03%, slightly surpassing VGG-16, which reached an accuracy of 84.71%. This result underscores the advantage of deeper architectures like VGG-19, which are capable of capturing more complex features from the data. However, the small difference in performance between the two models raises important questions regarding the trade-off between network depth and computational efficiency. Future research could explore alternative methods, such as model pruning or the use of lighter architectures, to maintain or even surpass these accuracy levels while reducing training time and resource usage.

In conclusion, our extensive experiments demonstrate that deep learning models, particularly VGG-19, significantly outperform traditional image processing methods across all evaluation metrics. The superior performance of these models, achieving accuracy rates of up to 85.03%, reinforces the paradigm shift towards deep learning approaches in modern image classification tasks. These findings have important implications for both theoretical understanding of deep architectures and practical applications in real-world scenarios.

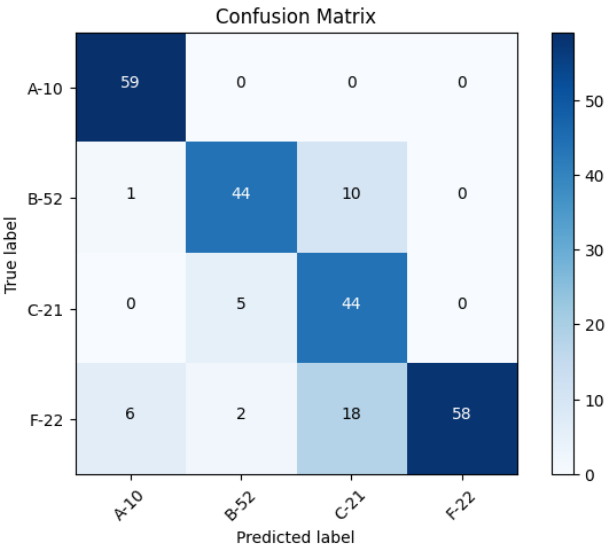

Figure 10: Confusion matrix for VGG-16.

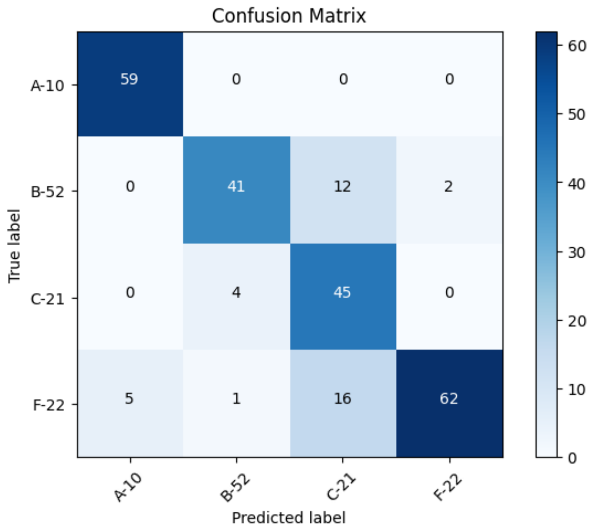

Figure 11: Confusion matrix for VGG-19.

The performance results of two different deep learning models (VGG-16 and VGG-19) are shown in the confusion matrices. Figure 10 presents the results of the VGG-16 model. In this model, there were 59 correct predictions for the A-10 class, 44 for the B-52 class, 44 for the C-21 class, and 58 for the F-22 class. Overall, the model demonstrated good classification performance although some classes exhibited confusion. Figure 11 displays the results of the VGG-19 model. In this model, there were 59 correct predictions for the A-10 class, 41 for the B-52 class, 45 for the C-21 class, and 62 for the F-22 class. The VGG-19 model performed better than VGG-16, particularly for the F-22 class, but it achieved slightly lower success for the B-52 class. Both models managed to predict the A-10 class exceptionally well.

Table 1 presents the accuracy rates of various machine learning (ML) and deep learning (DL) models across four distinct classes: A-10, B-52, C-21, and F-22. As highlighted in recent studies, deep learning models consistently outperform traditional machine learning approaches in classification accuracy. Specifically, convolutional neural networks (CNNs), such as VGG-16 and VGG-19, show exceptional performance across nearly all classes when compared to traditional methods like SIFT + BOWN, HOG + SVM, ScSPM, and LLC. These findings are consistent with recent advancements in deep learning-based image classification, which have demonstrated improved accuracy in complex tasks,

Table 1: Algorithms' comparison results.

Method	A-10	B-52	C-21	F-22
SIFT [17] + BOWN	0.49	0.56	0.60	0.48
HOG[18] + SVM	0.56	0.60	0.58	0.53
ScSPM [19]	0.61	0.61	0.60	0.51
LLC [20]	0.59	0.63	0.63	0.59
VGG-16 (The proposed model)	**1.00**	**0.80**	0.89	0.69
VGG-19 (The proposed model)	**1.00**	0.74	**0.91**	**0.73**

Several traditional machine learning techniques were evaluated for image classification across the four classes. The SIFT [17] + BOWN method, which combines Scale-Invariant Feature Transform (SIFT) for feature extraction and Bag-of-Words (BOWN) for classification, achieves accuracy rates of 49% for A-10, 56% for B-52, 60% for C-21, and 48% for F-22. The Histogram of Oriented Gradients (HOG) [18] combined with Support Vector Machines (SVM) achieves 56% for A-10, 60% for B-52, 58% for C-21, and 53% for F-22. The ScSPM [19] method, using spatial pyramid matching with sparse coding, reaches 61% for A-10, 61% for B-52, 60% for C-21, and 51% for F-22. Lastly, the LLC [20] method, which employs locality-constrained linear coding, achieves accuracy rates of 59% for A-10, 63% for B-52, 63% for C-21, and 59% for F-22. The hyperparameters, including the number of clusters for SIFT and kernel choice for SVM, are discussed in the experimental results section.

In terms of deep learning models, both VGG-16 and VGG-19 achieve significantly higher accuracy across all classes compared to traditional methods. The VGG-16 model achieves a perfect accuracy rate of 100% for A-10, 80% for B-52, 89% for C-21, and 69% for F-22. Similarly, the VGG-19 model reaches 100% accuracy for A-10, 74% for B-52, 91% for C-21, and 73% for F-22. These results align with the findings in recent literature, where VGG architectures were demonstrated to outperform other deep learning models in similar classification tasks. The choice of hyperparameters, such as learning rate, batch size, and the number of layers, plays a crucial role in model performance and is further detailed in the experimental results section.

Performance analysis by class reveals that the VGG-16 and VGG-19 models achieve the highest accuracy in the A-10 class, both attaining 100%, while the traditional SIFT + BOWN method demonstrates the lowest accuracy of 49%. In the B-52 class, the VGG-16 model yields the highest accuracy of 80%, whereas the SIFT + BOWN method achieves the lowest at 56%. The C-21 class sees the VGG-19 model lead with an accuracy of 91%, while the HOG + SVM method results in the lowest accuracy of 58%. Lastly, in the F-22 class, the VGG-19 model achieves the highest accuracy of 73%, with the lowest accuracy of 48% again observed for the SIFT + BOWN method. These results highlight the clear advantages of deep learning models, particularly VGG-19, in achieving higher accuracy across all classes.

In conclusion, deep learning models, especially the VGG-16 and VGG-19 architectures, significantly outperform traditional machine learning methods across all four classes. The VGG-19 model stands out, achieving the highest accuracy across all classes, including a perfect 100% accuracy for the A-10 class. The superior performance of these models, particularly in complex image classification tasks, emphasizes the potential of deep learning in overcoming the limitations of traditional methods. Unlike previous studies that primarily focused on individual models, this study demonstrates the clear advantages of VGG-16 and VGG-19 in a multi-class classification scenario, positioning them as preferred choices for machine learning applications in similar domains.

Table 2 presents a comparison of the accuracy rates achieved by various image classification methods. Traditional image processing and machine learning techniques, such as SIFT [17] combined with Bag-of-Words of Visual Words (BOVW) and Histogram of Oriented Gradients (HOG) [18] with Support Vector Machines (SVM), yield relatively lower accuracy rates of 53.25% and 56.75%, respectively. Other conventional methods, such as ScSPM [19] and LLC [20], demonstrate slightly higher performance, achieving accuracy rates of 58.25% and 61.00%, respectively. These results reflect the limitations of traditional approaches in handling more complex image classification tasks.

Table 2: Accuracy comparison.

Method	Accuracy
SIFT [17] + BOWN	53.25%
HOG[18] + SVM	56.75%
ScSPM [19]	58.25%
LLC [20]	61.00%
VGG-16 (The proposed model**)**	**84.71%**
VGG-19 (The proposed model**)**	**85.03%**

In contrast, deep learning models demonstrate a marked improvement in performance. Specifically, our experiments with the VGG-16 and VGG-19 models yield accuracy rates of 84.71% and 85.03%, respectively. These results underscore the superior capability of deep learning approaches in image classification tasks when compared to traditional methods. The higher accuracy achieved by these models is consistent with recent research highlighting the advantages of deep learning in complex classification problems. The success of deep learning models can be largely attributed to their deep, layered architectures and the large-scale datasets they are trained on, which enable these models to learn and distinguish complex patterns in images with greater efficiency. In particular, the VGG-19 model, with its deeper architecture, exhibits a slight performance advantage over VGG-16 in terms of accuracy. This reflects the potential of deeper models to capture more intricate features and improve classification outcomes.

In conclusion, deep learning models, particularly the VGG-19 architecture, have demonstrated superior accuracy rates compared to traditional image processing methods. This reinforces the growing evidence supporting the effectiveness of deep learning techniques in image classification tasks, especially in handling complex data and achieving high-performance results. The findings of this study contribute to the increasing body of research advocating for the use of deep learning in practical classification applications.

6. Conclusions

In this study, we investigated the application of VGG-16 and VGG-19 architectures for military aircraft classification using satellite imagery, achieving accuracies of 84.71% and 85.03% respectively. Additionally, our experiments showed that maximum efficiency was reached at 10 epochs, demonstrating efficient model convergence. While these results demonstrate improvement over traditional methods such as SIFT+BOWN (53.25%) and HOG+SVM (56.75%), it is important to acknowledge that our approach primarily utilized standard implementations of established architectures without significant novel modifications. The performance metrics across different scenarios varied considerably, with the highest accuracy achieved for A-10 classification (1.00) and lower performance for B-52 (0.74) and F-22 (0.73) classifications, suggesting room for improvement in handling certain aircraft types. Our comparative analysis reveals that while the results are promising, the improvements are incremental rather than transformative in nature.

The study's limitations highlight several opportunities for future research directions, including the development of custom architectural modifications specifically designed for satellite imagery analysis, integration of domain-specific preprocessing techniques, and exploration of hybrid approaches combining traditional computer vision methods with deep learning. Furthermore, the field would benefit from investigation into more recent architectural innovations and the incorporation of domain-specific knowledge into model design. Looking ahead, we believe that advancing this research area requires moving beyond standard implementations to develop novel methodological approaches that specifically address the unique challenges of satellite-based aircraft classification. This could include developing specialized layers or modules within the neural network architecture, implementing advanced data augmentation techniques specific to aerial imagery, and creating more robust feature extraction methods that better handle variations in aircraft orientation and atmospheric conditions. While our current results demonstrate the viability of deep learning approaches for military aircraft classification, they also underscore the need for more innovative solutions to push the boundaries of what is possible in this specialized domain.

Article Information Form

Financial Disclosure: The author (s) has no received any financial support for the research, authorship or publication of this study.

Authors' Contribution: The authors contributed equally to the study.

Conflict of Interest/Common Interest: No conflict of interest or common interest has been declared by the authors.

Ethics Committee Approval: This study does not require ethics committee permission or any special permission.

References

[1] Chen, H., Zhao, J., Gao, T., and Chen, W. (2018). Fast Airplane Detection with Hierarchical Structure in Large Scene Remote Sensing Images at High Spatial Resolution. *IEEE International Geoscience and Remote Sensing Symposium, Valencia, Spain, July 22-27, 4846–4849.*

[2] Luo, Q., and Shi, Z. (2016). Airplane detection in remote sensing images based on Object Proposal. *International Geoscience and Remote Sensing Symposium (IGARSS), 1388–1391.*

[3] Fukushima, K. N. (1980). A self-organizing neural network model for a mechanism of pattern recognition unaffected by shift in position. *Biol. Cybern., 36(4): 193–202.*

[4] Hubel, D. H. and Wiesel, T. N. (1968). Receptive fields and functional architecture of monkey striate cortex. *J. Physiol., 195(1):215–243.*

[5] Le Cun, Y., Bottou, L., Bengio, Y., and Haffner, P. (1998). Gradient-based learning applied to document recognition. *Proc. IEEE, 8(11): 2278–2324.*

[6] Le Cun, Y., Bengio, Y., and Hinton, G. (2015). Deep learning. *Nature*, 521: 436–444.

[7] Le Cun, Y., (1989). Handwritten digit recognition: applications of neural network chips and automatic learning. *IEEE Commun. Mag., 27(11): 41–46.*

[8] Cirean, D., Meier, U., and Schmidhuber, J. (2012). Multi-column Deep Neural Networks for Image Classification., Feb. 2012.

[9] Cirean, D. C., Meier, U., Masci, J., and Gambardella, L. M. (2012). Flexible, High Performance Convolutional Neural Networks for Image Classification. *in Proceedings of the 22nd International Joint Conference on Artificial Intelligence, 1237–1242.*

[10] Farfade, S. S., Saberian, M., and Li, L.-J. (2015). Multiview Face Detection Using Deep Convolutional Neural Networks. *Proceedings of the 5th ACM on International Conference on Multimedia Retrieval. 643–650.*

[11] Grefenstette, E., Blunsom, P., de Freitas, N., and Hermann, K. M. (2014). A Deep Architecture for Semantic Parsing. *The Semantic Parsing Workshop, April.*

[12] Shen, Y., He, X., Gao, J., Deng, L., and Mesnil, G. (2014). Learning semantic representations using convolutional neural networks for web search. *23rd International Conference on World Wide Web - WWW '14 Companion, 373–374.*

[13] Kalchbrenner, N., Grefenstette, E., and Blunsom, P. (2014). A Convolutional Neural Network for Modelling Sentences. *Proceedings of the 52nd Annual Meeting of the Association for Computational Linguistics. 655-665.*

[14] Kim, Y. (2014). Convolutional neural networks for sentence classification. *Conference on Empirical Methods in Natural Language Processing (EMNLP). 1746-1751.*

[15] Collobert, R. and Weston, J. (2008). A unified architecture for natural language processing: Deep neural networks with multitask learning. *25th International conference on Machine learning. 20(1):160–167.*

[16] Wallach, I., Dzamba, M., and Heifets, A. (2015). AtomNet: A Deep Convolutional Neural Network for Bioactivity Prediction in Structure-based Drug Discovery.

[17] Lowe, D.G. (2004). Distinctive image features from scale-invariant keypoints, Int. *J. Comput. Vision. 60(2): 91–110.*

[18] Dalal, N., Triggs, B. (2005). Histograms of oriented gradients for human detection, *IEEE Computer Society Conference on Computer Vision and Pattern Recognition (CVPR 2005), San Diego, CA, USA. 886–893.*

[19] Yang, J., Yu, K., Gong, Y., Huang, T.S. (2009). Linear spatial pyramid matching using sparse coding for image classification, *IEEE Computer Society Conference on Computer Vision and Pattern Recognition (CVPR 2009). 1794–1801.*

[20] Yu, K., Zhang, T. and Gong, Y. (2009) Nonlinear learning using local coordinate coding, *Advances in Neural Information Processing Systems, Vancouver, Canada, 2223–2231.*

J Inno Sci Eng, 2025, 9(1):15-27

DOI:https://doi.org/ 10.38088/jise.1569070

Research Article

A case study on the impact of Micromobility on Four-Arm Signalized Intersection Performance

Mehmet Rizelioglu [1]

[1] *Department of Civil Engineering, Uludag University, Bursa, Türkiye*

ARTICLE INFO

Received Date: 17/10/2024
Accepted Date: 17/02/2025

Cite this paper as:
Rizelioglu M. (2025). *A case study on the impact of Micromobility on Four-Arm Signalized Intersection Performance.*Journal of Innovative Science and Engineering. 9(1): 15-27

*Corresponding author: Mehmet Rizelioglu
E-mail:rizelioglu@btu.edu.tr

Keywords:
Micromobility
PTV VISSIM
Intersection

ABSTRACT

With increasing urbanization, problems such as traffic congestion and environmental pollution have become more pronounced. Alternative modes of transportation such as micromobility (bicycles, e-scooters, e-bikes, segways) have the potential to reduce these problems. This study analyzes the effects of micromobility on the performance of an intersection using a simulation-based approach. A four-arm signalized intersection in Nilüfer, Bursa, is taken as a model, and the impact of micromobility on intersection performance is evaluated in terms of "average vehicle speed", "queue delay", and "vehicle travel time" performance indicators. In the study, the inclusion of micromobility at low levels (2.5% and 5%) improves intersection performance, while at higher levels (7.5% and 10%) this improvement is reversed, resulting in longer travel times and lower speeds. Signal modification has shown an improvement in the performance of the intersection. However, these results suggest the need for special signaling studies for micromobility vehicles at intersections. The study provides important findings for transportation management and policy makers in micromobility planning.

1. Introduction

The increase in urban populations leads to transportation problems such as traffic congestion, environmental pollution and stress. Transportation has a major impact on air pollution; 80% of air pollution in Asian cities is caused by transportation [1]. In addition, private car use reduces people's physical activity, leading to unhealthy lifestyles. Therefore, transportation policy makers are working to reduce these negative impacts. In particular, they effort focus on reducing traffic congestion and encourage people to public transportation and micromobility (bicycles, e-scooters, etc.) solutions. Reducing the use of private cars in cities and promoting environmentally friendly modes of transportation are the basis of sustainable transportation policies [2-4]. Multimodal and personalized transportation services are being developed with solutions such as Mobility as a Service (MaaS) [6,7].

Micromobility can contribute to improving the coverage of public transport services by replacing short-distance trips (e.g. daily round trips) made by private vehicles [1,7]. Comi and Polimeni [1] note that micromobility is an important lever supporting the transition from motorized modes of transport. In this context, traffic simulations are required to assess the impact of micromobility in a mixed traffic environment and its contribution to sustainability [8].

Studies on micromobility have focused on different areas. Some studies examine how micromobility promotes the transition to zero-emission sustainable modes of transportation [9]. Other studies have focused on cultural, legal and political factors that may hinder the use of this environmentally friendly transportation [10]. The environmental performance of micromobility has been addressed through life cycle assessment [11,12], with [12] comparing shared and private micromobility. Sun and Ertz [11] emphasized that the low utilization rates of shared micromobility are not enough to reduce emissions and stated that more incentive policies are needed. In addition, it is possible to come across some studies on the effects of micromobility on traffic safety in the literature. Asensio et al. [13] stated that some cities have banned MM vehicles due to personal safety and other concerns. Comi et al. [14] stated that the absence of any restrictions for MM users is a threat to traffic safety and that appropriate traffic regulations and education programs should be made for MM users. According to a study conducted in Lithuania by Asiūnienė and Tumavičė [15], e-scooter users increased the number of accidents by 58.06% between 2019 and 2020, and nearly 65% of them were involved in accidents with motor vehicles. They observed that accidents mostly occurred at intersections and pedestrian crossings.

For this purpose, this study investigates the changes in intersection performance when micromobility vehicles are included in the traffic. For this, the current situation is analysed in the traffic simulation program (PTV VISSIM). Then, bicycles, e-bikes, e-scooters and segways, which are micromobility vehicles, are modelled in the simulation program and included in the study. Roller skates, push scooters, hoverboards, solowheels, etc. are not included in this study due to their low usage and very rare occurrence in traffic. Intersection performance is considered in terms of queue delay, average vehicle speeds and travel times. The second section of the paper presents the methodology, the next section presents the results, and the fourth section presents the conclusions.

2. Material and Methods

In this study, we investigate the changes in the performance of an intersection when non-motorized vehicles, i.e., micromobility vehicles, are substituted for the travel demands of a certain proportion of motorized vehicles in normal traffic. For this purpose, Uğur Mumcu intersection (400 13' 13" N, 280 54' 53" E) in Özlüce district of Nilüfer county of Bursa province is selected as a field study (Fig. 1). This intersection is chosen because it is close to the main arteries and signalizations are planned for pedestrian crossings.

Figure 1: View of Uğur Mumcu signalized interseciton

This signalized four-arm roundabout type intersection has traffic lights inside the intersection in addition to the approach arms. Yüzüncüyıl (YY) and hospital arms are two lanes, Özlüce and İzmir arms are three lanes. Lane widths are 3.5m. At this intersection, 15-minute video recordings are taken on weekdays between 17:00-18:00 on Friday (08.03.2024), which is the peak hour. The video recordings are analyzed and vehicle counts are made to determine the traffic volumes and vehicle composition at the intersection arms, as well as the vehicle flow rates. Signalization times of the intersection are obtained from Bursa Transportation Coordination Center (UKOME). VISSIM, a traffic simulation program, is used to analyze the behavior of micromobility vehicles and their impact on the intersection. The flowchart of the study is given in Fig. 2.

2.1. Substitution of micromobility vehicles for motorized vehicles

In the study, existing vehicle compositions will be replaced by micromobility vehicles. This requires the number of passengers in various vehicle classes to be known. Thus, micromobility vehicles will be added to the simulation network according to the number of vehicles and, thus, the number of passengers pulled from the intersection.

Table 1: Occupancy rates and number of trips by vehicle composition

	Car	Bus	Minibus	Service	Truck	Motorbike	Total
				Yüzüncüyıl (YY)			
Vehicle rate (%)	91	0.7	3	0.7	1.1	3	100
Number of Vehicle	888	7	29	7	11	32	974
Occupancy rate	1.6	28.2	28.2	12.14	1	1	
Number of trips	1421	198	818	99	11	32	2579
Trip rate (%)	55	7.6	32	3.9	0.4	1.2	100
				Özlüce			
Vehicle rate (%)	82.57	0.27	4.46	3.38	5.00	4.32	100
Number of Vehicle	1222	4	66	50	74	64	1480
Occupancy rate	1.6	28.2	28.2	12.14	1	1	
Number of trips	1955	113	1861	607	74	64	4674
Trip rate (%)	41.82	2.41	39.8	12.98	1.58	1.36	100
				Hospital			
Vehicle rate (%)	87.43	0.40	2.57	3.76	1.39	4.46	100
Number of Vehicle	883	4	26	38	14	45	1010
Occupancy rate	1.6	28.2	28.2	12.14	1	1	
Number of trips	1413	113	733	461	14	45	2779
Trip rate (%)	50.83	4.05	26.38	16.59	0.50	1.62	100
				İzmir			
Vehicle rate (%)	87.05	0.11	2.91	3.75	4.03	2.13	100
Number of Vehicle	1553	2	52	67	72	38	1784
Occupancy rate	1.6	28.2	28.2	12.14	1	1	
Number of trips	2484	56	1466	813	72	38	4931
Trip rate (%)	50.39	1.14	29.73	16.49	1.46	0.77	100

The number of passengers in a vehicle indicates its occupancy rate. While each vehicle type has different occupancy rates, this varies according to different travel types, travel timing, countries and regions, the number of vehicles in the household, and even income. There are many studies in the literature on the determination of vehicle occupancy rates.

Barton-Aschman Associates [16] found that the lowest vehicle occupancy rates are associated with home-to- work travel. The National Travel Survey 2010-2012 found that vehicle occupancy rates vary by trip purpose, being lowest for commuting and work (1.2 passengers/vehicle) and highest for vacations/day trips and education (2 passengers/vehicle). In studies, vehicle occupancy rates vary from country to country. According to the European Environment Agency (EEA 2010), in Eastern European countries such as the Czech Republic, Slovakia and Hungary, it is 1.8 passengers per vehicle (1.4 passengers per vehicle in the Czech Republic, 2 passengers per vehicle in Slovakia and 1.9 passengers per vehicle in Hungary, respectively). A study led by a World Bank team (2010) found that vehicle occupancy rates for passenger cars, pickups, motorcycles, taxis, microbus, minibuses and buses in Cairo were 1.5, 1.3, 1.0, 2.5, 13, 21 and 49 passengers/vehicle respectively.

In this study, the vehicle occupancy values of the Istanbul Transportation Master Plan [17] are used for vehicle occupancy rates (Table A1), since they refer to the same country/region and similar working hours. For this purpose, travel data are collected from 9 different regions and occupancy values are determined by dividing the total number of passengers by the number of vehicles. In terms of vehicle volumes, the number of motor vehicles coming from each intersection arm is reduced by 2.5% to 10%. Table 1 shows the number and proportions of micromobility vehicles that should replace motorized vehicles with the percentages mentioned above.

2.2. Simulation study

The fact that urban infrastructure is conducive to the use of micromobility vehicles will, of course, have a significant impact on people's use of these modes of transportation. This also reflects the necessary conditions for sustainable transportation. Studies have been conducted in different cities on how users would change their transportation mode choice behavior in the presence of micromobility infrastructure [1]. In a survey conducted in Paris, Christoforou et al. [18] found that micromobility is used for trips of more than 4 km and less than 15 minutes. It is observed that 21% of these trips are made by motorized vehicles and 35% on foot. In another study in Oslo, 60% of micromobility users walked, 23% used transit systems, 3% used private vehicles and the rest used other modes [19]. In this study, micromobility vehicles such as roller skates and skateboards were not included in the simulation because they are used more for recreational purposes and are much less common than vehicles such as bicycles or e-scooters. In addition, e-scooter and Segway vehicles are not defined in the simulation, so these vehicles are modeled separately and included in the simulation (Fig. 2).

The intersection is modeled in VISSIM [20], one of the most important traffic simulation programs. The maximum value of the 15-minute vehicle count data obtained from traffic counts is entered as hourly volume. The vehicle composition (cars, trucks, buses, motorcycles, service vehicles, etc.) is entered into the program as a proportion of the traffic volume. The directional distribution of vehicles is also specified as relative traffic flow (see Table A2). The flowchart of the simulation model is shown in Fig. 3. The design started with the simulation modeling of urban and bicycle roads with micromobility vehicles and continued with the tuning of the driving behavior parameters of the micromobility (MM) vehicles, which is described in detail at the end of this section.

In the VISSIM simulation program, the driving behavior parameters of the vehicles are specified with Wiedemann 99. The acceptable error difference between the observed values of the driving behavior parameters and the simulation results should be within 15% [21,22]. A total of four data collection points are set up, one at each exit point of the intersection arms, considering the traffic counts every 15 minutes passing through the intersection arms (Fig. 4a).

The simulation run is run 10 times with different seed numbers (42 random seeds and 51 random seed increments) after each calibration run of the driving behavior parameters. The resolution of the simulation is set to 0.1 seconds (see Fig. 3). In addition, since the presence of signals inside the island at the intersection changes the simulation values considerably, and to get closer to the observed values, these signals inside the island (5,6,7, and 8 signals, see Fig. 4 b) are removed.

The error between 15-minute traffic volumes is considered as the margin of error (MOE). The percentage error between simulated data and field observed data for the data collection points specified at the intersection is calculated using Equation (1);

$$\%\ Error = (OTV - STV)/OTV \quad (1)$$

where:

OTV: Observed traffic volume

STV: Simulated traffic volume

Lewis [23] reported a good fit for MAPE between 10% and 20%, but excellent for MAPE values below 10%.

Mean absolute percentage error (MAPE), one of the goodness-of-fit indices, is used to find the difference in error between the observed values and the simulated values according to the calibration.

$$MAPE = \frac{1}{N}\sum_{i=1}^{N}\left|\frac{(x_i - \hat{x}_i}{x_i}\right| * 100 \quad (2)$$

where, N is the total number of traffic measurement observations, x and $\hat{x}$ are, respectively, observed and simulated data points at a time-space domain. In addition, Table 2 shows the MAPE results between the traffic data obtained from the field and the simulated data.

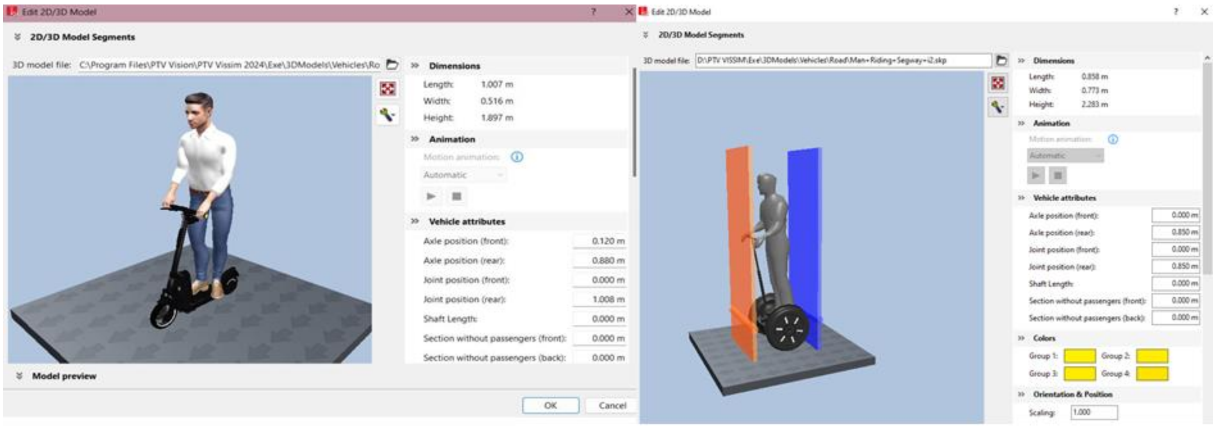

Figure 2: Modeling vehicles of e-scooter and segway at VISSIM.

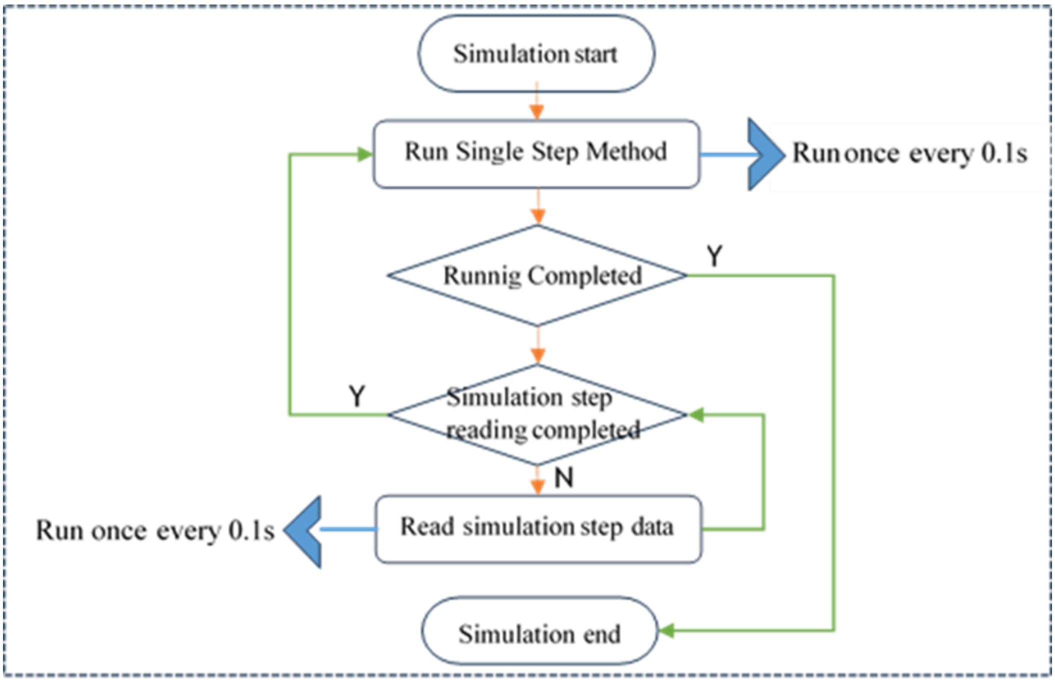

Figure 3: Simulation run update flow chart.

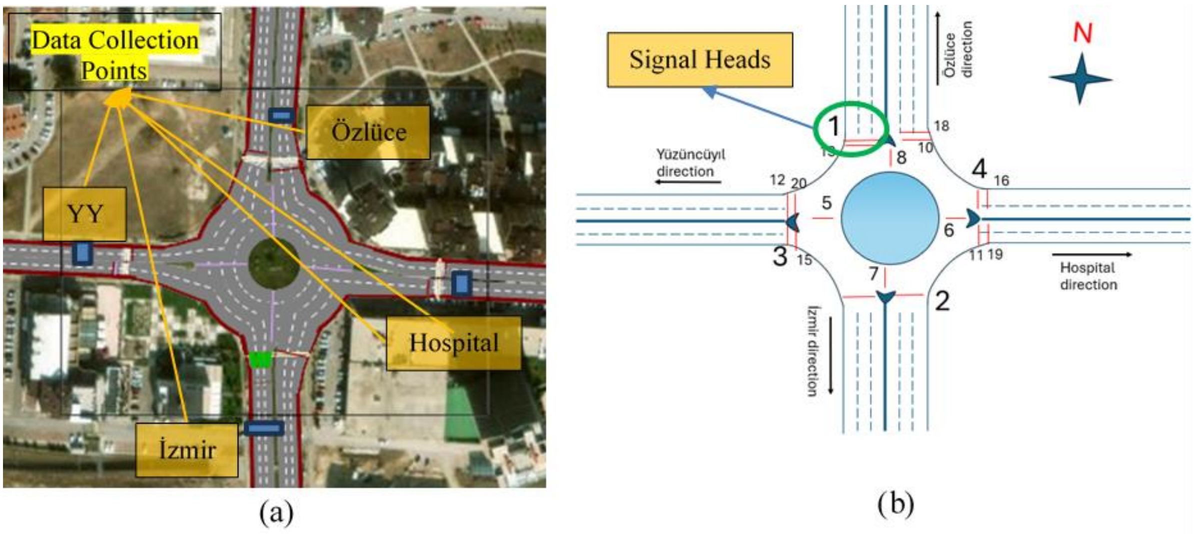

Figure 4: Data collection points on the intersection (a) and signal heads (b).

Table 2: MAPE values according to observed datas and simulated results at Uğur Mumcu intersection

Data Collection Points	Time interval	OTV	STV	% Error	MAPE (%)
1	17:00-17:15	222	194	0.13	5.53
	17:15-17:30	244	239	0.02	
	17:30-17:45	229	229	0.00	
	17:45-18:00	266	246	0.08	
2	17:00-17:15	342	334	0.02	8.32
	17:15-17:30	382	345	0.10	
	17:30-17:45	417	341	0.18	
	17:45-18:00	337	351	-0.04	
3	17:00-17:15	213	184	0.14	9.18
	17:15-17:30	228	218	0.04	
	17:30-17:45	249	212	0.15	
	17:45-18:00	214	227	-0.06	
4	17:00-17:15	460	339	0.26	9.36
	17:15-17:30	481	440	0.09	
	17:30-17:45	471	419	0.11	
	17:45-18:00	419	423	-0.01	

In addition, the driving behavior parameters of e-bicycle, e-scooter and segway vehicles are also modeled for the bicycle driving behavior parameters of the simulation program. In previous studies, acceleration and deceleration and average speeds for comfortable, sudden and unexpected situations for these vehicles are examined [24-26]. In this study, the acceleration and deceleration acceleration values of e-bicycle, e-scooter and segway vehicles are based on the findings of [24] (Table 3). The design of the bicycle lanes in the simulation is modeled to be right next to the normal roadway and at a separate service level from this roadway and their width is arranged to be 1.5m (T.S 9826).

3. Results and Discussions

A microsimulation program is used to evaluate the intersection performance. Average speed, vehicle travel time and queue delay are selected as performance metrics. Fig. 5 shows the simulation results at different arms of the intersection according to the scenario where motor vehicles are removed from the traffic at certain rates and micromobility vehicles (MM) are included. Fig 5(a) shows how the average speeds change with the increase of micromobility vehicles. At Yüzüncüyıl (YY), Hospital and İzmir, there is an increase in the average speed of the vehicles because of removing up to 7.5% of motor vehicles from the traffic and replacing them with the micromobility vehicles shown in Table 4. However, as more motor vehicles are withdrawn from traffic and replaced with MM vehicles (-10%), there is a steady decrease in average speeds. At Özlüce, there is a significant decrease in average speed from 5% onwards. This may indicate that the traffic flow at Özlüce is more sensitive to micromobility. In general, it is possible to say that as the proportion of micromobility vehicles in traffic increases, a decrease in average speeds is observed.

Fig. 5b shows how queue delay changes with the increase of micromobility vehicles in traffic. For all locations, the introduction of MCCs up to 5% decreases the queue delay, but when this percentage increases to 7.5% and 10%, it increases the queue delay in the opposite direction and with a high output.

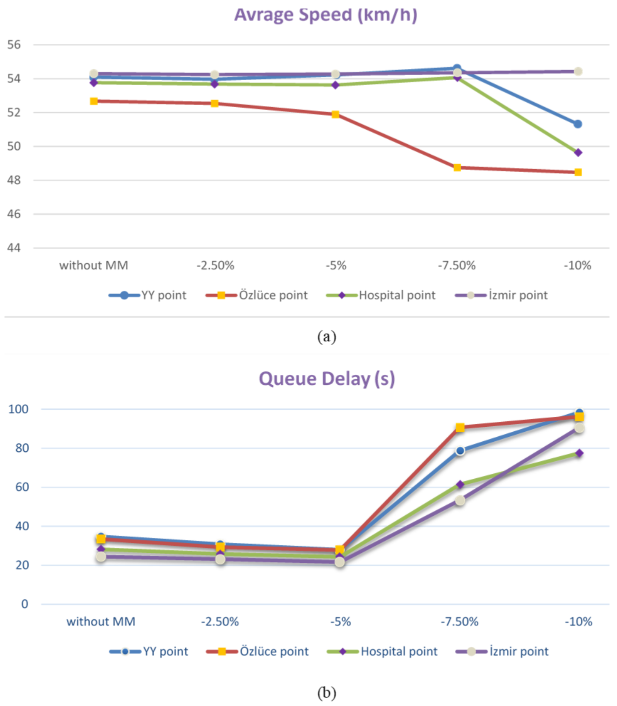

Figure 5: Average speed (km/h) and (b):queue delay

Fig. 6 shows how travel times on different routes change as micromobility vehicles increase in traffic. Each graph reflects the change in travel times for a given direction of travel as motorized vehicles are removed from traffic and replaced by micromobility vehicles. Fig. 6a shows the travel times of vehicles from YY to Hospital, İzmir and Özlüce, and shows an increase in travel times as motorized vehicles decrease and micromobility vehicles increase in traffic. In particular, the travel time to Hospital increases significantly with the increase of 7.5% and 10% of micromobility vehicles. Although there is also an increase in travel times to Izmir and Özlüce, this increase is not as significant as at Hospital. This can be explained by the fact that micromobility vehicles slow down the traffic flow at intersection crossings, thus increasing the travel time.

This is an indication that the signal durations for pedestrian crossing are not suitable for MM vehicles and a separate signalization study for MM is required.

Table 3: Behavioral parameters used in the study to simulate micromobility vehicles

VISSIM parameters	Reference	Bicycle	e-bicycle	e-scooter	Segway
Acceleration (Comfort) [m/s^2] (CC8)	Doza et al [24]	0.45 ± 0.11	0.70 ± 0.12	0.56 ± 0.19	0.67 ± 0.36
Acceleration (Harsh) [m/s^2] (CC8)	Doza et al [24]	0.76 ± 0.28	0.95 ± 0.14	0.70 ± 0.25	1.01 ± 0.34
Deceleration (Comfort)	Doza et al [24]	-1.50 ± 0.51	-1.65 ± 0.66	-1.28 ± 0.42	-0.93 ± 0.40
		3.00 ± 0.51	-3.10 ± 1.25	-2.21 ± 0.59	-1.65 ± 0.59
Deceleration (Harsh planned)	Doza et al [24]	-3.60 ± 1.28	-3.66 ± 1.07	-2.23 ± 0.71	-1.60 ± 0.49

Fig. 6(b) shows the travel times from Özlüce to YY, Izmir and Hospital. There are significant increases in travel times starting from 5% of micromobility vehicles. Travel time to Hospital shows the largest increase compared to other points as the micromobility rate increases. Travel times to YY and Izmir also increase, but not as dramatically as to Hospital. This graph reveals that the impact of micromobility on travel time is greater, especially in the Hospital direction.

Fig. 6(c) shows a rapid increase in travel times with the increase of micromobility vehicles in traffic, especially from 7.5% onwards. Travel times to Hastane and Özlüce are quite close to each other, and travel times increase almost at the same level with the increase in the micromobility rate. The travel time to YY shows a slower increase. This may indicate that the roads from Izmir to the hospital and Özlüce are more sensitive to micromobility.

Fig. 6(d) shows that travel times to YY and Izmir routes start to increase significantly after a 5% increase in micromobility. The travel time to Özlüce remains at the lowest levels, but reaches a similar level to the other points with an increase in the micromobility rate to 10%. This may indicate that travel times in the direction of the hospital vary less according to the micromobility rate.

It is possible to say that the increase of micromobility vehicles in traffic has significantly increased travel times. However, the response of each route to this change is different; in particular, vehicles traveling in the Hospital direction seem to be more sensitive to the increase of micromobility vehicles in traffic.

These performance cases show us that removing motor vehicles from traffic and replacing them with micromobility vehicles, with the occupancy rates of motor vehicles, will not always be beneficial, especially in key areas of road networks, such as intersections. This is because up to 2.5% and 5%, intersection performance in queuing delays, average speeds, and vehicle travel times is found to improve at the current signal level. However, as this ratio increases (after 5%), contrary to expectations, a decrease in these performance criteria is observed. The reason for this can be said to be that the signalization between the intersection arms prevents the passage of motor vehicles. This is because as the proportion of MM vehicles increases in these areas, MMs also create queues on the road, preventing the passage of motor vehicles. This situation is similar at all intersection arms. For this reason, signal optimization studies should be carried out in appropriate places in the current situation.

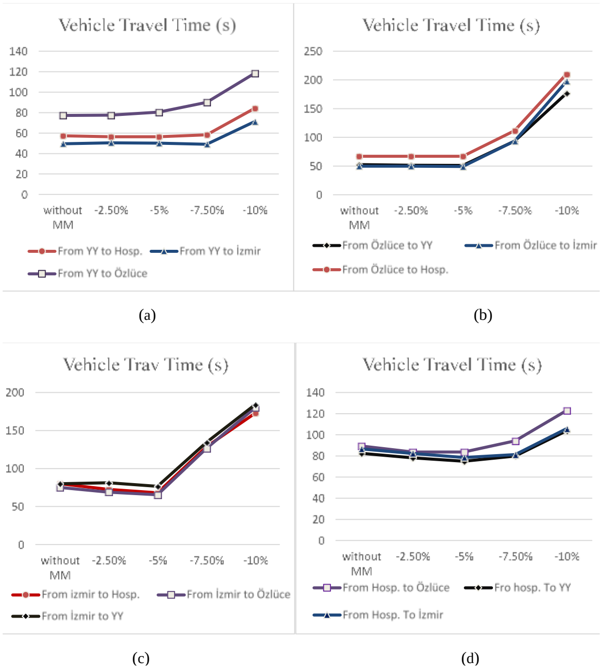

Figure 6: Travel time; (a): from YY, (b): from Özlüce, (c): from İzmir, (d): from Hospital

The adjustments in signal timings resulted in significant improvements in performance indicators. Signal timing plans are given in Fig. A1. As shown in Fig. 7, these adjustments optimized the passage times on both main arteries and intersection approaches. As a result, there is a noticeable improvement in all performance metrics. As seen in Fig. 7a, vehicle travel times improved by up to 7.5% MM. Similarly, while the queuing delay in the existing signal timings worsened after 5% MM, the adjusted signal timings showed an improvement of up to 7.5% MM (Fig. 7b). In addition, Fig. 8 shows the change in average speed after signal adjustment. That is, the decrease after 5% MM before signal adjustment increased up to 7.5% MM after signal adjustment. This also improved the performance in each direction of the intersection. To illustrate the improvement in intersection performance, a comparison of the queuing delay results only is given as an example in Table 4.

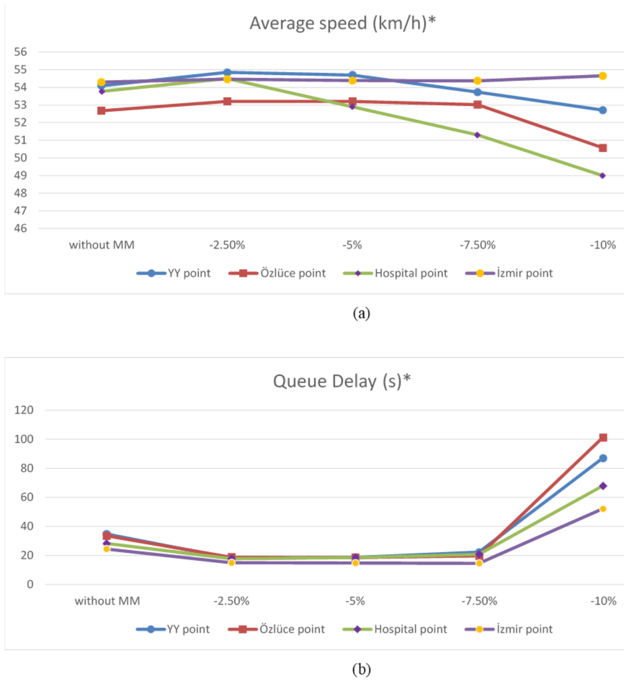

*After signal modification

Figure 7: Intersection performance after signal modification, (a):Average speed (km/h), (b): Queue delay

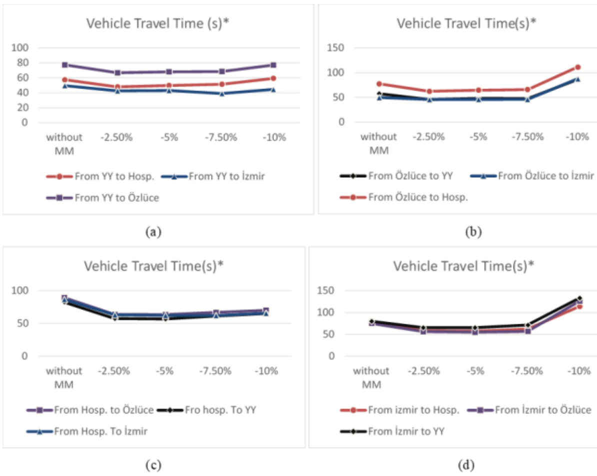

*after signal modification

Figure 8: Travel time after signal modification; (a): from YY, (b): from Özlüce, (c): from Hospital, (d): from İzmir

Table 4: Comparisons of queue delay results after adjusting signal duration

	Without MM	-2.50%	-2.50%*	-5%	-5%*	-7.50%	-7.50%*	-10%	-10%*
YY point	34.770	30.792	18.083	27.924	18.712	78.754	22.284	98.413	86.970
Özlüce point	33.496	29.361	18.862	27.871	18.608	90.665	19.728	96.182	101.146
Hospital point	28.235	25.793	17.874	24.350	18.586	61.469	20.825	77.545	67.935
İzmir point	24.475	23.121	15.042	21.711	14.774	53.306	14.594	90.595	52.130

*Considering adjusted signal duration

However, when MM vehicles constitute 10% of the traffic, a sudden deterioration in intersection performance is observed. This occurs because the traffic signals, which regulate the flow between different directions of the intersection, fail to allocate sufficient time for the passage of MM vehicles. As a result, MM vehicles form queues on the roadway, obstructing the movement of motorized vehicles (Fig. 9). This leads to increased queue delays and travel times, while average speeds decrease.

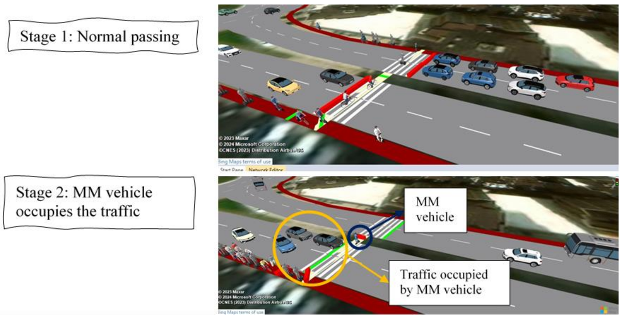

Figure 9: Effecting of MM vehicles on traffic

In the end, it is seen that the performance of intersections, especially MM intersections, can be improved with an adjustment in signal durations, but it is still necessary to conduct a signal optimization study to achieve the best performance.

4. Conclusion

This study investigates changes in an intersection's performance due to micromobility (MM). For this purpose, a four-arm signalized intersection in the Bursa Nilüfer region is modeled in a simulation environment. To analyze the performance of MM vehicles at the intersection, hypothetical bicycle roads are added to the simulation environment, and bicycles, e-scooters, and segway vehicles, which are micromobility vehicles, are also modeled in the simulation environment with driving behavior parameters. The MM equivalent of the area occupied by the vehicles in the traffic is calculated based on the data obtained from previous studies. Thus, motorized vehicles are removed from the traffic at the rates of 2.5%, 5%, 7.5%, and 10% without micromobility (MM), and MM vehicles are included in the system in proportion to the area (number of passengers) occupied by these vehicles in the traffic. Thus, the performance of the intersection is analyzed for these five different cases in terms of three performance indicators, including average vehicle speed, queue delay, and vehicle travel times. When the MM ratio at the intersection is low (2.5%-5%), the average vehicle speed increases by up to 8.2%, while the queuing time decreases by 13.5% and the vehicle travel time improves. However, the intersection performance deteriorated when the MM ratio increased above 5%. At 10% MM, queuing delays increased by 35%, average speeds decreased by 14%, and vehicle travel times worsened due to inefficient signal phasing for MM vehicles. This is also because MM vehicles have to wait while crossing between intersection arms due to inappropriate signaling, which prevents the passage of other motor vehicles. This worsens the performance of the intersection as MM vehicles enter the traffic after a certain percentage. All performance indicators show a better trend with the adjustment of the signal duration. After this adjustment, queuing delays for 7.5% MM decreased by 21% and travel times improved by 9% compared to the previous signal conditions. However, there is still poor performance, especially at 10% MM in traffic. This situation requires a special signalization study for MM vehicles at intersection crossings. Additionally, this study guides policymakers and transportation management decision-makers in their non-motorized transportation planning and future decision-making processes by demonstrating the effects of MM vehicles on intersection performance. This study can be further developed through a priority signal optimization study for MM users. Furthermore, the impact of MM vehicles on traffic safety and MM user behavior under different traffic conditions can be investigated. Such studies will contribute to making urban transportation more efficient.

Article Information Form

Funding

The author (s) has no received any financial support for the research, authorship or publication of this study.

Authors' Contrtibution

The author confirms sole responsibility for the study.

The Declaration of Conflict of Interest/Common Interest

No conflict of interest or common interest has been declared by the authors.

The Declaration of Ethics Committee Approval

This study does not require ethics committee permission or any special permission.

References

[1] Comi, A., Polimeni, A. Assessing potential sustainability benefits of micromobility: a new data driven approach. Eur. Transp. Res. Rev. 16, 19 (2024). https://doi.org/10.1186/s12544-024-00640-6.

[2] Vitetta, A. (2022). Sentiment Analysis Models with Bayesian Approach: A Bike Preference Application in Metropolitan Cities. Journal of Advanced Transportation, 2022, 1-12. https://doi.org/10.1155/2022/2499282 .

[3] Redman, L., Friman, M., Gärling, T., & Hartig, T. (2013). Quality attributes of public transport that attract car users: A research review. Transport Policy, 25, 119-127. https://doi.org/10.1016/j.tranpol.2012.11.005 .

[4] Musolino, G., Rindone, C., & Vitetta, A. (2022). Models for Supporting Mobility as a Service (MaaS) Design. Smart Cities, 5(1), 206-222. https://doi.org/10.3390/smartcities5010013

[5] Alyavina, E., Nikitas, A., & Tchouamou Njoya, E. (2020). Mobility as a service and sustainable travel behaviour: A thematic analysis study. Transportation Research Part F: Traffic Psychology and Behavior, 73, 362-381. https://doi.org/10.1016/j.trf.2020.07.004

[6] Hensher, D. A. (2017). Future bus transport contracts under a mobility as a service (MaaS) regime in the digital age: Are they likely to change? Transportation Research Part A: Policy and Practice, 98, 86-96. https://doi.org/10.1016/j.tra.2017.02.006.

[7] Fan, Z., & Harper, C. D. (2022). Congestion and environmental impacts of short car trip replacement with micromobility modes. Transportation Research Part D: Transport and Environment, 103, 103173. https://doi.org/10.1016/j.trd.2022.103173.

[8] Reck, D. J., Haitao, H., Guidon, S., & Axhausen, K. W. (2021). Explaining shared micromobility usage, competition and mode choice by modeling empirical data from Zurich, Switzerland. Transportation Research Part C: Emerging Technologies, 124, 102947. https://doi.org/10.1016/j.trc.2020.102947.

[9] Abduljabbar, R. L., Liyanage, S., & Dia, H. (2021). The role of micro-mobility in shaping sustainable cities: A systematic literature review. Transportation Research Part D: Transport and Environment, 92, 102734. https://doi.org/10.1016/j.trd.2021.102734.

[10] Bardal, K. G., Gjertsen, A., & Reinar, M. B. (2020). Sustainable mobility: Policy design and implementation in three Norwegian cities. Transportation Research Part D: Transport and Environment, 82, 102330. https://doi.org/10.1016/j.trd.2020.102330.

[11] Sun, S., & Ertz, M. (2022). Can shared micromobility programs reduce greenhouse gas emissions: Evidence from urbantransportation bigdata. Sustainable Cities and Society, 85 104045. https://doi.org/10.1016/j.scs.2022.104045.

[12] Bortoli, A. (2021). Environmental performance of shared micromobility and personal alternatives using integrated modal LCA. Transportation Research Part D: Transport and Environment, 93, 102743. https://doi.org/10.1016/j.trd.2021.102743.

[13] Asensio, O.I., Apablaza, C.Z., Lawson, M.C. et al. Impacts of micromobility on car displacement with evidence from a natural experiment and geofencing policy. Nat Energy 7, 1100–1108 (2022). https://doi.org/10.1038/s41560-022-01135-1.

[14] Comi, A., Hriekova, O., & Nigro, M. (2024). Exploring road safety in the era of micro-mobility: evidence from Rome. Transportation Research Procedia, 78, 55–62. https://doi.org/10.1016/j.trpro.2024.02.008.

[15] Jasiūnienė, V., & Tumavičė, A. (2022). Impact of E-Scooters on Road Safety: A Case Study in Lithuania. The Baltic Journal of Road and Bridge Engineering, 17(4), 18–34. https://doi.org/10.7250/bjrbe.2022-17.577.

[16] Barton-Aschman Associates. "Vehicle Occupancy Determinators" Arizona Department of Transportation, Virginia, Final Report, Report Number, FHWA-AZ89-252, August 1989.

[17] IBB, (2011). Istanbul Metropolitan Area Urban Transportation Master Plan.

[18] Christoforou, Z., de Bortoli, A., Gioldasis, C., & Seidowsky, R. (2021). Who is using e-scooters and how? Evidence from Paris. Transportation Research Part D: Transport and Environment, 92, 102708. https://doi.org/10.1016/j.trd.2021.102708.

[19] Fearnley, N., Johnsson, E., & Berge, S. H. (2020). Patterns of E-Scooter Use in Combination with Public Transport. Findings. https://doi.org/10.32866/001c.13707.

[20] PTV Group, 2020. Areas of Application for PTV Vissim [online cit.: 2020-08-16]. Available from: https://www.ptvgroup.com/en/solutions/products/ptv-vissim/areas-of-application/.

[21] Brockfeld, E., Kühne, R. D., & Wagner, P. (2005). Calibration and Validation of Microscopic Models of Traffic Flow. Transportation Research Record: Journal of the Transportation Research Board, 1934(1), 179-187. https://doi.org/10.1177/0361198105193400119.

[22] Raju, N., Chepuri, A., Arkatkar, S.S., & Joshi, G. (2020). A Simulation Study for Improving the Traffic Flow Efficiency of an Intersection Coupled with BRT.

[23] Lewis, C.D. (1982) International and Business Forecasting Methods. Butterworths, London.

[24] Dozza, M., Li, T., Billstein, L., Svernlöv, C., & Rasch, A. (2023). How do different micro-mobility vehicles affect longitudinal control? Results from a field experiment. Journal of Safety Research, 84, 24-32. https://doi.org/10.1016/j.jsr.2022.10.005 .

[25] Lee, O., Rasch, A., Schwab, A. L., & Dozza, M. (2020). Modeling cyclists' comfort zones from obstacle avoidance manoeuvres. Accident Analysis & Prevention, 144, 105609. https://doi.org/10.1016/j.aap.2020.105609.

[26] Garman, C., Como, S. G., Campbell, I. C., Wishart, J., O'Brien, K., & McLean, S. (2020). Micro-Mobility Vehicle Dynamics and Rider Kinematics during Electric Scooter Riding. SAE Technical Papers. https://doi.org/10.4271/2020-01-0935.

Appendix

Table A1: Vehicle occupancy rates determined according to the city of Istanbul

	Region								
	1	**2**	**3**	**4**	**5**	**6**	**7**	**8**	**9**
Car	1.5	1.5	1.6	1.5	1.5	1.5	1.5	1.7	1.6
Public Transport	17.8	15.4	22.1	42.4	44.5	21.1	22.6	30.4	28
Service car	14.1	12.3	8.5	9.4	11.7	9.6	11.9	10.7	10.3
Commercial vehicle	2	1.7	1.6	1.7	1.4	1.6	1.9	2.2	2
Intercity buses	39.9	34.4	26.3	34.7	28.7	35.3	60.7	50.7	38.5
Motorcycle	2.1	2.5	1.9	1.8	1.2	1.2	2.3	2.3	2.1
Total	3.5	4.4	3.1	3.4	4.3	3.4	4.5	4.5	3.3

Table A2: Traffic routes

Point	**Number of vehicle**	**Traffic flow**	**Route**
1	151	17%	YY → İzmir
	335	38%	YY → Hospital
	398	45%	YY → Özlüce
3	125	13%	Özlüce → YY
	673	70%	Özlüce → İzmir
	163	17%	Özlüce → Hospital
5	281	19%	Hospital → YY
	666	36%	Hospital → Özlüce
	532	45%	Hospital → İzmir
7	355	18%	İzmir → Hospital
	857	58%	İzmir → Özlüce
	266	24%	İzmir → YY

(a)

(b)

Figure A1: Signal time tables; (a): current situation, (b): adjusted signal table

J Inno Sci Eng, 2025, 9(1):28-38

DOI:https://doi.org/ 10.38088/jise.1471047

JISE

Research Article

Adapting Vision Transformer-Based Object Detection Model for Handwritten Text Line Segmentation Task

Osman Furkan KARAKUŞ[1]*, Ayla GÜLCÜ[2], Ali Can KARACA[1]

[1] *Department of Computer Engineering, Yıldız Technical University, İstanbul, Turkey*

[2]*Department of Software Engineering, Bahçeşehir University, Istanbul, Turkey*

ARTICLE INFO

Received Date: 21/04/2024
Accepted Date: 27/01/2025

Cite this paper as:
Karakus, O.F., Gulcu, A. and Karaca, A.C. (2025). *Adapting Vision Transformer-Based Object Detection Model for Handwritten Text Line Segmentation Task.*Journal of Innovative Science and Engineering. 9(1): 28-38

*Corresponding author: Osman Furkan Karakuş
E-mail:osman.karakus@yildiz.edu.tr

Keywords:
Vision transformers
Handwritten text line segmentation
Object Detection
Optical Character Recognition

ABSTRACT

This study introduces a novel approach for segmenting lines of text in handwritten documents using a vision transformer model. Specifically, we adapt DEtection TRansformer (DETR) model to detect line segments in images of handwritten documents. In order to adapt DETR for the line segmentation task, we applied a pre-processing step that involves dividing each line into fixed-size image patches followed by adding positional encoding. We benefit from DETR model with a ResNet-101 backbone pretrained on the Common Objects in Context (COCO) object detection training dataset, and re-train this model using our novel, complex line segmentation dataset consisting of 1,610 handwritten forms. To evaluate the performance, another line segmentation method named Bangla Document Recognition through Instance-level Segmentation of Handwritten Text Images (BN-DRISHTI) is implemented. This method utilizes the You Only Look Once (YOLO) object detection model. Both object detection-based methods involve a learning phase during which the model is trained or fine-tuned on the dataset. For a diverse set of baselines methods, we have also implemented two learning-free algorithms such as A* Search Algorithm and the Genetic Algorithm (GA). Experimental results based on the Intersection over Union (IoU) metric demonstrate that the proposed method outperforms all other methods in terms of the detection rate, recognition accuracy, and Text Line Detection Metric (TLDM). The quantitative results also indicate that two learning-free algorithms fail to segment highly skewed lines successfully in the dataset. The A* algorithm achieves a high recognition accuracy of 0.734, compared to GA and BN-DRISHTI, which achieve recognition accuracies of 0.498 and 0.689, respectively. Our proposed approach achieves the highest recognition accuracy of 0.872, outperforming all other methods. We show that the DETR model which requires only a single fine-tuning phase for adapting to line-segmentation task, not only simplifies the training and implementation process but also improves accuracy and efficiency in detecting and segmenting handwritten text lines. DETR's use of a transformer's global attention mechanism allows it to better understand the entire context of an image rather than relying solely on local features. This is particularly beneficial for managing the diverse and complex patterns found in handwritten text where traditional models might struggle with issues such as overlapping text lines or varied handwriting styles.

1. Introduction

Handwritten document analysis has gained significant attention in the field of document image analysis and recognition, primarily due to the surge in the digitization of historical documents and the need for automated tools capable of understanding and processing handwritten texts. This process involves several steps such as pre-processing, line and word segmentation, feature extraction, and interpretation. The text line segmentation process is essential for accurate recognition in handwritten documents, as emphasized by Barakat et al. [1].

The primary challenges in segmenting lines of handwritten text stem from the diverse nature of handwriting. Variations in handwriting styles, line spacing, the presence of artifacts, and noise in scanned documents pose significant hurdles for segmentation algorithms. These complexities were effectively addressed using deep learning techniques, such as Mask R-CNN, which has demonstrated robust performance on historical documents containing various artifacts [2]. Additionally, cursive writing and overlapping text further complicate the segmentation process, requiring sophisticated methods capable of accurately identifying and separating text lines under these conditions. Many researchers have tackled this problem, and numerous methods have been introduced for efficiently segmenting and extracting lines from text documents.

The earliest applications of text segmentation methods involve learning-free statistical approaches, which have been thoroughly reviewed and detailed by Likforman-Sulem et al. [3]. Recent advancements in deep learning have enabled the use of learning-based methods for many document analysis tasks, including text line segmentation. These methods have shown significant improvements in handling the variability of handwriting styles and the complexity of text documents. Multi-dimensional Long Short-Term Memory (LSTM) Networks and Fully Convolutional Networks (FCN)-based models have been successfully utilized for line segmentation problems [4], [5], [6].

Object detection frameworks, originally designed for identifying and locating objects within images, have also been adapted to the task of text line segmentation. The application of object detection frameworks, such as Ren et al.'s Faster R-CNN [7] and Redmon et al.'s YOLO [8], to text line segmentation represents a significant shift from traditional segmentation methods. By treating text lines as objects, these frameworks leverage deep neural networks to learn from the complexities and variations present in handwritten documents and achieve remarkable accuracy in segmentation tasks. Despite the efficiency of object detection frameworks, such as Faster R-CNN and YOLO, in segmenting text lines, their generic design for general object detection poses challenges in accurately handling the specific intricacies of handwritten text, such as overlapping lines and script variability. This has led us to explore a new detection approach.

Our method aligns with the approach of BN-DRISHTI by treating text lines as objects and utilizing established object detection frameworks. However, our approach differs significantly from that study and other works in the literature. The contributions of this study, highlighting these differences, can be summarized as follows:

In this study, the DETR vision transformer model is applied to the line segmentation task for the first time. We utilized a pre-trained DETR model and adapted it specifically for the line segmentation. Fine-tuning requires image preprocessing, where each line in the dataset is divided into fixed-size image patches, followed by the addition of positional encoding. It is shown that the DETR model requires only a single-stage fine-tuning process to adapt to the line segmentation task, with no additional post-processing steps, unlike other methods such as BN-DRISHTI. In this regard, our study demonstrates that DETR not only simplifies the training and implementation process but also improves accuracy and efficiency in detecting and segmenting handwritten text lines.

DETR uses the Hungarian algorithm to optimally match the set of predicted objects with the set of ground truth objects. Once the assignment is complete, the matching loss, which combines the class prediction loss and the bounding box localization loss, is calculated. During fine-tuning, we slightly modified this combined loss to consider only two object classes: one representing a line and the other representing a non-line object.

We have selected a diverse set of methods for comparison instead of focusing on a single method. First, we used another object-detection based method, BN-DRISHTI, along with two learning-free algorithms recognized for their success in line segmentation tasks. For this purpose, we selected the A* Search Algorithm and the Genetic Algorithm.

All experiments are performed on a novel line segmentation dataset of 1,610 forms, which contains highly skewed and challenging samples compared to publicly available handwritten text datasets.

The structure of this paper is as follows: Section 2 reviews related work on handwritten text line segmentation, focusing on object detection models in this field. Section 3 details our approach, in which we adapt the DETR framework specifically for handwritten line segmentation. This section includes an overview of our Turkish Line Segmentation Dataset and the customization of vision transformers for this task. Additionally, we introduce the baseline methods for comparison, including a YOLO-based approach for Bangla line segmentation, an A path-planning method, and a Genetic Algorithm-based technique. Section 4 presents the results and discussion. Finally, Section 5 concludes the paper and outlines future research directions.

2. Related Work

The task of handwritten text line segmentation has been extensively studied, with approaches ranging from tradi-tional image processing techniques to advanced machine learning algorithms. Projection profile-based approaches have been the most widely used methods due to their simplicity; however, horizontal projections cannot handle skewed, curved, or fluctuating lines. Many improvements to these methods have been proposed in the literature, such as [9], [10], and [11]. [12] provide an overview of text line segmentation methods.

There are also heuristic-based approaches that analyze the structural properties of handwritten texts, such as the spaces between lines and the alignment of text to segment lines [13]. While effective for documents with clear and consistent handwriting, these methods often struggle with cursive or overlapping text and documents containing noise and artifacts. Surinta et al. introduced an innovative approach to line segmentation of handwritten docu-ments using the A path-planning algorithm, which employs soft cost functions for separating text fields. This method addresses the challenge of overlapping text by calculating near-optimal paths and demonstrates effective application on historical and contemporary manuscripts with minimal adjustments required for implementation [14].

Toiganbayeva et al. introduced the Kazakh Offline Handwritten Text Dataset (KOHTD), significantly enriching Handwritten Text Recognition (HTR) research, especially for the Kazakh language. This dataset, notable for its extensive collection, underpins various HTR methodologies, showcasing adaptability through both traditional and contemporary models. A highlight of their work is the innovative application of a GA for line and word segmenta-tion, streamlining the process with improved precision and efficiency [15].

With the rise of deep learning, researchers have shifted towards data-driven approaches, applying Convolutional Neural Networks (CNNs) and Recurrent Neural Networks (RNNs) to learn complex patterns in handwritten docu-ments for segmentation tasks. These methods have shown significant improvements in handling the variability of handwriting styles and the complexity of historical documents. Graves et al. [16] presented an innovative RNN model for unconstrained handwriting recognition that employs Connectionist Temporal Classification (CTC) for direct mapping from input sequences to labels without requiring pre-segmentation, demonstrating the potential of RNNs in handling complex pattern recognition tasks. Voigtlaender et al. [17] advanced handwriting recognition by employing multidimensional long short-term memory (MDLSTM) networks, showcasing their study's ability to achieve state-of-the-art results on handwriting databases. Their work emphasizes the importance of deep network architectures and introduces an efficient GPU-based implementation, highlighting the significant impact of MDLSTM networks in the field. Moysset et al. [6] use a similar model for handwritten text line location problem of the Maurdor database [18] which is a multi-lingual database (French, English, Arabic) with both handwritten documents and printed documents. Barakat et al. [5] provide a document dataset with multi-skewed, multi-directed and curved handwritten text lines and apply line segmentation using FCNs. Renton et al. [4] propose an-other line segmentation method based on FCNs with dilated convolutions.

While CNNs and RNNs have revolutionized the field of handwritten document segmentation by learning complex patterns directly from data, these methods exhibit certain limitations. For instance, CNNs and RNNs typically re-quire extensive data preprocessing and augmentation to effectively handle the variability in handwriting styles. They often depend on large, annotated datasets and substantial computational resources for training, which can be prohibitive. Additionally, methods such as those proposed by Graves et al. [16] and Voigtlaender et al. [17], while effective, might struggle with real-time applications due to the computational demands of RNNs, particularly MDLSTM networks. Moreover, while FCNs, as used by Barakat et al. [5] and Renton et al. [4], provide robust segmentation capabilities, they may suffer from issues related to scale and translation invariance due to their fully convolutional nature.

Recent studies have explored the adaptation of object detection models for text line segmentation, demonstrating promising results in accurately segmenting lines of text from a various handwritten document [19]. Baek et al. [20] introduced a novel approach to character region awareness in text detection, significantly advancing the field. Furthermore, Qu et al. [21] provided insights into robust tampered text detection in document images, presenting both a new dataset and a solution to enhance document security and integrity. Jubaer et al. [22] introduce a novel method called BN-DRISHTI for the recognition of handwritten Bangla text documents. By integrating the YOLO framework with Hough and Affine transformations for skew correction, they achieve state-of-the-art segmentation results. Their method's effectiveness is further validated on several external datasets, showcasing superior performance on unseen samples [22].

3. Materials and Methods

Our approach to handwritten text line segmentation utilizes the architecture of vision transformers, a paradigm shift in leveraging self-attention mechanisms to process images, which has shown remarkable success in various computer vision tasks. In this study, we adapt the DETR [23] model for the handwritten text line segmentation task. By adapting this architecture, we propose a novel strategy for segmenting handwritten text lines by training the model to predict ground truth text lines bounding boxes instead of traditional object bounding boxes. In this section, we first briefly mention the datasets used in this study. Then, we provide details about the adaptation of a vision transformer-based object detection method for the line segmentation task. Finally, we introduce the baseline methods employed for performance comparison.

3.1. Turkish Line Segmentation Dataset

In this paper, we created a dataset for the line segmentation task by collecting handwriting samples from various authors using excerpts from 14 distinct literary books. Participants were given A4-sized forms with one of these excerpts printed at the top and were instructed to transcribe it by hand. The area where participants transcribed the excerpt was enclosed by two fixed solid lines that were later used to extract the handwriting. No lines were provided to guide participants' handwriting, resulting in highly skewed entries that are considered challenging samples, as illustrated in Figures 1 and 2. In the figures, the lines exhibit non-uniform orientations and variable spacing. In this regard, this dataset is instrumental for evaluating the performance of segmentation algorithms when faced with real-world handwriting variations and irregularities and facilitates a robust evaluation framework for comparing the effectiveness of various segmentation algorithms.

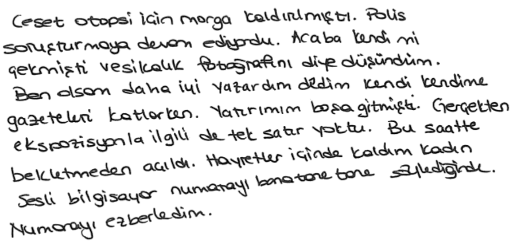

Figure 1: A hard example from our Dataset.

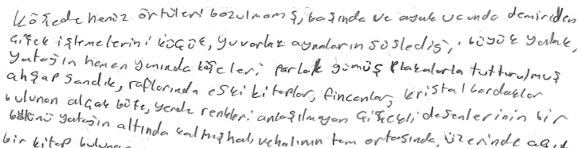

Figure 2: Another hard example from our Dataset.

The dataset comprises 1,610 forms written by 183 individuals, resulting in an average of approximately 9 forms per author. A semi-manual labeling approach was used to generate the ground truth line segments for each form. Each form was cross-checked to ensure the integrity of the dataset.

3.2. Vision Transformer for Line Segmentation

In this section we first provide a brief description on the vision transformers. Then, we present the details regarding fine-tuning process of the selected vision transformer.

3.2.1. Vision Transformers

Transformers have shown remarkable performance in natural language processing (NLP) due to their powerful self-attention mechanism. Given their significant success in NLP, researchers have started exploring how Transformers can be used in computer vision (CV). Although CNNs have long been the backbone of vision tasks, Transformers are increasingly proving to be a strong alternative. They are being applied not only to image classification but also to tasks such as object detection, semantic segmentation, and even video analysis. Unlike traditional CNNs that analyze images through localized filters, vision transformers treat an image as a sequence of patches and apply self-attention across these patches. This approach allows the model to capture global dependencies across the image, making it particularly well-suited for identifying the nuanced patterns of handwritten text lines.

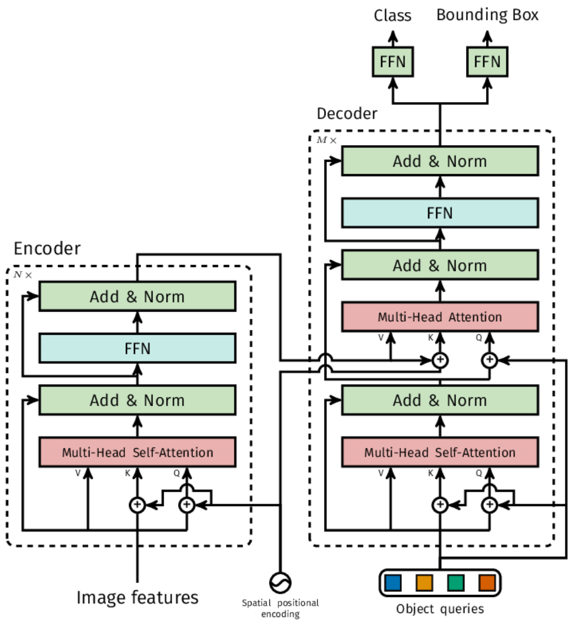

Figure 3: Architecture of DETR Model [23].

In recent years, new transformer-based vision models have emerged at a rapid pace. Han et al. [24] provide an extensive review of vision transformers. DETR is one of the most successful vision transformer models for the object detection task. DETR, an end-to-end object detector, approaches object detection as a straightforward set prediction problem, removing the need for traditional hand-crafted components like anchor generation and non-maximum suppression (NMS) post-processing. The process begins with a CNN backbone to extract features from the input image. After fixed positional encodings are added to the flattened features, these vectors are fed into the Transformer's encoder-decoder. Each encoder layer includes a multi-head self-attention module and a feed-forward network (FFN). The decoder then takes N learned positional encodings, known as object queries, as input (see Figure 3). It additionally attends to the encoder output to produce N output embeddings. Here, N is a predefined parameter, typically set larger than the number of objects expected in an image. FFNs are used to compute the final predictions, which include bounding box coordinates and class labels to specify the object class. Unlike the original Transformer, DETR decodes N objects in parallel. It employs a bipartite matching algorithm to align predicted objects with ground-truth objects and uses the Hungarian loss to calculate the loss function across all matched pairs.

3.2.2. Adaptation for Line Segmentation Task

We use a DETR model with a ResNet-101 backbone pretrained on the COCO object detection training dataset [coco2024], which contains more than 200,000 images and 80 object categories. We fine-tune this model using our line segmentation dataset. The transformer encoder processes sequences of patch embeddings, allowing the model to learn contextual relationships between different parts of the image. The key adaptation of the proposed approach lies in the training process. Instead of training the model to identify generic objects, we train it specifically to recognize and predict the bounding boxes of text lines.

To adapt the vision transformer for line segmentation, we first pre-processed the input images by dividing them into fixed-size patches. These patches are then flattened and passed through a linear projection layer, along with positional encoding to retain information about each patch's location within the image. These image preprocessing steps are illustrated in Figure 4.

We fine-tuned the DETR model using our fully annotated dataset of 1,610 forms. A total of 100 pages are reserved for testing. We ensured that the test split included pages with varying levels of difficulty, ranging from particularly challenging images to those that were somewhat easier. A key aspect of DETR is its unique loss function, which employs bipartite matching via the Hungarian algorithm. This algorithm efficiently computes the optimal assignment that minimizes matching loss between the set of predicted objects and the set of ground truth objects. Once each ground truth object in each image is assigned a prediction, the matching loss, accounting for both class prediction and the similarity between predicted and ground truth bounding boxes, is calculated. We adopted this combined loss function during the fine-tuning process, though the number of classes was reduced to two: one representing a line and the other a non-line object.

For the training parameters, we adopt most of the values used to train DETR initially. The AdamW optimizer with a learning rate of 0.0001 was used, and a batch size of 16 was adopted. The pretrained DETR model was fine-tuned for 50 epochs using a dataset of approximately 1,500 pages on a single A100 GPU. DETR fine-tuning steps are given in the pseudo-code in Algorithm 1.

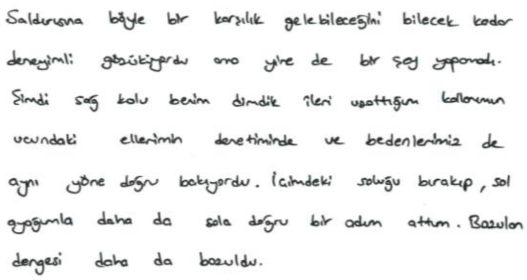

(a) Original Text

(b) Original Text with Flattened Patches

(c) Linear Projection Presented on Patches

(d) Positional Encoding Shown on Patches

Figure 4: Image preprocessing steps: original image (a), image with fixed size patches and flattening (b), linear projectionapplied on flattened image patches (c), positional embedding added to image patches (d).

Algorithm 1: DETR: End-to-End Object Detection with Transformers

Require: Image set $S = \{I_1, I_2, \dots I_n\}$
Ensure: Detected objects with class labels and bounding boxes for each image
Initialize CNN backbone and Transformer encoder-decoder architecture
Initialize a fixed set of learned object queries
for each image I in S **do**
Extract feature map F from I using the CNN backbone
Flatten F into a sequence of feature vectors
Add positional encodings to the sequence
Pass the sequence through the Transformer encoder to obtain encoded features
Pass encoded features and object queries through the Transformer decoder
for each output embedding from the decoder **do**
Apply FFN to predict class label and bounding box
Store the predicted class label and bounding box
end for
end for
return Predicted class labels and bounding boxes for all images

3.3. Baseline Methods

To better assess the effectiveness of the proposed approach, we employ another object detection framework, YOLO, which was previously utilized in [22] for a similar line segmentation task. Since this method, like our DETR-based approach, is learning-based and requires a rigorous training phase, we selected two learning-free algorithms recognized for their success in line segmentation tasks. For this purpose, we chose the A Search Algorithm and the Genetic Algorithm, implementing each. Each of these three benchmarking methods is explained in this section.

3.3.1. YOLO-based Bangla Line Segmentation Method

Jubaer et al. [22] propose integrating of the YOLO deep learning-based object detection framework with skew correction techniques for Bangla Handwriting Segmentation. They name their method BN-DRISHTI which stands for Bangla Document Recognition through Instance-level Segmentation of Handwritten Text Images. Their approach is shown in Algorithm 2.

Algorithm 2: BN-DRISHTI

Require: Set of Bangla handwritten document images
Ensure: Segmented lines with bounding boxes
Load pre-trained YOLO model for object (text line) detection
for each image in the input set **do**
Apply preprocessing (e.g., skew correction) on the image
Detect text lines using YOLO model
for each detected line **do**
Calculate and store bounding box
end for
end for
return All detected lines with their bounding boxes

3.3.2. A* Path Planning

The A* Path Planning algorithm adapts the classic pathfinding technique to navigate through the intricacies of handwritten text segmentation. This adaptation prioritizes efficient traversal of text regions, guided by cost functions designed to distinguish between upper and lower text boundaries [14]. Please see Algorithm 3 for a step-by-step explanation.

Algorithm 3: A* Path Planning for Line Segmentation

Require: Start node, Goal node
Ensure: Path from Start to Goal
Initialize OpenSet with Start node
Initialize ClosedSet as empty
while OpenSet is not empty **do**
Current ← node in OpenSet with lowest f-score
if Current is Goal then M
return path reconstructed from Current
end if
Move Current from OpenSet to ClosedSet
for each neighbor of Current **do**
if neighbor is in ClosedSet **then**
continue
end if
if neighbor is not in OpenSet **then**
Add neighbor to OpenSet
end if
Update neighbor's scores based on Current
end for
end while

3.3.3. Genetic Algorithm-based Line Segmentation

The Genetic Algorithm employs evolutionary strategies to optimize the segmentation task. Through selection, crossover, and mutation, it iteratively refines solutions and converges on an optimal segmentation strategy [15]. The steps of this method are outlined in Algorithm 4.

Algorithm 4 Genetic Algorithm for Line Segmentation

Require: Initial population, Fitness function
Ensure: Optimal individual representing segmentation solution
Generate initial population randomly
while termination condition is not met **do**
Evaluate fitness of each individual
Select individuals for reproduction
Crossover selected individuals to create offspring
Mutate offspring with a given probability
Select individuals for the next generation
end while
return the best individual from final generation

4. Results and Discussion

In this section, we first briefly describe the performance evaluation metrics used in the study, followed by the experimental results. Our first evaluation metric, IoU, quantifies the overlap between predicted bounding boxes and ground truth. IoU, the primary evaluation metric for object detection algorithms, is calculated as the area of overlap divided by the area of the union between the predicted and ground truth bounding boxes. An IoU threshold was established to classify predictions as accurate, facilitating a direct comparison of the methods' efficacy based on their average IoU scores across the dataset.

We also calculate the detection rate, recognition accuracy, and TLDM as detailed by Louloudis et al. [25]. The detection rate evaluates how well the proposed method can identify individual text lines in each document. For each line, a matching score is assigned based on the proportion of the predicted pixels that fall into the ground truth region. All the lines with a score above a threshold are accepted as a match. The detection rate is then computed as the proportion of correctly identified text lines out of the total number of ground-truth text lines in the document. Recognition accuracy, on the other hand, is computed as the proportion of correctly identified text lines out of the total number of detected text lines in the document. In this regard, one can consider the detection rate as recall and the recognition accuracy as precision. TLDM combines detection rate and recognition accuracy to provide a balanced measure of overall performance. It is calculated as the harmonic mean of detection rate and recognition accuracy, similar to the F1-score in traditional classification metrics.

The segmentation performance of each of the four methods, measured by average IoU, is presented in Table 1. These results indicate that our approach, which adapts vision transformer-based object detection methods for handwritten text line segmentation, outperforms all other baseline methods. Table 2 provides a comparison of all methods based on detection rate, recognition accuracy, and TLDM. The experimental results suggest that our approach achieves the highest scores across all metrics.

Table 1: Average IoU comparison of text line segmentation methods.

Method	Average IoU
A* Path Planning:	0.298
Genetic Algorithm:	0.655
BN-DRISHTI:	0.762
Our Approach:	0.925

Table 2: Accuracy-based performance comparison of the line segmentation methods

Method	Detection Rate	Recognition Accuracy	TLDM
A* Path Planning:	0.2485	0.7340	0.3715
Genetic Algorithm:	0.655	0.4978	0.4940
BN-DRISHTI:	0.762	0.6890	0.6830
Our Approach:	0.925	0.8720	0.8610

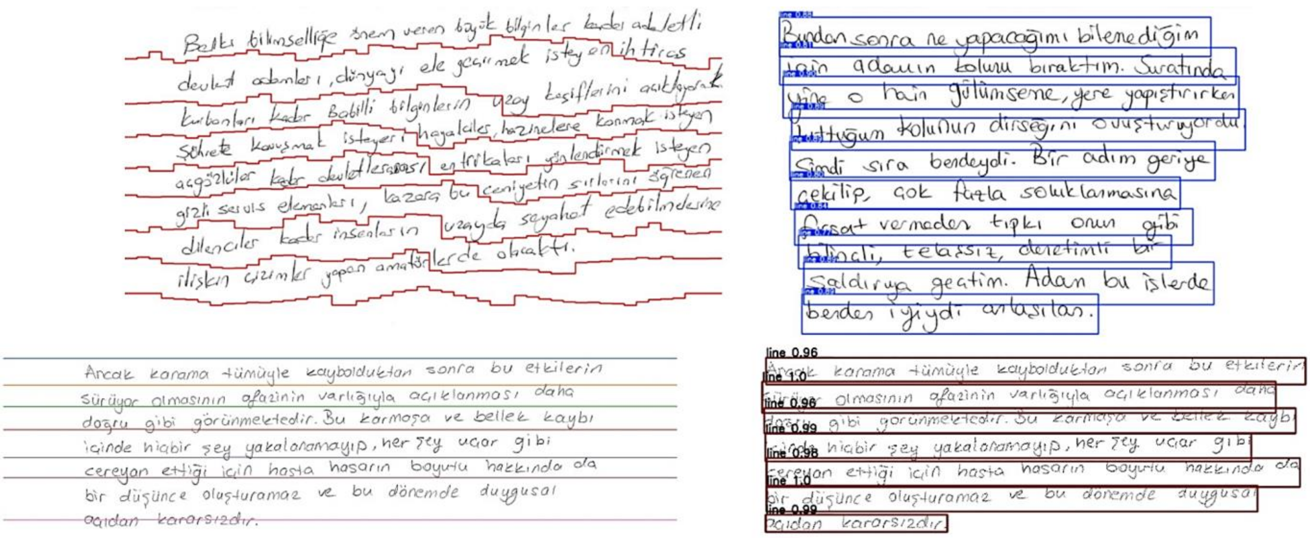

Figure 5: Visualization of the results of line segmentation algorithms: Genetic Algorithm (a), BN-DRISHTI (b), A* Path Planning (c), and our Vision Transformer-based approach (d).

In addition, we visualized the results of the line segmentation methods in Figure 5. Here, the Genetic Algorithm appears to have some difficulty accurately segmenting the lines, as indicated by several misalignments. This suggests that the algorithm may require a more comprehensive hyperparameter tuning process for better performance. The BN-DRISHTI method shows better performance than the Genetic Algorithm but still makes some errors in line segmentation, particularly at points where the line curves or where text is closely packed. The A* algorithm, which is generally efficient in many search scenarios, performed moderately well, although there are areas where the segmentation cuts through the text. The effectiveness of the A* algorithm in this context heavily relies on how the problem is framed as a graph search and how the heuristic is designed. The segmentation results in the figure suggest that our approach provides the cleanest line segmentation with no visible errors. Specifically, our approach solves the misalignment and overlapping problems through the text.

5. Conclusion

In this study, we introduce a novel approach for segmenting lines of text in handwritten documents using a vision transformer model. Specifically, we adapt the DETR model, recognized for its state-of-the-art performance in object detection, to detect line segments in images of handwritten documents. For comparison, another line segmentation method based on an object detection framework is included: the BN-DRISHTI method, which utilizes the YOLO object detection model. Both object detection-based methods involve a learning phase, during which the model is trained or fine-tuned on the dataset. Additionally, we selected two learning-free algorithms from the literature that have been successfully applied to line segmentation tasks and included them in the comparison.

Experimental results based on the Intersection over Union (IoU), one of the most widely used performance evaluation metrics for object detection, demonstrate that our method outperforms all other methods. The quantitative results further support these findings. Our line segmentation dataset primarily contains highly skewed and challenging samples, highlighting that the learning-free algorithms, A* and GA, fail to successfully segment these lines. Additionally, the BN-DRISHTI method, which is specifically designed and trained for Bangla handwriting, is less effective compared to our approach.

In terms of the detection rate, recognition accuracy, and TLDM, our approach outperforms all baseline methods across each criterion. Experimental results demonstrate that, the A* algorithm achieves a high recognition accuracy of 0.734, compared to GA, BN-DRISHTI, and our approach, which achieve recognition accuracies of 0.4978, 0.689 respectively. Our proposed approach achieves the highest recognition accuracy of 0.872, outperforming all other methods. This demonstrates that A* has higher precision than the other learning-free algorithm, GA. However, in terms of the detection rate, GA outperforms A*. Given the relatively poor performance of these two learning-free algorithms on this challenging dataset, evaluating their performance on other test datasets with less complex samples would be beneficial. Investigating datasets where these methods perform well would provide valuable insights, as they require no learning phase and are therefore less costly than learning-based methods. This consideration should also be addressed in future studies. Accordingly, we plan to compare these four methods across line segmentation datasets of varying difficulty in future work.

In conclusion, this study represents a notable advancement in the field of handwritten text line segmentation through the application of a vision transformer model. DETR's use of a transformer's global attention mechanism allows it to better understand the entire context of an image, rather than relying solely on local features. This is particularly beneficial for handling the diverse and complex patterns found in handwritten text, where traditional models might struggle with issues such as overlapping text lines or varied handwriting styles. Our experimental results confirm that DETR not only simplifies the training and implementation process but also improves accuracy and efficiency in detecting and segmenting handwritten text lines. With the growing demand for digitizing handwritten texts, the development of robust segmentation techniques has become increasingly essential. This research thus provides a valuable contribution to the domain of document image analysis and recognition, promoting more efficient and comprehensive digitization processes.

In our future work, we plan to conduct cross-domain evaluations of line segmentation methods that exploit domain relations across different datasets. Furthermore, we plan to work on an end-to-end text recognition task, which is crucial for properly utilizing segmented lines and words.

Article Information Form

Funding

The authors have no received any financial support for the research, authorship or publication of this study.

Authors' Contrtibution

The authors confirm sole responsibility for the study.

The Declaration of Conflict of Interest/Common Interest

No conflict of interest or common interest has been declared by the authors.

The Declaration of Ethics Committee Approval

This study does not require ethics committee permission or any special permission.

References

[1] Barakat, K., Berat, Rafi Cohen, Ahmad Droby, Irina Rabaev, and Jihad El-Sana. "Learning-free text line segmentation for historical handwritten documents." Applied Sciences 10, no. 22 (2020): 8276.

[2] Droby, A., Barakat, B., Alaasam, R., Madi, B., Rabaev, I., & El-Sana, J. "Text Line Extraction in Historical Documents Using Mask R-CNN." Signals, vol. 3, pp. 535–549, Aug. 2022, doi: 10.3390/signals3030032.

[3] Likforman-Sulem, L., Zahour, A., & Taconet, B. "Text Line Segmentation of Historical Documents: A Survey." International Journal on Document Analysis and Recognition (IJDAR), vol. 9, May 2007, doi: 10.1007/s10032-006-0023-z.

[4] Renton, Guillaume, Yann Soullard, Clément Chatelain, Sébastien Adam, Christopher Kermorvant, and Thierry Paquet. "Fully convolutional network with dilated convolutions for handwritten text line segmentation." International Journal on Document Analysis and Recognition (IJDAR) 21 (2018): 177-186.

[5] Barakat, Berat, Ahmad Droby, Majeed Kassis, and Jihad El-Sana. "Text line segmentation for challenging handwritten document images using fully convolutional network." In 2018 16th International Conference on Frontiers in Handwriting Recognition (ICFHR), pp. 374-379. IEEE, 2018.

[6] Moysset, Bastien, Christopher Kermorvant, Christian Wolf, and Jérôme Louradour. "Paragraph text segmentation into lines with recurrent neural networks." In 2015 13th international conference on document analysis and recognition (ICDAR), pp. 456-460. IEEE, 2015.

[7] Ren, S., He, K., Girshick, R., & Sun, J. "Faster R-CNN: Towards real-time object detection with region proposal networks." CoRR, vol. 28, 2015.

[8] Redmon, J., Divvala, S., Girshick, R., & Farhadi, A. "You Only Look Once: Unified, Real-Time Object Detection." CoRR, vol. abs/1506.02640, 2015.

[9] Arivazhagan, Manivannan, Harish Srinivasan, and Sargur Srihari. "A statistical approach to line segmentation in handwritten documents." In Document recognition and retrieval XIV, vol. 6500, pp. 245-255. SPIE, 2007.

[10] Sanasam, Inunganbi, Prakash Choudhary, and Khumanthem Manglem Singh. "Line and word segmentation of handwritten text document by mid-point detection and gap trailing." Multimedia Tools and Applications 79, no. 41 (2020): 30135-30150.

[11] dos Santos, Rodolfo P., Gabriela S. Clemente, Tsang Ing Ren, and George DC Cavalcanti. "Text line segmentation based on morphology and histogram projection." In 2009 10th International Conference on Document Analysis and Recognition, pp. 651-655. IEEE, 2009.

[12] Louloudis, Georgios, Basilios Gatos, Ioannis Pratikakis, and Constantin Halatsis. "Text line and word segmentation of handwritten documents." Pattern recognition 42, no. 12 (2009): 3169-3183.

[13] Smith, R. "An overview of the Tesseract OCR engine." In Ninth International Conference on Document Analysis and Recognition (ICDAR 2007), vol. 2, 2007, pp. 629–633, IEEE.

[14] Surinta, O., Holtkamp, M., Karabaa, F., Van Oosten, J.-P., Schomaker, L., & Wiering, M. "A Path Planning for Line Segmentation of Handwritten Documents." In 2014 14th International Conference on Frontiers in Handwriting Recognition, pages 175-180, IEEE, 2014.

[15] Toiganbayeva, N., Kasem, M., Abdimanap, G., Bostanbekov, K., Abdallah, A., Alimova, A., & Nurseitov, D. "KOHTD: Kazakh offline handwritten text dataset." Signal Processing: Image Communication, vol. 108, pages 116827, Elsevier BV, Oct. 2022.

[16] Graves, A., Liwicki, M., Fernández, S., Bertolami, R., Bunke, H., & Schmidhuber, J. "A novel connectionist system for unconstrained handwriting recognition." IEEE Transactions on Pattern Analysis and Machine Intelligence, vol. 31, no. 5, pp. 855–868, 2009.

[17] Voigtlaender, P., Doetsch, P., & Ney, H. "Handwriting Recognition with Large Multidimensional Long Short-Term Memory Recurrent Neural Networks." In 2016 15th International Conference on Frontiers in Handwriting Recognition (ICFHR), pp. 228–233, 2016.

[18] Brunessaux, Sylvie, Patrick Giroux, Bruno Grilheres, Mathieu Manta, Maylis Bodin, Khalid Choukri, Olivier Galibert, and Juliette Kahn. "The maurdor project: Improving automatic processing of digital documents." In 2014 11th IAPR international workshop on document analysis systems, pp. 349-354. IEEE, 2014.

[19] Long, S., He, J., Yao, C., Hu, W., Wang, Q., & Bai, X. "TextSnake: A Flexible Representation for Detecting Text of Arbitrary Shapes." CoRR, vol. abs/1807.01544, 2018.

[20] Baek, Y., Lee, B., Han, D., Yun, S., & Lee, H. "Character Region Awareness for Text Detection." CoRR, vol. abs/1904.01941, 2019.

[21] Qu, C., Liu, C., Liu, Y., Chen, X., Peng, D., Guo, F., & Jin, L. "Towards Robust Tampered Text Detection in Document Image: New Dataset and New Solution." In Proceedings of the IEEE/CVF Conference on Computer Vision and Pattern Recognition (CVPR), June 2023, pp. 5937–5946.

[22] Jubaer, S. M., Tabassum, N., Rahman, M. A., & Islam, M. K. "BN-DRISHTI: Bangla Document Recognition Through Instance-Level Segmentation of Handwritten Text Images." In Document Analysis and Recognition – ICDAR 2023 Workshops, Mickael Coustaty and Alicia Fornés, Eds., Springer Nature Switzerland, Cham, pages 195–212, 2023.

[23] Carion, N., Massa, F., Synnaeve, G., Usunier, N., Kirillov, A., & Zagoruyko, S. "End-to-End Object Detection with Transformers." CoRR, vol. abs/2005.12872, 2020.

[24] Han, K., Wang, Y., Chen, H., Chen, X., Guo, J., Liu, Z., Tang, Y., Xiao, A., Xu, C., Xu, Y. and Yang, Z., 2022. A survey on vision transformer. IEEE transactions on pattern analysis and machine intelligence, 45(1), pp.87-110.

[25] Louloudis, Georgios, Basilios Gatos, Ioannis Pratikakis, and Constantin Halatsis. "Text line detection in handwritten documents." Pattern recognition 41, no. 12 (2008): 3758-3772.

DOI:https://doi.org/ 10.38088/jise.1563076

Adomian Decomposition and Variational Iteration Methods in the Context of Partial Differential Equations

Khadeejah James Audu [1*], Lawrence Linus [1], Yusuph Amuda Yahaya [1], Sıkırulaı Akande [2]

[1] *Federal University of Technology, Minna, Nigeria*

[2] *North-Eastern University, Gombe, Nigeria*

ARTICLE INFO

Received Date: 17/10/2024
Accepted Date: 14/02/2025

Cite this paper as:
Audu, K.J., Linus, L., Yahaya, Y.A., and Akande, S. (2025). *Adomian Decomposition and Variational Iteration Methods in the Context of Partial Differential Equations.* Journal of Innovative Science and Engineering. 9(1): 39-53

*Corresponding author: Khadeejah James Audu
E-mail:k.james@futminna.edu.ng

Keywords:
Partial Differential Equation
Semi-analytical Methods
Decomposition Method
Variational Iteration Method
Comparative Analysis

ABSTRACT

Partial Differential Equations (PDE) help model problems in science and engineering, given their abilities to capture complex phenomena compared to Ordinary Differential Equations. This paper aims to investigate two semi-analytical techniques called the Adomian Decomposition Method (ADM) and the Variational Iteration Method (VIM), how these methods can be used in practice, and to make a comparative study of the two methods for solving linear and nonlinear PDEs. The efficiency of ADM and VIM is assessed by comparing their errors relative to the exact solutions of the examined numerical experiments. The results obtained from the numerical experiments revealed that ADM proved to be a more efficient and accurate method for solving PDEs than VIM.

1. Introduction

In physics and engineering, partial differential equations (PDEs) are utilized to model diverse problems, given their ability to describe the change of a system concerning multiple independent variables. Investigating solutions of differential equations has been significant to scientists and researchers [14]. Given the challenges faced in obtaining analytical solutions for PDEs, especially those with non-linearity, numerical methods have been employed to address these problems [18,20]. Nevertheless, despite the various numerical methods for solving differential equations, significant limitations remain in numerical analysis for tackling PDE problems [10,11]. Some works on semi-analytical methods have been proposed in extant literature to approximate solutions to such problems [1,14,20,27,28].

Considering the Adomian Decomposition Method (ADM), George Adomian was the first to begin using ADM to find the solution of functions by illustrating them in the form of a series. This method uses an iterative formula to calculate subsequent series parts based on initial and boundary conditions. Wazwaz and El-Sayed further re ned ADM to address this, enabling rapid convergence and easily computable components. Researchers have developed modified techniques to enhance ADM's efficiency. For instance, a new approach was proposed to solve time-fractional diffusion equations with initial and boundary conditions, Volterra-Fredohlm integral-equations, demonstrating improved accuracy and convergence [4.21]. Additionally, ADM has been effectively applied to systems of second-order differential-algebraic equations and systems of PDEs, providing approximate solutions that align closely with exact results [6,24]. Meanwhile, He and Wu developed the Variational Iteration Method (VIM), which involves constructing a correction function related to the solved equation, incorporating a Lagrange multiplier [2,12].

The VIM is a highly effective technique commonly employed in analyzing various mathematical models. Unlike other methods, it does not necessitate any transformation of the given problem, allowing for direct application similar to the ADM. Implementing VIM for various types of linear and nonlinear partial differential equations was carried out by Shihab et al. [25]. Fatima et al. [15] used the VIM to solve nonlinear partial differential equations in fluid dynamics. At the same time, authors [5, 23,30] utilized a blend of VIM with the Sumudu transform to resolve some nonlinear equations. Recent studies [1,12,13,17,19,22] have explored the efficacy of the ADM and the VIM in solving specific complex differential equations. Comparative studies have also been conducted to evaluate the effectiveness of ADM and VIM in solving nonlinear differential equations, providing insights into their respective advantages and applications [7.8,16,29, 31,32]. This work compares ADM and VIM methods to solve both linear and nonlinear partial differential equations. The methods, their numerical solution, and errors will be analyzed to aid understanding of the application of both methods to solve PDE problems. Novel contributions include a comparative analysis of the ADM and the VIM in solving linear and nonlinear PDEs, which introduces new understanding and insights into the suitability of the two methods for different types of PDE problems and bridges research gaps in the literature.

The subsequent section of this work is segmented into four (4) parts. The first part provides an overview of the ADM and the VIM development for both linear and nonlinear PDEs. The second part declares the numerical experiments via which the methods' efficiency and accuracy are evaluated and the results of the numerical experiment after computations have been carried out. Following this, the third part discusses the results that were attained to provide context for their implications in applications. Lastly, a conclusion is made, and recommendations are proposed for researchers seeking to improve this body of work in the last part.

2. Material and Methods

2.1. Description of Adomian Decomposition Method (ADM)

The study Given the general differential equation in the form:

$$Fv(u,t) = g(u,t) \quad (1)$$

With conditions (initial) $v(u,0) = f(u)$, where F denotes a differential operator involving nonlinear and linear terms. Hence, Equation (1) can take the form

$$L_t v(u,t) + Rv(u,t) + Nv(u,t) = g(u,t) \quad (2)$$

where $L_t = \frac{\partial}{\partial t}$, R denotes a linear operator containing partial derivatives with respect to u,N represents a nonlinear operator and g is the source term or a nonhomogenous term that is independent of v. Algebraically,

$$L_t v(u,t) = g(u,t) - Rv(u,t) - Nv(u,t) \quad (3)$$

Inversion of the operator L_t, (L_t^{-1}) and application of it to both sides of equation (3) gives

$$L_t^{-1} L_t v(u,t) = L_t^{-1} g(u,t) - L_t^{-1} Rv(u,t) - L_t^{-1} Nv(u,t) \quad (4)$$

Which results into

$$v(u,t) = f(u) + L_t^{-1}g(u,t) - L_t^{-1}Rv(u,t) - L_t^{-1}Nv(u,t) \qquad (5)$$

where f(u) denotes constant of integration concerning that satisfies L_t f=0. The unknown function v(u, t) is decomposed into an infinite series as:

$$v(u,t) = \sum_{p=0}^{\infty} v_p(u,t) \qquad (6)$$

The nonlinear operator N(v) is decomposed as:

$$Nv(u,t) = \sum_{p=0}^{\infty} A_p\left(v_0,\ v_1\ v_2, \cdots, v_p\right) \qquad (7)$$

where sequence $\left[A_p\right]_{p=0}^{\infty}$is called the Adomian polynomial sequence and explicit computation of the nonlinear A_p terms is given by

$$A_0(v_0) = N(v_0)$$
$$A_1(v_0,\ v_1) = N^{'}(v_0)v_1$$
$$A_2(v_0,\ v_1,\ v_2) = N^{'}(v_0)v_2 + \frac{{v_1}^2}{2!}N^{''(v_0)}$$
$$A_3(v_0,\ v_1,\ v_2,\ v_3) = N^{'}(v_0)v_3 + N$$
$$^{'}(v_0)_{1\,2}\ \frac{{v_1}^3}{3!}\,^{,'(v_0)}\ \vdots$$

Hence the summarized format is given by the relation

$$A_p\left(v_0,\ v_1\ v_2, \cdots, v_p\right) = \frac{1}{p!}\frac{d^p}{d\beta^p}\left[N\left(\sum_{j=0}^{p} \beta^j v_j\right)\right]_{\beta=0} \qquad (8)$$

Thus, substituting equations (6), (7) and (8) into (5) results into

$$\sum_{p}^{\infty} v_p(u,t) = f(u) + L_t^{-1}g(u,t) - L_t^{-1}R\sum_{p}^{\infty} v_p(u,t) - L_t^{-1}\sum_{p=0}^{\infty} A_p\left(v_0,\ v_1\ v_2, \cdots, v_p\right) \qquad (9)$$

Identification of v_0 as $f(u) + L_t^{-1}g(u,t)$, it is possible to write

$$\vdots$$
$$v_{p+1}(u,t) = -L_t^{-1}Rv_p(u,t) - L_t^{-1}A_p\left(v_0,\ \cdots\ ,\ v_p\right) \qquad (10)$$

By isolating the linear and nonlinear components and equating terms having the same order, the resulting recursive algorithm becomes

$$\begin{cases} v_0(u,t) = f(u) + L_t^{-1}g(u,t) \\ v_{p+1}(u,t) = L_t^{-1}Rv_p(u,t) \\ \quad -L_t^{-1}A_p\left(v_0,\ v_1,\ \cdots,\ v_p\right) \end{cases}, \quad p = 0,\ 1,\ 2,\ 3,\ \cdots \qquad (11)$$

Using the recursive algorithm defined in Equation (11), an approximate solution to Equation (1) can be obtained through a series expansion.

$$v_j(u,t) = \sum_{p=0}^{j} v_p(u,t)$$

where

$$\lim_{j\to\infty}\sum_{p=0}^{j} v_p(u,t) = v(u,t) \qquad (12)$$

Given the right conditions, the series$\sum_{p=0}^{\infty} v_p(u,t)$ converges to the solution v(u,t) of the initial problem. The decomposition of the series solution tends to converge rapidly, requiring only a few terms for effective solution analysis. The conditions governing this convergence have been extensively studied in references [8,17,21,22].

2.2. Description of Variational Iteration Method (VIM)

Consider the following general nonlinear differential equation:

$$Lv(u,t) + Rv(u,t) + Nv(u,t) = g(u,t) \qquad (13)$$

where L denotes a linear operator, N represents a nonlinear operator, v(u,t) is a known function, and g(u,t) is a known analytical function. The correction functional can be constructed thus

$$v_{p+1}(u,t) = v_p(u,t) + \int_0^t \lambda(\eta) [Lv(u,\eta) + N\tilde{v}(u,\eta) - g(u,\eta)] d\eta \quad , \quad p \geq 0 \tag{14}$$

where $\lambda(\eta)$ denotes the Lagrange multiplier, which can be determined optimally using the variational theory. The subscript p refers to the p^{th} approximation and $\tilde{v}_p$ is considered a restricted variation, meaning $\delta\tilde{v}_p = 0$. By first determining the Lagrange multiplier λ through integration by parts, the successive approximation $v_{p+1}, p \geq 0$, can be obtained using the selected Lagrange multiplier and any initial function v_0. It can be obtained through the stationary functions

$$\begin{aligned} 1 + \lambda|\eta = t = 0 \\ \lambda'|\eta = t = 0 \end{aligned} \tag{15}$$

where one can find the next Lagrange multiplier as follows

$$\begin{aligned} \lambda = -1 \quad for \quad r = 1 \\ \lambda = \eta - t \ for \quad r = 2 \end{aligned} \tag{16}$$

In addition, the standard formula for the Lagrange multiplier in the scenario $r \geq 1$ is denoted as

$$\lambda(\eta) = \frac{(-1)^r (\eta - t)^{r-1}}{(r-1)!} \tag{17}$$

After determining the value of $\lambda(\eta)$, substituting it into the corrective function in equation (14) enables us to derive the following iteration formula.

$$v_{p+1}(u,t) = v_p(u,t) + \int_0^t \frac{(-1)^r (\phi - t)^{r-1}}{(r-1)!} [Lv(u,\eta) + N\tilde{v}(u,\eta) - g(u,\eta)] d\eta \tag{18}$$

For $\lambda = -1$, the iteration formula becomes:

$$v_{p+1}(u,t) = v_p(u,t) - \int_0^t [Lv(u,\eta) + N\tilde{v}(u,\eta) - g(u,\eta)] d\eta \tag{19}$$

Applying the iterative formula in equations (18) or (19) yields the sequence from a suitable initial guess. Advanced computing allows repeated iterations until the desired precision is achieved. The approximate solution is then given by

$$v(u,t) = \lim_{p\to\infty} v_p(u,t) \tag{20}$$

3. Numerical Experiments

The two methods are applied to a range of linear and nonlinear PDEs with known solutions to evaluate the accuracy of the VIM and ADM methods. The methods' performance is assessed by comparing computed results obtained using Python's Jupyter Notebook 2022 to analytical solutions. The findings are presented in Tables 1-6 and illustrated in Figures 1-3, highlighting the computed solutions and corresponding errors.

Experiment 1: Using ADM and VIM, solve the following linear PDE

$$au_a + u_y = 3u \tag{21}$$

with the following initial conditions:

$u(a,0) = a^2, u(0,y) = 0$, and analytical solution: $u(a,y) = a^2 l^y$

ADM Solution: Re-write (21) in an operator form as

$$L_y u(a,y) = 3u(a,y) - aL_a u(a,y) \tag{22}$$

The inverse operator is applied to both sides of (22) alongside the given condition $u(a,0) = a^2$ results in

$$u(a,y) = a^2 + L_y^{-1}(3u - aL_a u) \tag{23}$$

Substitute $u(a,y) = \sum_{p=0}^{n} u_p(a,y)$ into both sides of (23)

$$u_p(a,y) = a^2 + L_y^{-1} \sum_{p=0}^{\infty} \left(\begin{array}{c} 3\left(\sum_{p=0}^{\infty} u_p(a,y)\right) \\ -aL_a\left(\sum_{p=0}^{\infty} u_p\,(a,y)\right) \end{array} \right) \tag{24}$$

Taking few components of the decomposition of $u(a,y)$, equation (24) becomes

$$u_0 + u_1 + u_2 + \cdots = a^2 + L_y^{-1}\begin{pmatrix} 3(u_0 + u_1 + u_2 + \cdots) - \\ aL_a(u_0 + u_1 + u_2 + \cdots) \end{pmatrix} \quad (25)$$

The recursive terms are identified

$$u_o(a,y) = a^2$$

$$u_{q+1}(a,y) = L_y^{-1}\left(3a_q - aL_a u_q\right), \quad q = 0 \quad (26)$$

The first four components are obtained thus

$$u_0(a,y) = a^2$$
$$u_1(a,y) = L_y^{-1}(3u_0 - aL_a u_0) = a^2 y,$$

$$u_2(a,y) = L_y^{-1}(3u_1 - aL_a u_1) = \frac{a^2y^2}{2!},$$

$$u_3(a,y) = L_y^{-1}(3u_2 - aL_a u_2) = \frac{a^2y^3}{3!}, \quad (27)$$

VIM Solution: The correction functional is constructed as

$$u_{p+1}(a,y) = u_p(a,y) + \int_0^y \lambda(\eta)\begin{pmatrix} \dfrac{\partial u_p(a,\eta)}{\partial \eta} + \\ a\dfrac{\partial \tilde{u}_p(a,\eta)}{\partial a} - 3\tilde{u}_p(a,\eta) \end{pmatrix} d\eta \quad (28)$$

The stationary conditions are

$$1 + \lambda|\eta = a = 0$$

$$\lambda'|\eta = a = 0 \quad (29)$$

which results in

$$\lambda = 1 \quad (30)$$

Substituting the Lagrange multiplier (30) into (28), the following iteration formula is obtained

$$u_{p+1}(a,y) = u_p(a,y) - \int_0^y \begin{pmatrix} \dfrac{\partial u_p(\eta,y)}{\partial \eta} \\ +a\dfrac{\partial u_p(\eta,y)}{\partial a} - 3u_p \end{pmatrix} d\eta, \quad p \geq 0 \quad (31)$$

Selecting $u_0(a,y) = a^2$ from the given conditions and substitute it into (31) results in the first four successive approximations as follows

$$u_0(a,y) = a^2$$

$$u_1(a,y) = a^2 - \int_0^y \left(\frac{\partial u_0(a,\eta)}{\partial \eta} + a\frac{\partial u_0(a,\eta)}{\partial a} - 3u_0(a,\eta)\right) d\eta = a^2 + a^2 y,$$

$$u_2(a,y) = a^2 + a^2 y - \int_0^y \left(\frac{\partial u_1(a,\eta)}{\partial \eta} + a\frac{\partial u_1(a,\eta)}{\partial a} - 3u_1(a,\eta)\right) d\eta = a^2 + a^2 y + \frac{1}{2!}a^2y^2,$$

$$u_3(a,y) = a^2 + a^2 y + \frac{1}{2!}a^2y^2 - \int_0^y \begin{pmatrix} \dfrac{\partial u_2(a,\eta)}{\partial \eta} + \\ a\dfrac{\partial u_2(a,\eta)}{\partial a} - 3u_2(a,\eta) \end{pmatrix} d\eta = a^2 + a^2 y + \frac{1}{2!}a^2y^2 + \frac{1}{3!}a^2y^2, \quad (32)$$

Experiment 2: Compute the nonlinear PDE by applying ADM and VIM

$$u_y + uu_a = 0 \quad (33)$$

given the following initial condition:

$$u(a,0) = a \quad y > 0$$
$$\text{where } u = u(a,y)$$

and analytical solution: $u(a,y) = \dfrac{a}{1+y}, \ |y| < 1$

ADM Solution: Re-write (33) in an operator form as

$$L_y u(a,y) = -uu_a \quad (34)$$

where $L_y$is defined using

$$L_y = \frac{\partial}{\partial y} \quad (35)$$

The inverse operator L_y^{-1} is added to both sides of (34) with the initial condition to obtain

$$u(a,y) = a - L_y^{-1} u u_a \tag{36}$$

Substituting

$$u(a,y) = \sum_{p=0}^{\infty} u_p(a,y) \tag{37}$$

and the nonlinear term

$$u u_a = \sum_{p=0}^{\infty} u_p(a,y) \tag{38}$$

into equation (34) results in

$$\sum_{p=0}^{\infty} u_p\,(a,y) = a - L_y^{-1}\left(\sum_{p=0}^{\infty} A_p\right) \tag{39}$$

hence, the recursive relation is obtained as

$$u_0(a,y) = a,$$

$$u_{q+1}(a,y) = -L_y^{-1}\big(A_q\big), \quad q \geq 0 \tag{40}$$

Thus, the result of the first four components are as follows

$$\begin{aligned}
&u_0(a,y) = a \\
&u_1(a,y) = -L_y^{-1}A_0 = -L_y^{-1}(a) = -ay \\
&u_2(a,y) = -L_y^{-1}A_1 = -L_y^{-1}(-2ay) = ay^2 \\
&u_3(a,y) = -L_y^{-1}A_2 = -L_y^{-1}(3ay^2) = -ay^3
\end{aligned}$$

VIM Solution: The correction functional for (33) is given by

$$u_{p+1}(a,y) = u_p(a,y) + \int_0^y \lambda(\eta)\left(\frac{\partial u_p(a,\eta)}{\partial \eta} + \tilde{u}_p(a,\eta)\frac{\partial \tilde{u}_p(a,\eta)}{\partial a}\right) d\eta \tag{41}$$

and the stationary conditions

$$1 + \lambda|\eta = y = 0$$

$$\lambda'|\eta = y = 0 \tag{42}$$

gives

$$\lambda = -1 \tag{43}$$

To obtain the iteration formula, the Lagrange multiplier $\lambda = -1$ is substituted into the functional (41) as

$$u_{p+1}(a,y) = u_p(a,y) - \int_o^y \left(\frac{\partial u_p(a,\eta)}{\partial \eta} + u_p(a,\eta)\frac{\partial u_p(a,\eta)}{\partial a}\right) d\eta, \quad p \geq 0 \tag{44}$$

The first four successive approximations obtained by selecting $u_0(a,y) = a$ from the given initial condition are as follows

$$\begin{aligned}
&u_0(a,y) = a, \\
&u_1(a,y) = a - ay, \\
&u_2(a,y) = a - ay + ay^2 - \frac{1}{3}ay^3, \\
&u_3(a,y) = a - ay + ay^2 - ay^3 + \frac{2}{3}ay^4
\end{aligned}$$

Experiment 3: Resolve the nonlinear PDE using ADM and VIM

$$u_y = a^2 + \frac{1}{4}u_a^2 \tag{45}$$

given the following initial condition:

$$u(a,0) = 0$$
$$where\ u = u(a,y)$$

and analytical solution: $u(a,y) = a^2 \tan y$

ADM Solution: Re-write (45) in an operator form as

$$u(a,y) = a^2 y + \frac{1}{4}L_y^{-1}u_a^2 \tag{46}$$

$u(a,y)$ is defined by

$$u(a,y) = \sum_{p=0}^{\infty} u_p\,(a,y) \tag{47}$$

having the nonlinear terms u_a^2 as

$$u_a^2 = \sum_{p=0}^{\infty} A_p \tag{48}$$

where A_p, $p \geq 0$ are the Adomian polynomials. Applying these assumptions yields

$$\sum_{p=0}^{\infty} u_p\,(a, y) = a^2 y + \frac{1}{4} L_y^{-1} \left(\sum_{p=0}^{\infty} A_p \right) \tag{49}$$

which results in the recursive relation

$$u_0(a, y) = u_{0_a}^2,$$

$$u_{q+1}(a, y) = \frac{1}{4} L_y^{-1} A_q, q \geq 0 \tag{50}$$

For this form of nonlinearity, the Adomian polynomials A_p are given by

$$A_0 = u_{0_a}^2,$$

$$A_1 = 2u_{0_a} u_{1_a},$$

$$A_2 = 2u_{0_a} u_{2_a} + u_{1_a}^2,$$

$$A_3 = 2u_{0_a} u_{3_a} + 2u_{1_a} u_{2_a} \tag{51}$$

and so on. The first four components are obtained as follows

$$\begin{aligned}
&u_0(a, y) = a^2 y, \\
&u_1(a, y) = \frac{1}{4} L_y^{-1} A_0 = \frac{1}{4} L_y^{-1}(4a^2 y^2) = \frac{1}{3} a^2 y^3, \\
&u_2(a, y) = \frac{1}{4} L_y^{-1} A_1 = \frac{1}{4} L_y^{-1} \left(\frac{8}{3} a^2 y^4 \right) = \frac{2}{13} a^2 y^5, \\
&u_3(a, y) = \frac{1}{4} L_y^{-1} A_2 = \frac{1}{4} L_y^{-1} \left(\frac{68}{45} a^2 y^6 \right) \\
&\qquad\qquad = \frac{17}{312} a^2 y^7
\end{aligned}$$

VIM Solution: Proceeding from the methods used in experiments 1 and 2, the correction function for the equation is

$$u_{p+1}(a, y) = u_p(a, y) - \int_0^y \lambda(\eta) \begin{pmatrix} \dfrac{\partial u_p(a, \eta)}{\partial \eta} \\ -\dfrac{1}{4} u_{p_2}^2(a, \eta) - a^2 \end{pmatrix} d\eta \tag{52}$$

The iteration formula is obtained as

$$u_{p+1}(a, y) = u_p(a, y) - \int_0^y \begin{pmatrix} \dfrac{\partial u_p(a, \eta)}{\partial \eta} \\ -\dfrac{1}{4} u_{p_2}^2(a, \eta) - a^2 \end{pmatrix} d\eta\,, \quad p \geq 0 \tag{53}$$

By using $u_0(a, y) = 0$ the given initial condition, the first four successive approximations are obtained as follows

$$\begin{aligned}
&u_o(a, y) = 0, \\
&u_1(a, y) = a^2 y \\
&u_2(a, y) = a^2 y + \frac{1}{3} a^2 y^3, \\
&u_3(a, y) = a^2 y + \frac{1}{3} a^2 y^3 + \frac{2}{15} a^2 y^5 + \frac{1}{63} a^2 y^7
\end{aligned}$$

The results of the experiments are computed in the following tables and figures.

Table 1. Computed Solution for Experiment 1

a/y	Solution of VIM	Solution of ADM	Analytical Solution
0.1	0.011051709180756	0.011051709180756	0.011051709180756
0.2	0.048856110326406	0.048856110326406	0.048856110326406
0.3	0.122487292681836	0.122487292681840	0.122487292681840
0.4	0.238691951622429	0.238691951622503	0.238691951622603
0.5	0.412180317671841	0.412180317672584	0.414280317675032
0.6	0.655962768106149	0.655962768140221	0.655962768140584
0.7	0.986737736402845	0.986738826635423	0.986738826660535
0.8	1.424346192769120	1.424246193675318	1.424346194235180
0.9	1.992278513156301	1.992278518003713	1.992278520037130
1.0	2.718281801146383	2.718281814564905	2.718281828459050

Table 1 presents the result of ADM and VIM numerical solution with the analytical solution for experiment 1.

Table 2. Comparison of Error for Experiment 1

a/y	Error of VIM	Error of ADM
0.1	0.000000000000000	0.000000000000000
0.2	0.000000000000000	0.000000000000000
0.3	0.000000000000004	0.000000000000000
0.4	0.000000000000174	0.000000000000100
0.5	0.000000000003191	0.000000000002448
0.6	0.000000000034435	0.000000000000363
0.7	0.000000009742310	0.000000000025112
0.8	0.000000001475060	0.000000000559862
0.9	0.000000006880829	0.000000002033417
1.0	0.000000027312667	0.000000013894145

Table 2 computes the comparison between the errors of ADM and VIM for experiment 1. The ADM is observed to exhibit lesser error than the VIM solution.

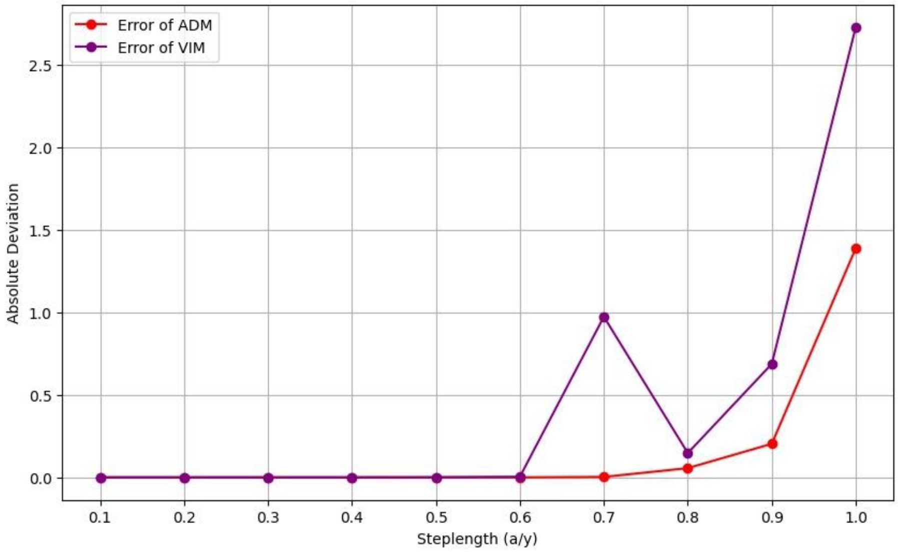

Figure 1. Error Plot for Experiment 1

Figure 1 illustrates the computed errors of ADM and VIM for experiment 1. The ADM is observed to exhibit a better performance than the VIM.

Table 3. Computed Solution for Experiment 2

a/y	Solution of VIM	Solution of ADM	Analytical Solution
0.1	0.087801242011922	0.090910000000000	0.090909090909091
0.2	0.175602484023843	0.181820000000000	0.181818181818182
0.3	0.263403726035765	0.272730000000000	0.272727272727273
0.4	0.351204968047687	0.363640000000000	0.363636363636364
0.5	0.429006210059608	0.454540000000000	0.454545454545455
0.6	0.526807452071530	0.545460000000000	0.545454545454545
0.7	0.614608694083452	0.636370000000000	0.636363636363636
0.8	0.702409936095374	0.727280000000000	0.727272727272727
0.9	0.790211178107295	0.818190000000000	0.818181818181818
1.0	0.878012420119217	0.909010000000000	0.909090909090909

Table 3 presents the result of ADM and VIM numerical solution with the analytical solution for experiment 2.

Table 4. Comparison of Error for Experiment 2

a/y	Error of VIM	Error of ADM
0.1	0.003107848897169	0.000000909090909
0.2	0.006215697794338	0.000001818181818
0.3	0.009323546691508	0.000002727272727
0.4	0.012431395588677	0.000003636363636
0.5	0.015539144485846	0.000004545454545
0.6	0.018647093383015	0.000005454545455
0.7	0.021754942280184	0.000006363636364
0.8	0.024862791177540	0.000007272727273
0.9	0.027970640074523	0.000008181818182
1.0	0.031078488971692	0.000009090909091

Table 4 computes the comparison between the errors of ADM and VIM for experiment 2. The errors of the ADM are lesser in contrast with the VIM errors.

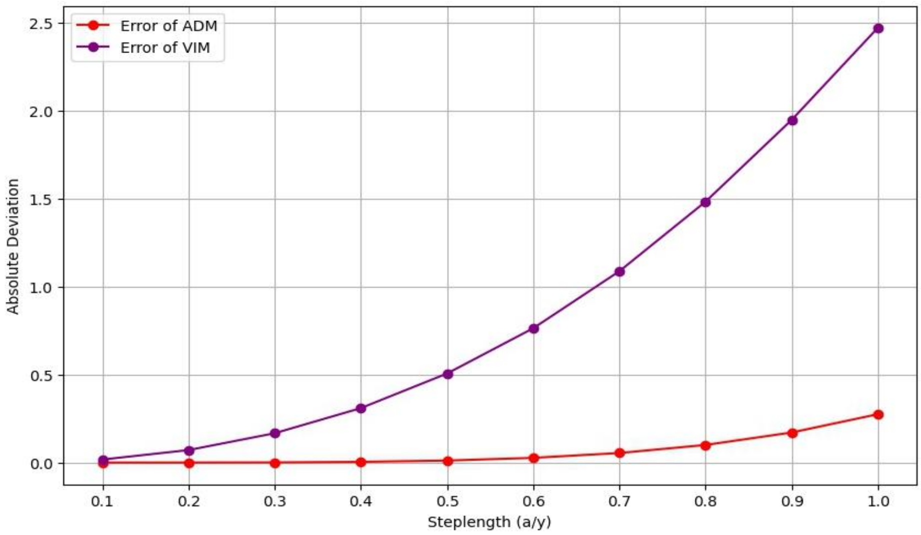

Figure 2. Error Plot for Experiment 2

Figure 2 illustrates the computed errors of ADM and VIM for experiment 2. The ADM is seen to have better performance than the VIM.

Table 5. Computed Solution for Experiment 3

a/y	Solution of VIM	Solution of ADM	Analytical Solution
0.1	0.009983300463875	0.009983341666667	0.010000000000000
0.2	0.047121963272002	0.047214724187292	0.047500000000000
0.3	0.086777157401376	0.088656075000000	0.090000000000000
0.4	0.129763366662727	0.146646247985667	0.148000000000000
0.5	0.179461103563882	0.244171933030667	0.253000000000000
0.6	0.313587006669394	0.353878880000000	0.360000000000000
0.7	0.449683972599175	0.496823975095917	0.511000000000000
0.8	0.597860722776229	0.641515607222667	0.697000000000000
0.9	0.685154967050886	0.705078675000000	0.810000000000000
1.0	0.800666439370880	0.841666666666667	1.000000000000000

Table 5 presents the result of ADM and VIM numerical solution with the analytical solution for experiment 3.

Table 6. Comparison of Error for Experiment 3

a/y	Error of VIM	Error of ADM
0.1	0.000000000000000	0.000000000000000
0.2	0.000000000000000	0.000000000000000
0.3	0.000000000000004	0.000000000000000
0.4	0.000000000000174	0.000000000000100
0.5	0.000000000003191	0.000000000002448
0.6	0.000000000034435	0.000000000000363
0.7	0.000000009742310	0.000000000025112
0.8	0.000000001475060	0.000000000559862
0.9	0.000000006880829	0.000000002033417
1.0	0.000000027312667	0.000000013894145

Table 6 computes the comparison between the errors of ADM and VIM for experiment 3. The error of the ADM is lesser than that of the VIM.

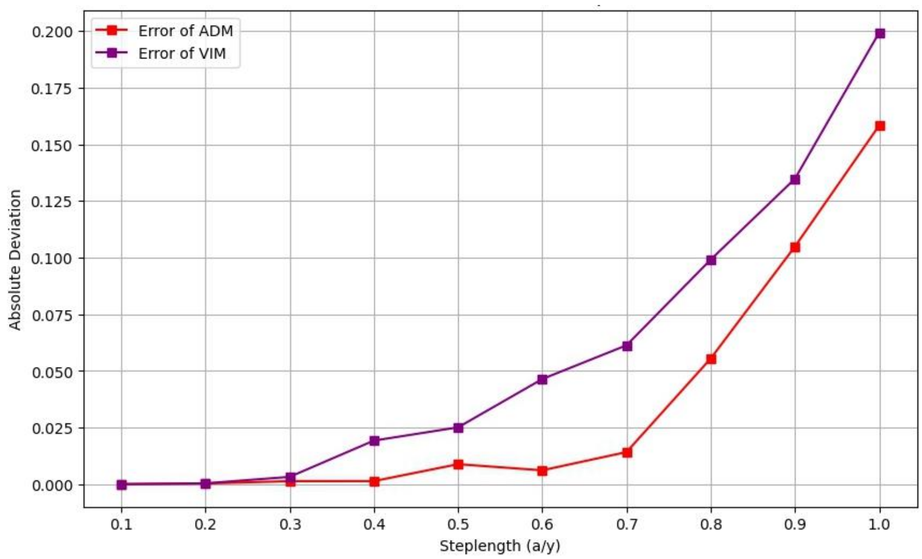

Figure 3. Error Plot for Experiment 3

Figure 3 illustrates the computed errors of ADM and VIM for experiment 3. Again, the ADM solution outperforms the VIM solution, as illustrated in the plot.

4. Conclusion

The ADM and VIM were applied to solve various linear and nonlinear Partial Differential Equations to assess these methods' effectiveness in addressing PDEs. Applying these methods resulted in some solutions, showing how the methods converge to a highly accurate exact solution. These results are thoroughly analyzed. Tables 1, 3, and 5 compute numerical solutions of ADM and VIM, tables 2, 4, and 6, and figures 1 to 3 compute the respective errors and show that the ADM method effectively solves these selected PDEs.

Numerical approximations (Tables 1, 3 and 5):

i. The tables for all three problems show the solutions from applying the two methods as well as the effectiveness of the methods in producing results that converge towards the analytical solution.
ii. A Notable difference is observed from the results of the two methods; this enhances the understanding of the accuracy of the methods and also influences selection.
iii. The results computed shows that the ADM is more effective and accurate than the VIM in solving these types of PDE problems.

Error of Numerical Approximations (Tables 2, 4 and 6; Figures 1-3):

i. The tables and graphs are representations of errors resulting from the application of the two methods.
ii. The ADM method consistently produced more accurate results and exhibited fewer errors in contrast to the VIM, thereby suggesting what method is most effective.
iii. The margin between the errors of the ADM and VIM from the figures clearly reveals that the ADM performs better.

Outcomes:

i. From the comparative analysis carried out, it is evident that the performance of the ADM is superior to that of the VIM, thereby influencing the choice of an effective numerical method to solve specific types of problems.
ii. The ADM demonstrates effectiveness and higher accuracy through its consistent convergence to the analytical solution and display of minimal error.

5. Conclusion

Various linear and nonlinear partial differential equations have been solved using ADM and VIM approaches. Both techniques yielded almost accurate results for linear and nonlinear partial differential equations, as demonstrated in problems 1 and 3, supported by the numerical data in the tables. From the analysis of Tables 1 to 6 and Figures 1 to 3, it is clear that ADM outperforms VIM in effectiveness accuracy; hence, the absolute error plots further support the conclusion. Consequently, the results have shown that ADM is a highly efficient

and accurate approach for solving linear and nonlinear partial differential equations, proving that ADM is more effective in solving linear and nonlinear PDEs than VIM. Future research will explore ADM's comparison with other numerical methods and its application to real-world problems. While this study used simplified examples to highlight accuracy and convergence, future work will incorporate practical case studies in physics, engineering, and mathematical biology to demonstrate the effectiveness of ADM and VIM.

Article Information Form

Funding

The author (s) has no received any financial support for the research, authorship or publication of this study.

Authors' Contrtibution

The contributions to this work were as follows: Khadeejah James Audu was responsible for the concept, design, and critical review of the manuscript. Yusuph Amuda Yahaya provided supervision and resources. Jamiu Garba handled data collection and analysis, while Lawrence Linus conducted the literature search and contributed to writing the s.

The Declaration of Conflict of Interest/Common Interest

No conflict of interest or common interest has been declared by the authors.

The Declaration of Ethics Committee Approval

This study does not require ethics committee permission or any special permission.

The Declaration of Research and Publication Ethics

The authors of the paper declare that they comply with the scientific, ethical and quotation rules of SAUJS in all processes of the paper and that they do not make any falsification on the data collected. In addition, they declare that Sakarya University Journal of Science and its editorial board have no responsibility for any ethical violations that may be encountered, and that this study has not been evaluated in any academic publication environment other than Journal of Innovative Science and Engineering.

References

[1] Abbas, T., Haq, E. U., Hassan, Q. M. U., Majeed, A. and Ahmad, B. (2022). Application of Adomian Decomposition, Variational Iteration, and Series Solution Methods to Analysis of Integral Differential Equations. Journal of Science and Arts, 22(3), 655–662.

[2] Adeniji, A. A., Mogbojuri, O. A., Kekana, M. C. and Fadugba, S. E. (2023). Numerical solution of rotavirus model using Runge-Kutta-Fehlberg method, differential transform method and Laplace Adomian decomposition method. Alexandria Engineering Journal, 82, 323–329.

[3] Albert, B., Titus, R. and Michael, O. (2022). Variational iteration method for solving coupled nonlinear system of Klein-Gordon equations. International Journal of Statistics and Applied Mathematics, 7(1), 107–111.

[4] Ahmad, N. and Ansari, A. (2023). Numerical Solution for nonlinear Volterra-Fredholm Integro-Differential Equations using Adomian and Modified Adomian Decomposition Method. Journal of Science and Arts, 23, 625-638.

[5] Aibinu, M. O. and Moyo, S. (2023). Solutions of fractional differential equations by using a blend of variational iteration method with Sumudu transform and application to price adjustment equations. Partial Differential Equations in Applied Mathematics, *8*, 100590.

[6] Al-Sharai, A. A.A., Wedad M. and Journal, A. U. (2024). Exact Solution of Linear and Nonlinear System of Partial Differential Equations by Double Aboodh-Shehu and Adomian Decomposition Method. Albaydha University Journal, 5(5), 273-286.

[7] Alao, S., Akinboro, F. S.and Oderinu, R. A. (2021). Numerical Solution of Integro-differential Equation using Adomian Decomposition Method and Variational Iteration Method. Journal of Mathematics, 10(4), 18-22

[8] Altaie, H. O. (2020). Comparison the solutions for some kinds of differential equations using iterative methods. Journal of Interdisciplinary Mathematics, 24(5), 1113–1118.

[9] Wazwaz, A. M. (2009). Partial Differential Equations and Solitary Wave, Springer.

[10] Audu, K. J. and Ameh, S. (2023). Implementation of New Iterative Method for Solving Partial Differential Equations. International Physical Science Conference, 237-242

[11] Audu, K. J. (2024). Numerical Solutions of Higher Order Differential Equations via New Iterative Method. Proceedings of International Conference on Mathematical Modelling Optimization and Analysis of Disease Dynamics, 285-294.

[12] Audu, K. J. and Babatunde, O. (2024). A Comparative Analysis of Two Analytic Approaches in Solving Systems of First-Order Differential Equations, Scientific Journal of Mehmet Akif Ersoy University, 7(1), 8-24.

[13] Audu, K. J., Tiamiyu, A. T., Akpabio, J. N., Ahmad, H. and Adebayo, M. (2024). Numerical Assessment of Some Semi-Analyical Techniques for Solving a Fractional Order Leptospirosis Model, Malaysian Journal of Science, 43(3), 68-85.

[14] Bhadgaonkar, V. N. and Sontakke, B. R. (2021). Exact solution of space-time fractional partial differential equations by adomian decomposition method. Journal of Advances in Mathematics and Computer Science, 75–87.

[15] Fatima, N. and Haque, S. (2023). Variational iteration method for solving nonlinear partial differential equations in fluid dynamics. MDPI AG, 201-217.

[16] Hamoud, A. and Ghadle, K. (2021). A comparative study of VIM and ADM for solving volterra-fredholm integro-differential equations. MDPI AG, 116-129.

[17] Liberty, E., Kubugha, W. B. and Onengiyeofori, A. D. (2023). Comparison of Adomian decomposition method with differential transformation method for unsteady MHD flow and heat transfer over a stretching/shrinking permeable sheet with ohmic heating. African Journal of Mathematics and Statistics Studies, *6*(3), 70–85.

[18] Li, W. and Pang, Y. (2020). Application of Adomian decomposition method to nonlinear systems. Journal of Advances in Difference Equations, 67(2020), 1-17.

[19] M. Elzaki, T. and E. Ahmed, S. (2021). Solution of nonlinear partial differential equations by mixture Adomian decomposition method and sumudu transform. Advances in the Solution of Nonlinear Differential Equations. 16, 97-108.

[20] Ozdogan N. (2024). Application of Mohand Transform. Journal of Informative Science and Engineering, 8(1), 18-24.

[21] Oswaldo, G., G. (2022). Solution of nonlinear partial differential Equations by Adomian decomposition method. Studies in Engineering and Exact Sciences, *3*(1), 61–78.

[22] S, K. and Mulimani, M. (2022). Comparative study of Adomian decomposition method and Clique polynomial method. Partial Differential Equations in Applied Mathematics, 6, 100454.

[23] Sahu, S. K., Derke, S. and Duressa, A. (2022). Solutions of 1D hyperbolic quasi-linear partial differential equations by variational iteration method. Journal of Science and Arts, 22(3), 432-445.

[24] Singh, P. (2020). Accelerated adomian decomposition method for the system of nonlinear equations. Journal of Physics: Conference Series, 1531(1), 012084.

[25] Shihab, M. A., Taha, W. M., Hameed, R. A., Jameel, A. and Sulaiman, I. M. (2023). Implementation of variational iteration method for various types of linear and nonlinear partial differential equations. International Journal of Electrical and Computer Engineering, 13(2), 21-31.

[26] Yindoula, J. B. (2022). A comparative study of Adomian Decomposition Method and Variational Iteration Method.Universal Journal of Mathematics and Mathematical Sciences, 17, 1–30.

[27] Falade, K. I, Tiamiyu A.T (2020). Numerical Solution of Partial Differential Equations with

Fractional Variable Coefficients Using New Iterative Method (NIM), I.J. Mathematical Sciences and Computing, 3, 12-21.

[28] Falade, K. I. (2022). Algorithm analytic-numeric solution for nonlinear gas dynamic partial differential equation, Engineering and Applied Science Letter, 5(2), 32-40.

[29] Baghdadi, S. K. A., and Ahammad, N. A. (2024). A Comparative Study of Adomian Decomposition Method with Variational Iteration Method for Solving Linear and Nonlinear Differential Equations. Journal of Applied Mathematics and Physics, 12(8), 2789-2819.

[30] Sinha, V. K., and Maroju, P. (2023). New Development of Variational Iteration Method Using Quasilinearization Method for Solving Nonlinear Problems. Mathematics, 11(4), 935.

[31] Rilwan, M. A., and Akanbi, M. A. (2022). A Comparison of the Variational Iteration Method and Adomian Decomposition Methods in Solving the Problem of Squeezing Flow Between Two Circular Disks. The Journals of the Nigerian Association of Mathematical Physics, 64, 91-98.

[32] Dehraj, S., Maitlo, A. A., Siyal, W. A., Memon, M., Arain, L. N., Arain, L., and Umrani, K. (2023). A Comparison of the Adomian Decomposition Method and Variational Iteration Method for a Two-Dimensional Nonlinear Wave Equation. Journal of Hunan University Natural Sciences, 50(2), 28-37.

J Inno Sci Eng, 2025, 9(1):54-61

DOI:https://doi.org/ 10.38088/jise.1570132

Research Article

The Impact of Internal Energy Consumption on Efficiency and Emissions in Maritime Transport

Onur Elma [1*], **Özgür T. Kaymakçı** [1], **Hasan Mercan** [2]

[1] *Department of Electrical and Electronics Engineering, Çanakkale Onsekiz Mart University, 17100 Çanakkale, Türkiye*

[2] *Department of Marine Sciences and Limnology, Çanakkale Onsekiz Mart University, 17100 Çanakkale, Türkiye*

ARTICLE INFO

Received Date: 19/10/2024
Accepted Date: 28/02/2025

Cite this paper as:
Elma, O., Kaymakçı, Ö.T., Mercan, H. (2025). *The Impact of Internal Energy Consumption on Efficiency and Emissions in Maritime Transport.* Journal of Innovative Science and Engineering. 9(1): 54-61

*Corresponding author: Onur Elma
E-mail:onurelma@gmail.com

Keywords:
Gen-set Efficiency
Maritime Transport Emissions
Energy consumption
System analysis

ABSTRACT

Maritime transportation plays a crucial role in moving passengers, vehicles, and freight. However, emissions from this sector have become a focus of environmental concerns. Therefore, accurate analysis is important to reduce ship emissions and develop more efficient solutions. The study investigates the energy usage and emissions of a ferry, which is an example of analyzing the impact of internal energy consumption on efficiency and emissions in maritime transport. The analysis concentrates on the fuel consumption of the gen-set. Although the main engine is responsible for most of the ferry's emissions, the gen-set, running at an average load of 37.5%, also significantly contributes to emissions. By using emission factors for pollutants such as CO_2, NOx, SOx, CO, and PM, the study calculated the emissions from both the main engine and the gen-set. The results show that the gen-set is accountable for 10% of the total emissions despite its lower load. These points to the potential for enhancing electrical energy efficiency on board, primarily through load optimization, gen-set modernization, and waste heat recovery. By implementing these strategies, the ferry can decrease fuel consumption, reduce emissions, and transition to a more sustainable and environmentally friendly operation. The findings underscore the importance of focusing on the ferry's electrical energy efficiency to minimize its overall environmental impact.

1. Introduction

As a critical sector that drives a large portion of global trade, maritime transport creates significant environmental impacts in terms of energy consumption and emissions. Traditional fossil fuels used to meet the energy needs of ships result in high greenhouse gas emissions. The environmental issues caused by this have accelerated the industry's pursuit of sustainability and emission reduction. According to the International Maritime Organization (IMO), maritime transport accounts for nearly 2.5% of global greenhouse gas emissions, contributing approximately one billion tons of CO2 annually [1]. This significant environmental impact underscores the importance of targeted efforts to reduce emissions within the shipping sector. The regulations and targets of the International Maritime Organization (IMO) aim to significantly reduce emissions by 2030 and 2050, and in this context, initiatives to increase energy efficiency are encouraged [2].

In addition, an important cause of emissions on ships is the gen-sets that provide the electrical energy demand. In other words, the internal energy consumption of ships is a critical factor that directly affects their efficiency and emissions. As additional information, a gen-set is a combination of a generator and an engine (typically a diesel internal combustion engine). Similarly, load rates refer to the proportion of a generator’s maximum rated capacity that is currently being utilized. Higher load rates generally improve fuel efficiency and reduce specific emissions, whereas lower load rates can lead to inefficiencies and increased fuel consumption per unit of power generated. In addition, power quality problems can arise due to electrical disturbances such as voltage fluctuations, harmonics, and reactive power imbalances, which may negatively impact the stable operation of onboard electrical systems, leading to efficiency losses and increased maintenance requirements. In this context, analyzing the impact of internal energy consumption on efficiency and emissions in maritime transportation is of vital importance for the sustainability and future of the sector. Ships consume significant amounts of energy to operate their propulsion systems, generate electricity, power their air conditioning and cooling systems, provide lighting, and meet all other operational needs. This energy consumption increases operating costs by increasing fuel costs, while also causing environmental problems by causing greenhouse gas emissions and air pollution. The impact of internal energy consumption on efficiency is directly related to fuel consumption and therefore emissions. More efficient energy use means less fuel consumption, which provides both economic and environmental benefits. For example, measures such as energy-efficient lighting systems, heat recovery systems, optimized route planning, and speed control can reduce ship energy consumption and increase efficiency.

In terms of emissions, greenhouse gases emitted by ships are a major contributor to global climate change. Recent studies highlight the importance of comparing different maritime transport methods for efficiency and emissions reductions. For instance, hybrid diesel-electric ferries show a 12% improvement in efficiency over traditional full-diesel ferries, while high-speed passenger ships have up to 79% lower efficiency than medium-speed passenger ships. Similarly, energy consumption and emissions analysis of electric container ships suggests that transitioning to electric propulsion can offer substantial environmental benefits. These comparisons provide valuable insights into optimizing maritime energy efficiency [3]. The internal energy consumption of ships directly affects the amount of these emissions. Energy efficiency measures and the use of alternative fuels play an important role in reducing the carbon footprint of ships. In this context, increasing the energy efficiency of ships is an important issue. For this purpose, significant effects can be achieved in the efficiency of gen-sets according to their loading rates. In a study, it was stated that up to 22% emission reductions were achieved when the gen-sets were operated at 80% load rate instead of 40% [4]. In addition, ships are equipped with very different power systems depending on their intended use and design parameters. Hybrid propulsion systems and zero-emission ferry concepts have been studied extensively as potential solutions to reduce fuel consumption and emissions in maritime transport. Energy optimization strategies for small passenger ferries with hybrid propulsion indicate that adopting hybrid and electric propulsion systems can significantly improve efficiency while meeting operational demands [5]. Some ships may even have microgrids. This can lead to an increase in power electronics-based converters, which can lead to power quality problems. Power quality problems are also important in terms of internal consumption efficiency and energy continuity [6]. Pulse loads on some ships, such as cranes, may have an impact on the voltage profile of the power systems. Such voltage fluctuations can also negatively affect the stable operation of gen-sets, causing efficiency problems [7]. The unique off-grid configuration of ships necessitates an in-depth examination of power quality conditions, as the reactive power demand, the primary source of voltage and frequency fluctuations, has the potential to create circumstances that could negatively impact gen-sets. Consequently, existing power quality standards and assessment methodologies might be inadequate to fulfill the distinctive requirements of ship microgrids. The incorporation of novel techniques, such as ship system modeling and signal processing methods, could prove essential for effectively addressing power quality concerns [8]. Different methods can be used to increase the efficiency of gen-sets on ships. One of these studies proposed an optimization method to determine the best operating schedule of gen-sets for the next day of the ship's trip under the pre-trip strategy [9]. In this way, fuel savings and emissions reduction are achieved by operating gen-sets at the most suitable loads. Another solution to reduce emissions is low carbon, LNG etc. fuels [2]. Another study has shown that significant gains in energy and exergy efficiency are achieved with an energy production system operating with the waste heat of the main drive engine [10]. In addition, load sharing applications for gen-set are emerging as an important operational efficiency enhancing measure that does not require any investment among the types of energy saving applications for ships [11]. Another issue is the timing of maintenance of these systems. Proper and periodic maintenance of gen-sets also contributes significantly to efficiency. A study showed a 21.6% reduction in carbon emissions after a timed turbo charger overhaul [12]. Also, alternative energy sources can be used instead of directly from gen-sets to provide the ship's energy needs. For this purpose, energy storage systems and solar and/or wind energy systems can be utilized in existing ships [13]. Thus, significant reductions in ship emission rates can be achieved. When literature studies are examined, it is seen that considerable research has been done on reducing emission releases on ships. In addition, it is seen that the correct determination of ship internal energy consumption and categorization of load demands are not considered necessary, and the focus is more on energy sources and fuel types. However, with today's technological possibilities, the new concept in existing classical electrical networks and the applicability of the dual-sided management logic on ships will provide more effective benefits in maximizing efficiency.

While existing studies on maritime transport emissions focus mainly on fuel types, alternative energy sources, or compliance with environmental regulations, research on internal energy consumption and its direct impact on ship efficiency remains limited. This study fills this gap by providing a detailed case study of a ferry operating in real-world conditions. Unlike previous studies, which often rely on theoretical models or broad estimations, our approach is based on actual operational data, offering a data-driven analysis of gen-set efficiency, load management, and emissions reduction strategies. The results highlight key opportunities for improving energy efficiency by optimizing internal energy consumption, which can be applied to various ship types. Thus, this study contributes to maritime sustainability research by shifting the focus from fuel alternatives to onboard energy optimization, providing a practical framework for industry professionals and policymakers.

In this study, the efficiency potentials in internal electrical energy consumption in ships were categorized and analyzed. In addition, an efficient analysis was made on the parameters of a ferry carrying passengers and vehicles. The effects of reducing emissions, especially on ferries operating close to cities and used effectively on cabotage lines, have been demonstrated.

2. Energy Consumption and Emissions on Ships

Ships are among the most energy-intensive forms of transportation due to their size, propulsion systems, and onboard energy demands. Energy consumption on vessels can be broadly categorized based on different electric load demands, which typically fall into three categories: propulsion systems, auxiliary systems, and passenger loads as given in Figure 1. Understanding the nuances of these load demands and their impact on energy efficiency and emissions is essential for improving ship performance and reducing their environmental footprint.

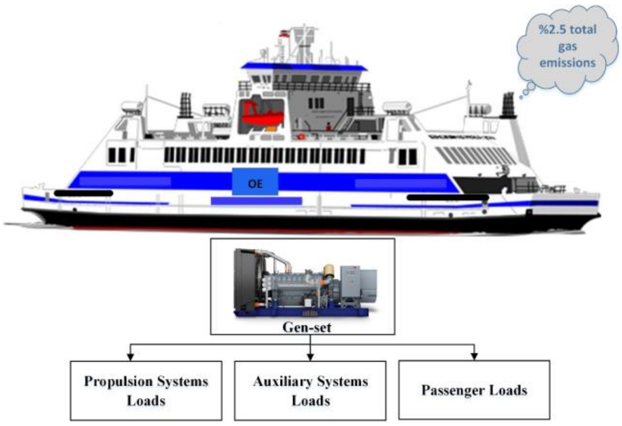

Figure 1: Energy consumption on vessel.

Propulsion Systems: The propulsion system, responsible for moving the vessel, is the largest energy consumer on most ships. This system primarily consists of the main engines, which are powered by marine diesel or heavy fuel oil. Modern ships may also utilize gas turbines or dual fuel engines that can switch between diesel and liquefied natural gas (LNG). The choice of propulsion system heavily influences fuel efficiency and emissions.

Electric propulsion, where the ship's propellers are driven by electric motors instead of mechanical systems, has gained traction in recent years, especially in cruise ships and ferries. Electric propulsion allows for more flexibility in load distribution and can improve efficiency by decoupling engine speed from propeller speed. However, the primary challenge remains the fuel consumption of the gen-set sets that power these electric motors, which, depending on the fuel used, can result in high levels of emissions.

Auxiliary Systems: Auxiliary systems include essential functions such as lighting, ventilation, cargo handling, and navigation equipment. These systems, though not as energy intensive as propulsion, still demand significant power, particularly in large vessels. The trend toward more automated and energy-efficient auxiliary systems has led to reductions in energy consumption. For example, the adoption of LED lighting, energy-efficient HVAC systems, and automated engine management systems contribute to overall fuel savings.

Passenger Loads: Hotel loads refer to the energy used to meet the needs of passengers and crew onboard, particularly on cruise ships and ferries. This includes heating, air conditioning, water desalination, and other amenities. As the demand for luxurious accommodations increases, so do the hotel loads, making energy efficiency improvements in these systems vital for reducing overall fuel consumption. Efficient energy management systems, combined with renewable energy sources such as solar panels for auxiliary loads, have begun to offset some of the energy demand in these areas.

2.1. Emissions from Ships

Emissions from maritime transport have significant environmental implications, particularly in port areas where ship exhaust emissions contribute to local air pollution. Research on cruise port emissions suggests that anchorage limitations and berth constraints can exacerbate air pollution by increasing fuel consumption during maneuvering and berthing. These findings highlight the necessity of energy-efficient solutions and optimized operational strategies to mitigate emissions in ferry and passenger ship operations [14]. Ship emissions are primarily the result of fuel combustion in propulsion engines and onboard gen-sets. These emissions include carbon dioxide (CO_2), nitrogen oxides (NOx), sulfur oxides (SOx), and particulate matter (PM) [15]. The number of emissions produced varies significantly based on the size of the vessel, the type of fuel used, and the operational profile of the ship.

In particular, ferries, which often operate in coastal or inland waters, have characteristic emission profiles due to their frequent stops, variable speeds, and relatively short distances. Ferries typically use large diesel engines for main propulsion and smaller auxiliary gen-sets for onboard power. The emissions from ferries are generally higher in proportion to their size compared to other vessels due to the frequent engine idling and low-speed maneuvers they perform.

Emissions on Ferries: In ferries, the main propulsion engines are the primary source of CO_2 and NOx emissions, particularly when the vessel is at high speeds or under full load. However, gen-sets, which provide power for hotel loads and auxiliary systems, also contribute to emissions, especially when the ferry is docked or operating at lower speeds. On some ferries, gen-sets may account for up to 30-40% of the total emissions, particularly in vessels with high hotel loads (e.g., passenger ferries with substantial lighting, heating, and air conditioning requirements). The emission details relation with ship size and main usage has been given in Table 1 [1].

Table 1: Emission details by ship size and usage.

Ship Size/Type	Main Usage	CO_2 Emissions (tons/year)	NOx Emissions (kg/year)	SOx Emissions (kg/year)
Small (< 5,000 GT)	Coastal ferries	3,000 - 5,000	15,000 - 25,000	5,000 - 7,000
Medium (5,000 - 20,000 GT)	Cargo ships, ferries	10,000 - 25,000	50,000 - 100,000	10,000 - 20,000
Large (> 20,000 GT)	Cruise ships, large tankers	50,000 - 100,000	150,000 - 300,000	50,000 - 80,000

Managing energy consumption and emissions on ships requires an understanding of the ship's load demands, efficient use of propulsion and auxiliary systems, and adherence to global emission regulations. Ferries face unique challenges due to their operational profile, making them a key focus for emission reduction strategies. Therefore, under the following section, a case study is presented on a ferry that operates between the island and mainland of Turkey, transporting both passengers and vehicles. The case study specifically examines the ferry's energy consumption and the associated emission values.

3. Case Study: Internal Energy Consumption in a Ferry

The case study focuses on the energy consumption and emission profile of a ferry operating between the ports of Bozcaada and Geyikli in Turkey which is shown in Figure 2.

The study analyzes how much fuel is consumed by the ferry's main engine and gen-sets, and how this fuel consumption leads to emissions based on the energy demand. Additionally, strategies to reduce these emissions are evaluated, aiming to improve energy efficiency and achieve a more sustainable operation.

The ferry travels approximately 7 km between the two ports. The ferry’s average speed ranges from 7 to 8.5 knots, allowing it to cover the distance in roughly 30 minutes. The ferry operates four trips per day, making it a critical vessel for local transport. The ferry is equipped with:

- Main Engine: 515 kW (1 engine)

- Gen-set: 2 x 120 kW gen-sets, where only one operates at a time

- Average Power Consumption: 45 kW.

The ferry schedule shows four round trips between Geyikli and Bozcaada, as shown in Table 2. Each one-way trip takes approximately 30 minutes. The ferry departs from Geyikli at set times and arrives at Bozcaada 30 minutes later, followed by a return trip starting from Bozcaada. This pattern repeats throughout the day, ensuring consistent travel between the two ports.

Figure 2: A ferry operating between the ports of Bozcaada and Geyikli in Turkey.

Table 2: Schedule of the ferry

Trip No	Departure Time (Geyikli)	Arrival Time (Bozcaada)	Departure Time (Bozcaada)	Arrival Time (Geyikli)	Sailing Duration (minutes)
1	08:00	08:30	09:00	09:30	30
2	11:00	11:30	12:00	12:30	30
3	15:00	15:30	16:00	16:30	30
4	19:00	19:30	20:00	20:30	30

The ferry uses diesel engines for both propulsion and electricity generation. This analysis focuses on the energy consumption and emissions generated by the ferry's main engine and gen-sets. Additionally, the study explores ways to optimize energy efficiency and reduce emissions.

3.1. Emissions and Electrical Energy Consumption in Ferry

Fuel consumption on a ferry primarily comes from two main sources. The first is the main propulsion engine, which is responsible for the vessel's movement and maneuvers [16]. The second source is the gen-set/s, which produce the electrical power required on board. Together, these two systems are the primary contributors to the ship's overall emissions.

While the main engine is the primary source of fuel consumption and emissions, the gen-set also contributes significantly to overall emissions. In this study, the harmful gas emissions were calculated based on the operational characteristics of the ferry’s main engine and gen-set. The carbon emission factor for diesel engines was assumed to be an average of 220 g/kWh [17], [18]. Also, the emission factors of pollutants caused by the engines have been given in Table 3 [19], [20].

$$E = FC \times EF \quad (1)$$

where E represents the emission rate (g/kWh), FC is the fuel consumption in kg/hour, and EF is the emission factor given in grams per kilogram of fuel consumed.

Table 3: Emission factors of pollutants caused by engines.

Pollutant	Full Name	Emission Factor
CO_2	Carbon Dioxide	3.16 kg per kg of fuel
NOx	Nitrogen Oxides	15 g/kWh
SOx	Sulfur Oxides	1.75 g/kWh
CO	Carbon Monoxide	1.5 g/kWh
PM	Particulate Matter	0.15 g/kWh

Using these factors, the emissions of the ferry were estimated per one-way trip, as well as on a daily, monthly, and annual basis. Calculations are made separately for the main engine and gen-set, and their totals are also given. These results are presented in Table 4.

Table 4: The emissions of the ferry were estimated per one-way trip, as well as on a daily, monthly, and annual basis.

Metric	One-Way Trip [kg]	Daily Emissions [kg]	Monthly Emissions [kg]	Yearly Emissions [kg]
CO_2 (Main Engine)	179.014	1432.11	42963.36	522720.88
CO_2 (Gen-set)	15.64	12.51	37.54	45674.64
Total CO_2	194.656	1557.25	46717.44	568395.52
NOx (Main Engine)	38.625	30.9	927	11278.5
NOx (Gen-set)	0.3375	2.7	81	985.50
Total NOx	4.20	33.6	1008	12264
SOx (Main Engine)	0.450625	3.605	108.15	1.315.825
SOx (Gen-set)	0.039375	0.315	9.45	114.975
Total SOx	0.49	3.92	117.6	1430.8
CO (Main Engine)	0.38625	3.09	92.69	1127.85
CO (Gen-set)	0.03375	0.27	8.10	98.55
Total CO	0.42	3.36	100.8	1226.39
PM (Main Engine)	0.038625	0.309	9.27	112.785
PM (Gen-set)	0.003375	0.027	0.81	9.855
Total PM	0.042	0.336	10.08	122.64

From these values, it is clear that the gen-set contributes a smaller portion of the total emissions. However, improving the load factor and energy efficiency of the gen-set can help reduce further these emissions. When operating at low loads, the gen-set's efficiency decreases. By improving load management, the gen-set can operate more efficiently. Also, modernizing the gen-set can result in lower fuel consumption and fewer harmful emissions. Newer gen-set technologies are significantly more efficient and environmentally friendly than older models. Moreover, recovering waste heat can substantially enhance the gen-set's energy efficiency. This recovered energy can be used for other onboard needs, thereby reducing overall energy consumption and fuel use.

3.2. Load Factor and Emission Analysis of Gen-set

The gen-set load factor is the ratio of average power consumption to the gen-set's nominal capacity. The gen-set's nominal capacity is 120 kW, but its average instant consumption is 45 kW. Therefore, the calculated values show that the gen-set operates at around 37.5% load. The fuel consumption for the gen-set is taken as 220 g/kWh. Accordingly, the gen-set's average fuel consumption is calculated as 9.90 kg/hour. Based on this fuel consumption, the emissions from the gen-set have been calculated. Emissions from the gen-set andthe main engine are analyzed separately, and their contributions to total emissions are assessed as percentages, which are given in Table 5.

4. Conclusion

The emissions generated during the widespread use of ferries in urban transportation as well as island transportation have attracted attention due to today's environmental concerns. In this context, it is important to conduct accurate analyses in reducing emissions caused by ferries in order to produce more efficient solutions. An analysis of the ferry's energy consumption and emissions reveals that the main propulsion engine is responsible for most of the fuel consumption and emissions, contributing around 90% to the overall CO_2, NOx, SOx, CO, and PM emissions. However, the ferry's gen-set, while operating at only 37.5% of its nominal capacity, still accounts for approximately 10% of the total emissions. Fuel consumption and emissions can be significantly reduced by optimizing the gen-set's load factor. For instance, improving the load distribution or using energy storage solutions could raise the efficiency of gen-set, resulting in lower emissions. Additionally, modernizing the gen-set with more efficient technology could further reduce the ferry's environmental impact.

On the other hand, this study is based on a single ferry operating between Geyikli and Bozcaada. While the findings provide valuable insights into internal energy consumption and emissions reduction strategies, the results may not be directly generalized to all ship types; however, ferry-type ships may have similar internal energy consumption processes. Different vessel sizes, operational conditions, and power system configurations could influence energy efficiency outcomes. Future research should extend the analysis to multiple vessel types, including cargo ships, large ferries, and cruise liners, to validate the applicability of these findings in diverse maritime contexts.

Article Information Form

Funding

We thank Gestaş Deniz Ulaşım Tic. A.Ş. for their technical support. Also, this work was supported by the Office of Scientific Research Projects Coordination at Çanakkale Onsekiz Mart University, Grant number: FBA-2023-4192.

Authors’ Contrtibution

The authors contributed equally to the study.

The Declaration of Conflict of Interest/Common Interest

No conflict of interest or common interest has been declared by the authors.

The Declaration of Ethics Committee Approval

This study does not require ethics committee permission or any special permission.

References

[1] IMO, “Fourth IMO GHG Study 2020 Full Report,” *Int. Marit. Organ.*, vol. 6, no. 11, p. 524, 2021, [Online]. Available: https://wwwcdn.imo.org/localresources/en/OurWork/Environment/Documents/Fourth IMO GHG Study 2020 - Full report and annexes.pdf

[2] Z. Wang, B. Dong, M. Li, Y. Ji, and F. Han, “Configuration of Low-Carbon fuels green marine power systems in diverse ship types and Applications,” *Energy Convers. Manag.*, vol. 302, no. October 2023, 2024, doi: 10.1016/j.enconman.2024.118139.

[3] C. C. Chou, H. P. Hsu, C. N. Wang, and T. L. Yang, “Analysis of energy efficiencies of in-port ferries and island passenger-ships and improvement policies to reduce CO2 emissions,” *Mar. Pollut. Bull.*, vol. 172, no. July 2021, p. 112826, 2021, doi: 10.1016/j.marpolbul.2021.112826.

[4] K. Yiğit, “Examining the Effect of Generator Load Sharing Practices on Greenhouse Gas Emissions for a Ship,” *Konya J. Eng. Sci.*, vol. 10, no. 2, pp. 301–311, 2022, doi: 10.36306/konjes.1056500.

[5] M. Kunicka, “Optimisation of the Energy Consumption of a Small Passenger Ferry with Hybrid Propulsion,” *Polish Marit. Res.*, vol. 31, no. 2, pp. 77–82, 2024, doi: 10.2478/pomr-2024-0023.

[6] D. Kumar and F. Zare, “A Comprehensive Review of Maritime Microgrids: System Architectures, Energy Efficiency, Power Quality, and Regulations,” *IEEE Access*, vol. 7, pp. 67249–67277, 2019, doi: 10.1109/ACCESS.2019.2917082.

[7] M. Falahi, K. L. Butler-Purry, and M. Ehsani, “Reactive power coordination of shipboard power systems in presence of pulsed loads,” *IEEE Trans. Power Syst.*, vol. 28, no. 4, pp. 3675–3682, 2013, doi: 10.1109/TPWRS.2013.2253809.

[8] T. Tarasiuk *et al.*, "Review of Power Quality Issues in Maritime Microgrids," *IEEE Access*, vol. 9, pp. 81798–81817, 2021, doi: 10.1109/ACCESS.2021.3086000.

[9] S. I. Taheri, G. G. T. T. Vieira, M. B. C. Salles, and S. L. Avila, "A trip-ahead strategy for optimal energy dispatch in ship power systems," *Electr. Power Syst. Res.*, vol. 192, no. November 2020, 2021, doi: 10.1016/j.epsr.2020.106917.

[10] M. E. Demir and F. Çıtakoğlu, "Design and modeling of a multigeneration system driven by waste heat of a marine diesel engine," *Int. J. Hydrogen Energy*, vol. 47, no. 95, pp. 40513–40530, 2022, doi: 10.1016/j.ijhydene.2022.05.182.

[11] K. Yiğit, "Evaluation of energy efficiency potentials from generator operations on vessels," *Energy*, vol. 257, 2022, doi: 10.1016/j.energy.2022.124687.

[12] A. J. Nyongesa *et al.*, "Experimental evaluation of the significance of scheduled turbocharger reconditioning on marine diesel engine efficiency and exhaust gas emissions," *Ain Shams Engineering Journal*, vol. 15, no. 8. 2024. doi: 10.1016/j.asej.2024.102845.

[13] K. Yiğit, "An Examination of the Potential Usage of Alternative Energy Systems in Ship Technology," *J. Sh. Mar. Technol. J.*, no. December, pp. 2651–530, 2018, [Online]. Available: https://dergipark.org.tr/tr/pub/gdt/issue/42891/518677

[14] G. Ling, C. Han, Z. Yang, and J. He, "Energy consumption and emission analysis for electric container ships," *Ocean Coast. Manag.*, vol. 261, no. August 2024, p. 107505, 2025, doi: 10.1016/j.ocecoaman.2024.107505.

[15] A. Roy and M. Chakraborty, "A review of ship emissions impacts on environmental, health, societal impacts and IMO's mitigation policies," *Reg. Stud. Mar. Sci.*, vol. 81, no. November 2024, p. 103964, 2025, doi: 10.1016/j.rsma.2024.103964.

[16] R. D. Geertsma, R. R. Negenborn, K. Visser, and J. J. Hopman, "Design and control of hybrid power and propulsion systems for smart ships: A review of developments," *Applied Energy*, vol. 194. pp. 30–54, 2017. doi: 10.1016/j.apenergy.2017.02.060.

[17] U.S. Department of Energy, "Fuel Properties Comparison," Alternative Fuels Data Center. Accessed: Sep. 20, 2024. [Online]. Available: https://afdc.energy.gov/files/u/publication/fuel_comparison_chart.pdf

[18] Infineon, "Why ships of the future will run on electricity." Accessed: Oct. 01, 2024. [Online]. Available: https://www.infineon.com/cms/en/discoveries/electrified-ships/

[19] İ. A. Reşitoğlu, K. Altinişik, and A. Keskin, "The pollutant emissions from diesel-engine vehicles and exhaust aftertreatment systems," *Clean Technol. Environ. Policy*, vol. 17, no. 1, pp. 15–27, Jan. 2015, doi: 10.1007/s10098-014-0793-9.

[20] T. I. Council and on Combustion Engines, "Guide to Diesel Exhaust Emissions Control of NOx, SOx, Particulates, Smoke and CO2," 2008. [Online]. Available: https://www.cimac.com/cms/upload/Publication_Press/Recommendations/Recommendation_28.pdf

Comparison of Levenberg-Marquardt and Bayesian Regularization Learning Algorithms for Daily Runoff Forecasting

Aslı Bor [1,2*], **Merve Okan**[2]

[1] *Norwegian University of Science and Technology, Department of Civil and Environmental Engineering, N-7491, Trondheim, Norway*

[2] *İzmir University of Economics, Department of Civil Engineering, 35330, İzmir, Türkiye*

ARTICLE INFO

Received Date: 14/10/2023
Accepted Date: 17/01/2025

Cite this paper as:
Bor, A., & Okan, M. (2025). Comparison of Levenberg-Marquardt and Bayesian Regularization Learning Algorithms for Daily Runoff Forecasting. *Journal of Innovative Science and Engineering.* 9(1), 62-77.

*Corresponding author: Aslı Bor
E-mail:asli.turkben@ieu.edu.tr

Keywords:
Discharge forecasting
Rainfall-runoff process
Artificial neural network
Euphrates-Tigris basin

ABSTRACT

In this study, Multilayer Perceptron (MLP) with Levenberg-Marquardt and Bayesian Regularization algorithms machine learning methods are compared for modeling of the rainfall-runoff process. For this purpose, daily flows were forecast using 5844 discharge data monitored between 1999 and 2015 of D21A001 Kırkgöze gauging station on the Karasu River operated by DSI. 6 scenarios were developed during the studies. Our findings indicate that the estimated capability of the Bayesian Regularization algorithm were close to with Levenberg-Marquardt algorithm for training and testing, respectively. This study shows that different network structures and data representing land features can improve prediction for longer lead times. We consider that the ANN model accurately depicted the Karasu flows, and that our study will serve as a guide for more research on flooding and water storage.

1. Introduction

In order to estimate the rainfall-runoff response of catchments and forecast hydrological droughts and flood events that result in fatalities and financial loss, hydrological models are essential applications [1]. To determine water capacities, countries establish a sparse hydrometric data collection network on the surface of rivers. However, estimating water capacity is not an easy work because of the complexity of physical parameters affecting stream flows. This complicated system, and the limits to existing hydrological information create significant uncertainty. The accuracy and capability of flow estimation models may have a direct effect on decisions related to water resources management. That's why; new estimation methods can be investigated to improve the existing ones. Machine learning is a term used to refer to the area of artificial intelligence that is data-based and contains traits that enable self-adaptability. In recent years, artificial neural network (ANN), is a widespread artificial intelligence method while solving some problems of hydraulic and water resource engineering. While physical models are expensive to build and need elaborate input data, a data-driven model such as ANN is simpler to use and depends just on the availability of climate data [2]. The study findings display that ANN can more accurately forecast when it is compared with both the traditional regression techniques and the current physical-based models, using a wider range of conditions [3-21]. Within the context of hydrological forecasting, the latest experiments demonstrate that ANNs can be a promising alternative for simulating the flow. ANN captures the behaviour of a system by using a training algorithm that minimizes the error function when finding the most suitable connection weights.

The principal objective of the study is to compare the performance of the artificial intelligence techniques, Multilayer Perceptron (MLP) with training algorithms of Levenberg-Marquardt (LM) and Bayesian Regularization (BR) in the forecasting of daily flows. For this purpose, D21A001 Kırkgöze gauging station on the Karasu River, a branch of the Euphrates River, one of the major water sources of Turkey, was selected for case study. Daily runoff forecasting for Euphrates-Tigris Basin is worth to be studied due to encountered frequent flood and drought times in the basin at the past. 6 different scenarios were developed for the forecasts and the optimal scenario was identified.

2. Methodology

2.1. Study site

The Euphrates-Tigris basin covers approximately 127304 km^2 area and it has 1009.87 m height. The average rainfall in the Euphrates-Tigris Basin is 540.1 mm year^{-1}, and the average annual flow is 31.61 km^3 which makes it the largest basin in Turkey in terms of average annual flow rate. There have been frequent flood and drought times in the basin since ancient times, causing serious damage to the country's economy. Hence, the estimation of the stream flow in the Euphrates-Tigris basin is particularly important in terms of the effective operation of water resources systems and the reduction of flood damage. Daily rainfall and runoff (discharge) data set is used at D21A001 Kırkgöze gauging station on the Karasu River (Figure 1), a branch of the Euphrates River, for 16 years from 1 October 1999 to 30 September 2015 (5844 data).

The daily runoff data was obtained from DSI flow observation annuals, and temperature and precipitation data was obtained from NASA POWER Data Access Viewer. Information about D21A001 Kırkgöze gauging is given in Table 1.

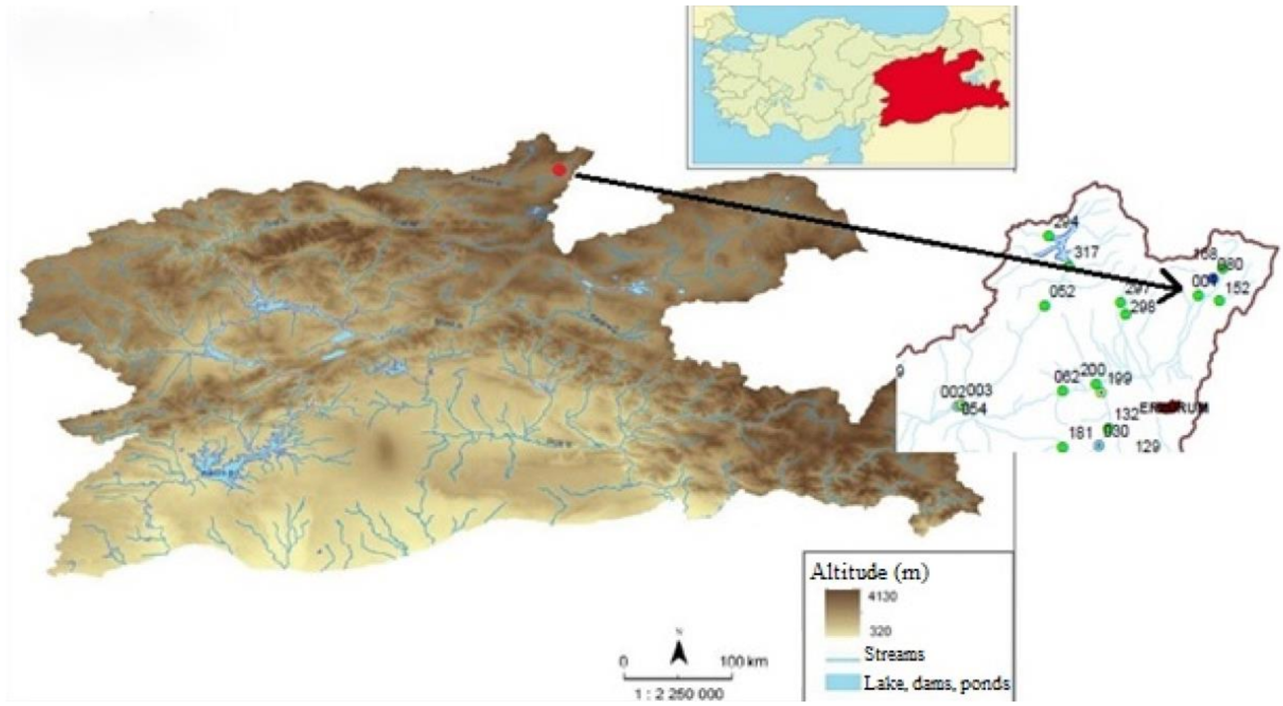

Figure 1: Euphrates-Tigris basin and location of the D21A001 Kırkgöze gauging.

Table 1: Information about Karasu River Kırkgöze gauging.

Station Number:	D21A001
Stream:	Karasu
Station:	Kırkgöze
Management:	DSİ
Altitude (m):	1830
Drainage Area (km²):	232.2
Observation Period:	1961-2016
Latitude:	40°6'29" N
Longitude:	41°23'8" E

2.2. Artificial Neural Networks

One of the most commonly known artificial intelligence techniques in the discipline of water resources engineering is the artificial neural network (ANN). Learning, association, classification, generalization, feature determination, and optimization are just a few applications of artificial neural networks (ANN), which are implemented to nonlinear and mathematical modelling problems [22]. ANN was inspired by the working principle of biological neural networks, which are composed of synapses, axons, dendrites, and nuclei in the brain. In the field of hydrology, a multilayer perceptron is one of the most prevalent network structures (MLP). MLP is used for problems such as classification, prediction, recognition, interpretation, and identification. In recent years, researchers have studied the capabilities of Multilayer Perceptron (MLP) models for the estimation of river flow [11], [13], [23]–[25]. MLP is composed of 3 principal layers as the input, hidden and output layer (Figure 2). MLP can have multiple hidden layers. Haykin (1998) [26] explains MLP more elaborately.

ANN itself generates output data against the input data, that is, it trains the examples given, and then aims to predict the desired data according to its generalization. It is not certain how many hidden neurons there should be in an ANN, the number may vary depending on the problem, data and number of variables. Therefore, when estimating with an ANN model, different hidden neuron numbers should be tested to find the network structure that can optimize the estimation.

The main disadvantage of ANN is that it may not obtain optimum estimates at the first time because different ANN structures are created for different hidden neuron numbers and weight coefficient values, and each ANN makes a different estimate. It is necessary to the method of use trial and to determine which network can optimally predict from the created networks. This does not guarantee that the solution found is the best solution; in other words

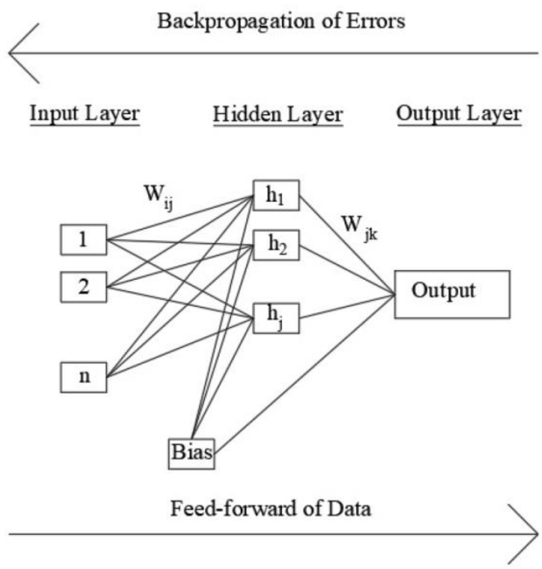

Figure 2: Architecture of multi-layer ANN.

ANN can produce acceptable solutions without guaranteeing these are the best solutions [27].
MLP is trained according to the instructional learning strategy. This approach involves providing the network with both inputs and outputs, enabling the network to comprehend the type of link between input and output. The network adjusts the weight coefficient values it assigns as it gains knowledge of the relationship between input and output until the difference between the estimated value and the actual output falls to a predetermined level. The error value for ANN refers to the difference between the network's estimated value and its actual output. The smaller this value, the closer the network predicted output value will be to the actual output value. The coefficients assigned by the network are changed according to certain learning rules. MLP updates the weighting coefficients according to the "Generalized Delta Rule" learning rule. Forward calculation and backward calculation are the two stages of the Generalized Delta Rule. Feed-forward backpropagation ANN calculates output against given input while feeding forward. Neurons in the input layer are connected to the hidden layer with certain weight connections to the output layer, with certain weight connections in the hidden layer. After the data in the input layer is multiplied by the weights to which they are connected and collected in the addition function, it passes through the activation function to the hidden layer, in the same way, the data received from the input layer in the hidden layer is multiplied by the weights they are connected to, and is collected in the addition function and sends it to the output layer as output data. Usually, the preferred activation function for MLP is the sigmoid function.

The equation (1) of the addition function is as follows.

$$Net = \sum_{i=1}^{n} w_{ij} x_i + b_j \qquad (1)$$

where; x_i is the input value of neuron ($i = 1,2, \ldots, n$), w_{ij} is the weight coefficient, n is the overall number of inputs going to a neuron and b_j is the Bias value. b_j is a threshold value that the Net value must surpass to generate an outcome. Usually, threshold value neurons assigned as -1 or +1 are assigned as input values [28]. However, the threshold input does not have to be assigned to ANN. In MLP, which is the most widely used today, the tangent-sigmoid function is used as the activation function in this study.

While calculating the network output in the forward calculation phase, the weight coefficients are updated in the reverse calculation phase. In the backpropagation learning algorithm, there is a forward flow of information between the layers, while backward error spreads so that the total square error is minimized. In this context, backpropagation algorithms have been developed to minimize the specified performance function. Two of the most used backpropagation algorithms when training ANN are Levenberg-Marquardt and Bayesian Regularization algorithms. With these algorithms, in order to bring the predicted data of the network as close as possible to the actual data, that is, to minimize the error value, the weight coefficients are changed, and the estimated outputs are recalculated until they fall below a certain value. In this study, the existing flows of the Karasu River have been estimated by using the feed-forward back-propagation ANN model and used two backpropagation algorithms when training ANN are Levenberg-Marquardt and Bayesian Regularization algorithms. With these algorithms, in order to bring the predicted data of the network as close as possible to the actual data, that is, to minimize the error value, the weight coefficients are changed, and the estimated outputs are recalculated until they fall below a certain value. Levenberg-Marquardt and Bayesian Regularization training algorithms are employed and their performances are compared in this study.

2.2.1. Levenberg-Marquardt Algorithm

Levenberg-Marquardt algorithm, which removes the constraints of Gauss-Newton and gradient-descent algorithms and consists of the best features, is a least-squares calculation method. It is a simplified version of the classical Newton method used in training MLP. The performance function can be taken as mean squared error (Equation (2)) which given below.

$$E_d = MSE = \frac{1}{n} \sum_{i=1}^{n} (T_i - Y_i)^2) \qquad (2)$$

where; T_i is the expected value, Y_i is the output and E_d is the mean squared error of the network.

The Jacobian matrix, $J(w)$, is obtained from the first derivatives of the network errors according to the weights. At the backpropagation stage of the network error, firstly, the gradient of the network, *G(w)* is computed by using the transposition of the Jacobian matrix and the network errors (Equation (3)).

$$G(w) = J^T(\mathrm{w})\, e(w) \qquad (3)$$

where; e is the error vector. After calculating the gradient of the network, the vector change in the weights of the network, $\Delta w = w_{new} - w_{old}$, is determined by multiplying the inverse of the Hessian matrix (Equation (4)) with the gradient of the network.

$$H(w) = J^T(w) J(w) + \mu I \qquad (4)$$

where; μ is the Marquardt parameter, I is the Unit matrix and w is the weight vector.

While the network is trained with the Levenberg-Marquardt algorithm and minimizing the performance function with respect to weight vector, the weight change of the network is calculated as in Equation (5).

$$\Delta w = -[H(w)]^{-1} G(w) \qquad (5)$$

where $H(w)$ is the Hessian matrix and $G(w)$ is the gradient.

μ parameter is identified as a numerical number for the Levenberg-Marquardt algorithm. The process continues to work as Newton's algorithm if μ is getting closer to zero; if μ is enlarging, the algorithm switches to the gradient reduction method [29], [30]. Newton's method is more rapid and precise when it is close to a minimum error. Therefore, the goal becomes switching to Newton's method at the earliest time. μ decreases when reduction in performance function occurs and only increases when there is an increment in the performance function depending on a decay rate, thus, each time the algorithm iterates, the performance function always declines [31].

2.2.2. Bayesian Regularization Algorithm

Unlike the traditional neural network backpropagation, which adjusts the optimum weight coefficients by minimizing the error function, the Bayesian regularization algorithm uses the probability distribution of the network's weights [32]. In other words, the estimates made by the network are based on probability distribution. In training with Bayesian Regularization algorithm, the weight and bias values are refreshed according to Levenberg-Marquardt optimization. Bayesian Regularization approach, which automatically arranges the appropriate performance function to achieve successful generalization, was developed by MacKay (1992) [33]. Large-value weights can cause output to vary excessively, and Regularization is the traditional method of addressing the negative impact of large-value weights. Bayesian Regularization approach includes probability distribution of network weights. Consequently, the estimates made for the network are also a probability distribution. Bayesian Regularization involves modifying the performance function commonly used, such as the sum of mean square errors (MSE). Bayesian Regularization algorithm aims to enhance the model's capacity for generalization of the model. In the training phase, the E_w term, which is the sum of the squares of the performance function net weights is expanded to improve the generalization ability of the network (Equation (6)) [32];

$$F = \beta E_d + \alpha E_w \tag{6}$$

where; E_w is the sum of squares of the network weights and F is the regularized objective function. The α and β parameters need to be estimated and adjusted according to the Bayesian Regularization algorithm. If $\alpha << \beta$, the Bayesian Regularization training algorithm shrinks errors further. If $\alpha >> \beta$ will emphasize the reduction of training weight size, thus producing a smoother network response [34] and decreasing chance of overfitting with better generalization. Adjusting the proper values for α and β parameters is the key challenge in regularization implementation [34]. Overfitting may be inevitable if α is too big and the network does not properly fit the training data if it is too small.

According to the Bayesian Regularization rule, the posterior distribution of the weights of ANN can be updated using Equation (7):

$$P(w|D,\alpha,\beta,M) = \frac{P(D|w,\beta,M)\times P(w|\alpha,M)}{P(D|\alpha,\beta,M)} \tag{7}$$

where; M is the specific ANN architecture used and D is the training set consisting of input and target data. In the implementation of the Bayesian Regularization algorithm, optimum weights should maximize the posterior probability, $P(w|D,\alpha,P,M)$, because maximizing the posterior probability of the weights corresponds to minimizing the regularized objective function (Equation 7) [34], [35].

Foresee and Hagan (1997) [34] put forward the procedure to achieve optimum values of α and β parameters:

Firstly; α, β and the weights are initialized. Initially, α is selected as 0.

Then, one step of the Levenberg-Marquardt algorithm is taken to minimize the regularized objective function, F.

The effective number of parameters, γ, which measures how many network parameters, such as weights and biases, are utilized by the neural network to minimize the error function, is calculated.

New predictions for α and β parameters are executed.

Lastly, iterations from step 2 to step 4 is performed until convergence.

3. Performance Measures

Performance evaluation was carried out with the root mean squared error (RMSE), mean absolute error (MAE), Percent Bias (PBIAS), Nash-Sutcliffe efficiency (NSE), and the coefficient of determination (R^2).

The standard deviation of the prediction errors can be identified as Root Mean Square Error (RMSE). In forecasting and regression analysis studies, root mean square error, RMSE, is frequently used to validate experimental results.

$$RMSE = \sqrt{\frac{\sum_{i=1}^{n}(T_i - Y_i)^2}{n}} \tag{8}$$

The average absolute variance between the observed and the estimated values is referred as the mean absolute error (MAE). It is not considered to examine under and overestimation and changes linearly. Like RMSE, it is a preferable metric in forecasting studies.

$$MAE = \frac{1}{n}\sum_{i=1}^{n}|T_i - Y_i| \tag{9}$$

Both RMSE and MAE show that the closer the error values are to 0, the more predicted values approach to the expected values.

Underestimation or overestimation of the forecast is quantified by the bias ratio. According to Gupta et al. (1999) [36] and Moriasi et al. (2007) [37], positive PBIAS indicates model underestimation bias and negative PBIAS shows model overestimation bias.

$$PBIAS = \frac{\sum_{i=1}^{n}(T_i - Y_i) * 100}{\sum_{i=1}^{n}(T_i)} \tag{10}$$

Prediction ability of hydrological models is frequently evaluated using the Nash-Sutcliffe efficiency statistic [38]. According to theory, the NSE statistic ranges from -∞ to 1, with 1 denoting the ideal model.

$$NSE = 1 - \left[\frac{\sum_{i=1}^{n}(T_i - Y_i)^2}{\sum_{i=1}^{n}(T_i - \bar{T})^2}\right] \tag{11}$$

A measurement of the linear correlation between two quantities is the coefficient of determination, R^2. The coefficient of determination R^2 is defined as the square of the correlation coefficient. The determination coefficient, the R^2 values demonstrate how well the forecasted and observed values correspond and it is a value ranging from 0-1, the closer to 1, the more predicted values converge to the real results.

$$R^2 = \left(\frac{n\sum_{i=1}^{n} T_i Y_i - (\sum_{i=1}^{n} T_i)(\sum_{i=1}^{n} Y_i)}{\sqrt{\left[n(\sum_{i=1}^{n} {T_i}^2) - (\sum_{i=1}^{n} T_i)^2\right]\left[n(\sum_{i=1}^{n} {Y_i}^2) - (\sum_{i=1}^{n} Y_i)^2\right]}}\right)^2 \tag{12}$$

where $\bar{T}$ denotes the mean of experimental findings.

By considering Moriasi et al. (2007) [37], the performance is determined in this study as follows:

0.75<NSE≤1: “very good”; 0.65<NSE≤0.75: “good”; 0.50<NSE≤0.65: “satisfactory”,

PBIAS<±10%: “very good”; ±10% ≤PBIAS <±15%: “good”; ±15%≤PBIAS<±25%: “satisfactory”.

4. Results and Discussion

This study presents modelling of the rainfall-runoff process of D21A001 Kırkgöze gauging station on the Karasu River by using the artificial intelligence method, MLP. ANNs were created by updating the code produced by Neural Network Toolbox Fitting Tool in the MATLAB environment. Training, validation, and testing sets of data were created. The first 70% of the data series were chosen to serve as the training set, the next 5% as the validation set, and the final 25% as the testing set for the Levenberg-Marquardt algorithm. For the Bayesian Regularization algorithm, the first 75% of the data series were chosen as the training set and the next 25% of the data series were picked as the testing set. The tangent-sigmoid function was utilized as an activation function. Input runoff and rainfall scenarios were evaluated. Following the creation of several network designs, for training, it was decided on the scenario inputs and the quantity of neurons in the hidden layer. In order to make an evaluation for the ANN which gives the best result, some performance functions were utilized, i.e., the minimum root mean square errors, RMSE and the maximum determination coefficients, R^2 for the testing period. Then, accordingly, the scenario inputs and the number of the neurons in the hidden layer used in this study were investigated.

The scenarios were created using the past and current rainfall, temperature which is presented in Table 2. The inputs include the previously observed daily discharge(Q) and rainfall (P) and temperature (T), (Q(t-1),Q(t-2),Q(t-3), P(t-1),P(t-2),P(t-3), T(t-1),T(t-2), and T(t-3)), and the output is assigned as the current runoff (discharge) (Q(t)) (t is the current time).

First, all the scenarios were trained to use as odd numbers from 3 to 21 hidden neurons, their performance was examined, and the best 6 were selected for further calculations. As a result, 6 scenarios including a variety of inputs of Q, P, and T data were presented in Table 2 and both of the training algorithms were applied in modelling of rainfall-runoff to identify the ideal scenarios.

Table 2: Various input model scenarios.

Scenarios	Inputs	Output
1	P(t-1),T(t-1),Q(t-1)	Q(t)
2	P(t-2),T(t-2),Q(t-2)	Q(t)
3	P(t-3),T(t-3),Q(t-3)	Q(t)
4	P(t-1),Q(t-1)	Q(t)
5	Q(t-1)	Q(t)
6	Q(t-1),Q(t-2)	Q(t)

Training took place in accordance with the training parameters. The μ was increased by increase factor for μ until the change in performance reached a reduced performance value. Then, the change was performed to the network and μ was decreased by the decrease factor for μ. When the maximum number of epochs was reached, the performance gradient fell below the minimum performance gradient, the performance was minimized to the target, or μ exceeded the maximum value for μ, training was terminated. Besides, while training occurred with Levenberg-Marquardt algorithm, training stopped when validation performance has increased more than maximum validation failures since the last time it decreased while using validation. However, validation stops were not utilized by arranging maximum validation failures as infinite for Bayesian Regularization algorithm so that training was able to proceed until an optimal combination of errors and weights were obtained.

Maximum number of epochs to train was taken maximum as 1000, performance goal for all the data as 0. For Levenberg-Marquardt training algorithm, the number of maximum validation failures was taken as 6. Maximum time to train in seconds was taken as infinite, minimum performance gradient as 10^{-7}. For Levenberg-Marquardt algorithm, initial μ was taken as 0.001 and for Bayesian Regularization Algorithm; Marquardt adjustment parameter was taken as 0.005. The decrease factor for μ was as 0.1, increase factor for μ as 10, maximum value for μ as 10^{10}.

For activation function, tangent-sigmoid was used and performance function was taken as mean squared error, MSE, function during the process. The learning rate was arranged as 0.01 and the momentum constant as 0.9 for gradient descent with momentum weight and bias learning function. During the process of creating ANNs, the input and target data were normalized from its original range to the range [-1, 1].

For both algorithms, the number of hidden neurons was chosen as the odd numbers from 3 to 21, respectively, and 50 independent ANNs were created for each selected hidden number of neurons. When the number of hidden neurons has been taken more than 21, it has been observed that there became a decline in the performance of ANN. That's why; the maximum number of neurons was taken as 21. The mean squared error (MSE) and determination coefficient (R^2) results of the 50 created independent ANNs were averaged, and the best-hidden neuron number was selected considering the test results of the smallest mean MSE and largest mean R^2 values of these 50 ANNs. This process was repeated for each scenario. Then, conducted 50 ANNs according to the best selected hidden neuron number were examined for each scenario and by taking into account the test results of the network with the smallest RMSE, MAE, and PBIAS with the largest NSE and R^2 values between each 50 ANNs, the best scenario was selected. For RMSE, MAE and PBIAS, lower numbers are preferable, whereas NSE and R^2 is better with levels near 1.

Overfitting is one of the issues that arise during the training of neural networks. When the network is provided with new data, the error is much larger than it is when the training set is used. The network internalizes the training samples; however, it is incapable of generalizing to unexpected situations. The regularization and early stopping techniques can be considered as two ways to enhance generalization.

Three selected sets of the present data are used in the early stopping method. The training set, which is the first set, is utilized to compute the gradient and update the weights and biases of the network. Validation set composes the second set. Throughout the training process, the validation set error is tracked. Both the training set error and the validation set error commonly decrease during the first stage of training. Nonetheless, the validation set error can begin to increase when the network starts to overfit the data.

Early stopping method was applied to prevent the network from becoming overfit to the training data set while training with Levenberg-Marquardt algorithm. The training was terminated and the weights and biases with the smallest validation error were returned after the validation error increased for a predetermined number of iterations. The number of maximum validation failures is a measure of subsequent iterations during which the validation performance does not improve. The training came to end when this predetermined number of iterations achieved 6.

The value of the performance function was plotted against the number of iterations in the performance plot. Performances throughout training, validation, and testing were depicted. The iteration at which the least validation performance achieved was shown with the best epoch. Six additional iterations were executed until training was terminated.

It can be pointed that there is no significant problem with training according to Figure 3. The validation and test curves are very similar. It is likely that some overfitting may have taken place if the test curve had increased sufficiently before the validation curve did.

This graph demonstrates how training and validation errors decrease until the epoch indicated. Since the validation error did not grow prior to epoch 5, overfitting does not seem to have been place.

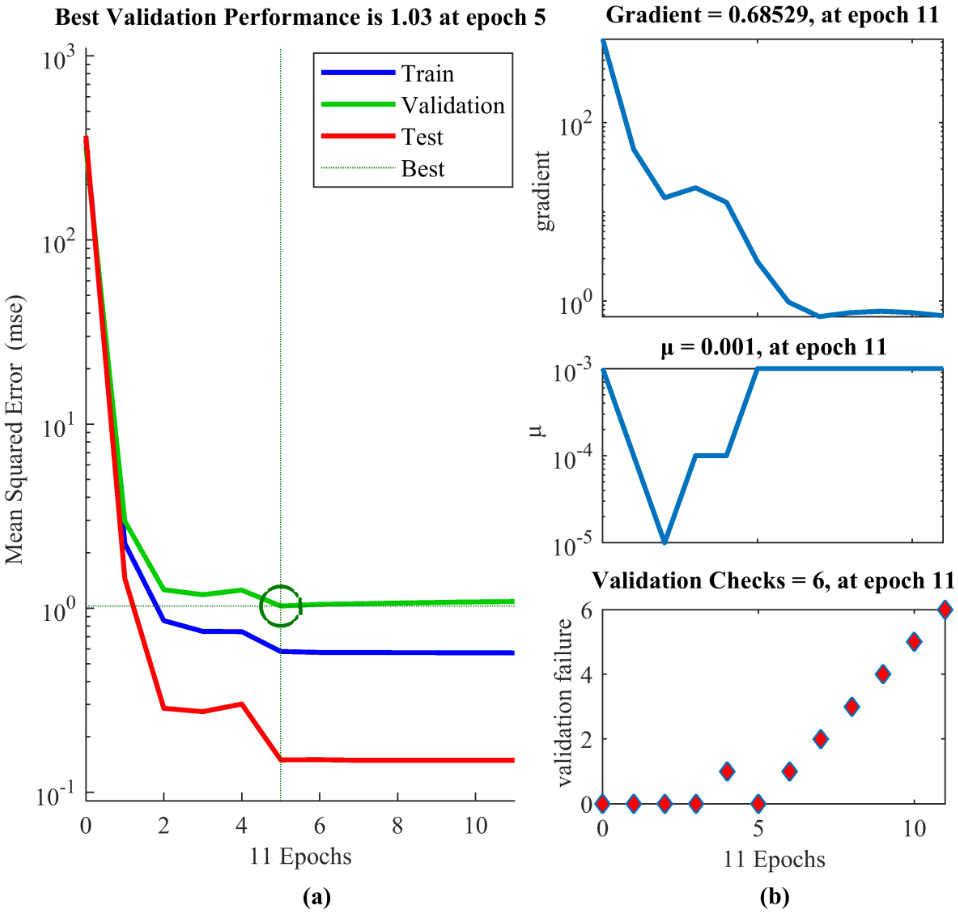

Figure 3: a) Performance curves and b) training states for Levenberg-Marquardt.

Regularization is the other method for improving generalization. It might be used instead of validation during training in order foster effective generalization. Validation is typically employed as a sort of regularization; however, training with Bayesian Regularization has its own sort of validation integrated into the algorithm. There is no validation check during training with Bayesian Regularization so that no validation set since the goal of verifying validation is to see whether the validation set error improves or worse over time. Thus, it is possible to keep training until the optimal combination of errors and weights is discovered. The errors observed while training with Bayesian Regularization not only originating from the performance of the model, but also from the weights because greater weights result in higher error. That's why; determining a number of maximum validation failures can prevent the network to experience greater weights so that prevent searching for an ideal combination of squared errors and weights with increasing number of iterations.

It's crucial to train the network until convergence when using Bayesian regularization. The sum squared weights (SSW) and the sum squared error (SSE) should all achieve constant values after multiple iterations once the network has converged [39]. Besides, the algorithm should be allowed to run until the effective number of parameters, γ, converges without considering how many parameters there are in the network [39]. If training is terminated when μ reaches maximum, the algorithm will be in fact converged.

It can be seen that the effective number of parameters, γ, and sum squared weights achieved constant values after multiple iterations and performance curves were converged (Figure 4). The best training performance was obtained at epoch 374.

Eventually, while training stopped due to reaching maximum validation failures at epoch 11 in Levenberg-Marquard and since maximum μ was reached at epoch 491 in Bayesian Regularization. Table 3 and Table 4 give performance evaluation of Levenberg-Marquardt and Bayesian Regularization algorithms through the R^2, NSE, RMSE, MAE and PBIAS indexes.

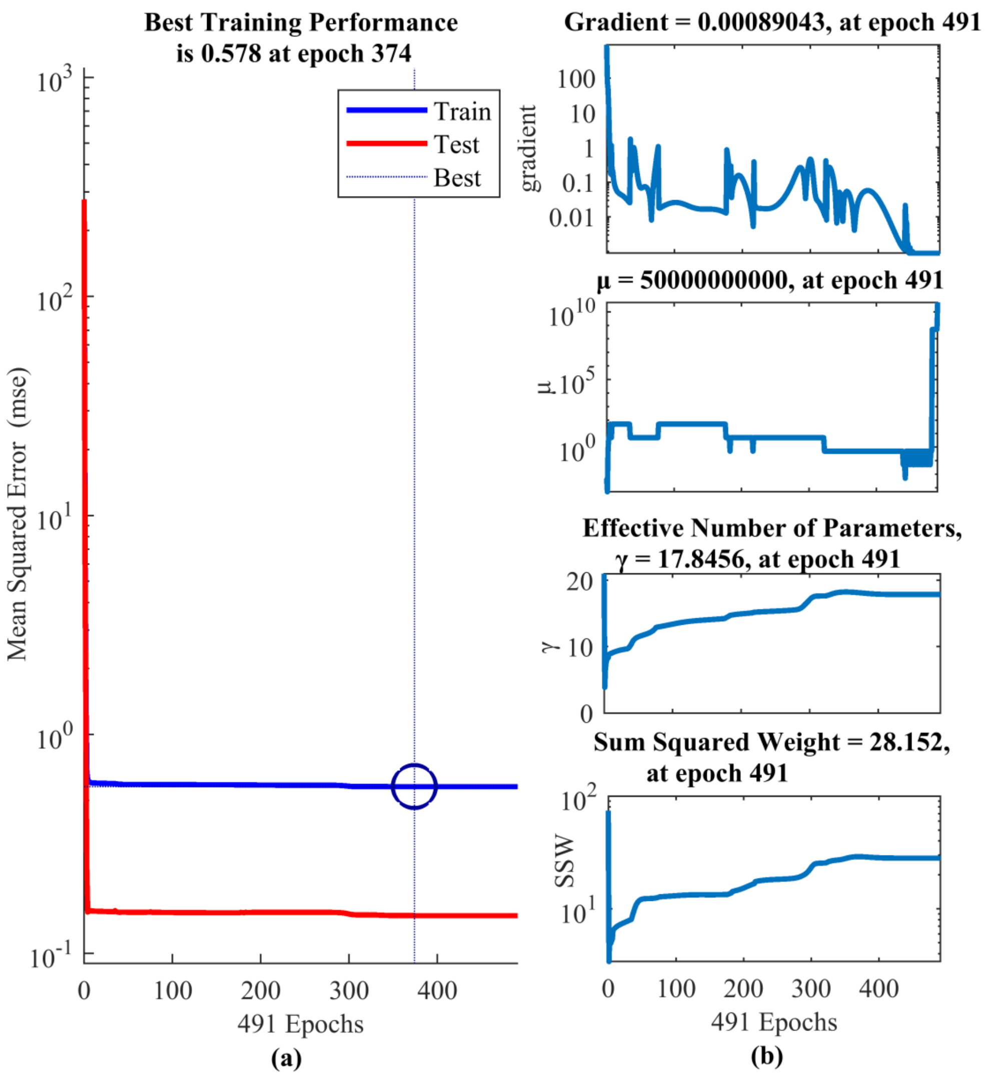

Figure 4: a) Performance curves and b) training states for Bayesian Regularization.

Table 3: Testing statistics of the LM according to the best hidden neuron number.

Scenario	Number of Hidden Neurons	Training RMSE (m^3/s)	Training MAE (m^3/s)	Training PBIAS (%)	Training NSE	Training R^2	Testing RMSE (m^3/s)	Testing MAE (m^3/s)	Testing PBIAS (%)	Testing NSE	Testing R^2
		Levenberg-Marquardt (LM)									
1	3	0.738	0.323	0.34	0.95	0.95	0.391	0.202	2.42	0.97	0.97
2	9	0.982	0.473	1.16	0.91	0.91	0.572	0.306	4.44	0.93	0.93
3	13	1.203	0.585	-5.81	0.86	0.86	0.674	0.358	-1.75	0.90	0.90
4	3	0.762	0.315	0.001	0.94	0.94	0.397	0.186	1.11	0.96	0.97
5	13	0.762	0.321	0.03	0.94	0.94	0.401	0.189	1.41	0.96	0.96
6	**3**	**0.763**	**0.303**	**-1.96**	**0.94**	**0.94**	**0.387**	**0.177**	**-1.08**	**0.97**	**0.97**

Table 4: Testing statistics of the BR according to the best hidden neuron number.

Scenario	Number of Hidden Neurons	Bayesian Regularization (BR)									
		Training					Testing				
		RMSE (m^3/s)	MAE (m^3/s)	PBIAS (%)	NSE	R^2	RMSE (m^3/s)	MAE (m^3/s)	PBIAS (%)	NSE	R^2
1	15	0.692	0.306	0.00003	0.96	0.96	0.386	0.200	2.15	0.97	0.97
2	17	0.975	0.463	0.01	0.92	0.91	0.571	0.297	3.19	0.93	0.93
3	9	1.206	0.586	0.0003	0.87	0.87	0.677	0.360	3.68	0.90	0.90
4	3	0.773	0.323	0.0002	0.95	0.95	0.399	0.188	1.18	0.96	0.96
5	3	0.792	0.324	0.01	0.94	0.94	0.402	0.186	1.22	0.96	0.96
6	**5**	**0.760**	**0.313**	**-0.02**	**0.95**	**0.95**	**0.386**	**0.184**	**1.48**	**0.97**	**0.97**

Networks created with rainfall and temperature data alone did not work effectively, thus they were not added to the tables. 50 independent networks were created for each hidden number of neurons and the best numbers of hidden neurons were chosen according to their average performance values.

This is because each network is different from others, although all are created with the same hidden number of neurons. Because during the creation of each network, there are changes in the weight and threshold values given to the network, therefore, the same network is not created for the same number of hidden neurons, and the performance of each network changes. However, it has been observed that the error values and performance values of the ANNs created according to the number of hidden neurons are similar, but not exactly the same, so 50 networks are created, and their performance is averaged, and the results of the overall performance are taken into account.

Additionally, each ANN model's structures are provided in Table 3 and Table 4 with their hidden layer counts. It is clear from Table 3 that the Q(t-1), Q(t-2) scenario with 3 hidden neuron numbers has the lowest RMSE, MAE, PBIAS and the largest NSE and R^2 values taking into account the test results for Levenberg-Marquardt algorithm.

Accordingly, it is seen that the MLP trained by the Levenberg-Marquart algorithm has a successful performance in the current flow estimation considering the R^2 results. It can be said that the best scenario for the application for the Bayesian Regularization algorithm is the Q(t-1), Q(t-2) scenario with 5 hidden neuron numbers has the lowest RMSE, MAE and largest NSE and R^2 values. The results show that the Bayesian Regularization algorithm can produce formulas that are both well fitted to the data and have very low mean errors. However, when scenarios were conducted by taking only precipitation and temperature data as input, it has been obtained a low performance of for both the Bayesian Regularization and Levenberg-Marquardt algorithm which are not shown in this study.

Figures 5 and 6 display the ideal ANN's observed and predicted runoff values (created by the Levenberg-Marquart and the Bayesian Regularization algorithms) during both training, validation and test periods by using scatter diagrams and continuous graphs, respectively.

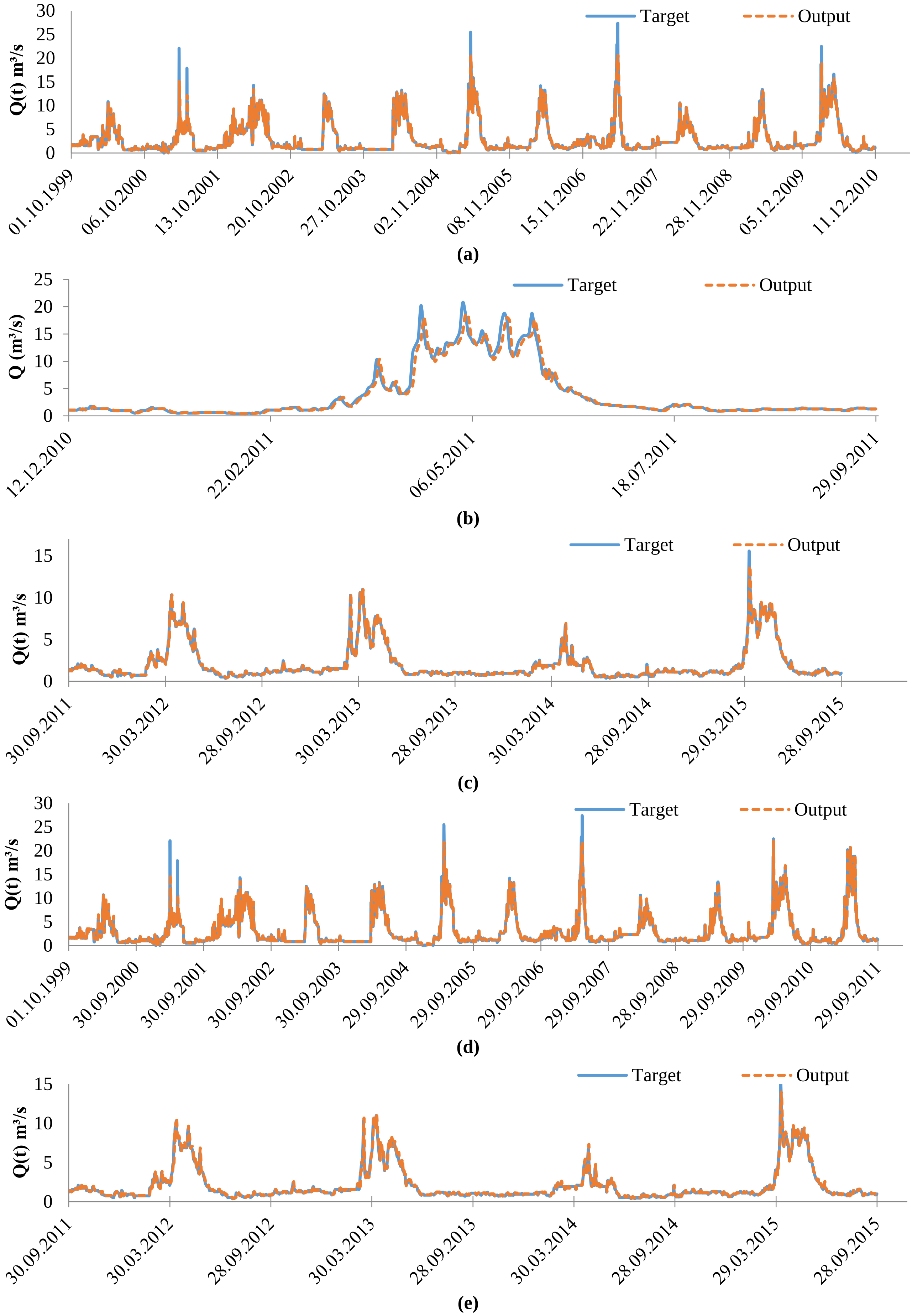

Figure 5: Observed and predicted runoff (discharge) values for scenario 6 using both LM for a) training, b) validation and c) testing cases and BR for d) training and e) testing cases.

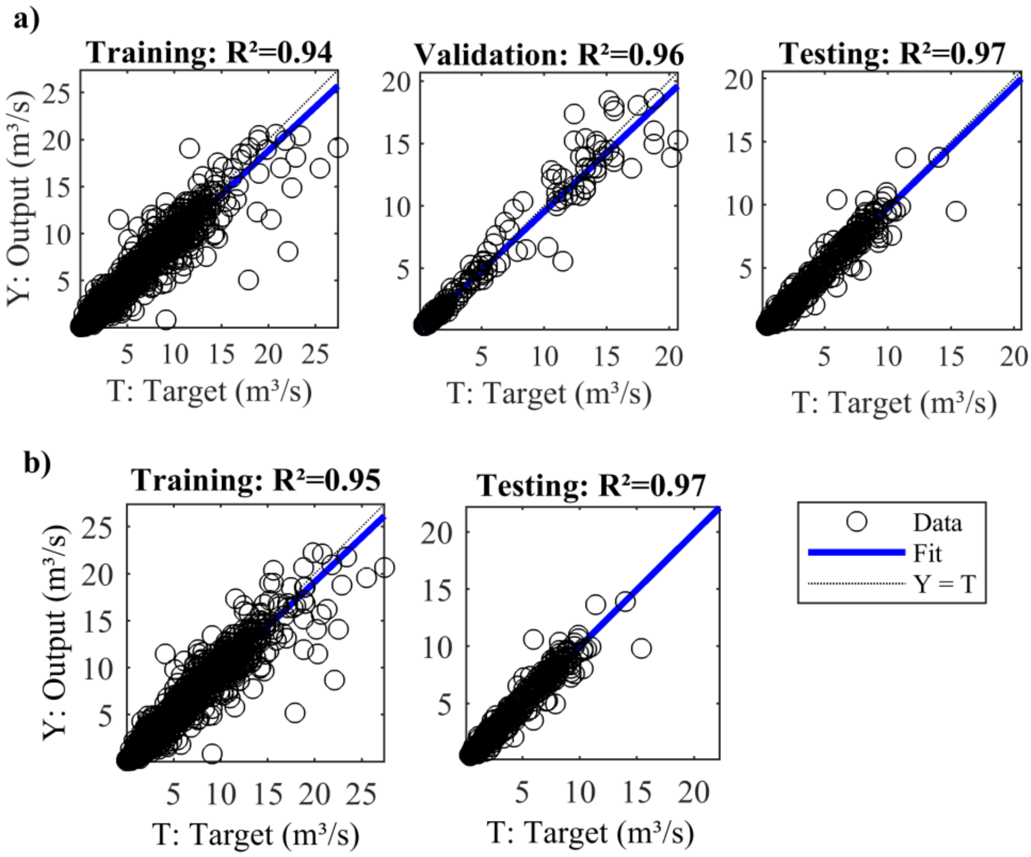

Figure 6: The scatter plots of scenario 6 for both a) LM and b) BR algorithms for training, validation and testing cases.

To more clearly investigate the performance of the training algorithms used in this study, a series of graphs in Figure 5 shows the target and output values for these clusters. The situation is shown by the diagonal line connecting the expected and observed values where the predicted values differ slightly from the observed ones. In fact, overlapping is not impossible to achieve, practically. However, the data points build up around this line, even for larger data. The performances of the same scenarios of the two algorithms are generally close to each other. In both algorithms, it has been observed that, when the flow inputs are added to scenarios with only rainfall and temperature inputs, the current day's current forecast performance is significantly increased.

According to evaluations by NSE and PBIAS, performance ratings can be considered as very good. The comparison of the findings in Table 5 demonstrates that ANN model created by the Bayesian Regularization algorithm and Levenberg-Marquart algorithm shows close performance in term of RMSE, MAE and PBIAS as well as NSE and R^2 indexes.

Table 5: The performance comparison of ANN (created by the LM and BR algorithms).

Method	Training					Testing				
	RMSE (m^3/s)	MAE (m^3/s)	PBIAS (%)	NSE	R^2	RMSE (m^3/s)	MAE (m^3/s)	PBIAS (%)	NSE	R^2
ANN-LM	0.763	0.303	-1.96	0.94	0.94	0.387	0.177	-1.08	0.97	0.97
ANN-BR	0.760	0.313	-0.02	0.95	0.95	0.386	0.184	1.48	0.97	0.97

These best ANN models for the Levenberg-Marquart and the Bayesian Regularization algorithms have R^2 and NSE values of 0.94 and 0.95 for training, 0.97 and 0.97, for testing, respectively. Besides, when RMSE values are compared, the Levenberg-Marquart and the Bayesian Regularization algorithms have 0.763 m^3/s and 0.760 m^3/s for training and 0.387 m^3/s and 0.386 m^3/s, respectively. It is seen that these values are too close. For MAE and PBIAS, there are insignificant differences.

5. Conclusion

Based on the study of rainfall-runoff modelling using ANN, the following conclusions can be drawn:

First, all scenarios were trained to use as odd numbers from 3 to 21 hidden neurons and their performance was compared. 6 scenarios with the best performance were selected, and the calculations continued over these 6 scenarios. For both ANN algorithms, the number of hidden neurons was chosen as odd numbers from 3 to 21, respectively, and 50 different ANNs were created for each selected hidden number of neurons. The reason was that there is a change in the weight and threshold values given to the network while the studies are being carried out and each network is being formed, so the same network is not created for the same number of hidden neurons, and it was discovered that the performance of each network changes. However, it is taken into account that the error values and performance values of ANNs created according to the number of hidden neurons are similar, but not exactly the same, therefore the performance of 50 networks is averaged and the overall results are obtained.

A major factor affecting the precision of model prediction is the selection of training and testing data. The model will not be able to make accurate future forecasts if the testing data don't accurately reflect basin and climate characteristics. Looking at the ANN scenarios trained with two different algorithms, it was observed that temperature and rainfall data alone were insufficient in estimating the current runoff data. It was reached that the ANN gives much improved performance by adding the past time runoff data to the inputs. This result was observed during the trial-and-error stage of our research, and scenarios related only to the past time runoff data were also added. In addition, it can be said that adding both past time rainfall and past time temperature data as input to the past time runoff, does not considerably improve the current day runoff (discharge) data estimation.

By comparing the results, the application of the used models to the rainfall-runoff process was indicated as successful. Bayesian Regularization and Levenberg-Marquardt algorithm models have close performance.

Evaluate all scenarios individually; it was reached that the higher the number of hidden neurons increases, in general, the better the Bayesian Regularization algorithm trains the networks. However, it was observed that the performance of the network decreased while testing the case. The Levenberg-Marquardt algorithm has advantages such as working with less iteration, and in less time. However, although the Bayesian Regularization algorithm worked for longer with more iterations, the best scenario yielded better results while training and testing the network. However, comparing the results of the scenarios of the two different training algorithms, it can be concluded that the values are generally close.

When looking at the graphs of the predicted and observed runoff data among the 2 methods used in this study, it can be said that the performance of the estimation of the suddenly increasing data is less successful than the performance of the estimation of the normal progressing data, but that the estimates can be improved with the application of these methods. In addition, comparing scenarios 1, 2, and 3 for all 2 methods, it is seen that the nearer in time the rainfall, temperature and runoff data is to the time of the current to be predicted, the better the predictions for each method.

As a result of the study, for the best scenario of the ANN, the past runoff data is decisive, and there is no rainfall and temperature data considered.

In this study, the ANN models can work well to forecast small number of time step ahead values and it executes a good performance as indicated by performance statistics. However, for long forecasting periods, some new scenarios can be investigated since input includes the data just one or two steps back. For large number of time step ahead forecasting, the models used in this study will not be efficient since predicted values will be needed to utilize and forecasted runoff values will include uncertainties.

It is preferable to use ANN models for applications since they can recreate hydrological models through experience-based learning. Compared to traditional regression analysis, these models are better able to forecast flood discharges. Depending on the results, we recommend that ANN models be used in the modelling of rainfall-runoff data, and flood forecasting.

Article Information

Financial Disclosure: The author (s) has no received any financial support for the research, authorship or publication of this study.

Authors' Contrtibution: Concept: Bor; Design: Bor, Okan; Supervision: Bor; Resources: Bor; Data Collection: Bor; Analysis: Okan; Literature Search:

Okan; Writing Manuscript: Bor, Okan; Critical Review: Bor.

Conflict of Interest/Common Interest: Not applicable.

Ethics Committee Approval: Not applicable**.**

Declaration of the Author(s): The author(s) declare that there is no conflict of interest regarding the publishing of the paper by the Journal of Innovative Science and Engineering, that the paper has been not published elsewhere, and not include any form of plagiarism. All the authors listed above have approved the manuscript and have agreed with the submission of the manuscript to the Journal of Innovative Science and Engineering.

Acknowledgements: The authors would like to thank the DSI (General Directorate of State Hydraulic Works), Department of Survey, Planning, and Allocations for the providing of the data.

Data availability statement: The data that support the findings of this study are available from [DSI (General Directorate of State Hydraulic Works), Department of Survey, Planning, and Allocations, Environment Branch Directorate] but restrictions apply to the availability of these data, which were used under license for the current study, and so are not publicly available. Data are however available from the authors upon reasonable request and with permission of [DSI (General Directorate of State Hydraulic Works)].

References

[1] Tan Kesgin, R. I., Demir, I., Kesgin, E., Abdelkader, M., & Agaccioglu, H. (2023). A data-driven approach to predict hydrometeorological variability and fluctuations in lake water levels. *Journal of Water and Land Development*, (58), 158-170. https://doi.org/10.24425/jwld.2023.146608.

[2] Demirel, M. C., Özen, A., Orta, S., Toker, E., Demir, H. K., Ekmekcioğlu, Ö., Tayşi, H., Eruçar, S., Sağ, A. B., Sarı, Ö., Tuncer, E., Hancı, H., Özcan, T. İ., Erdem, H., Koşucu, M. M., Başakın, E. E., Ahmed, K., Anwar, A., Avcuoğlu, M. B., Vanlı, Ö., Stisen, S., Booij, M. J. (2019). Additional Value of Using Satellite-Based Soil Moisture and Two Sources of Groundwater Data for Hydrological Model Calibration. *Water*, 11(10), 2083. https://doi.org/10.3390/w11102083.

[3] Shamseldin, A. Y. (1997). Application of a neural network technique to rainfall-runoff modelling. Journal of Hydrology, 199(3): 272–294.

[4] Tokar, S. A., and Johnson, P. A. (1999). Rainfall-Runoff Modeling Using Artificial Neural Networks. Journal of Hydrologic Engineering, 4(3): 232–239.

[5] Chang, F.-J., and Chen, Y.-C. (2001). A counterpropagation fuzzy-neural network modeling approach to real time streamflow prediction. Journal of Hydrology, 245: 153–164.

[6] Öztopal, A., Kahya, C., and Asilhan, S. (2001). Yapay Sinir Ağları ile Akış Tahmini. 1. Türkiye Su Kongresi, İstanbul, Türkiye, 8 - 10 Ocak 2001, cilt.1. pp. 311–318.

[7] Jayawardena, A. W., and Fernando, T. M. K. G. (2001). River flow prediction: An artificial neural network approach. Regional Management of Water Resources, Maastricht, The Netherlands. pp. 239–246.

[8] Sivakumar, B., Jayawardena, A., and Fernando, T. M. K. G. (2002). River Flow Forecasting: Use of Phase-Space Reconstruction and Artificial Neural Networks Approaches. Journal of Hydrology, 265: 225–245.

[9] Dorado, J., RabuñAL, J. R., Pazos, A., Rivero, D., Santos, A., and Puertas, J. (2003). Prediction and modeling of the rainfall-runoff transformation of a typical urban basin using ann and gp. Applied Artificial Intelligence, Taylor & Francis, 17(4): 329–343.

[10] Kişi, Ö. (2005). Daily River Flow Forecasting Using Artificial Neural Networks and Auto-Regressive Models. Turkish Journal of Engineering and Environmental Sciences, 29: 9–20.

[11] Demirpençe, H. (2005). Köprüçay Akımlarının Yapay Sinir Ağları ile Tahmini. Antalya Yöresinin İnşaat Mühendisleri Sorunları Kongresi.

[12] Yurdusev, M. A., Acı, M., Turan, M. E., and İçağa, Y. (2008). Akarçay Nehri Aylık Akımlarının Yapay Sinir Ağları ile Tahmini. Celal Bayar Üniversitesi Fen Bilimleri Dergisi, 4(1): 73–88.

[13] Okkan, U., and Mollamahmutoğlu, A. (2010). Çoruh Nehri Günlük Akımlarının Yapay Sinir Ağları ile Tahmin Edilmesi. Süleyman Demirel Üniversitesi Fen Bilimleri Enstitüsü Dergisi, 14(3): 251–261.

[14] Okkan, U., and Dalkilic, H. Y. (2010). Demirköprü Barajı Aylık Buharlaşma Yüksekliklerinin Yapay Sinir Ağları ile Tahmin Edilmesi. DSİ Teknik Bülten, 108: 30–36.

[15] Chen, S. M., Wang, Y. M., and Tsou, I. (2013). Using artificial neural network approach for modelling rainfall-runoff due to typhoon. Journal of Earth System Science, 122(2): 399–405.

[16] Kızılaslan, M. A., Sağın, F., Doğan, E., and Sönmez, O. (2014). Aşağı Sakarya Nehri akımlarının yapay sinir ağları ile tahmin edilmesi. SAÜ Fen Bilimleri Dergisi, 18(2): 99–103.

[17] Singh, G., Panda, R. K., and Lamers, M. (2015). Modeling of daily runoff from a small agricultural watershed using artificial neural network with resampling techniques. Journal of Hydroinformatics, 17(1): 56–74.

[18] Khan, M. Y. A., Hasan, F., Panwar, S., and Chakrapani, G. J. (2016). Neural network model for discharge and water-level prediction for Ramganga River catchment of Ganga Basin, India. Hydrological Sciences Journal, Taylor & Francis, 61(11): 2084–2095.

[19] Altunkaynak, A., and Başakin, E. E. (2018). Zaman Serileri Kullanılarak Nehir Akım Tahmini ve Farklı Yöntemlerle Karşılaştırılması. Erzincan University Journal of Science and Technology, 11(1): 92–101.

[20] Nacar, S., Hınıs, M. A., and Kankal, M. (2018). Forecasting Daily Streamflow Discharges Using Various Neural Network Models and Training Algorithms. KSCE Journal of Civil Engineering, 22(9): 3676–3685.

[21] Bor, A., and Okan, M. (2019). FIRAT HAVZASI karasu günlük akimlarinin yapay sinir ağlari ile modellenmesi. 10. Ulusal Hidroloji Kongresi, Muğla, Türkiye, Cilt 2. pp. 857-869.

[22] Fırat, M., and Dikbaş, F. (2006). Göllerde üç boyutlu hidrodinamik modellemede pom ve yapay sinir ağlari yöntemlerinin kullanilmasi : gökpinar baraj gölü örneği. Pamukkale University Engineering College Journal of Engineering Sciences, 12(1): 43–50.

[23] Coulibaly, P., Anctil, F., and Bobée, B. (1999). Prévision hydrologique par réseaux de neurones artificiels : état de l’art. Canadian Journal of Civil Engineering, 26: 293–304.

[24] Minns, A. W., and Hall, M. J. (1996). Artificial neural networks as rainfall-runoff models. Hydrological Sciences Journal, 41: 399–417.

[25] Gümüş, V., Başak, A., and Yenigün, K. (2018). Yapay Sinir Ağları ile Şanlıurfa İstasyonunun Kuraklığının Tahmini. Gazi Üniversitesi Fen Bilimleri Dergisi, 6(3): 621–633.

[26] Haykin, S. (1998). Neural Networks : A Comprehensive Foundation. Prentice-Hall. Upper Saddle River, NJ.

[27] Öztemel, E. (2006). Yapay Sinir Ağları. Papatya Publishing, Istanbul, Turkey.

[28] Şen, Z. (2004). Yapay Sinir Ağları İlkeleri. Turkish Water Foundation, Istanbul,Turkey.

[29] Chen, T. C., Han, D. J., Au, F. T. K., and Tham, L. G. (2003). Acceleration of Levenberg-Marquardt Training of Neural Networks with Variable Decay Rate. Proceedings of the International Joint Conference on Neural Networks, IEEE. pp. 1873–1878.

[30] Hagan, M. T., and Menhaj, M. B. (1994). Training Feedforward Networks with the Marquardt Algorithm. IEEE Transactions on Neural Networks, 5(6): 989–993.

[31] trainlm Levenberg-Marquardt backpropagation. https://www.mathworks.com/help/deeplearning/ref/trainlm.html [Accessed: 07 september 2023].

[32] Xu, M., Zeng, G., Xu, X., Huang, G., Jiang, R., and Sun, W. (2006). Application of Bayesian regularized BP neural network model for trend analysis, acidity and chemical composition of precipitation in North Carolina. Water, Air, and Soil Pollution, 172(1–4): 167–184.

[33] MacKay, D. J. C. (1992). Bayesian Interpolation. Neural Computation, 4(3): 415–447.

[34] Foresee, F. D., and Hagan, M. T. (1997). Gauss-Newton approximation to bayesian learning. IEEE International Conference on Neural Networks - Conference Proceedings, Houston, TX, USA, 9–12 June 1997. pp. 1930–1935.

[35] Kayri, M. (2016). Predictive abilities of Bayesian Regularization and Levenberg-Marquardt Algorithms in Artificial Neural Networks: A Comparative Empirical Study on Social Data. Mathematical and Computational Applications, 21(2).

[36] Gupta, H. V., Sorooshian, S., and Yapo, P. O. (1999). Status of automatic calibration for hydrologic models: comparison with multilevel expert calibration. Journal of Hydraulic Engineering, 4(2): 135–143.

[37] Moriasi, D. N., Arnold, J. G., Liew, M. W. Van, Bingner, R. L., Harmel, R. D., and Veith, T. L. (2007). Model evaluation guidelines for systematic quantification of accuracy in watershed simulations. American Society of Agricultural and Biological Engineers, 50(3): 885–900.

[38] Nash, J. E., and Sutcliffe, J. V. (1970). River flow forecasting through conceptual models part I — A discussion of principles. Journal of Hydrology, 10(3): 282–290.

[39] Improve Shallow Neural Network Generalization and Avoid Overfitting. The MathWorks, Inc. https://www.mathworks.com/help/deeplearning/ug/improve-neural-network-generalization-and-avoid-overfitting.html [Accessed: 07 september 2023].

J Inno Sci Eng, 2025, 9(1):78-88

DOI:https://doi.org/ 10.38088/jise.1531963

Research Article

Comprehensive Carbon Footprint Assessment Using EPA and DEFRA: A Case Study of Bursa Technical University

Somaia Shahin [1], **Samet Öztürk**[1*]

[1] *Bursa Technical University, Department of Environmental Engineering, 16310, Bursa, Türkiye*

ARTICLE INFO

Received Date: 12/08/2024
Accepted Date: 14/02/2025

Cite this paper as:
Shahin, S. & Ozturk, S. (2025). Comprehensive Carbon Footprint Assessment Using EPA and DEFRA: A Case Study of Bursa Technical University. *Journal of Innovative Science and Engineering.* 9(1), 78-88.

*Corresponding author: Samet Öztürk
E-mail:samet.ozturk@btu.edu.tr

Keywords:
Sustainability
Carbon Footprint
EPA
DEFRA
GHG
SDHs

ABSTRACT

Bursa Technical University (BTU) is committed to achieving sustainability goals and has taken significant steps in this direction. This study was conducted in accordance with the emission factors of the Environmental Protection Agency (EPA) and the conversion factors of the Department of Environment, Food and Rural Affairs (DEFRA). The study was carried out in line with International Organization for Standardization (ISO) 14064 and ISO 14001 standards and in harmony with the Sustainable Development Goals (SDGs), drawing on the experiences of five Turkish universities. This paper provides detailed information on BTU's carbon footprint calculation methodology, the standards used, and its alignment with the SDGs. The application of two distinct emission factors, those of EPA and DEFRA, yielded divergent carbon footprint (CF) values for BTU. The EPA approach yielded a value of 2697 tCO2e while the DEFRA-based assessment resulted in a lower CF of 1526 ton of CO2 equivalent (tCO2e). It is noted that most of the carbon emissions in the university is due to electricity consumption followed by natural gas usage. A prioritized action plan could be reducing the electricity consumption with automated lighting and laboratory equipment, subsequently increasing energy efficiency in the buildings.

1. Introduction

The rapid depletion of natural resources has accelerated due to anthropogenic and industrial activities since the Earth's formation. Simultaneously, a rise in global temperatures and observable climate change have been evident since 1974 [1]. Accordingly, the 1992 Rio Summit said that the increase in greenhouse gas emissions has significantly contributed to global warming and climate change. Greenhouse gases trap a portion of the sun's energy, heating the Earth's atmosphere. This heat-catching phenomenon is identified as the greenhouse effect and is the primary driver of climate change [2]. Greenhouse gases disrupt the atmospheric heat balance, increasing the occurrence and strength of extreme weather events. These events include droughts, floods, storms, and extreme temperatures. Rising greenhouse gas emissions also contribute to

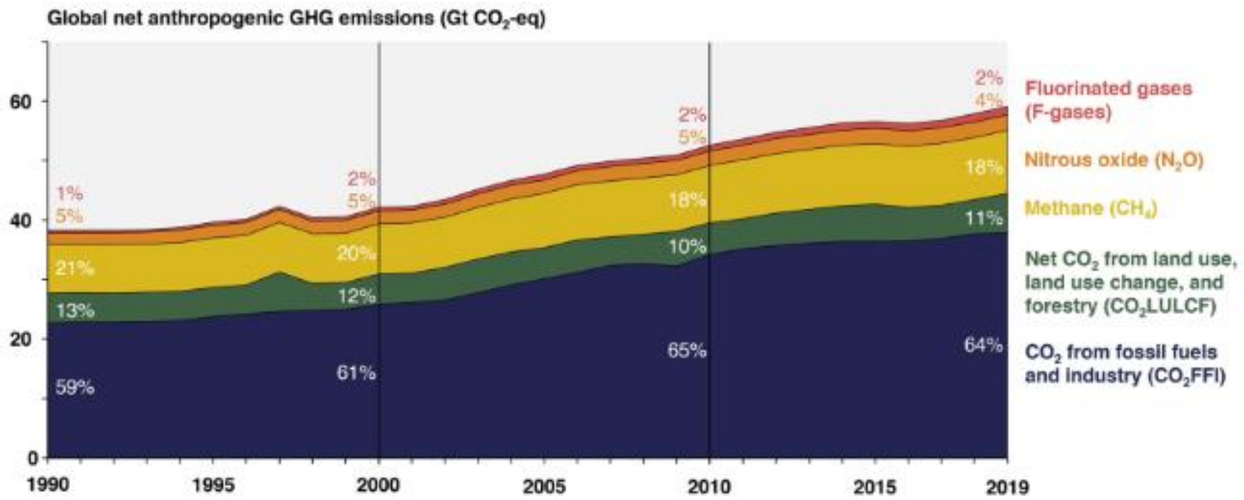

Figure 1: Global net anthropogenic GHG emissions [5]

sea level escalation, glacial melting, and ecosystem degradation [3]. In 2019, 64% of global greenhouse gas emissions were CO2, 11% net CO2, 18% N2O, 4% F-gases, and 2% other gases (Figure 1) [4].

Figure 2: Aerial views of Bursa Technical University campuses

Bursa Technical University (BTU) operates its educational and research activities on two campuses: Mimar Sinan and Yıldırım Bayezid. Both campuses are located at the city center and close by to public transportation and metro stations. The Mimar Sinan campus has four faculties, a graduate education institute, four research centers and business and laboratory management units. The Yıldırım Bayezid Campus has two faculties and a foreign language preparatory school. As of 2024, BTU has 11,205 students, 569 academic staff, and 350 administrative staff [6]. Figure 2 shows the aerial views of the campuses of Bursa Technical University

BTU stands out as an educational institution with a campus that covers approximately 30% green space. These green areas play a significant role in student well-being and air quality, in addition to adding aesthetic value. However, BTU has many opportunities to further its sustainability journey. In this context, the university is committed to working in areas such as energy efficiency, waste management, water conservation, and sustainable education. BTU is determined to work with all stakeholders to achieve these goals and make the campus even more sustainable. By doing so, BTU believes it can contribute to building a more livable world for future generations.

There are several studies which estimated carbon footprints of university campuses in the literature. Erzincan Binali Yıldırım University (EBYU)'s primary carbon footprint was estimated as 2753,20 tCO2e for 2019 while it was calculated as 2383,74 tCO2e for 2020[7]. In comparison to 2019, there was a 13,42% decrease in the carbon footprint at EBYU in 2020. EBYU's primary carbon footprint was calculated as 2314,53 tCO2e for 2019 and 1826,53 tCO2e for 2020 using DEFRA conversion factors. Relative to 2019, there was a 21,08% reduction in carbon footprint [7]. Manisa Celal Bayar University's carbon footprint was calculated to be 8.953,91 tons of CO_2 using the IPCC Model Tier 1 approach [8]. It was determined that 87,85% of carbon emissions originated from electricity consumption, while the least amount originated from gasoline consumption at 0,09% [8]. Carbon footprint for Çankırı Karatekin University was estimated for its campus in 2017 as 5.633,13 tCO_2e/year using data obtained from greenhouse gas emission sources classified into categories 1, 2, and 3. The calculation revealed an average annual greenhouse gas emission of 4,54 tCO_2e/person and a daily average carbon emission of 15,44 tCO_2e/day [9]. The total CO_2e emissions from Burdur Mehmet Akif Ersoy University Bucak Health College due to sum of all scope levels – Scope 1, 2 and 3 was found to be 217,50 tCO_2e/year [10]. The calculations revealed that the most significant impact on carbon emissions comes from combustion of natural gas for heating system, followed by electricity consumption, emissions from diesel, gasoline, and LPG-powered vehicles [10]. CF calculated for the total carbon emissions from natural gas consumption at Osmaniye Korkut Ata University's Karacaoğlan campus to be 2659 tCO_2e in 2021 [11]. GIt was noted for Osmaniye Korkut Ata University that in the periods of 2020 and 2021, there was a transition from face-to-face education to online education, therefore, the pool and cafeteria were closed. Consequently, natural gas consumption in common areas and for heating purposes was significantly reduced [11]. Hünerli et al. utilized IPCC Tier 1 and DEFRA methods to estimate carbon footprint of Muğla Sıtkı Koçman University campus for 2020 and 2021. They have found that the emissions indicate a rising trend [12].

Most of the reviewed papers applied a single method for several consecutive years [8-12]. Even though two papers calculated carbon footprint by using both methods, in those papers, Scope 3 was not included in the analyses [7, 12]. However, no paper, to the authors' knowledge have compared the carbon footprint results with different methods considering all Scope levels for carbon footprint estimation. The novelty of this paper is being the most comprehensive carbon footprint evaluation considering different emission factors, namely EPA and DEFRA for Bursa Technical University campus. This is a novel approach in the context of Turkish universities.

2. Materials and Methods

2.1. Material

In this study, BTU's carbon footprint was determined using the EPA and DEFRA emission factors for carbon footprint calculations between August 2022 and July 2023. The EPA and DEFRA methods are employed in this study due to their distinct advantages. Firstly, they are standardized approaches grounded in internationally recognized frameworks, ensuring reliability and consistency. Secondly, these methods encompass a wide range of sectors, including energy, transportation, industrial processes, and waste management, all of which are integral to the operations and activities of a university. Lastly, their databases are readily accessible, and the associated emission factors are comprehensively documented, enhancing clarity and ease of use. These methods also have notable disadvantages. A common limitation of both is their reliance on region-specific emission factors. For instance, emission factors for electricity grids are tailored to specific countries or states, which can restrict their applicability in other regions. Additionally, in certain sectors, there may be gaps in available emission factors or reliance on generalized or averaged data. This can lead to inaccuracies and potential miscalculations in carbon emissions estimations, particularly in cases requiring granular or localized analysis. Several standards are followed to conduct carbon footprint analysis in this study. ISO 14064-1 is a standard that identifies the fundamentals for publishing greenhouse gas (GHG) emissions [13] while ISO 14067 standard states principles, requirements, and guidelines for evaluating and informing the carbon footprint (CFP) of a product [14]. GHG Protocol provide guidelines for users to calculate GHG emissions from specific bases or businesses [15]. The Intergovernmental Panel on Climate Change (IPCC) is a United Nations organization that measures the knowledge regarding climate change. The IPCC prepares inclusive GHG inventories to estimate carbon footprints of businesses or products [16].

2.2. BTU Campus Consumption Data

In this study, Scope 1, Scope 2, and Scope 3 CO_2 Emissions at Bursa Technical University (BTU) were calculated for the period from August 2022 to July 2023. BTU contributes to greenhouse gas emissions through natural gas and diesel consumption due to the operation of laboratories, the use of motor vehicles and operations' machinery on its campuses. These emissions constitute an organization's Scope 1.

However, the environmental impact of BTU's activities is not limited to the emissions that occur in its own facilities. Scope 2 emissions consist of emissions from electricity consumption inside the organization. Moreover, activities that occur outside BTU's control, such as the production and transportation of purchased materials, and the use of products and services sold, also lead to greenhouse gas emissions constitute BTU's Scope 3.

In general, a significant portion of university campus consumption-based emissions come from sources such as heating and cooling systems, air conditioners, ambient lighting, office equipment, and elevators [8].

Another factor affecting consumption of electricity is the climate. The increase in air conditioning use due to rising temperatures in the summer months leads to an increase in electricity consumption and therefore carbon emissions. In winter, on the other hand, the widespread use of natural gas heating systems reduces the need for electricity to meet heating needs but leads to an increase in natural gas emissions.

In this study, consumption data are gathered to conduct a comprehensive analysis of the university's greenhouse gas emissions to calculate its carbon footprint (Table 1).

Table 1: BTU consumption data for August 2022-July 2023

Scope 1		Scope 2	Scope 3				
Natural Gas (m^3)	Diesel (l)	Electricity (kWh)	Water (m^3)	GES (kWh)	Paper and board (t)	Passenger-Car (km)	Mixed Plastics (t)
352.414	19.416,10	3.498.921	99.293	10.800	4,70	156.379	2,66

2.3. Methodology

This study adopted methodologies widely used in the European Union (EU) and the United States (US) for calculating Bursa Technical University's Carbon Footprint (CF). In this context, EPA and DEFRA emission factors were used. The calculations provided BTU's annual carbon emissions in CO2 equivalents.

EPA (Environmental Protection Agency) is a self-governing federal organization in the United States responsible for environmental security. The EPA's Greenhouse Gas Emissions Factors Hub is intended to offer organizations with a recurrently revised and user-friendly set of default emission factors for greenhouse gas reporting for businesses [4].

Department of Environment, Food and Rural Affairs (DEFRA) is a United Kingdom (UK) administrative organization which is responsible for policy and legislation in subjects for example the ecosystem, variety of biological creatures. It works with various organizations to implement these policies [16]. The DEFRA emission factor is a value that represents the correlation between the quantity of contaminant yielded and the quantity of natural resource handled or burned. This factor is used in greenhouse gas emissions calculations and environmental impact assessments. DEFRA is responsible for determining and updating emission factors used in the UK [17].

The carbon footprint is presented as a value in CO2 equivalents. The CO2 value is determined using mathematical calculations and methods. In this study, emission factors are determined using core performance indicators and are also used by organizations that voluntarily report on various environmental issues. The calculations of the carbon footprint estimation were done using the following steps.

1. Go to the activity-specific page to calculate emissions: In the Excel report, this is the step of opening the page for the activity for which we want to calculate emissions.

2. Read the guide: This is the step of reviewing the emission calculation guide for the activity on the page to learn how to apply the desired method.

3. Collect activity data: This is the step of collecting data related to the activity for which we are calculating emissions. For example, this includes data such as the amount of electricity used or the distance traveled.

4. Multiply the activity data by the corresponding conversion factor: This is the step of multiplying the collected or estimated activity data by the emission factor determined for the relevant activity. This process allows us to calculate an estimate of the greenhouse gas emissions from the activity in question, as shown in Equation 1.

$$\text{GHG emissions} = \text{Activity data} \times \text{Emission conversion factor} \quad (1)$$

2.3.1. EPA Emission Factors

A greenhouse gas inventory report is a comprehensive written document that provides the methodologies and data used to prepare a set of standard reporting tables and estimates covering categories and years. The 2006 IPCC Guidelines provide an internationally accepted standard for the preparation of greenhouse gas inventories. These guidelines ensure the comparability and consistency of inventories prepared by different countries by providing standardized reporting tables and methodologies.

The 2006 Guidelines also include worksheets to facilitate the implementation of the basic (or Tier 1) estimation methodology transparently. These sheets allow countries to calculate their greenhouse gas emissions from basic data and prepare reports in accordance with international standards.

The IPCC method uses the emission factors (EFs) provided by the EPA to calculate greenhouse gas emissions. A similar multiplication operation is used in the DEFRA method. However, the emission factors given by EPA differs depends on the electricity grid in the USA, therefore the emission factor from electricity consumption is taken as the closest one with the Turkish electricity grid [18].

Since the EPA's emission factors are specific to the United States, the units used are also English units. Therefore, when making calculations with our data, the units have been converted. Table 2 shows the emission factors used in this study.

2.3.2. DEFRA Emission Factors

This section includes emission calculation guides and conversion factors for various activities suggested by DEFRA. By carefully reviewing the guide and conversion factor for each activity for which emissions are calculated, multiplying the activity data by the relevant conversion factor will result in an estimate of the greenhouse gas emissions from the activity in question. The equivalents of the emission factors used in the DEFRA method are given in different units. Table 3 shows the emission factor suggested by DEFRA.

Table 2: Emission factors provided by EPA

Scopes	Usage Type	Unit	Emission Factor (kg CO2e)
	Natural Gas	scf	35,32
Scope 1	Diesel	Gallon	10,21
Scope 2	Electricity	MWh	550,00
	Water Supply	m^3	0,18
	Water Usage	m^3	0,20
Scope 3	Paper/Cardboard	Metric Ton	0,03
	Electricity GES	kWh	0,02
	Travel	Vehicle-mile	0,31

Table 3: Emission Factors by DEFRA

Scopes	Usage Type	Unit	Emission Factor (kg CO2e)
	Natural Gas	m^3	2,04
Scope 1	Diesel	L	2,51
Scope 2	Electricity	kWh	0,21
	Water Supply	m^3	0,18
	Water Usage	m^3	0,20
Scope 3	Paper/Cardboard	ton	0, 02
	Electricity (GES)	kWh	0,02
	Travel	Passenger-Km	0,10

3. Results and Discussion

3.1. Results from EPA and DEFRA emission factors

In this study, a comprehensive carbon footprint calculation is applied for Bursa Technical University campuses using the EPA and DEFRA emission factors to estimate carbon footprint. This calculation, which determines CO_2 emissions for the period between 2022 August and July 2023, provides a framework for developing concrete strategies to achieve emission reduction goals in the future.

- For Scope 1 emissions, direct emissions from natural gas and diesel consumption in the university's operations are considered. Electricity is the most consumed type of energy on campus. Scope 2 emissions represent emissions by electricity consumption which is calculated by summing up the electricity usage values of every area within the university. This value is analyzed more comprehensively by considering the emission conversion factor, the electricity production source (indirect), and electricity losses from the grid. Scope 3 emissions are indirect emissions which include emissions from 15 categories such as purchase goods and services, fuel and energy related activities, processing and sold of use products and business travel [15]. Scope 3 for BTU's carbon emission is estimated considering following activities due to the data limitation:
- Travel: Business travel, commuting, and student travel all contribute to Scope 3 emissions.
- Waste: The disposal of waste, including paper, cardboard, and food scraps, generates Scope 3 emissions.
- Water: The extraction, treatment, and distribution of water also contribute to Scope 3 emissions.
- Renewable energy: The solar panels which use electricity and its waste contributes to Scope 3 emissions.

Table 4 presents the total CO2 equivalent emissions from Scope 3. The university has achieved nearly 80% recycling rate for paper and cardboard and efforts are ongoing to further improve this rate. Scope 3 emissions are also affected by water usage. Table 4 shows the water consumption and associated CO2 equivalent emissions. The EPA does not currently provide an estimation method specifically for Solar Energy Generation Systems (SEGS) and water consumption. As a result, the methodology outlined here is using DEFRA's emission factors for only SEGS and water consumption.

The results indicate that BTU's total CO2 equivalent emissions amount to 2697,06 tons as shown in Table 4. Scope 2 emissions contribute the most with 1924,41 tons of CO2, followed by 724,43 tons of CO2 from Scope 1 direct emissions. Within Scope 3, the most significant emissions were attributed to travel, totaling 30,40 tons of CO2. Emissions from renewable sources were observed to be very low, amounting to only 0,193 tons of CO2.

Table 4: The total of FC using EPA emission factors

Scope	Emission	Quantity	Unit	Result of CF (Ton CO2e)
Scope 1	Natural Gas	352.414	m^3	672,06
	Diesel	19.416	m^3	52,37
	CF Total			724,43
Scope 2	Electricity	3.498.921	kWh	1924,41
Scope 3	Water (Municipal/Usage)	99.293	m^3	17,58
	Electricity SEGS	1.080	kWh	0,19
	Travel	156.379	Passenger-Km	30,40
	Paper/Cardboard	4,70	Ton	0,14
	CF Total			48,69
CF Grand Total				2.697,06

By using DEFRA's emission factors Scope 1 emissions at Bursa Technical University (BTU) arise from the combustion of oil and gas-based fuels, such as natural gas and diesel, in heating and equipment machinery. The greenhouse gases released because of the combustion of these fuels are listed in Table 5 in CO2 equivalents. It should be noted that the EPA emission factors yielded higher CO2 emissions from diesel and natural gas consumptions comparing with the results from DEFRA method. Scope 3 emissions are indirect emissions that result from a company's activities but occur at sources that are not owned or controlled by the company. These emissions can be a significant portion of a company's total carbon footprint.

This study calculated emissions from all forms of transportation, including air, ground, and sea travel. The results show that travel emissions are the largest source of Scope 3 emissions for BTU. As a predominantly paper-based institution, Bursa Technical University (BTU) primarily generates waste in the form of paper and cardboard. DEFRA emission factors for paper and cardboard were utilized to quantify the associated emissions as outlined in Table 5. BTU's water usage is categorized into municipal water and grey water. The university's water consumption levels are considered moderate. Table 5 shows water-related CO2 emissions that account for energy consumption and source. The university has installed solar panels on its campus, which are generating electricity and helping to reduce emissions. However, even for generating electricity from solar panels carry CO2 emissions which are presented in Table 5. BTU's carbon footprint for the period of August 2022 and July 2023 has been calculated as 1525,92 tons of CO2 using the DEFRA method. Water use is identified as the highest emission source in Scope 3, contributing 17,55 tons of CO2 equivalent emissions. Scope 1 has the highest overall contribution with 767,66 tons of CO2 emissions, while the lowest is Scope 3 with emissions amount to 30,98 tons of CO2. Indirect emissions from electricity are shown as 724,54 tons of CO2.

3.2. Discussion

In this study, it is noted that comparing the IPCC method with the DEFRA method, the IPCC method provides a higher total CO2 emission value. This discrepancy is due to the emission factors used in different methods. As shown in Figure 3, for the same amount of natural gas, the IPCC method covers 7% while the DEFRA method covers 6% with the same data. This difference is because each country has different approaches and values for evaluating CO2 emissions.

Table 5: Total of CF by the DEFRA emission factors

Scopes	Emission	Quantity	Unit	Result of CF (Ton CO2e)
Scope 1	Natural Gas	352.414	m^3	718,92
	Diesel	19.416	m^3	48,73
	CF Total			767,66
Scope 2	Electricity	3.498.921	kWh	724,54
Scope 3	Water (Municipal/Usage)	99.293	m^3	17,55
	Electricity SEGS	1.080	kWh	0,19
	Travel	156.379	Passenger-Km	15,98
	Paper/Cardboard	4,70	Ton	0,09
	CF Total			30,68
CF Grand Total				1.525,92

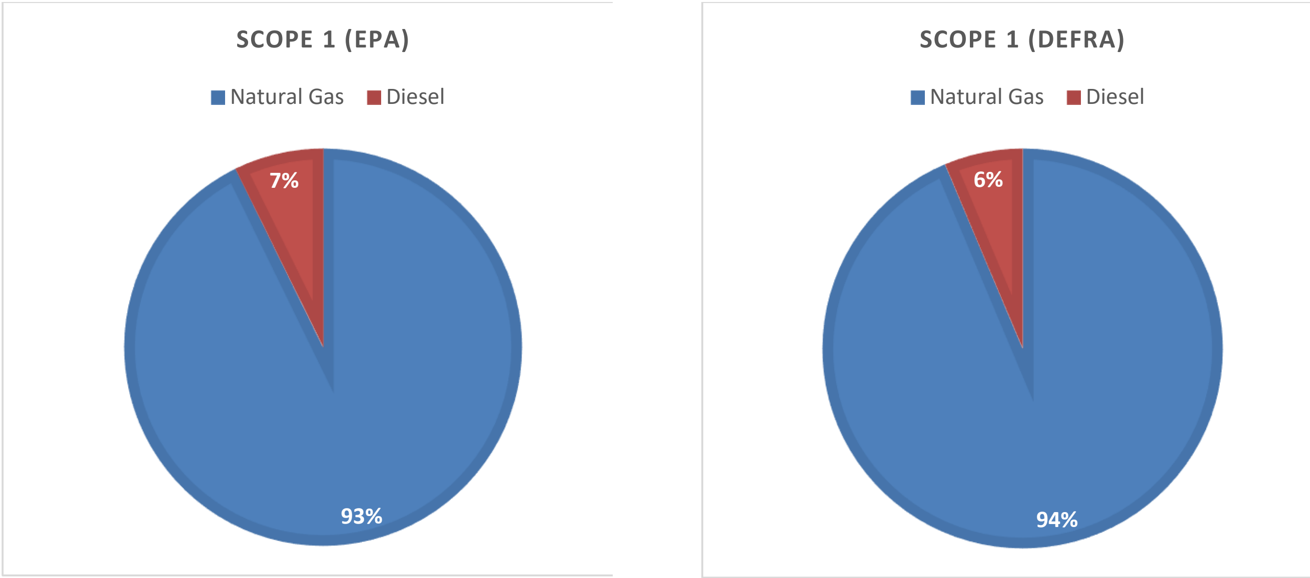

Figure 3: Shares of emissions in Scope 1

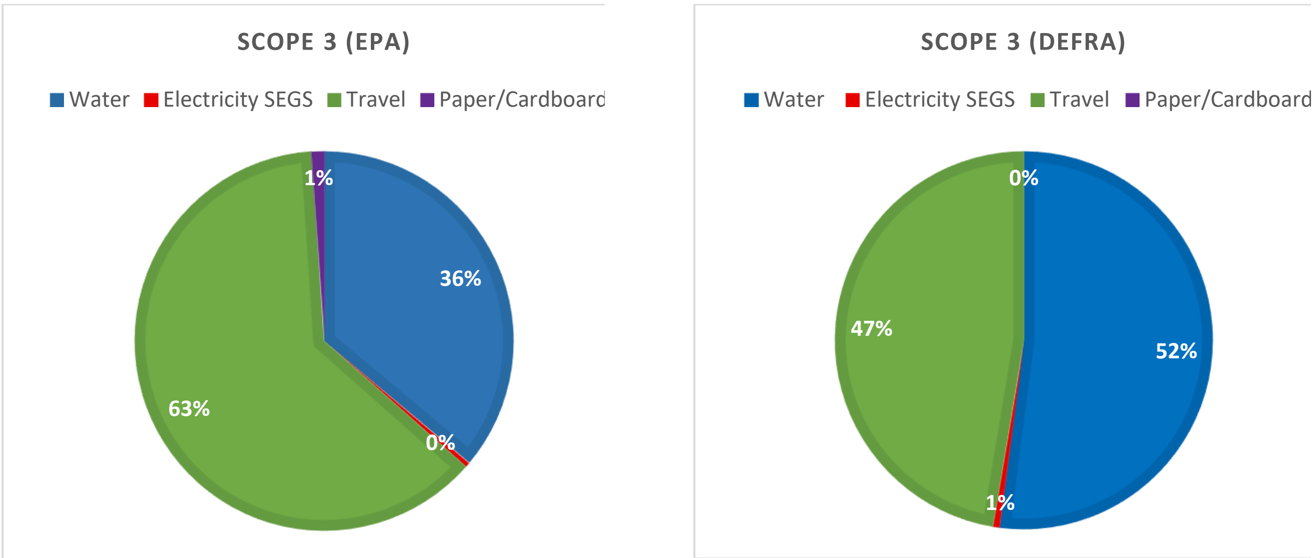

Figure 4: Shares of emissions in Scope 3

For Scope 3 emission calculations, this study used data from water, solar panels, travel, and paper/cardboard. In this context, the equivalence between the EPA and DEFRA emission factors is quite high. Both methodologies yield similar results, confirming the consistency and accuracy of the approach.

Figure 5 illustrates the distribution of emissions across the three scopes according to the DEFRA and IPCC methodologies. In the DEFRA method, Scope 1 and Scope 2 emissions have a larger share compared to the IPCC method. This difference arises from the variations in emission conversion factors. Specifically, the conversion factor used for electricity consumption is higher in the IPCC method, resulting in higher electricity-related emissions calculated by that method. Additionally, it was found that Scope 1 emissions accounted for the largest share under the DEFRA method, comprising 50% of the total. At the same time, Scope 2 emissions (electricity consumption) made up 71%.

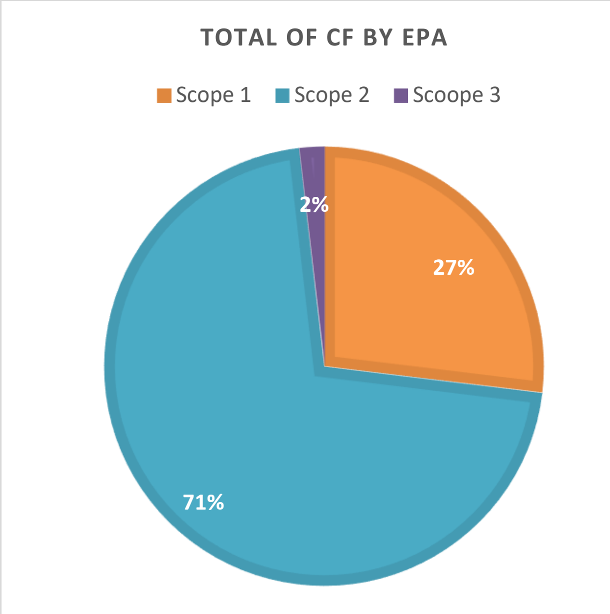

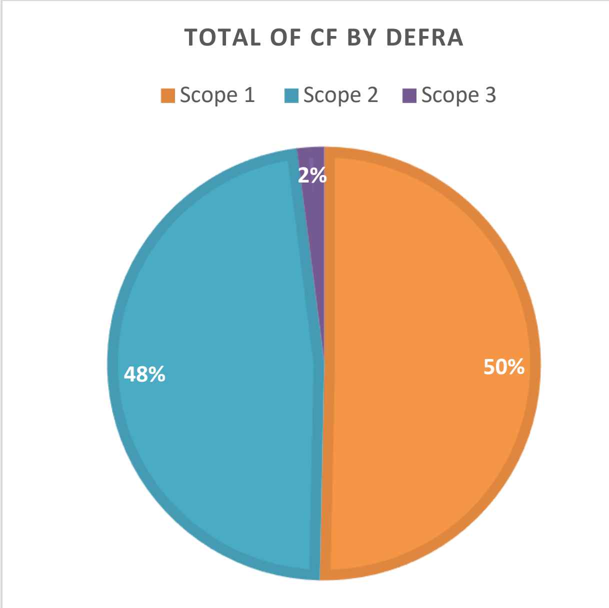

Figure 5: The distribution of total CO2 emissions

The primary cause of climate change is the greenhouse gases emitted into the atmosphere due to human activities, particularly carbon dioxide (CO_2). Reducing carbon emissions is crucial to mitigating the effects of climate change [7]. Using two different approaches, carbon footprint of one-year period for Bursa Technical University found as 2.697 tons of CO_2 equivalent emissions with the EPA emission factors whereas it is estimated as 1.526 tons of CO_2 equivalent emissions with the DEFRA emission factors. The difference in the results could be attributed to the difference between the emission factors of electricity consumption of EPA and DEFRA. In both approaches, the largest share of greenhouse gas emissions comes from electricity consumption. On the other hand, the value for Scope 3 emissions is not very robust due to the lack of comprehensive data. Direct CO_2 emissions yield different results depending on the method used. As this is the first time calculating BTU's carbon footprint, the results should be reviewed more comprehensively and inclusively to support future emissions calculations and projections.

The results from this study compares well with the other studies in the literature in terms of ton CO2-eq per student values. Carbon footprint estimations swing between 0,12 to 0,60 ton CO2-eq per student in the studies that was published for Turkish universities in the literature [7-12] whereas, in this study, the result shows 0,26 tons of CO2-eq per student for Bursa Technical University. It must be noted that this comparison has been applied for only the sum of Scope 1 and 2 estimations since most of the earlier studies did not consider Scope 3.

4. Conclusions and Recommendations

This study analyzes the carbon footprint of Bursa Technical University operations using two different emission factors, namely EPA and DEFRA. The study finds out that the results from both methods are in the alignment, EPA approach yielding the greater value. Since, the emission factor of DEFRA is 0,207 kg/CO2eq which is lower than the emission factor of Turkish electricity grid, the results from the EPA approach could be considered more reliable. Furthermore, as per the shares of Scopes in the total emission value, Scope 2 constitutes a high rate due to the university's reliance on electricity usage. Finally, Scope 3 emissions could be extended with more data while in this study it is limited by the data available.

To reduce the carbon footprint of a university, various measures might be implemented. Followings are several recommendations.

- Electricity Use: Automated lighting and laboratory equipment systems can be vital in the relevant to reduce electricity consumption. Moreover, redundant use of electrical systems must be reviewed and eliminated.

- Energy Efficiency: Improving insulation in buildings can reduce heating and cooling needs, thereby decreasing energy consumption. This not only demonstrates an environmentally friendly approach but also saves on energy costs.

- Vehicle Usage: Although the university is in an area easily accessible by public transportation, high fuel consumption has been observed. One approach to reduce this is to install bicycle or electric scooter stations next to metro stations near each campus.

- Plastic Use: The significant impact of plastic on greenhouse gas emissions often stems from single-use consumption habits. Raising environmental awareness in the community is an effective way to reduce plastic use. For example, since plastic cups and bottles constitute 70% of daily solid waste at our university, we recommend switching to glass and reusable alternatives. Additionally, efforts should be made to reduce hazardous waste in laboratory operations.

- Digital Paper Usage: Replacing traditional paper with digital documents is an environmentally friendly alternative that enhances efficiency, reduces storage and archiving costs, and facilitates document access. Thus, digital paper usage plays a crucial role in both environmental sustainability and operational efficiency.

A prioritized action plan could be reducing the electricity consumption with automated lighting and laboratory equipment, followed by increasing energy efficiency in the buildings. Furthermore, vehicle usage might be limited by utilizing micro mobility or public transportation.

Article Information

Authors' Contrtibution:
Samet Ozturk: Conceptualization, Data Acquisition, Design, Analysis, Writing, Supervision, Critical review.
Somaia Shahin: Literature review, Resources, Data Acquisition, Analysis, Writing.

Conflict of Interest/Common Interest: The authors declare that they have no conflict of interest with respect to the author or publication of this article.

Ethics Committee Approval: There was no need for Ethical Approval for this study.

Declaration of the Author(s): The author(s) declare that there is no conflict of interest regarding the publishing of the paper by the Journal of Innovative Science and Engineering, that the paper has been not published elsewhere, and not include any form of plagiarism. All the authors listed above have approved the manuscript and have agreed with the submission of the manuscript to the Journal of Innovative Science and Engineering.

Acknowledgements: This study is done based on Bachelor's Thesis of Somaia Shahin.

References

[1] A. Üreden, "Sürdürülebilir yaşam için karbon ayak izi: (Çankırı Karatekin Üniversitesi örneği).," Çankarı Karatin Üniversitesi, 2019.

[2] UNFCCC, "United Nations Framework Convention on Climate Change (UNFCCC)." [Online]. Available: https://unfccc.int/process-and-meetings/the-rio-conventions

[3] IDB, "İklim Değişikliği Hakkında Sıkça Sorulan Sorular." [Online]. Available: https://iklim.gov.tr/sss/iklim-degisikligi

[4] EPA, "GHG Emission Factors Hub." 2023. [Online]. Available: https://www.epa.gov/climateleadership/ghg-emission-factors-hub

[5] T. Sokezan, A. M. Hagan, and A. Azillino, "European offshore renewable energy: Towards a sustainable future," Researchgate, [Online]. Available: https://www.researchgate.net/publication/369762557_European_offshore_renewable_energy_Towards_a_sustainable_future

[6] BTÜ, "BTÜ kampüsler." Accessed: May 22, 2024. [Online]. Available: https://btu.edu.tr/tr/sayfa/detay/3369/kampusler

[7] Seyhan, A. and Çerçi, M. "IPCC Tier 1 ve DEFRA Metot ları ile Karbon Ayak İzinin Belirlenmesi : Erzincan Binali Yıldırım Üniversitesi ' nin Yakıt ve Elektrik Tüketimi Örneğ i Determination of Carbon Footprint with IPCC Tier 1 and DEFRA Methods : The Case Study of Erzincan Binali Y," pp. 386–397, 2022, doi: 10.19113/sdufenbed.

[8] G. Binboğa and A. Ünel, "Sürdürülebilirlik Ekseninde Manisa Celal Bayar Üniversitesi'nin Karbon Ayak İzinin Hesaplanmasına Yönelik Bir Araştırma," p. 16, 2016.

[9] Üreden, A. (2019). Sürdürülebilir yaşam için karbon ayak izi: (Çankırı Karatekin Üniversitesi örneği). Yüksek Lisans Tezi. Çankırı Karatekin University.

[10] Kumaş, K., Akyüz, A. Ö., Zaman, M., & Güngör, A. (2019). Sürdürülebilir bir çevre için karbon ayak izi tespiti: MAKÜ Bucak Sağlık Yüksekokulu örneği. El-Cezeri, 6(1), 108-117.

[11] A. B. Yavuz, O. Kara, and B. Yanıktepe, “Karbon ayak izi tespiti: Osmaniye Korkut Ata Üniversitesi örneği,” 2023.

[12] Hünerli, E., Dolgun, G. K., Ural, T., Güllüce, H., & Karabacak, D. Calculation of Muğla Sıtkı Koçman University's Carbon Footprint with IPCC Tier 1 Approach and DEFRA Method. Kırklareli Üniversitesi Mühendislik ve Fen Bilimleri Dergisi, 10(1), 1-28.

[13] ISO 14064-1, “Specification with guidance at the organization level for quantification and reporting of greenhouse gas emissions and removals,” 2018. [Online]. Available: https://www.iso.org/standard/66453.html

[14] ISO 14067, “Greenhouse gases Carbon footprint of products,” 2018, [Online]. Available: https://www.iso.org/standard/71206.html

[15] GHG, “GHG Protocol,” 2020. [Online]. Available: https://ghgprotocol.org/guidance-0

[16] IPCC, “The Intergovernmental Panel on Climate Change (IPCC).” [Online]. Available: https://www.ipcc.ch/

[17] DEFRA, “Greenhouse gas reporting: conversion factors (2023).” UK, 2023. [Online]. Available: https://www.gov.uk/government/publications/greenhouse-gas-reporting-conversion-factors-2023

[18] Enerji ve Tabii Kaynaklar Bakanlığı. 2024. https://enerji.gov.tr/evced-cevre-ve-iklim-turkiye-ulusal-elektrik-sebekesi-emisyon-faktoru. Erişim tarihi Ağustos 7, 2024.

J Inno Sci Eng, 2025, 9(1):89-102

DOI:https://doi.org/ 10.38088/jise.1619782

Comparative Analysis of Electricity Consumption Forecast

Mehmet Ali Arslan [1*], **Tarık Talan** [1]

[1] *Department of Computer Engineering, Gaziantep Islam Science and Technology University, Gaziantep, Türkiye*

ARTICLE INFO

Received Date: 14/01/2025
Accepted Date: 17/04/2025

Cite this paper as:
Arslan, M.A. and Talan T. (2025). *Comparative Analysis of Electricity Consumption Forecast.*Journal of Innovative Science and Engineering. 9(1): 89-102

*Corresponding author: Mehmet Ali Arslan
E-mail:ali.arslan2278@gmail.com

Keywords:
Electrical energy
Electricity consumption forecast
Artificial intelligence
Deep learning

ABSTRACT

This study aims to make a comparative analysis of electricity consumption forecast using artificial intelligence (AI) and statistical models. In order to reduce the current deficits of countries, it is of great importance to predict the future electricity consumption amount and plan the power plant capacities accordingly. Electricity is an energy source that is extremely difficult to store when used in sectors such as industry and housing. Therefore, the electricity produced must be consumed immediately without causing energy losses and waste. In this context, ensuring the balance between electricity production and consumption can correctly contribute to the management of the current deficit by increasing economic efficiency. In the current study, Türkiye's hourly electricity consumption data between 2016 and 2024 were examined. These data were transformed into a 108-month consumption data set. Seven different models, namely Auto-ARIMA, Holt-Winters, Theta, ETS, TBATS, NNETAR and MLP, were used in the analyses. Among the models, NNETAR and MLP are AI based, and the others are statistical-based models. In this way, the effectiveness of different model types in electricity consumption estimations was compared. In this study, the Auto-ARIMA model stood out with a 3.77% MAPE error rate. When such studies are considered within the framework of countries' energy policies, they can make a significant contribution to reducing the current deficit of the country's economy. As a result of the study, it was concluded that the Auto-ARIMA model should be taken into consideration when making estimates on how many Megawatt power plants should be built in order to meet future energy needs in shaping energy policies in Türkiye.

1. Introduction

Energy is the most basic and indispensable need of today's modern societies. It plays a critical role in both economic growth and social welfare. Today, many devices and systems operate on energy. Energy is used as a fundamental resource for sustainable development and operational efficiency in various sectors such as homes, industry, transportation, production, and healthcare. Developing countries in particular experience a constant outflow of foreign currency because they import a large portion of their energy needs from abroad in foreign currency. This situation leads to a current account deficit in the country's economy. Meeting energy needs through imports negatively affects the economic development of these countries. In this context, it is of critical importance for developing countries to meet their energy needs with domestic and national resources in order to reduce their current account deficits and ensure their sustainable development. It can be said that the most widespread and most used type of energy is electrical energy. The production of electrical energy at low cost is of great importance in terms of closing the current account deficit in the national economy. Meeting the excessively consumed electricity need in the industrial and residential sectors with domestic and national resources is a critical step in terms of both economic efficiency and reducing foreign exchange outflow. Providing fuel through imports for electricity needs that cannot be met with domestic and national resources increases external dependency, resulting in a high amount of foreign exchange outflow and thus a current account deficit. Therefore, investments in electricity production with domestic and national resources should be continuously increased in order to meet the energy need. In Türkiye, especially in recent years, efforts to meet the energy need with domestic and national resources instead of imported oil and natural gas have gained momentum, and this process makes significant contributions to energy supply security [1]. However, it can be said that the electricity produced with domestic and national resources in Türkiye is currently not enough to meet the country's total electricity needs. In addition, in order to close the current account deficit in the country's economy, the production capacity in the industry should also be increased. On the other hand, increasing the production capacity will naturally create a greater need for electricity in the industry. In this case, the energy need should be met by increasing electricity production with domestic and national resources, and the production volume in the industrial sector should be increased. This approach aims to both provide foreign exchange inflow to the country and close the current account deficit in the country's economy. Thus, by ensuring energy independence, it will be possible to reduce external dependency and strengthen economic sustainability [2]. Figure 1 shows that 46% of electricity production is provided by imported energy sources, as stated in the 2024 Energy Statistics Bulletin of the Ministry of Energy and Natural Resources. The amount of electricity produced with domestic and national resources consists of 11% wind, 3% waste, 15% HES (Hydroelectric Power Plant) dam, 6% HES river, 3% geothermal and 14% lignite [3].

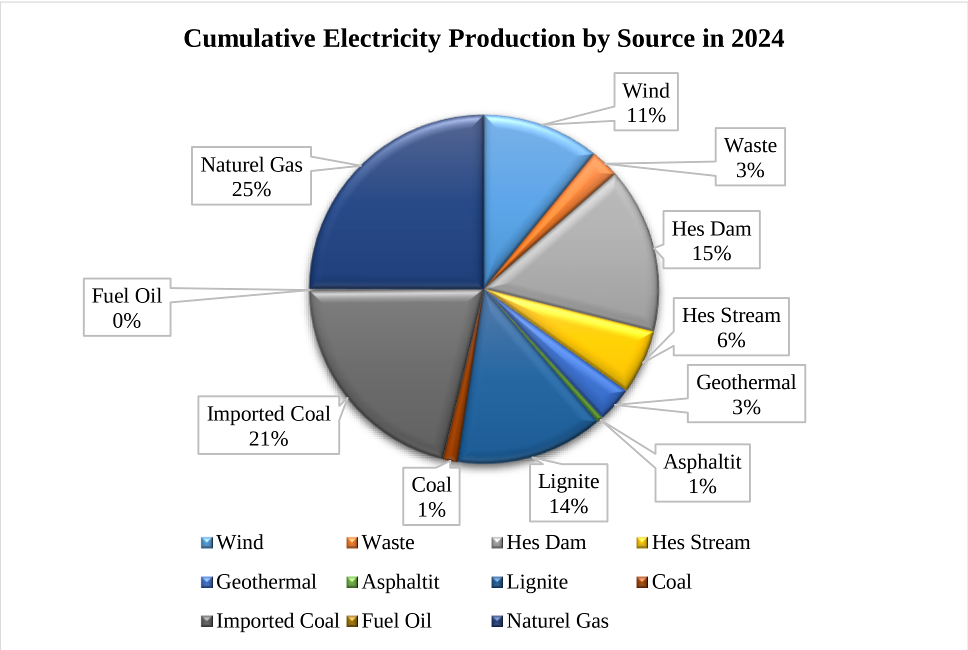

Figure 1. EIGM Reports [3].

The aim of this research is to encourage energy production with domestic and national resources instead of import-based energy resources and to contribute to closing the current deficit by ensuring that the budget allocated for energy remains within the country. In this context, the research emphasizes the importance of effective use of domestic energy resources. In a period when global energy crises and economic uncertainties are increasing, domestic energy production is of critical importance for the sustainability of the country's economy. In line with this goal, the research aims to reduce energy costs, create domestic added value and ensure more efficient use of the country's budget. As a result, reducing dependency on imports and encouraging domestic energy production emerge as an important step to ensure the country's economic and environmental sustainability.

1.1. Related Works

Energy is a critical factor for a country's economic growth and sustainable development. Therefore, energy production is at the core of economic and strategic decisions around the world. Many countries are developing various policies aimed at reducing energy dependency and using their domestic resources more efficiently. However, externally dependent energy production can threaten economic stability and prevent the efficient use of resources. Therefore, increasing domestic and national energy production is of great importance in terms of both economic and environmental sustainability. Studies in the literature on the contributions of domestic energy production to economic development and reducing external dependency reveal the importance of policies and strategies in this area. For example, Karaman and Bektaş (2023) [4] estimated energy consumption for the period 2020-2040 by using Türkiye's population, import, export and gross domestic product data between 1980-2019. Researchers used Particle Swarm Optimization (PSO), Gaussian Process Regression (GSR), Linear Regression (LR) models in their studies. As a result of the study, they found the coefficient of determination (R^2) of the models they used as GSR 0.9983, LR 0.9923 and PSO 0.9938, respectively [4]. Ekinci (2019) [5] made predictions by comparing the Artificial Neural Network (ANN) and Adaptive Network Based Fuzzy Logic Inference System (ANFIS) models, using electricity consumption data in Türkiye between 1970-2015. As a result of the study, the Mean Absolute Error Percentage (MAPE) for the test data of the ANN model was calculated as 3.69, and the ANFIS model as 3.35 [5]. Özden and Öztürk (2018) [6] applied the ANN model, using the electricity data consumed in the OSTİM Organized Industrial Zone between the years 2014-2016 and estimated the possible electricity consumption of the region [6]. Zeng et al. (2018) [7] estimated the electricity consumption for the period 2009-2015 by using the electricity consumption data between the years 1997-2008 in the commercial sector in Hong Kong. In the study, the possible electricity consumption for 2020 was calculated as 108,050 terajoules [7]. Similarly, Pençe et al. (2019) [8] examined the data between the years 1970-2016 in order to estimate the electricity consumption in the Turkish industry and made estimates for the period 2017-2023. As a result of the study, the RMSE value measuring the accuracy of the estimates was found to be 8.99 [8]. Işık and Şeker (2021) [9] estimated the future electricity demand by using an ANN model with data between 1985-2019, considering the electricity generation capacity in Türkiye. In this study, an ANN model consisting of 6 inputs, 4 outputs and 10 hidden layers was designed [9]. Lee et al. (2022) [10] estimated the electricity consumption in 2016 by using the ANN model, using 10-year electricity consumption data of Switzerland, Norway, Malaysia, Egypt and some other countries. In this study, it was determined that the Fuzzy Time Series (FTS) model showed the best performance for Algeria, Norway, Bulgaria and Kenya in short-term forecasts, while the ANFIS model was found to be more successful for Switzerland [10]. Tarmanini et al. (2023) [11] randomly selected 709 households in Ireland and applied 18-month daily electricity consumption data to ANN and ARIMA (Autoregressive Integrated Moving Average) models. As a result, they predicted that a better performance would be achieved when a hybrid model structure was used [11]. Lazzari et al. (2022) [12] examined the behavior of users on electricity consumption and established an ANN-based behavior clustering. Then, they tested it on 500 users in Spain and predicted future electricity consumption [12]. Ramos et al. (2020) [13] predicted future electricity consumption, using an ANN model with 16-month data of an industrial facility [13]. Pala (2023) [14] examined the electricity consumed per capita in Türkiye between 1965-2022. In the study, MLP (Multilayer Perceptron), NNETAR (Neural Network Time Series Forecasts), ELM (Extreme Learning Machine), ETS (Exponential Smoothing), Auto-ARIMA, TBATS (Trigonometric Seasonal + Exponential Smoothing Method + Box-Cox Transform + ARMA) models were used. In the analysis, the most successful model was found to be TBATS and the MAPE performance of the model was obtained with an error of 4.66% [14]. After examining the electricity consumption data on a sectoral basis between 1970-2004 in Türkiye, Hamzaçebi (2017) [15] estimated the total electricity consumption for 2020 as 499588.2 GWh with the ANN model. However, the total electricity consumption data announced by TÜİK for 2020 is 262702.1 GWh, which shows that there is a significant deviation in the researcher's estimate [15]. Qureshi et al. (2024) [25] emphasized that building energy management systems increase and optimize efficiency by monitoring energy consumption. In the study, electricity consumption was predicted by using LSTM-based time series analysis, and it was shown that the model achieved 95% accuracy [25]. On the other hand, Liu et al. (2024) [26] proposed a new gray Fourier model augmented with Fourier functions and fractional time-varying terms to accurately model seasonal fluctuations in electricity consumption. The study shows that the proposed model offers higher accuracy and flexibility compared to other traditional forecasting methods [26]. Peteleaza et al. (2023) [27] showed that the proposed time series dense encoder model for short and long-term forecasts of electricity consumption at the city level exhibits superior performance compared to traditional approaches [27]. Matos et al. (2024) [28] use machine learning techniques to forecast energy consumption of communities by addressing the transformation in the energy sector with the integration of renewable energy sources and the decentralization of electricity markets. The study shows that forecasts made with the eXtreme Gradient Boosting (XGBoost) algorithm are effective in reducing energy expenditures of communities and their dependence on the central distribution grid [28]. Kim et al. (2025) [29] studied the effect of data normalization on electricity consumption estimates in buildings with four different ANN algorithms. The study highlights that proper use of data normalization techniques can significantly increase the accuracy of electricity consumption estimates [29]. Leite Coelho da Silva et al. (2025) [30] emphasized that forecasting industrial sector electricity consumption is important for energy planning and control. The study reveals that the integration of classical forecasting models with Seasonal and Trend decomposition using Loess method can significantly increase the accuracy of electricity consumption forecasting [30]. Nazir and Li (2025) [31] stated that the quality of Pakistan's electricity consumption forecasts is critical for energy planning. The study demonstrates the effectiveness of a combined forecasting model based on LSTM and Monte Carlo simulation in accurately predicting the country's electricity consumption [31]. On the other hand, Zhang et al. (2020) [32] proposed a new gray model that takes into account spatial effects in electricity consumption estimates. The model exhibits higher accuracy and robustness compared to existing methods by using dynamic interaction matrix and Bayesian Optimization [32].

As a result, when the studies on electricity consumption estimation are examined, it is seen that both traditional statistical methods and machine learning-based approaches are widely used. While previous studies in the literature mainly focused on statistical techniques such as time series analysis and regression, in recent years it has been shown that deep learning and hybrid models offer significant advantages in improving the estimation performance. In this study, different statistical and artificial intelligence-based models for electricity consumption estimation were compared, and their performances were evaluated in detail. Auto-ARIMA, Holt-Winters, Theta, ETS, TBATS, NNETAR and MLP models were used in the study. These models offer different advantages and limitations in electricity consumption estimation. For example, Auto-ARIMA works efficiently with automatic parameter selection in small data sets, while it may have difficulty in large data sets. Holt-Winters is effective in pronounced seasonal patterns and may be weak in sudden changes. Theta adapts to both seasonal and non-seasonal components, but is sensitive to weak seasonal data. ETS performs well in simple data, but may be limited in complex data. TBATS is robust on multi-seasonal patterns but may suffer from performance degradation on small datasets. NNETAR and MLP are good at capturing nonlinear relationships but require large data and careful parameter tuning.

2. Material and Methods

Electrical energy consumption estimations are made with various techniques such as time series analysis, regression methods and machine learning. In this study, deep learning methods were used in addition to time series analysis in estimating electrical energy consumption. In the study, Auto-ARIMA, Holt-Winters, Theta, ETS and TBATS were used as statistical models, and MLP and NNTAR models were used as AI based models.

Time series, which are used in many sectors such as statistics, engineering, finance and energy, contain records of past observations taken according to a certain period. These series can be in seconds, minutes, hours, daily, weekly, monthly, seasonal, annual and periodic periods. Time series generally contain four elements: trend, conjectural fluctuation, seasonal fluctuation and random fluctuation. Time series consist of two parts: stationary and non-stationary. Statistical models are generally applied to stationary time series. However, in business life, industry and economy, time series are non-stationary at a certain average but rather have an up-and-down trend. In time series analysis, non-stationary series are made stationary and then applied to models [16][17][19].

2.1. ARIMA Model

ARIMA is a statistical model that allows estimating future values based on past data. This model is effectively used to predict future trends by analyzing time series data. ARIMA is preferred to solve unpredictable problems in many areas such as economy, finance, and energy demand. This model is used with the Auto.ARIMA function in the forecast library in the R programming language.

The ARIMA model is shown in the format ARIMA(p,d,q); p (AR) indicates the number of past values of the series, d (I) indicates the degree of difference iteration (how much difference is taken to make it stationary), and q (MA) indicates the component degree (the number of past errors). When applying the ARIMA model to time series data, determining the correct parameters is critical for prediction accuracy. Autocorrelation Function (ACF) and Partial Autocorrelation Function (PACF) plots indicate which ARIMA model to use. Akaike Information Criterion (AIC) and Schwarz Information Criterion or Bayesian Information Criterion (BIC) are used to evaluate the accuracy of the selected ARIMA model. Since there are many forms of the ARIMA model, the Auto.ARIMA function in the R programming language automatically selects the relevant ARIMA form for us to use. The mathematical formula of the general ARIMA(p,d,q) model [16][17] is as follows:

$$Y'_t = c + \phi_1 Y'_{\{t-1\}} + \cdots + \phi_p Y'_{\{t-p\}} + \theta_1 \varepsilon_{\{t-1\}} + \cdots + \theta_q \varepsilon_{\{t-q\}} + \varepsilon_t \quad (1)$$

Here Y'_t represents the differenced time series, ϕ_i AR parameters, θ_j MA parameters, ε_t error term.

2.2. Holt-Winter Model

Holt (1957) and Winters (1960) is a model used in the forecast analysis of time series with seasonality. This model creates observations and makes forward-looking predictions by taking into account the trend, level and seasonal effects in the time series. There are three components in the Holt-Winter additive model, which are level l_t, trend b_t and seasonality s_t. The correction parameters are α, β and γ. The additive formula of the model is shown below [17]:

$$Y_{(t+h|t)} = l_t + hb_t + s_{t+h-m(k+1)} \quad (2)$$

$$l_t = \alpha(y_t - s_{t-m}) + (1-\alpha)(l_{t-1} + b_{t-1}) \quad (3)$$

$$b_t = \beta^{*(l_t - l_{t-1})} + (1-\beta^*)b_{t-1} \quad (4)$$

$$s_t = \gamma(y_t - l_{t-1} - b_{t-1}) + (1-\gamma)s_{t-m} \quad (5)$$

2.3. Theta Model

Theta model is a model used in the prediction of time series. The model is based on changing the local trends of the time series. The trend of the time series is smoothed with a number called theta coefficient. Theta coefficient is given values that continuously decrease towards zero, and the trend curve is made a linear line. The mathematical formula of the model is shown below [17][18]:

$$\mathrm{X}''^{(\theta)}_{\mathrm{new}} = \theta \cdot \mathrm{X}''_{\mathrm{data}}, \mathrm{where} \mathrm{X}''_{\mathrm{data}} = \mathrm{X_t} - 2\mathrm{X_{t-1}} + \mathrm{X_{t-2}} \mathrm{at\,time t} \quad (6)$$

2.4. ETS Model

ETS (Error-Trend-Seasonality) model is a statistical model used in time series forecasting. The model, which considers Error, Trend and Seasonality, can express these components in additive or multiplicative forms. The general mathematical formula of the model is shown below [21]:

Formula in the observation equation:

$$y_t = l_{t-1} + b_{t-1} + s_{t-m} + \varepsilon_t \quad (Additive) \quad (7)$$

$$y_t = (l_{t-1} + b_{t-1}).s_{t-m}.\varepsilon_t \quad (Multiplicative) \quad (8)$$

$$\begin{gathered} y_t, observations; \\ l_{t-1}, level; \\ b_{t-1}, trend; \\ s_{t-m}, seasonality; \\ \varepsilon_t, error\ term. \end{gathered} \quad (9)$$

The formula in the level equation:

$$l_t = l_{t-1} + \alpha\varepsilon_t \quad (Additive) \quad (10)$$

$$l_t = l_{t-1}.(1 + \alpha\varepsilon_t) \quad (Multiplicative) \quad (11)$$

α is the correction coefficient for the level.

Formula in trend equation:

$$b_t = b_{t-1} + \beta\varepsilon_t \quad (Additive) \quad (12)$$

$$b_t = b_{t-1}.(1 + \beta\varepsilon_t) \quad (Multiplicative) \quad (13)$$

β is the trend correction coefficient.

Formula in seasonal equation:

$$s_t = s_{t-m} + \gamma\varepsilon_t \quad (Additive) \quad (14)$$

$$s_t = s_{t-m}(1 + \gamma\varepsilon_t) \quad (Multiplicative) \quad (15)$$

γ is the adjustment coefficient for seasonality.

2.5. TBATS Model

TBATS model is designed to model complex seasonal structures and nonlinear time series. The model has a wide range of time series applications by combining trigonometry-based Fourier series, Box-Cox transformation, ARMA error terms, trend and seasonality components. In particular, it can effectively model fractional and irregular seasonal cycles and double calendar effects. TBATS provides more accurate estimates, using maximum likelihood estimates and requires less computational load than other methods. The general mathematical formula of the model is shown below [20]:

$$y_t^{(\omega)} = \ell_{t-1} + \emptyset b_{t-1} + \sum_{i=1}^{T} s_{t-m_i}^{(i)} + d_t \qquad (16)$$

$y_t^{(\omega)}$, Box-Cox transformed observation; l_{t-1}, Previous period trend component (level); ϕb_{t-1}, Previous period trend (trend growth rate), multiplied by the damping parameter (ϕ\phiϕ); $s_{t-mi}^{(i)}$, i'th seasonal component; d_t, represents the values coming from ARMA errors.

2.6. NNAR Model

NNAR (Neural Network Auto Regressive) is an ANN model used to predict time-dependent data. This model is designed specifically for univariate time series and consists of a feed-forward layer. NNAR takes past observations (lag) as input and predicts future values based on these data. It is called with the nnetar() function in the forecast package in the R programming language. It is called nnetar (p, k), p represents the delayed input values, i.e. past observations, and k represents the number of neurons in the hidden layer. The general form of the model is NNAR(p,P,k)m, consisting of inputs $(y_{t-1}, y_{t-2}, \cdots, y_{t-p}, y_{t-m}, y_{t-2m}, y_{t-pm})$ and k is the number of neurons in the hidden layer. If k is not specified, k=(p+P+1)/2 is set [17].

2.7. MLP Model

MLP (Multi-Layer Perceptron) is a deep learning model used in time series and other fields. MLP is a forward-learning ANN model with at least three layers. The data received from the input unit is multiplied by a specified weight, and summed, and passed through the activation function and transmitted to the next layer or output. The mathematical formula of the model is shown below [22][23]:

$$Y = f(net) = f\left(\sum_{i=1}^{n} w_i x_i + b\right) \qquad (17)$$

$(x_1, x_2 \ldots x_n)$ data inputs; $(w_1, w_2 \ldots w_n)$ weights; b, bias, a fixed value: f, activation function; Y, output.

2.8. Performance Measurement Metrics

MAPE (Mean Absolute Percentage Error), RMSE (Root Mean Square Error) and MAE (Mean Absolute Error) metrics were used to evaluate the performance of the models.

$$MAE == \frac{1}{N} \sum_{t=1}^{N} \left| Y_t - \hat{Y}_t \right| \qquad (18)$$

$$MAPE = \frac{100}{N} \sum_{t=1}^{N} \left| \frac{Y_t - \hat{Y}_t}{Y_t} \right| \qquad (19)$$

$$RMSE = \sqrt{\frac{1}{N} \sum_{t=1}^{N} \left(Y_t - \hat{Y}_t\right)^2} \qquad (20)$$

Y_t represents the actual value, $\hat{Y}_t$ represents the predicted value, and N represents the number of samples.

MAE is the absolute average of the differences between the predicted value and the actual values. As a result of this process, negative values and positive values are prevented from canceling each other out. MAE is calculated by taking the sum of the absolute values of the errors and dividing the total error by the number "n".

MAPE expresses the percentage of the ratio of the prediction errors to the actual values. It is used especially when the units of the variables are different or when an error measure independent of the unit is desired. Since the results are presented as a percentage, comparisons between units can be made. The closer the MAPE value to zero, the more successful the result is considered. However, MAPE can only be calculated when applied to positive data.

RMSE is the square root of the mean square of the errors. It not only measures the magnitude of the errors but also gives more weight to large errors. Due to its sensitivity to large errors, it emphasizes the effect of errors more strongly, and since it penalizes large errors, it can ignore the importance of small errors [17][24].

2.9. Dataset

In the current study, Türkiye's hourly electricity consumption data between 2016-2024 were examined. The data were obtained from https://seffaflik.epias.com.tr (Energy Markets Operation Joint Stock Company). The data were obtained from hourly consumption data. These hourly data were converted to monthly consumption data. There is no loss in the data. No missing data filling or data reduction was done. As a result, 108 months of electricity consumption data were calculated.

3. Analysis

In the study, electricity consumption data were handled with statistical and AI based models. The estimates of each model on the consumption data were carried out, and the results obtained were analyzed and measured.

The data set was divided into 80% training and 20% test data. As a result of the analyses performed on the data set, the model with the highest performance was determined. Figure 2 shows Türkiye's monthly electricity consumption between 2016 and 2024 (108 months).

When the graph is examined, it is observed that there are significant fluctuations. Fluctuations are an indicator of seasonality rather than stationarity of the data. Each black dot shows the electricity consumption of that month. An increasing consumption trend is observed in the graph over time. Consumption, which was at lower levels in 2016, increased significantly by 2024. A short-term decrease is seen around 2020. In May 2020, less than 20 thousand MWh was consumed and consumption decreased. This situation may be related to the economic slowdown caused by the pandemic. However, the graph shows higher fluctuations and sudden increases in consumption starting from 2021. This may be related to economic growth, industrialization, population growth or changes in energy policies. These are important data in terms of planning energy policies, sustainability strategies and demand forecasting.

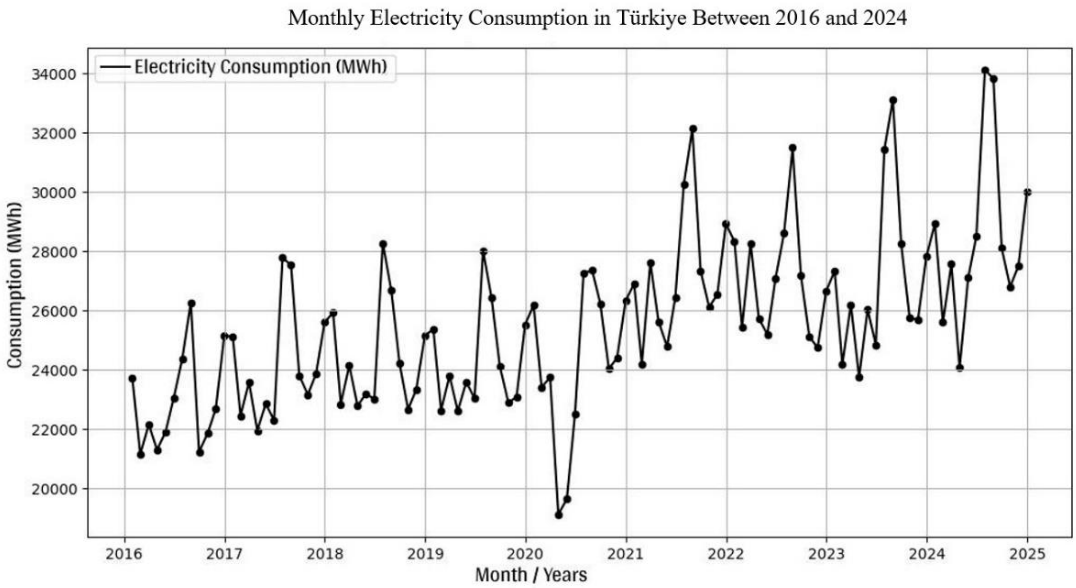

Figure 2. Monthly Electricity Consumption in Türkiye Between 2016 and 2024

4. Results and Discussion

In this study, the analyses made on electricity consumption data are visualized with separate graphs for each model. Figure 3 shows the analysis of the Auto-ARIMA model on the data, Figure 4 shows the analysis of the Holt-Winters model, Figure 5 shows the analysis of the Theta (THETAF) model, Figure 6 shows the analysis of the ETS model, Figure 7 shows the analysis of the TBATS model, Figure 8 shows the analysis of the NNETAR (NNAR) model, and Figure 9 shows the analysis of the MLP model. In the visuals in the figures, the black lines show the training data, the red lines show the test data, and the blue lines show the predictions of the relevant model. The light and dark gray areas represent the 95% and 80% confidence intervals of the model. Among the models used in the study, the Auto-ARIMA model was the model that approached the red test line the closest with the blue line compared to other models. Therefore, the model with the highest prediction rate is the Auto-ARIMA model.

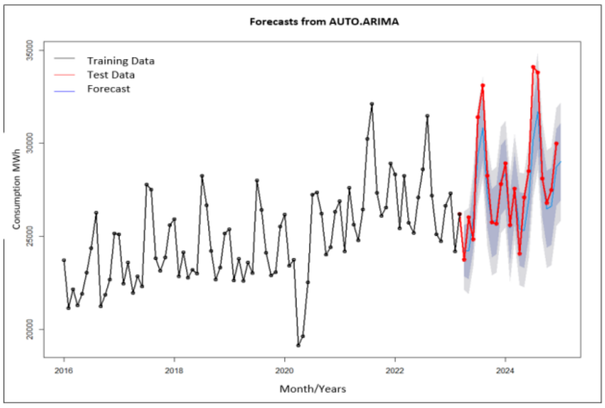

Figure 3. Performance Graph of Auto-ARIMA Model

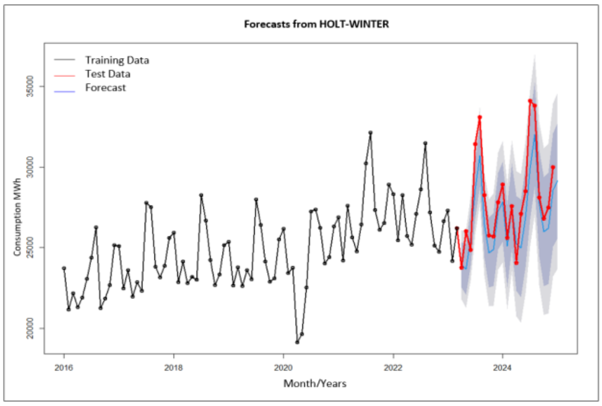

Figure 4. Performance Graph of Holt-Winter

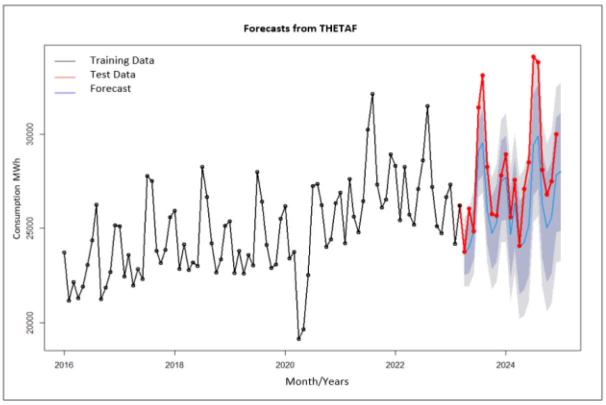

Figure 5. Performance Graph of Theta

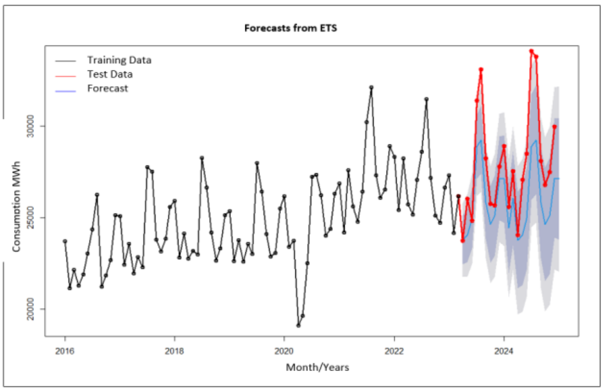

Figure 6. Performance Graph of ETS

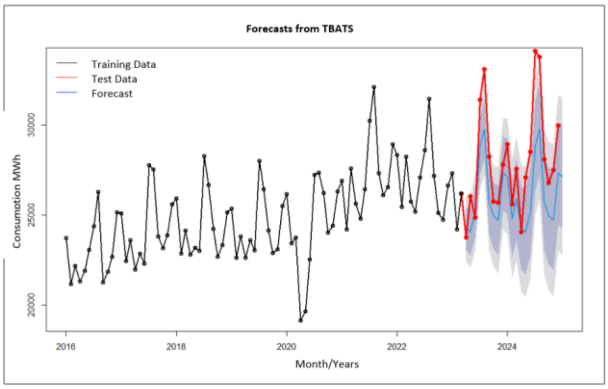

Figure 7. Performance Graph of TBATS

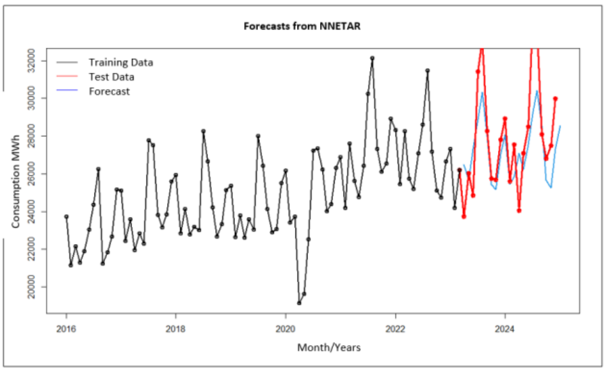

Figure 8. Performance Graph of NNETAR

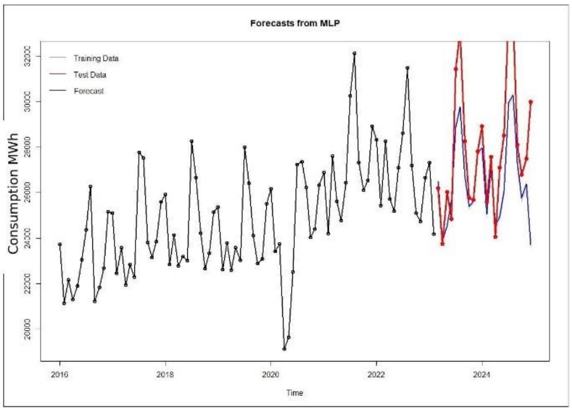

Figure 9. Performance Graph of MLP

Figure 10 shows the results of the time series analysis performed by using the Auto.ARIMA model. The model analyzed past data and made a 12-month consumption forecast for the future. The training data shown with black dots represent the consumption values of the past years (2016-2024). The data set shows a seasonal and general increasing trend. The blue line shows the estimated consumption values, while the gray shades around it represent the uncertainty range. The uncertainty range widens as time progresses. This indicates that the estimated values may vary more in the future and the uncertainty increases. When the graph is examined, although there are fluctuations in consumption according to the 12-month forecast result, a certain trend is maintained.

Performance measurements in all analyses were measured with RMSE, MAE and MAPE metrics. Table 1 presents the performances of all models together. Auto-ARIMA shows the highest accuracy by providing the lowest error rates among all models. It exhibits a significant superiority over other models in both training and test sets, especially in terms of RMSE and MAE values. On the other hand, THETAF, ETS, TBATS models attract attention with higher error values. NNETAR and MLP models have larger error rates, falling behind Auto-ARIMA in terms of prediction accuracy. This shows that Auto-ARIMA is a more robust and reliable option in time series predictions.

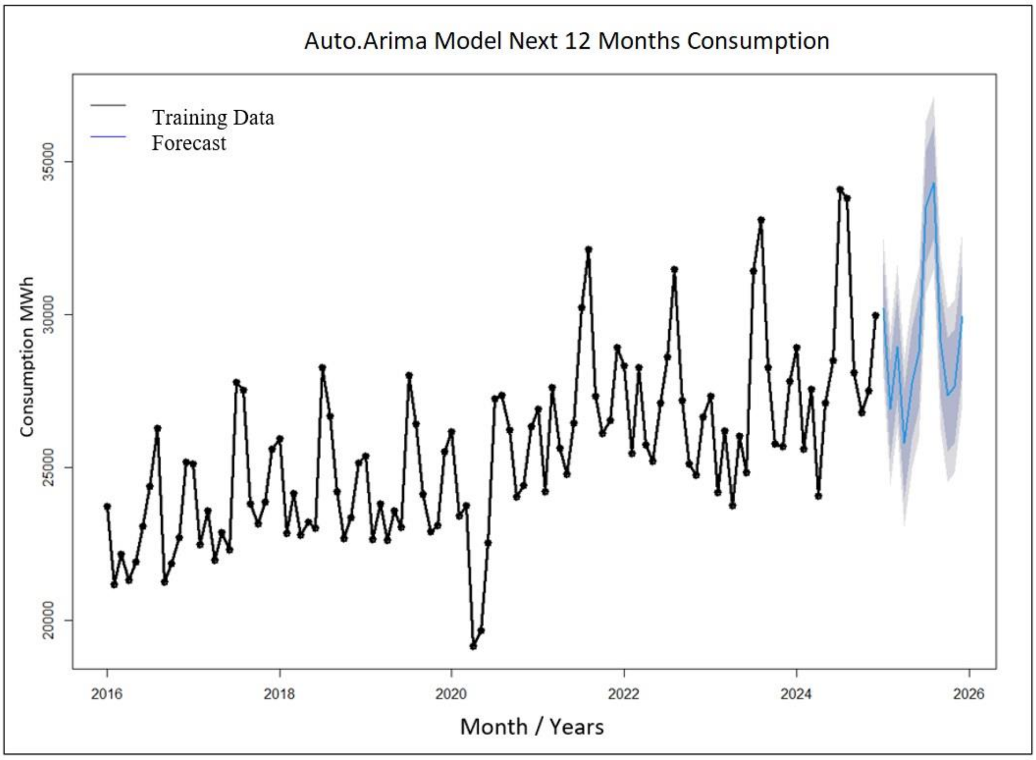

Figure 10. Auto-ARIMA Model Next 12 Months Consumption Forecast

Table 1: Error Measurement Performance Analysis of Models

Data Set	Training / Test Sets			
Türkiye Electricity Consumption 2016-2024 (108 Units)	Training / Test Length 80%-20%	RMSE Training / Test	MAE Training / Test	MAPE (%) Training / Test
Auto-ARIMA	86 - 22	**969.53 / 1470.09**	**622.33 / 1107.33**	**2.48 / 3.77**
Holt Winter	86 - 22	1092.90 / 1695.51	790.41 / 1386.16	3.15 / 4.77
THETAF	86 - 22	921.91 / 2225.95	676.41 / 1802.43	2.74 / 6.10
ETS	86 - 22	940.38 / 2512.18	729.60 / 2089.38	2.97/7.09
TBATS	86 - 22	933.70 / 2448.19	696.40 / 2068.11	2.83 / 7.05
NNETAR	86 - 22	1234.84 / 2107.46	897.83 / 1676,54	3.56 / 5.84
MLP	86 - 22	844.19 /2208.34	639.06 / 1573.37	2.59 / 5.28

The last 3-year monthly consumption average between 2022-2024 and the monthly consumption forecast of the Auto-ARIMA model for 2025 are shown in Table 2.

Table 2: 12 Months Electricity Consumption Forecast for 2025

Month	**Monthly Average Consumption of the Last Three Years 2022-2024 (MWh)**	**Auto-ARIMA 2025 Consumption Forecast (MWh)**
January	28.187	30.196
February	25.073	26.912
March	27.336	28.952
April	24.512	25.796
May	26.103	27.757
June	26.810	28.766
July	31.376	33.519
August	32.795	34.317
September	27.846	29.088
October	25.886	27.366
November	25.972	27.654
December	28.149	29.931

When Table 2 is examined, it is seen that electricity consumption reaches the highest levels especially in July (31.376 MWh → 33.519 MWh) and August (32.795 MWh → 34.317 MWh) and peaks in these months in the 2025 estimates. This can be associated with the widespread use of cooling systems along with the increasing temperatures in the summer months. Similarly, it is observed that consumption is high in January (28.187 MWh → 30.196 MWh) and December (28.149 MWh → 29.931 MWh). This trend can be evaluated as a result of the increased use of electricity for heating purposes in the winter months. On the other hand, it is observed that consumption levels are lower in April (24.512 MWh → 25.796 MWh) and October (25.886 MWh → 27.366 MWh) compared to other months. This decrease can be explained by the decrease in demand for air conditioning systems during seasonal transition periods. In addition, estimates made by the Auto.ARIMA model predict an average increase of 5-7% based on the data of the previous three years. This trend shows that there is a continuous increase in electricity consumption and that energy demand will increase even more in 2025. It is evaluated that this increase may be due to various socioeconomic factors such as industrialization, population growth and technological advances. These findings are of critical importance in terms of effective planning of energy policies and the development of sustainable electricity production strategies. Taking the necessary measures to ensure energy supply security, especially during peak demand periods, stands out as an important requirement in terms of energy management.

5. Conclusion

As a result of the study, it was determined that there are significant seasonal fluctuations in electricity consumption in Türkiye. It is understood that electricity consumption should be compatible with its production because storing the electricity produced is extremely difficult and costly. In this context, it is important to examine seasonal fluctuations in more detail, and to conduct studies on sectors where electricity consumption increases due to these fluctuations, and to optimize power plant capacities accordingly.

It is emphasized that power plants to be established in the future should be powered by renewable energy sources (such as wind, solar, wave energy and nuclear energy) instead of fossil fuels. In addition, meeting the electricity need with domestic and national resources will contribute to the country's economy becoming more sustainable by preventing foreign exchange outflow. This situation can also help reduce budget deficits based on energy imports.

In recent years, wars around the world have posed serious threats to energy security and supply, and this issue has become a priority for countries. For example, Russia's restriction of natural gas to Europe has led to a major energy crisis in western countries. In this context, energy supply security is a critical priority, especially for industrial countries that are dependent on foreign energy. In countries with high external dependency, economic problems such as disruption of industrial production, decrease in export revenues and increase in budget deficits may arise. Therefore, it is clear that domestic resources for energy supply must be increased and diversified.

To recap, in this study, electricity consumption estimates were compared by using AI and statistical-based models. The study shows that it can be an important reference source in determining Türkiye's future energy needs. The study is limited to hourly electricity consumption data between 2016-2024. In the future studies, it is recommended to use datasets belonging to different countries and organizations. Broader and longer-term data can contribute to the examination of various electricity consumption models and to obtaining more reliable results. Increasing the amount of data will also improve the accuracy of the forecast models.

Studies on electricity consumption prediction focus on determining the methods with the highest accuracy rate by comparing different models and approaches. Similar to our study results, in some studies, statistical-based models were found to be successful in short-term estimations [7][26][32][33]. However, machine learning and deep learning-based approaches provide an advantage in long-term forecasting by better capturing complex consumption patterns [25][27][28][29]. On the other hand, in some studies, it is emphasized that hybrid models using statistical and AI based methods together increase estimation accuracy [4][5][6][30][31]. These findings reveal that model selection is critical in terms of energy planning and management.

In this study, seven different models (Auto-ARIMA, Holt-Winter, Theta, ETS, TBATS, NNETAR, MLP) were used to estimate Türkiye's electricity consumption in 2025. The models used in the study showed different performances in electricity consumption estimates. As a result, the Auto-ARIMA model stood out with a MAPE error rate of 3.77%. The prominence of this model is based on several important factors. First, the small size of the dataset used in our study, combined with the ability of Auto-ARIMA to adapt to the available data, allowed successful results to be obtained. This model generally provides statistical accuracy when working with limited data. Second, the seasonal characteristics of the dataset helped Auto-ARIMA to make accurate predictions by taking seasonal components into account. Finally, Auto-ARIMA's ability to automatically select the optimum parameters increased prediction accuracy by ensuring the correct configuration of the model. When these factors came together, Auto-ARIMA exhibited strong performance even on small datasets, and showed superior results compared to other models. In future studies, it is recommended to improve electricity consumption estimates by using different models and methods. This study does not consider external variables such as economic indicators and weather patterns, which could influence electricity consumption. Future research could benefit from incorporating larger datasets and accounting for the effects of such external factors to enhance the robustness and accuracy of forecasting models.

Article Information Form

Funding

The author (s) has no received any financial support for the research, authorship or publication of this study.

Authors' Contrtibution

The authors contributed equally to the study.

The Declaration of Conflict of Interest/Common Interest

No conflict of interest or common interest has been declared by the authors.

The Declaration of Ethics Committee Approval

This study does not require ethics committee permission or any special permission.

The Declaration of Research and Publication Ethics

The authors declare that there is no conflict of interest regarding the publishing of the paper by the Journal of Innovative Science and Engineering, that the paper has been not published elsewhere, and not include any form of plagiarism. All the authors listed above have approved the manuscript and have agreed with the submission of the manuscript to the Journal of Innovative Science and Engineering.

References

[1] Yılankırkan, N., & Doğan, H. (2020). Türkiye'nin enerji görünümü ve 2023 yılı birincil enerji arz projeksiyonu. *Batman Üniversitesi Yaşam Bilimleri Dergisi*, *10*(2), 77-92.

[2] Kızıldere, C. (2020). Türkiye'de cari açık sorununun enerji tüketimi ve ekonomik büyüme açısından değerlendirilmesi: Ampirik bir analiz. *Business & Management Studies: An International Journal*, *8*(2), 2121-2139. http://dx.doi.org/10.15295/bmij.v8i2.1493

[3] EİGM Raporları—T.C. Enerji ve Tabii Kaynaklar Bakanlığı [- Republic of Türkiye Ministry of Energy and Natural Resources]. (2024). https://enerji.gov.tr/eigm-raporlari.

[4] Karaman, Ö. A., & Bektaş, Y. (2023). Makine öğrenmesi ve optimizasyon yöntemleri ile uzun dönem elektrik enerjisi tahmini: Türkiye örneği. *Mühendislik Bilimleri ve Araştırmaları Dergisi*, *5*(2), 285-292. https://doi.org/10.46387/bjesr.1306577

[5] Ekinci, F. (2019). YSA VE ANFIS tekniklerine dayalı enerji tüketim tahmin yöntemlerinin karşılaştırılması. *Düzce Üniversitesi Bilim ve Teknoloji Dergisi*, *7*(3), 1029-1044. https://doi.org/10.29130/dubited.485822

[6] Özden, S., & Öztürk, A. (2018). Yapay sinir ağları ve zaman serileri yöntemi ile bir endüstri alanının (ivedik OSB) elektrik enerjisi ihtiyaç tahmini. *Bilişim Teknolojileri Dergisi*, *11*(3), 255-261. https://doi.org/10.17671/gazibtd.404250

[7] Zeng, B., Tan, Y., Xu, H., Quan, J., Wang, L., & Zhou, X. (2018). Forecasting the electricity consumption of commercial sector in hong kong using a novel grey dynamic prediction model. *Journal of Grey System*, *30*(1), 159-174.

[8] Pençe, İ., Kalkan, A., & Çeşmeli, M. Ş. (2019). Türkiye sanayi elektrik enerjisi tüketiminin 2017-2023 dönemi için yapay sinir ağları ile tahmini. *Mehmet Akif Ersoy Üniversitesi Uygulamalı Bilimler Dergisi*, *3*(2), 206-228. https://doi.org/10.31200/makuubd.538878

[9] Işık, H., & Şeker, M. (2021). Yapay Sinir Ağı (YSA) kullanarak farklı kaynaklardan Türkiye'de elektrik enerjisi üretim potansiyelinin tahmini. *Computer Science*, *Special*, 304-311. https://doi.org/10.53070/bbd.991039

[10] Lee, M. H. L., Ser, Y. C., Selvachandran, G., Thong, P. H., Cuong, L., Son, L. H., Tuan, N. T., & Gerogiannis, V. C. (2022). A comparative study of forecasting electricity consumption using machine learning models. *Mathematics*, *10*(8), 1329. https://doi.org/10.3390/math10081329

[11] Tarmanini, C., Sarma, N., Gezegin, C., & Ozgonenel, O. (2023). Short term load forecasting based on ARIMA and ANN approaches. *Energy Reports*, *9*, 550-557. https://doi.org/10.1016/j.egyr.2023.01.060

[12] Lazzari, F., Mor, G., Cipriano, J., Gabaldon, E., Grillone, B., Chemisana, D., & Solsona, F. (2022). User behaviour models to forecast electricity consumption of residential customers based on smart metering data. *Energy Reports*, *8*, 3680-3691. https://doi.org/10.1016/j.egyr.2022.02.260

[13] Ramos, D., Faria, P., Vale, Z., Mourinho, J., & Correia, R. (2020). Industrial facility electricity consumption forecast using artificial neural networks and incremental learning. *Energies*, *13*(18), 4774. https://doi.org/10.3390/en13184774

[14] Pala, Z. (2023). Prediction of electricity consumption in Türkiye with time series. *Muş Alparslan Üniversitesi Mühendislik Mimarlık Fakültesi Dergisi*, *4*(1), 32-40.

[15] Hamzaçebi, C. (2007). Forecasting of Turkey's net electricity energy consumption on sectoral bases. *Energy policy*, *35*(3), 2009-2016. https://doi.org/10.1016/j.enpol.2006.03.014

[16] Box, G. E., Jenkins, G. M., Reinsel, G. C., & Ljung, G. M. (2015). *Time series analysis: Forecasting and control*. John Wiley & Sons. https://doi.org/10.1002/9781118619193

[17] Hyndman, R. J. (2018). *Forecasting: Principles and practice*. 2nd ed. Melbourne: OTexts.

[18] Assimakopoulos, V., & Nikolopoulos, K. (2000). The theta model: A decomposition approach to forecasting. *International journal of forecasting*, *16*(4), 521-530. https://doi.org/10.1016/S0169-2070(00)00066-2

[19] Özoğuz, K. (1986). Zaman serilerinde trend fonksiyon tipinin belirlenmesi ve yorumu. *İstanbul Üniversitesi İktisat Fakültesi Mecmuası*, *42*(1-4).

[20] De Livera, A. M., Hyndman, R. J., & Snyder, R. D. (2011). Forecasting time series with complex seasonal patterns using exponential smoothing. *Journal of the American Statistical Association*, *106*(496), 1513-1527. https://doi.org/10.1198/jasa.2011.tm09771

[21] Hyndman, R., Koehler, A. B., Ord, J. K., & Snyder, R. D. (2008). *Forecasting with exponential smoothing: The state space approach*. Springer Science & Business Media.

[22] Kaynar, O., & Taştan, S. (2009). Zaman serisi analizinde MLP yapay sinir ağları ve ARIMA modelinin karşılaştırılması. *Erciyes Üniversitesi İktisadi ve İdari Bilimler Fakültesi Dergisi*, *33*, 161-172.

[23] Pinkus, A. (1999). Approximation theory of the MLP model in neural networks. *Acta numerica*, *8*, 143-195. https://doi.org/10.1017/S0962492900002919

[24] Saigal, S., & Mehrotra, D. (2012). Performance comparison of time series data using predictive data mining techniques. *Advances in Information Mining*, *4*(1), 57-66.

[25] Qureshi, M., Arbab, M.A. & Rehman, S. (2024). Deep learning-based forecasting of electricity consumption. Sci Rep 14, 6489. https://doi.org/10.1038/s41598-024-56602-4

[26] Liu, X., Li, S., & Gao, M. (2024). A discrete time-varying grey Fourier model with fractional order terms for electricity consumption forecast. Energy, 296, 131065. https://doi.org/10.1016/j.energy.2024.131065

[27] Peteleaza, D., Matei, A., Sorostinean, R., Gellert, A., Fiore, U., Zamfirescu, B. C., & Palmieri, F. (2024). Electricity consumption forecasting for sustainable smart cities using machine learning methods. Internet of Things, 27, 101322. https://doi.org/10.1016/j.iot.2024.101322

[28] Matos, M., Almeida, J., Gonçalves, P., Baldo, F., Braz, F. J., & Bartolomeu, P. C. (2024). A machine learning-based electricity consumption forecast and management system for renewable energy communities. Energies, 17(3), 630. https://doi.org/10.3390/en17030630

[29] Kim, Y. S., Kim, M. K., Fu, N., Liu, J., Wang, J., & Srebric, J. (2025). Investigating the impact of data normalization methods on predicting electricity consumption in a building using different artificial neural network models.

Sustainable Cities and Society, 118, 105570. https://doi.org/10.1016/j.scs.2024.105570

[30] Leite Coelho da Silva, F., da Silva Cordeiro, J., da Costa, K., Saboya, N., Canas Rodrigues, P., & López-Gonzales, J. L. (2025). Time series forecasting via integrating a filtering method: an application to electricity consumption. Comput Stat. https://doi.org/10.1007/s00180-024-01595-x

[31] Nazir, M.U., Li, J. (2025). Forecasting of electricity consumption in Pakistan based on integrating machine learning algorithms and Monte Carlo simulation. Electr Eng. https://doi.org/10.1007/s00202-024-02923-6

[32] Zhang, X., Dang, Y., Ding, S., Wang, H., & Ding, F. (2025). Multi-output discrete grey model tailored for electricity consumption forecast. Applied Mathematical Modelling, 139, 115822. https://doi.org/10.1016/j.apm.2024.115822

[33] Mahia, F., Dey, A. R., Masud, M. A., and Mahmud, M. S. (2019). Forecasting electricity consumption using ARIMA model. 2019 International Conference on Sustainable Technologies for Industry 4.0 (STI), Dhaka, Bangladesh, pp. 1-6, https://doi.org/10.1109/STI47673.2019.9068076

J Inno Sci Eng, 2025, 9(1):103-117

DOI:https://doi.org/ 10.38088/jise.1630283

Research Article

The Effect of Half Wave Pulsed Current Charging on Age and Capacity Fade for Lithium-ion Batteries

Muhammed Reşit ÇORAPSIZ [*]

[*] *Department of Electrical & Electronics Engineering, Erzurum Technical University, Erzurum, TR-25100, Türkiye*

ARTICLE INFO

Received Date: 31/01/2025
Accepted Date: 4/05/2025

Cite this paper as:
Çorapsız, M. R. (2025). The effect of half wave pulsed current charging on age and capacity fade for Lithium-ion batteries. *Journal of Innovative Science and Engineering.* 9(1), 103-117.

*Corresponding author: Muhammed Reşit ÇORAPSIZ
E-mail:r.corapsiz@erzurum.edu.tr

Keywords:
Li-ion batteries
Continuous current – Continuous voltage charging (CC-CV)
Pulsed current charge (PPC)
Life cycle
Capacity fade

ABSTRACT

This study proposes a new pulsed charging current technique to reduce aging and capacity losses in lithium-ion battery cells. The charging techniques developed to minimize aging and capacity losses are critical for battery cells with longer life cycles and higher energy efficiency. Continuous Current – Continuous Voltage charging (CC-CV), Positive Pulsed Current (PPC), and proposed Alternating Half Wave Pulsed Current (AHWPC) techniques were tested on a $12.8V - 40Ah$ Li-ion battery. In PPC and AHWPC techniques, the pulse frequency of the charging current is chosen as $f_{i_{ch}} = 1\ Hz$. The average value of the charging current for PPC and AHWPC techniques is calculated based on the CC-CV technique. The aging and capacity losses caused by the three charging techniques in the battery were measured in five different scenarios: at various temperatures, different discharge currents, and different depths of discharge (DoD). Using the AHWPC technique, improvements of 45.93%, 46.57% and 46.29% were achieved in cell aging compared to the CC-CV technique at temperatures of 20°C, 30°C and 40°C, respectively. According to the results, the proposed AHWPC technique performed better than the PPC and CC-CV techniques in all test conditions.

1. Introduction

Due to the increasing need for mobile devices around the world, the demand for high-performance rechargeable batteries is increasing day by day. The market share of Lithium-ion batteries (LIBs) is rapidly growing, expanding their application areas [1]. According to the report published by Precedence Research, the size of the global LIBs market will be worth 70 Billion USD in the 2020s, and this value is expected to exceed 370.05 Billion USD by 2032 [2]. LIBs are considered to be one of the most promising power sources for mobile electronic products, portable power devices, and vehicles [3]. This is because they have advantages such as high energy density, highly efficient charge/discharge rates, and high cycle life. LIBs, which have been preferred especially in vehicle technology in recent years, pose a disadvantage in terms of charging time. This situation causes rapid aging and capacity loss problems in cells if efficient charging techniques are not provided. While chemical research focuses on material design [4,5] engineering studies aim to develop charging techniques that enhance cycle life, efficiency, and capacity retention [6-8]. In general, the expected performance of a battery cell is a short charge time, long discharge time, and sufficiently long service life. It is insufficient that a particular charging technique proposed by the researchers solves only one of these two problems. A commercialized battery cell has a limited charge and discharge current, and these values are provided by the manufacturer. During the charging and discharging processes, the reaction between the negative electrode and the electrolyte produces a passive layer called the solid electrolyte interphase (SEI). The growth of this layer causes the loss of active lithium ions, resulting in capacity loss [9,10] Reducing the capacity loss and extending the service life of a commercialized LIB is only possible with the development of efficient charging techniques. These techniques will prevent capacity loss at certain rates and contribute to the extension of the cycle life of LIBs. In the literature and industry, the Constant Current (CC) - Constant Voltage (CV) technique is a common approach for charging LIBs [11]. However, in a LIB cell charged by the CC-CV technique, the CV phase contributes about a quarter of the discharge capacity and accounts for about half of the charging time. In addition, the cell exposed to continuous charging current heats up more, leading to increased thermal losses. To solve these problems, pulsed charging current techniques have been proposed [12] in different techniques including Positive Pulsed Current (PPC) mode [13], Pulsed Current-Constant Current (PCCC) mode [14], Negative Pulsed Current (NPC) mode [15], Alternating Pulsed Current (APC) mode [14] Sinusoidal Ripple Current (SRC) mode [10] and Alternating Sinusoidal Ripple Current (ASRC) mode [16].

The SRC strategy is proposed to determine the optimal pulsed charging current frequency (fz_{min}) of a LIBs. It is argued that this technique improves the charging time by about 17%, charging efficiency by 1.9%, maximum temperature rise by 45.8%, and cycle life by 16.1% compared to the CC-CV technique [16]. The NPC technique is discussed in [17], which provides the battery cell with higher discharge capacity and longer cycle life by improving active material utilization with short relaxation times and short discharge pulses during charging. As a result of XRD (X-Ray Diffraction) and SEM (Scanning Electron Microscope) studies obtained from this technique, it was observed that pulsed charging maintains the stability of the cathode better than CC-CV and prevents the increase in SEI formation. Since different Li-ion cells were used in most of the studies, the same pulsed current profiles may not provide the same performance for all Li-ion cells. This is because the electrode and electrolyte materials, capacity values, maximum charge (I_{max-ch}) and maximum discharge ($I_{max-disch}$) rates are not the same for different cells. In addition, the maximum discharge currents of the cells are usually much higher than the maximum charge currents. For example, these values are $I_{max-ch} = 1.7A$ and $I_{max-disch} = 10A$ for the MOLICELL INR-18650-35A Li-ion cell while $I_{max-ch} = 2.5A$ and $I_{max-disch} = 20A$ for the ORION INR-18650P cell [18,19]. Therefore, the cycle life and capacity fade for a Li-ion cell are more affected by high charge currents than by high discharge currents [20].

In the literature, pulsed charging currents are widely claimed to increase cycle life and reduce capacity losses, but some studies claim the opposite. In [21], PCCC mode is proposed, and it is asserted that the periodic pulse effect is detrimental to Li-ion battery performance when compared to a constant current profile based on the same average current. There are some reasons why the effects of pulse charging techniques on capacity loss and aging are favorable for some studies and unfavorable for others. Among these reasons, the amplitude, duty cycle, and the frequency of the pulsed charge profile used to charge the battery can be shown. In [7], the cycle life and performance of LIBs were studied by applying the charging current in PPC technique with different duty ratio, frequency and amplitude. The simulation results obtained from the PPC technique showed that the duty ratio and amplitude of the charging current are inversely proportional to the charging capacity. In the application of pulsed charging techniques, it is important to maintain the discharge capacity, charge capacity, charge time and cell temperature at nominal values. In the study carried out to investigate the effects of dynamic and static charging currents considering these criteria, it was observed that the dynamic fast charging profile after 1700 cycles has a significant role in reducing the charging time and capacity fade [22]. This study proposes a new pulsed charging technique to protect the aging and capacity loss of LIBs. Compared with other studies in the literature, the main contributions of this study are as follows:

- CC-CV and PPC techniques are explained in detail.
- With the proposed AHWPC technique, rest and charge transitions of the cell are performed more smoothly.

- CC-CV, PPC and AHWPC are compared in five different scenarios, different temperatures, different discharge currents and different DoDs.

This paper is organized as follows: in the second section, extensive information about the used LIBs charging techniques is given. In the third section, the implementation of the simulation methodology is explained in detail. The fourth section is devoted to the results and discussion, while the last section contains the conclusions of this study.

2. Battery Model and Charging Techniques

In this study, CC-CV mode, PPC mode and alternating half-wave current (AHWC) mode, which is proposed for the first time in this study, are used to determine aging, cell temperature and capacity losses in a $12.8V - 40Ah$ LIB model. The main focus of the study is to compare the performance of different charging techniques on the same cell. For this reason, the charging techniques were carried out on a battery model whose effectiveness has been proven by many studies [23,24].

2.1. CC-CV Mode

This charging technique consists of two stages, CC-mode and CV-mode. The first stage consists of CC-mode until the charging voltage provided by the manufacturer is reached. It must be ensured that the maximum charging current provided by the manufacturer is not exceeded during charging. The second phase, CV mode, consists of the time between the battery terminal voltage reaching the charging voltage and the charging current reducing to a limit value.

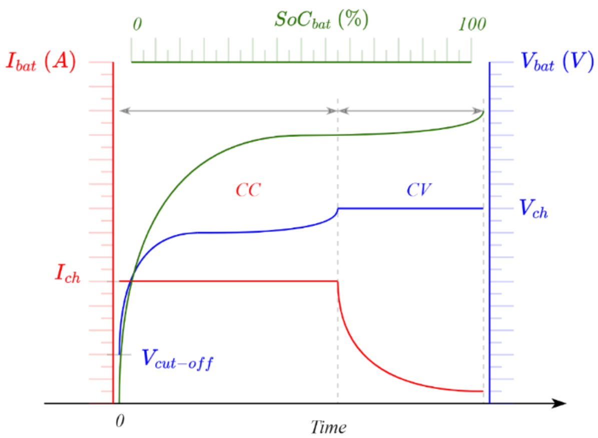

Figure 1: Variation of cell variables in CC-CV mode

Figure 1 represents the variation of cell voltage (V_{bat}), cell current (I_{bat}), and state of charge ratio (SoC_{bat}) of a fully discharged battery cell being fully charged by using CC-CV mode. In Figure 1, I_{ch} represents the battery charging current, V_{ch} represents the battery charging voltage, and $V_{cut-off}$ represents the discharge cut-off voltage. As can be seen, the battery cell, which was rapidly charging in CC-mode, shifted to CV-mode when the terminal voltage was equalized to the charging voltage. While the SoC curve changes rapidly in CC-mode, it changes very slowly in CV-mode. One of the biggest disadvantages of the CC-CV mode is that the CV-mode accounts for a significant portion of the charging time but a low portion of the discharge capacity. The relationship between SoC_{bat} and I_{ch} in Figure 1 can be given as follows:

$$SoC_{bat}(t) = SoC_{bat}(t-1) + \int_0^t \frac{I_{ch}}{Q_{bat}} dt \qquad (1)$$

In the notations in Equation 1, Q_{bat} is the rated battery capacity, and t is the time in seconds. Another disadvantage of using CC-CV mode in the charging protocol of LIBs is the growth of the SEI layer in the cell exposed to continuous charging current. This problem leads to capacity loss and therefore aging. The main causes of performance degradation in LIBs are loss of lithium inventory (LLI), loss of active material (LAM) and internal resistance which increases with time [25]. Among these reasons, it has been determined that LLI is the main cause of performance degradation [26]. Coulomb efficiency (CE) is usually used to determine the amount of LLI in a battery cell. CE is defined as follows:

$$\eta = \frac{C_d}{C_c} \qquad (2)$$

In Equation 2, η represents the Coulomb efficiency, C_d represents the discharge capacity in one cycle, and C_c represents the charge capacity in the same cycle.

2.2. PPC Mode

Positive Pulsed Current (PPC) mode consists of two phases within a certain period, namely the charging region and the relaxation region. In the charging region, a constant current is applied to the cell for a certain period of time, while this current is reduced to zero in the relaxation region. Figure 2a represents the implementation of the PPC technique. In this technique, a current source is connected to the battery via a switching element (S_t). By switching S_t periodically, pulsed charging currents are generated to charge the battery. Figure 2b shows the pulsed charging current waveforms. In the notations in Figure 2b, t_p represents the application time of the pulse currents, t_r the relaxation times of the battery cell, I_p is the amplitude of the applied pulse current, and T_p is the period of the pulse current. The relationship between the duty ratio (D_p), frequency (f_p), and T_p of the PPC is defined as follows:

$$f_p = \frac{1}{T_p} \tag{3}$$

$$D_p = \frac{t_p}{T_p} \tag{4}$$

When using the PPC mode, it should be noted that I_p does not exceed the maximum charging current, and t_r gives the battery cell sufficient relaxion time. In addition, for an objective comparison between the techniques, the average charging current in PPC mode must be equal to that in CC-CV mode. For example, a battery cell charged with 1C in CC-CV mode should be charged with 2C in PPC mode if D_p = %50. Research has shown that in addition to charging current, pulse frequency will also have a negative role in both fast charging and capacity fade. Among the pulse currents with the same amplitude and duty ratio at $50Hz$, $100Hz$, and $1kHz$, pulse currents at $50Hz$ and $1kHz$ showed more favorable results in terms of both fast charging and capacity losses compared to CC-CV mode. However, pulse currents of $100Hz$ result in both a significant increase in interfacial resistance and a decrease in interfacial capacity compared to CC-CV, which leads to an increase in SEI [27]. In addition, both experimental and simulation results have confirmed that it is possible to increase the cycle life of a battery cell by more than two times by using a suitable pulse current waveform [28]. Figure 3 shows the current, voltage and state of charge rate of a battery cell charged by PPC mode.

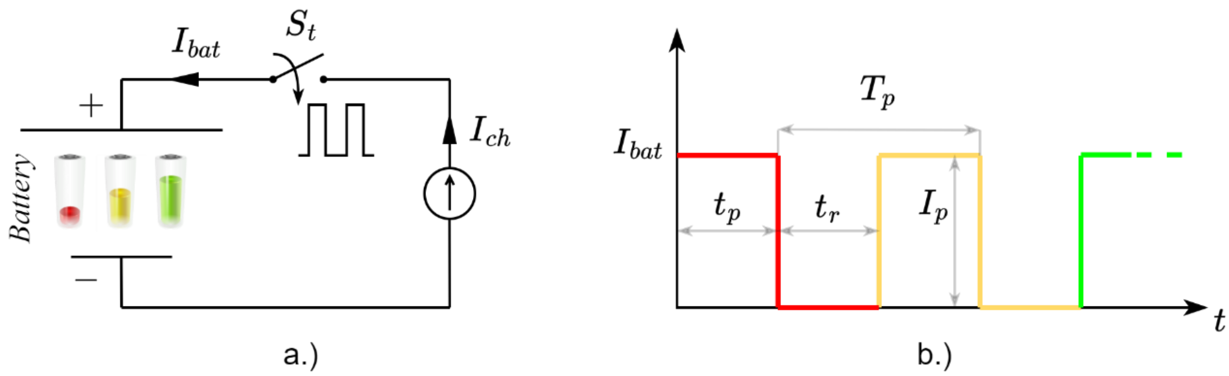

Figure 1: PPC mode a.) Equivalent circuit, b.) Pulsed current waveform

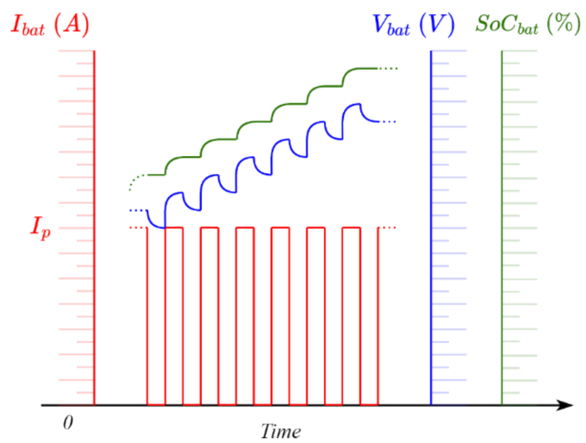

Figure 2: Variation of cell variables in PPC mode

The charging current I_p in Figure 3 is a pulsed current with an effective period of 50%. The average value of the pulsed current should not exceed the maximum charging current of the battery cell during a period. The pulse effects of the charging current are similarly observed on the cell voltage (V_{bat}) and the state of charge rate (SoC_{bat}). For highly efficient charging, pulse currents must be generated at maximum charging voltage. Each positive pulse results in a slight increase of V_{bat} and SoC_{bat}. As in CC-CV mode, the internal resistance of the cell plays an important role in all charging processes. If the internal resistance is high, a lower rise in the cell voltage is seen when the pulse current is applied, while when the pulse current is interrupted, the cell voltage will tend to drop rapidly due to the high internal resistance. This causes a longer charging time. Especially in the $SoC_{bat} < \%20$ and $SoC_{bat} > \%80$ ranges where the internal resistance is high [29] for each LIB cell, pulsed charging currents may be less effective than CC-CV mode. Another positive effect of PPC mode is that a certain rest time can be given to the battery cell in each period. This situation both reduces the LLI by preventing SEI growth and creates a natural commutation for the battery cell to cool down.

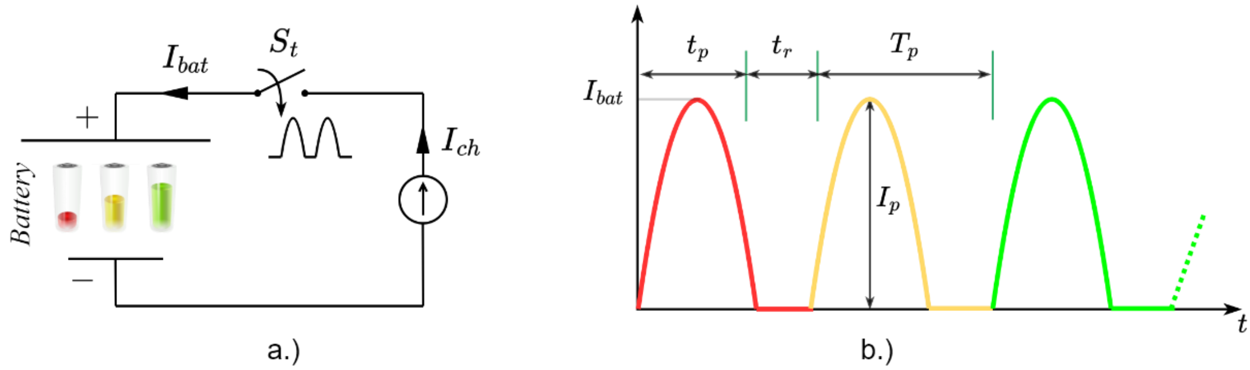

Figure 3: AHWPC mode a.) Equivalent circuit, b.) Alternating half wave pulsed current

2.3. Proposed AHWPC Mode

Alternating Half Wave Pulsed Current (AHWPC) mode is similar to PPC mode and consists of two stages, charging and resting regions. In the charging region, the charging current is applied to the cell as a sinusoidal half wave for a certain time (t_p). Then the cell is left to rest for a specific time (t_r). Figure 4 represents a battery cell charged by AHWPC mode. Figure 4a shows the electrical equivalent circuit of the AHWPC mode, and Figure 4b shows the pulse current waveform of the corresponding technique. This pulse current can be generated by using a half-wave rectifier circuit or a programmable DC power supply. When pulsed charging currents are applied, the average values of the applied charging current during t_p must be equal for all charging techniques. In this case, the average value expression of the pulsed current in Figure 4b can be written as follows:

$$I_{dc} = \frac{1}{T_p}\int_0^{T_p} I_{bat}\sin(wt)\, d(wt) \tag{5}$$

In Equation 5, I_{dc} represents the average current value, and w represents the angular frequency. When the charging and relaxation regions of the pulse currents in Figure 4b are taken into account, Equation 5 can be rewritten as follows:

$$I_{dc} = \frac{1}{t_p + t_r}\int_0^{t_p} I_{bat}\, sin(wt)\, d(wt) \tag{6}$$

Figure 5 compares the continuous CC-CV technique with the pulsed PPC and AHWPC techniques, highlighting their differences in current waveforms. In order to evaluate the charging techniques in terms of the aging and capacity fade, the areas $A_1 = A_2 = A_3$ must be equal. In Figure 5, A_{CC-CV}, A_{PPC}, and A_{AHWPC} represent the current amplitudes of CC-CV mode, PPC mode and AHWPC mode, respectively. For this study, $A_{CC-CV} = 0.5C$ is chosen. Therefore, the current applied to the battery cell for CC-CV mode during T_p can be expressed as follows:

$$I_{dc(CC-CV)} = 0.5C * T_p = A_1 \tag{7}$$

In Equation 7, $I_{dc(CC-CV)}$ represents the average current value of the battery cell charged by CC-CV mode. In case the PPC technique is used, taking into account the relationship $A_1 = A_2$, the amplitude of the charging current in the PPC technique can be expressed as follows:

$$A_{PPC} * t_p = A_{CC-CV} * T_p = A_2 \tag{8}$$

For $D = \%50$ duty ratio ($t_p = T_p/2$) in Equation 8, $A_{PPC} = 1C$ is obtained. With the use of the proposed AHWPC technique in the battery cell charging process and with the relationship $A_1 = A_3$ taken into account, the amplitude of the charging current can be expressed as follows:

$$\frac{A_{AHWPC}}{\pi} = A_{CC-CV} * T_p = A_3 \tag{9}$$

In Equation 9, $A_{AHWPC} = 1{,}5708C$ value is obtained. The electrical properties of the battery cell used in the study are given in Table 1.

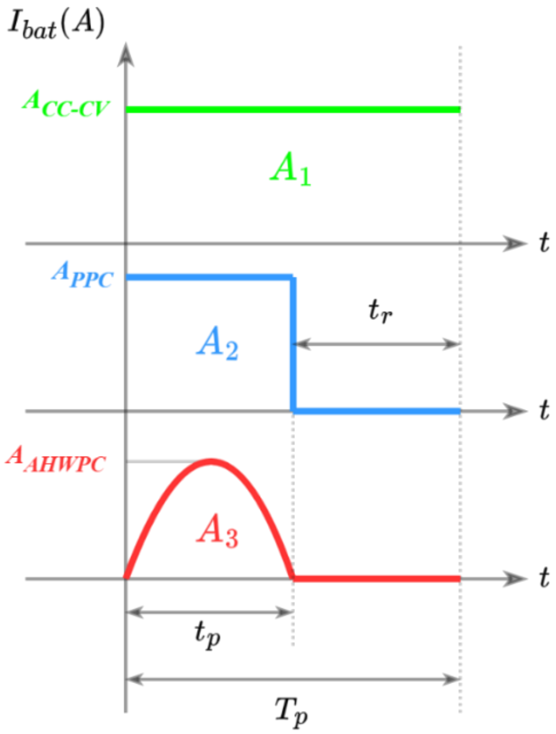

Figure 4: Continuous and pulsed charge current waveforms

Table 1: Electrical parameters of the battery cell

Parameter	Description	Value	Unit
R_{int}	Internal resistance	0.015	Ω
V_{nom}	Nominal voltage	12.8	V
C_{rated}	Rated capacity	40	Ah
$V_{cut-off}$	Cut-off voltage	10.5	V
V_{full}	Fully charged voltage	13.8	V
I_{d-nom}	Nominal discharge current	20	A

Thus, the amplitude of charging current in CC-CV technique is $A_{CC-CV} = 0{,}5C = 20A$, the amplitude of pulsed charging current in PPC technique is $A_{PPC} = 1C = 40A$ and the amplitude of sinusoidal pulsed charging current in AHWPC technique is $A_{AHWPC} = 1{,}5708C = 62{,}83A$.

3. Simulation Methodology

In order to compare the performances of CC-CV, PPC and the proposed AHWPC techniques described in detail in the previous section, the battery aging model available in MATLAB/SIMULINK environment is adopted as a reference.

In the simulation methodology used in this study, the battery cell was subjected to charge and discharge cycles at temperatures of $20°C$, $30°C$ and $40°C$ and at different depths of discharge (DoD) and different discharge rates for 1000 hours. The CC-CV mode simulation methodology for all temperature values is as follows:

$i.$) At $t = 0$, the battery cell with $SoC_{init} = \%100$ begins discharging with a rate of $0.5C$. Here, SoC_{init} represents the initial state of charge. The discharge process continues until $SoC = \%80$ ($DoD = \%20$). Then battery cell is charged at a rate of $0.5C$ until fully charged. This process is repeated for $200h$.

$ii.$) At $t = 200h$, the battery cell is discharged to $SoC = \%20$ and then fully charged again. This cycle is repeated for $200h$.

$iii.$) At $t = 400$, the methodology given in step one is applied again.

$iv.$) At $t = 600h$, the charge current is kept constant at $0.5C$ while the discharge current is increased to $2C$. This means that the battery will be charged with $0.5C$ and discharged with $2C$ in each cycle. These values are applied in the range $\%80 \leq SoC \leq \%100$.

$v.$) At $t = 800h$, the conditions in the first step are applied.

In PPC and AHWPC modes, DoD and discharge rates are applied similarly to the test procedure described above. However, positive and half sinusoidal pulse currents with 50% duty cycle at a frequency of $1Hz$ are applied to charge the battery cell. Figure 6 represents the application of the simulation methodology on the battery cell. In Figure 6, the programmable electronic load and the programmable DC power supply are connected to the battery cell via switches S_1 and S_2, respectively. Here, the programmable electronic load is used in the discharge process of the battery cell, and the programmable DC source is used in the charging process. Ratios of charging and discharging current (i_{ch}, i_{disch}), limit values of charging and discharging current (SoC_{min}, SoC_{max}), ambient temperature ($Ambient\ temp.$) are the data that must be provided externally for this methodology. Throughout the described methodology, the voltage, current, state of charge rate, temperature, aging and capacity values of the cell were measured. Since the charging and discharging processes will vary depending on the SoC when $SoC \leq SoC_{min}$, S_1 is turned on and S_2 is turned off to charge the battery cell with the selected charging rate and charging technique. Similarly, when $SoC \geq SoC_{max}$, S_1 is turned off and S_2 is turned on to discharge the battery cell with the selected discharge rate and DoD. For this study, $SoC_{min} = \%20$ in the fourth step of the test procedure and $SoC_{min} = \%80$ in the other steps. In all test procedures, $SoC_{max} = \%99$. More detailed information about the battery cell used in this study, aging and capacity measurements can be found in the following references [23,24,30]. Figure 7 illustrates the workflow of the simulation methodology.

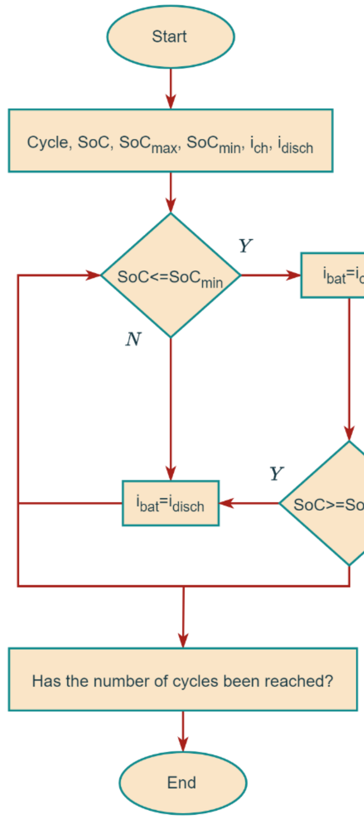

Figure 5: Flowchart of test methodology

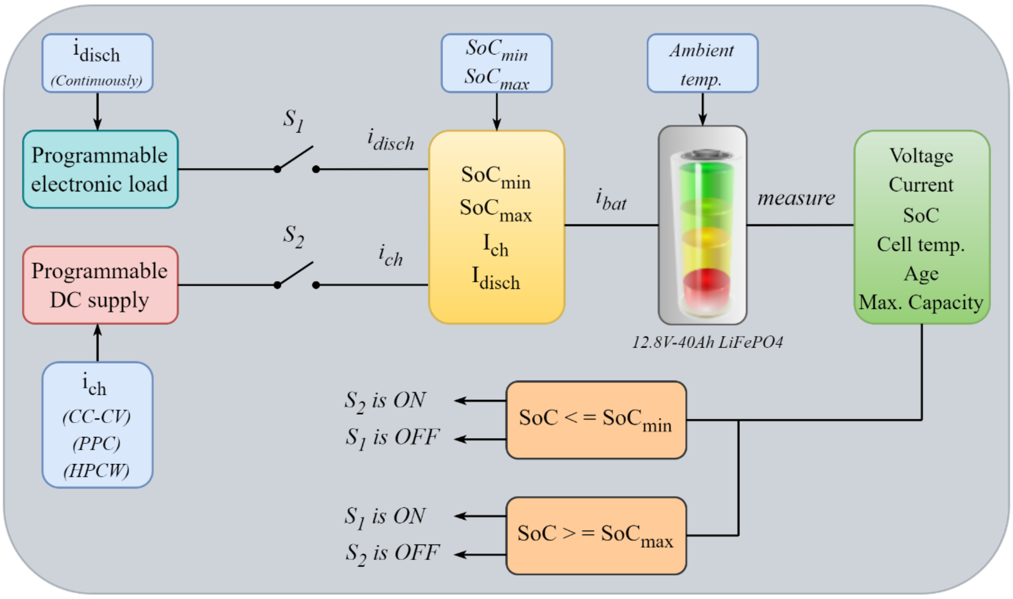

Figure 6: Demonstration of simulation methodology

4. Results and Discussion

Since the main framework of this study is to investigate the effects of pulsed charging currents on cell aging and capacity loss, the discharge currents are the same and continuous for all charging techniques. Five different cases were performed in each cycle as described in the test procedure. In addition, the effect of pulsed charging profiles at different temperatures was also investigated. The current profiles used for all temperature values are shown in Figure 8. The regions marked with the numbers i, ii, iii, iv, and v in Figure 8a represent the steps of the test procedure, respectively. In each of these regions, the specified charging and discharging techniques were applied to the cell for $200h$. As can be seen, the discharge current is the same for all cycles except for region ($i_{disch} = 20A = 0.5C$). In order to show the effect of cell aging, capacity loss and cell temperature at high currents, the discharge current was increased to $i_{disch} = 80A = 2C$ in region iv. The frequency of the pulsed charging currents during the whole cycle was chosen as $f_{i_{ch}} = 1\,Hz$. Although this value is frequently used in previous studies, further analysis on frequency optimization can improve the performance of pulsed charging techniques. Figure 8b represents a zoom-in view of the charging and discharging profiles applied to the battery cell over the whole cycle for a given period. It can be seen that the charging current, which is $0.5C$ in the CC-CV technique, is $1C$ and $1.5708C$ in the PPC and AHWPC techniques, respectively. As in the current profiles, it was observed that the cell voltages and state of charge were similar for all temperature values throughout the cycle.

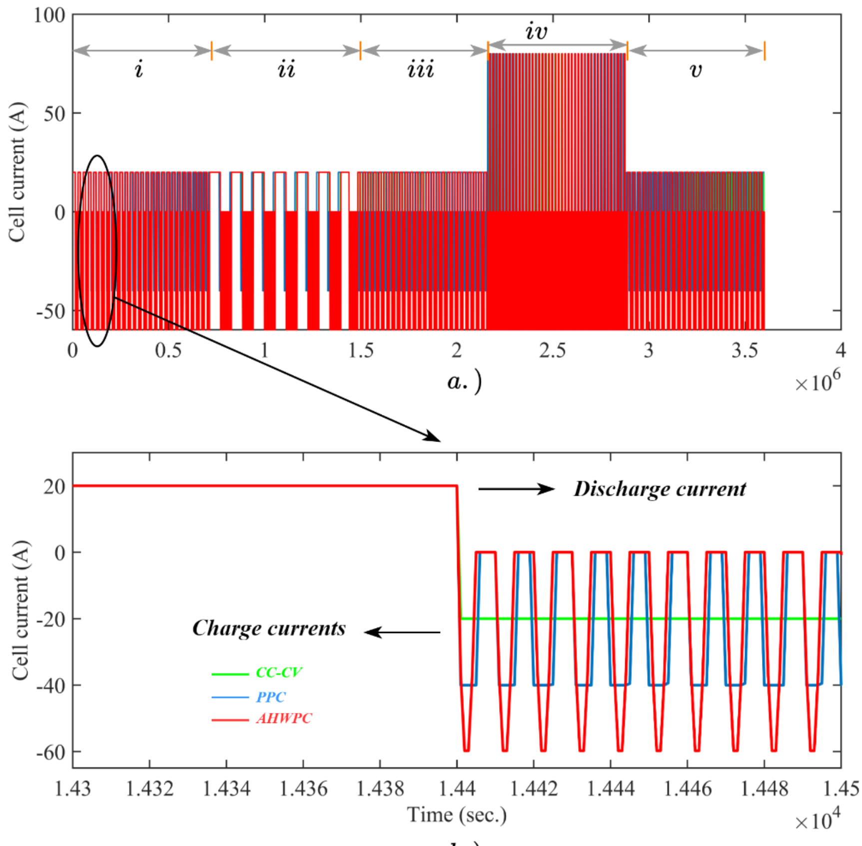

Figure 7: Continuous and pulsed current profiles used in the test procedure

Figure 9a and Figure 9b show the change in cell voltage and SoC, respectively. Due to the long cycle time, zoomed views are also shown at the bottom of the relevant images for a certain period of time to observe the changes clearly. The cell voltage in Figure 9a varies between approximately $13.2V$ and $15.8V$ in the first region. In the second region, by increasing $DoD = \%80$, the cell voltage begins to change more slowly between $12.5V$ and $14.8V$. This is an expected result as the DoD is increased. In the zoomed image in Figure 9a, the change of the cell voltage is similar to the change of the current profile. It can be concluded that this is due to the effect of the internal resistance (IR) of the cell changing at very small intervals. A similar result to the first region was observed in the third and fifth regions. In the fourth region, the cell voltage changed between $12.3V$ and $14.7V$ as the DoD increased to $2C$. When the SoC curves in Figure 9b are examined, it can be observed that the effect of all pulsed charging techniques on SoC is similar. Therefore, the similar changes in cell voltages and SoCs of CC-CV, PPC and the AHWPC techniques show the applicability of the proposed technique. Aging, capacity fade and temperature of the battery charged with the mentioned techniques when the ambient temperature is $20°C$ are shown in Figures 10a, 10b and 10c, respectively. Cell aging in Figure 10a equivalently corresponds to one cycle. Therefore, the battery cell charged with the CC-CV technique completed a full cycle of approximately 16.5145 times at the end of the cycle. It should be noted that a cycle occurs when a fully charged battery cell is first fully discharged and then fully charged again. In the first region (i), all charging techniques exhibit a similar ageing profile. In this region, the CC-CV mode aging factor was measured as 2.321. PPC and AHWPC techniques have an ageing value corresponding to 1.343 cycles in the same region. In the second region (ii), the increase in the aging rate is clearly seen by increasing the DoD to 80%. The aging factors at the end of this region are 6.343 in CC-CV mode and approximately 3.512 in PPC and AHWPC modes. In the third region (iii), it is seen that the aging rate decreases in all charging methods by decreasing the DoD to 20%. At the end of this cycle, the aging in the battery cell was observed to be approximately 8.968, 4.858 and 4.928 in CC-CV, PPC and AHWPC modes, respectively. In the fourth region (iv), the aging values were measured as 14.075, 7.741 and 7.576 in CC-CV, PPC and AHWPC techniques, respectively, as a result of the increase in the aging rate with increasing the discharge current to $2C$. In the fifth region (v), the aging rate decreased when the discharge current was reduced to $0.5C$. At the end of this region, the aging values were observed as 16.514 in CC-CV, 9.063 in PPC, and 8.929 in AHWPC.

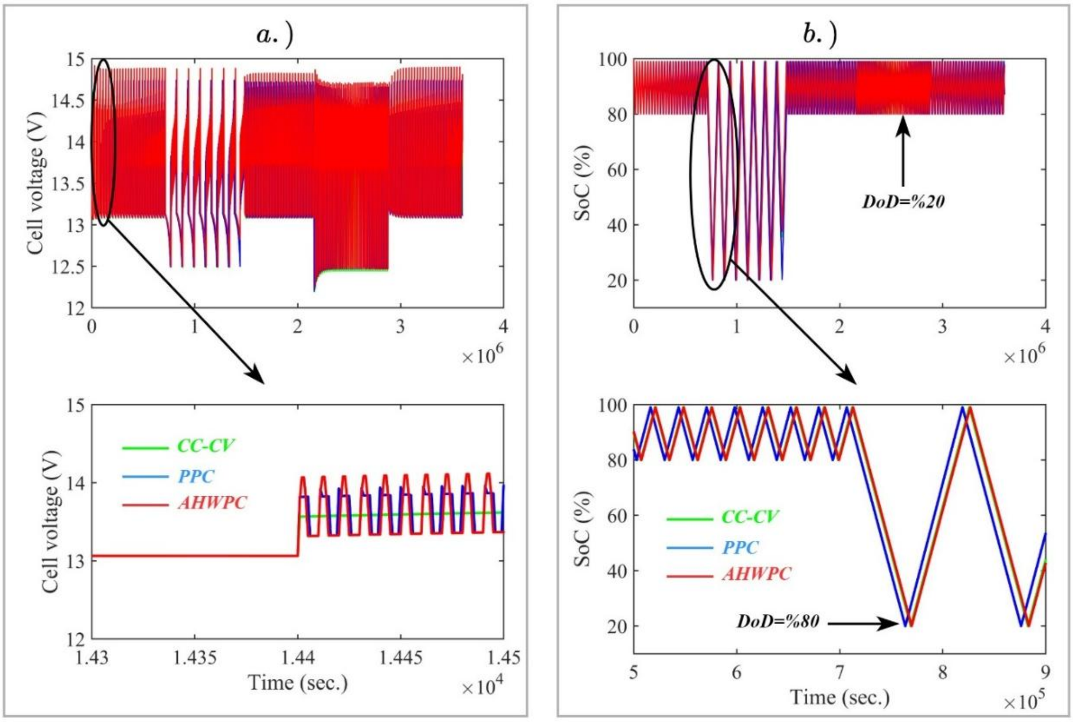

Figure 8: During the test procedure a.) Cell voltage, b.) SoC

Figure 10b represents the capacity losses in the battery cells during the test. It is seen that capacity fade increases rapidly in the regions where aging accelerates. At the end of the simulation, the capacity fades in the battery cell charged by CC-CV, PPC, and AHWPC methods were measured as 0.1826%, 0.1003%, and 0.0987%, respectively. In terms of capacity loss, it can be said that the PPC technique is superior to AHWPC in the second and third regions. In the first region, it can be stated that the capacity loss for both techniques is similar. However, in the fourth and fifth regions, the AHWPC technique outperformed PPC. The AHWPC technique will increase this superiority further if the charge and discharge cycles continue. Figure 10c shows the temperature change of the battery cell as a result of applying the relevant charging techniques to the battery cell at $20°C$ ambient temperature. In the first, second, and third regions, the cell temperature increased by approximately 35%. It is seen that the charging techniques have no significant effect on the cell temperature. However, by increasing the discharge current from $0.5C$ to $2C$ (region v), the cell temperature increased from $27°C$ to $37°C$. In addition, changing the DoD did not cause a significant change in battery cell temperature. The aging, capacity loss, and temperature of the battery charged by the aforementioned techniques at the ambient temperature of $30°C$ are shown in Figures 11a, 11b, and 11c, respectively. In the aging curves in Figure 11a, it is seen that aging is similar for all three techniques in the first region. In this region, the full cycle equivalent aging values were measured as 2.836, 1.596, and 1.645 for CC-CV, PPC, and AHWPC techniques, respectively. In the first region, the PPC technique outperformed the other two techniques. At the end of the second region, the aging effect, which was 8.376 in the CC-CV technique, and 4.539 in the PPC and the AHWPC techniques. At the end of the third region, similar to the second region, the aging rate increased in CC-CV while it was lower in PPC and AHWPC techniques. The proposed AHWPC mode is superior to the other two methods in the fourth and fifth regions. The aging values at the end of the cycle were 20.244 for CC-CV, 11.175 for PPC, and 10.816 for AHWPC. The capacity curves in Figure 11b show that the capacity loss in PPC and AHWPC techniques in the first, second, and third regions are similar, and they perform better than the CC-CV technique.

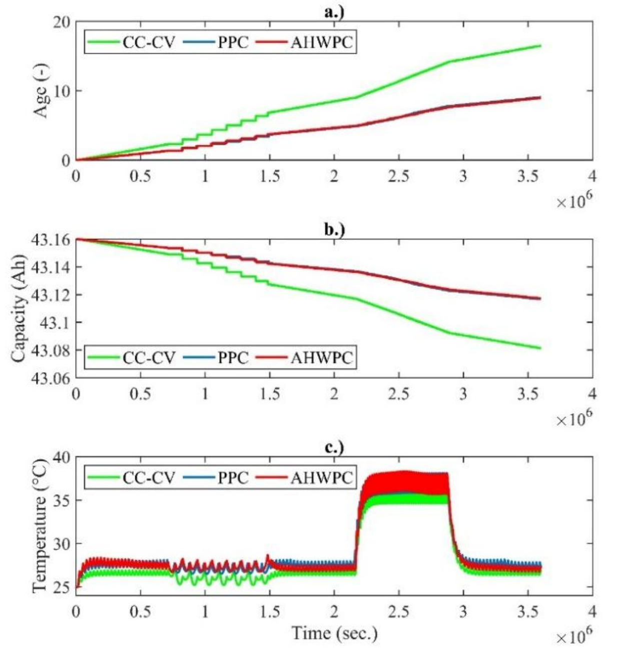

Figure 9: Simulation results, a.) Age, b.) Capacity fade, c.) Cell temperature (20 °C)

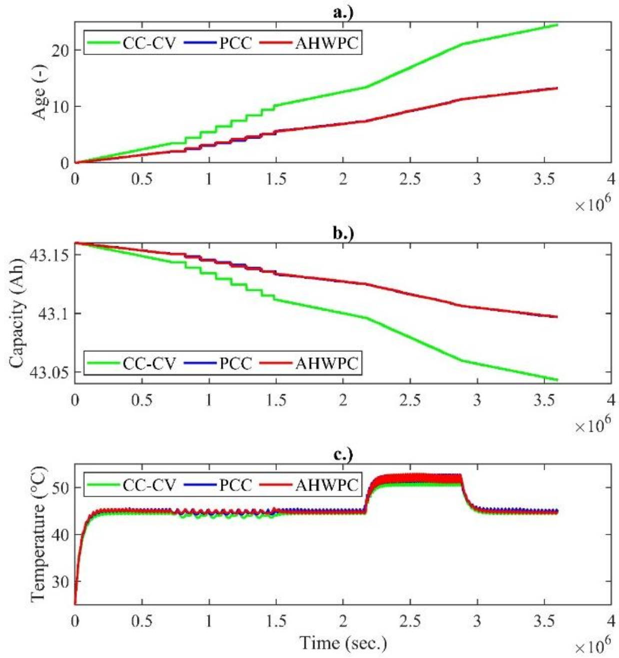

Figure 11: Simulation results, a.) Age, b.) Capacity fade, c.) Cell temperature (40 °C)

The proposed AHWPC technique was outstanding compared to the other methods in the fourth and fifth regions. In the fourth region, the maximum capacities were observed at 43.063 for CC-CV, 43.106 for PPC, and 43.108 for AHWPC.

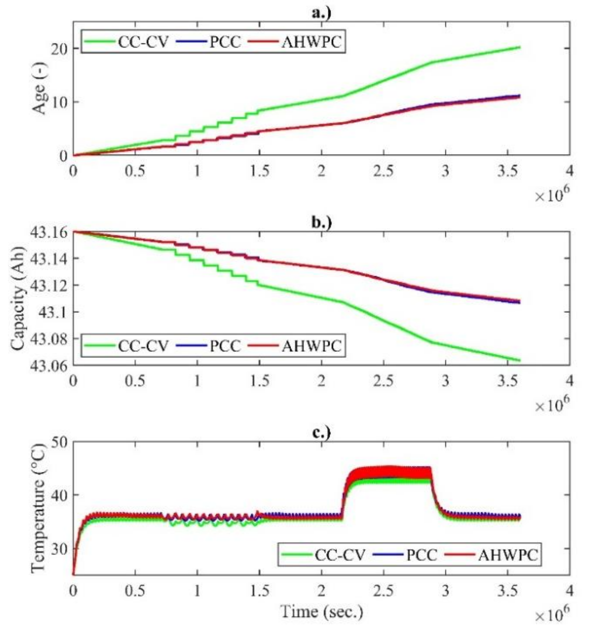

Figure 10: Simulation results, a.) Age, b.) Capacity fade, c.) Cell temperature (30 °C)

The capacity losses at the end of the cycle were calculated at 0.2238% for CC-CV, 0.1235% for PPC, and 0.1196% for AHWPC. In the cell temperature curves in Figure 11c, it is approximately $36°C$ in the first, second, and third regions. In this case, cell temperatures have increased by approximately 20%. However, it can be said that CC-CV performs better in terms of cell temperature, although at a low level. The aging, capacity loss, and temperature of the battery charged with the abovementioned techniques at $40°C$ ambient temperature is shown in Figures 12a, 12b, and 12c, respectively. When the aging curves in Figure 12a are examined, PPC and AHWPC exhibited similar results throughout the test procedure. In CC-CV, the aging rate increased even more with the increase in temperature. At the end of the simulation cycle, the equivalent full-cycle aging values were measured as 24.519 for CC-CV, 13.231 for PPC, and 13.167 for AHWPC. When the capacity losses in Figure 12b are evaluated, it is seen that PPC and AHWPC techniques outperform CC-CV. While the capacity loss in CC-CV is approximately 0.2711%, this value is 0.1464% in PPC and 0.1457% in AHWPC. In the cell temperature variations in Figure 12c, it can be said that the charging techniques yield similar results.

Table 2 summarizes the aging and maximum capacity retention of the battery under different charging techniques and temperatures. The lowest aging and highest capacity retention values, marked in bold, indicate the superior performance of AHWPC. As can be seen, the proposed AHPWC technique exhibited superior results compared to the other two methods in both maintaining the maximum capacity and delaying the aging effect. The aging curves of the charging techniques for different temperature values used in the simulation procedure are shown in Figure 13.

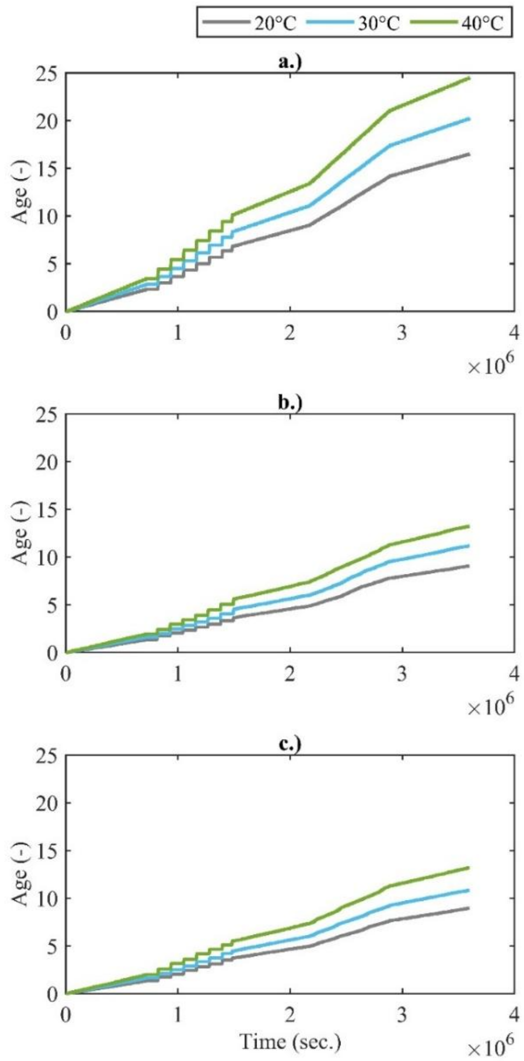

Figure 12: The aging effect of the battery cell at different temperatures a.) CC-CV, b.) PPC, c.) AHWPC

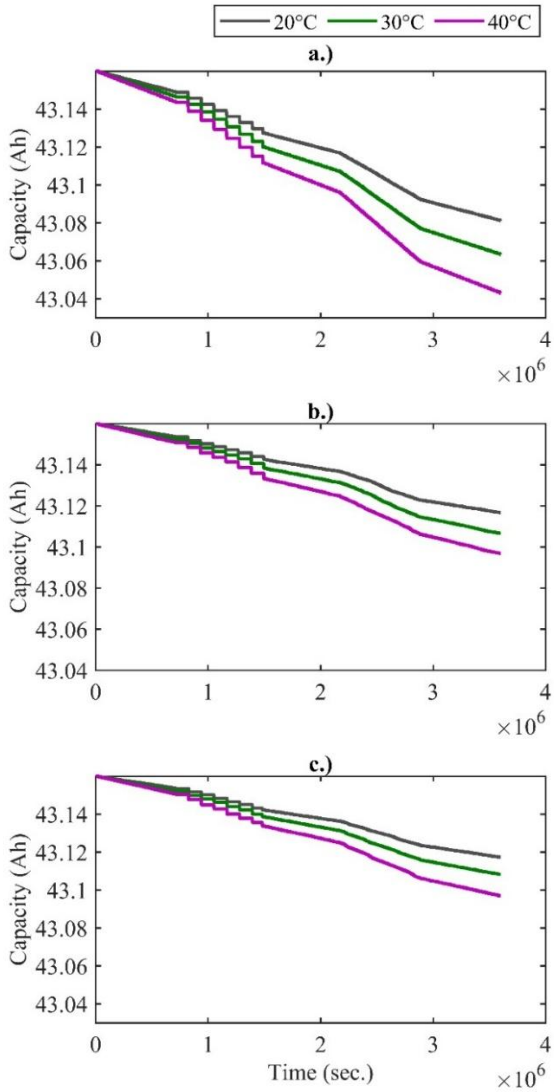

Figure 13: The capacity fades of the battery cell at different temperatures a.) CC-CV, b.) PPC, c.) AHWPC

These curves can also be obtained separately from the previous results. However, to demonstrate the superiority of the proposed AHWPC technique over PPC and CC-CV techniques, it is thought that comparing the performances of the same charging technique under different temperature values will emphasize the importance of the study. Figures 13a, 13b, and 13c show the aging performances of CC-CV, PPC, and AHWPC charging techniques at $20°C$, $30°C$, and $40°C$ ambient temperatures, respectively. As a result of completing the test cycle at $20°C$ ambient temperature with the CC-CV technique, the aging value of the battery cell corresponded to a cycle number of approximately 16.514.

By increasing the ambient temperature to $30°C$, this value increased by 18.425% compared to $20°C$. In the same technique, this rate increased to 32.648% when increasing the ambient temperature to $40°C$. According to the aging curves of the PPC technique in Figure 13b, the aging value at $20°C$ ambient temperature was measured to be equivalent to 9.063 cycles. By increasing the ambient temperature to $30°C$, the aging value increased by 18.899%. In the same technique, this rate increased to 31.501% when increasing the ambient temperature to $40°C$. When the aging curves of the AHWPC technique in Figure

13c are evaluated, the aging value at $20°C$ was measured as 8.929.

The aging value increased by 17.446% in the same technique at $30°C$ ambient temperature, and this rate increased to 32.186% at $40°C$ ambient temperature. Figure 14 shows the maximum capacity curves of the battery cell charged by CC-CV, PPC, and AHWPC techniques at different ambient temperatures. According to the results obtained by using the CC-CV technique in Figure 14a, the maximum capacity values were measured as 43.081, 43.063, and 43.043 at $20°C$, $30°C$ and $40°C$ ambient temperatures, respectively. These values are observed as 43.116, 43.106, and 43.096 in the curves of the PPC technique in Figure 14b, respectively. The results of the AHWPC technique in Figure 14c showed that the maximum capacities were 43.117 at $20°C$, 43.108 at $30°C$, and 43.097 at $40°C$. Since the numerical results in Table 2 are pretty close, comparing charging techniques may not be easy. Figure 15 compares the numerical results obtained from this study more clearly.

Table 2: Numerical test results

	Temperature (°C)					
	20		30		40	
	Age	Capacity	Age	Capacity	Age	Capacity
$CC-CV$	16.5145	43.0812	20.2448	43.0634	24.5196	43.0430
PPC	9.06535	43.1167	11.1754	43.1067	13.2316	43.0968
$AHWPC$	**8.92912**	**43.1174**	**10.8163**	**43.1084**	**13.1675**	**43.0971**

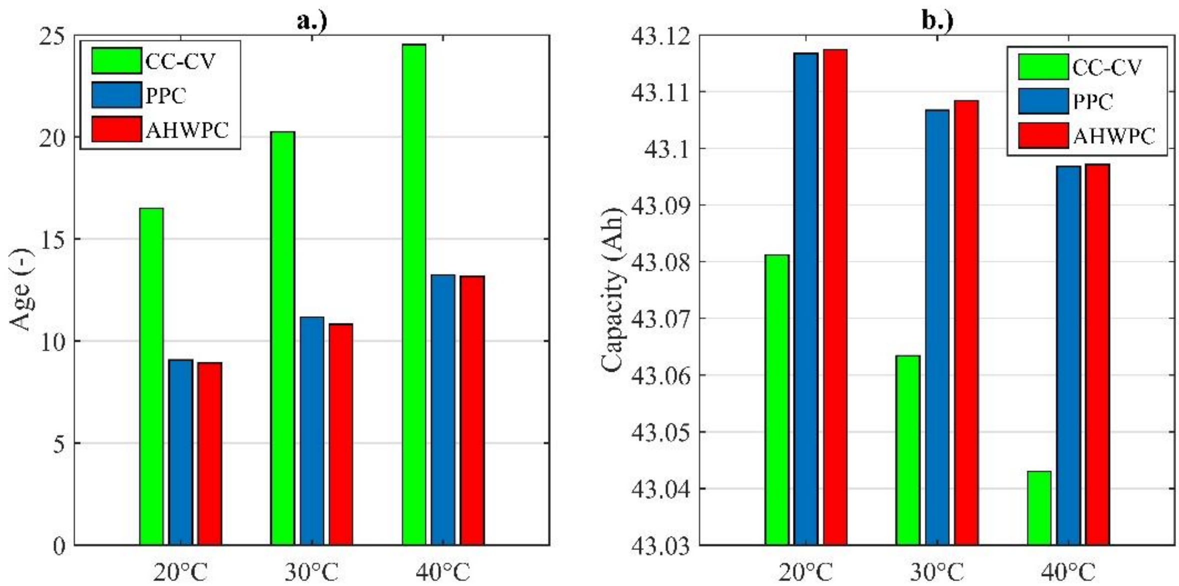

Figure 14: Effects of charging techniques at different temperatures a.) Age, b.) Maximum capacity

Figure 15a compares aging values for all charging techniques at the temperature values selected for this study. As seen, aging increases as temperature increases for all three techniques. However, it can be said that the CC-CV technique is more sensitive to temperature, and the aging rate rises more than that of the other two techniques as the temperature increases. Figure 15b represents a visualization of the capacity results obtained by using the relevant charging techniques at selected ambient temperatures. As the ambient temperature increases, the capacity loss in the CC-CV technique increases faster than the other two techniques. Pulsed charging techniques reduce heat accumulation compared to CC-CV mode by preventing continuous high current flow. This reduction in thermal stress is expected to slow down

SEI layer growth, potentially extending battery lifespan. For all three temperature values, the AHWPC technique performed better than the CC-CV and PPC techniques. Continuous charging currents in battery cells cause more thermal runaway. It is also known that suddenly changing the charging current causes more aging. Therefore, the superior performance of the AHWPC technique can be attributed to the smoother rise and fall of the charging current.

5. Conclusion

This paper presents a new pulsed charging technique for reducing aging and capacity losses in LIBs. The proposed AHWPC technique is compared with the CC-CV technique, which is widely used in existing studies, and the PPC technique, which was introduced in recent years to improve fast charging techniques. The three charging techniques mentioned above are compared regarding aging, capacity losses, and cell temperatures on a $12V - 40Ah$ lithium-ion battery. When the results obtained are evaluated together, it is seen that the CC-CV technique shows superior performance only at the cell temperature during the test cycle and is considerably weaker than the other two techniques in terms of aging and capacity fade. Also, it was observed that with increasing ambient temperature, the aging rate and capacity fade in the CC-CV technique increased more than the other two techniques. Although the PPC and the AHWPC techniques had similar aging and capacity fade values throughout the cycle, the AHWPC technique outperformed the PPC technique at all temperature values. At $20°C$, aging in PPC was reduced by approximately 45% compared to CC-CV. AHWPC technique provided a 2% improvement in aging compared to PPC. At $30°C$, PPC reduced cell aging by 44.79% compared to CC-CV, while AHWPC completed the test procedure with 3.21% less aging than PPC. At $40°C$, the PPC technique provided 46.03% superiority over CC-CV, while the AHWPC technique achieved approximately 0.5% lower aging performance than PPC. This result is attributed to the lower LAM and LLI loss in the AHWPC technique due to the smoother change of charging currents. As a result, the AHWPC technique is considered to be a serious competitor to existing charging techniques. The selection of $1\,Hz$ pulse frequency for pulse charging techniques is a limitation of this study. In future studies, the performance of pulse charging currents with different pulse frequencies and duty ratios on aging and capacity losses will be evaluated.

Article Information

Financial Disclosure: The author (s) has not received any financial support for the research, authorship or publication of this study.

Authors' Contrtibution: Concept, Design, Supervision, Resources, Data Collection, Analysis, Literature Search, Writing Manuscript, Critical Review: **Muhammed Reşit ÇORAPSIZ**

Conflict of Interest/Common Interest: No conflict of interest or common interest has been declared by the authors.

Ethics Committee Approval: This study does not require ethics committee permission or any special permission.

References

[1] Amanor-Boadu J. M., Guiseppi-Elie A., Sánchez-Sinencio E., The Impact of Pulse Charging Parameters on the Life Cycle of Lithium-Ion Polymer Batteries, Energies, 11 (8), 2162, 2018.

[2] Lithium-ion Battery Market. https://www.precedenceresearch.com/lithium-ion-battery-market#:~:text=The%20Asia%20Pacific%20lithium%2Dion,with%20revenue%20share%20of%2047%25.

[3] Su X., Xu X.-P., Ji Z.-Q., Wu J., Ma F., Fan L.-Z., Polyethylene Oxide-Based Composite Solid Electrolytes for Lithium Batteries: Current Progress, Low-Temperature and High-Voltage Limitations, and Prospects, Electrochemical Energy Reviews, 7 (1), 2, 2024.

[4] Gielinger S., Hein T., Ziegler A., Oeser D., Breitfelder S., Bohn G., A Short Time Expansion Measurement Method for the Detection of Aging Effect of Lithium Ion Cells Using a High Resolution Laser Interfometric Setup, IEEE Access, 11, 139924-139934, 2023.

[5] Diolaiti V., Andreoli A., Chauque S., Bernardoni P., Mangherini G., Ricci M., Zaccaria R. P., Ferroni M., Vincenzi D., Comparison of Porous Germanium Thin Films on SS and Mo as Anode for High-Performance LIBs, IEEE Transactions on Nanotechnology, 22, 552-557, 2023.

[6] Huang X., Liu W., Meng J., Li Y., Jin S., Teodorescu R., Stroe D. I., Lifetime Extension of Lithium-Ion Batteries With Low-Frequency Pulsed Current Charging, IEEE Journal of Emerging and Selected Topics in Power Electronics, 11 (1), 57-66, 2023.

[7] Huang X., Meng J., Liu W., Ru F., Duan C., Xu X., Stroe D. I., Teodorescu R., Lithium-Ion Battery Lifetime Extension With Positive Pulsed Current Charging, IEEE Transactions on Industrial Electronics, 71 (1), 484-492, 2024.

[8] Yan H. W., Farivar G. G., Beniwal N., Tafti H. D., Ceballos S., Pou J., Konstantinou G., Battery Lifetime Extension in a Stand-Alone Microgrid With Flexible Power Point Tracking of Photovoltaic System, IEEE Journal of Emerging and Selected Topics in Power Electronics, 11 (2), 2281-2290, 2023.

[9] Lv H., Huang X., Liu Y., Analysis on pulse charging–discharging strategies for improving capacity retention rates of lithium-ion batteries, Ionics, 26 (4), 1749-1770, 2020.

[10] Chen P.-T., Yang F.-H., Cao Z.-T., Jhang J.-M., Gao H.-M., Yang M.-H., Huang K. D., Reviving Aged Lithium-Ion Batteries and Prolonging their Cycle Life by Sinusoidal Waveform Charging Strategy, Batteries & Supercaps, 2 (8), 673-677, 2019.

[11] Li H., Zhang X., Peng J., He J., Huang Z., Wang J., Cooperative CC–CV Charging of Supercapacitors Using Multicharger Systems, IEEE Transactions on Industrial Electronics, 67 (12), 10497-10508, 2020.

[12] Lee Y. D., Park S. Y., Electrochemical State-Based Sinusoidal Ripple Current Charging Control, IEEE Transactions on Power Electronics, 30 (8), 4232-4243, 2015.

[13] Zhu S., Hu C., Xu Y., Jin Y., Shui J., Performance improvement of lithium-ion battery by pulse current, Journal of Energy Chemistry, 46, 208-214, 2020.

[14] Huang X., Li Y., Acharya A. B., Sui X., Meng J., Teodorescu R., Stroe D.-I., A Review of Pulsed Current Technique for Lithium-ion Batteries, Energies, 13 (10), 2458, 2020.

[15] Tang A., Gong P., Huang Y., Wu X., Yu Q., Research on pulse charging current of lithium-ion batteries for electric vehicles in low-temperature environment, Energy Reports, 9, 1447-1457, 2023.

[16] Chen L. R., Wu S. L., Shieh D. T., Chen T. R., Sinusoidal-Ripple-Current Charging Strategy and Optimal Charging Frequency Study for Li-Ion Batteries, IEEE Transactions on Industrial Electronics, 60 (1), 88-97, 2013.

[17] Li J., Murphy E., Winnick J., Kohl P. A., The effects of pulse charging on cycling characteristics of commercial lithium-ion batteries, Journal of Power Sources, 102 (1), 302-309, 2001.

[18] MOLICEL Lithium-ion Rechargeable Battery Cell Characteristics. https://www.molicel.com/wp-content/uploads/INR18650M35A-V2-80096.pdf. 29.02.2024.

[19] ORION 18650P/25 Lithium Ion Cell. https://static.ticimax.cloud/37661/uploads/dosyalar/orion-18650p-2500.pdf. 29.02.2024.

[20] Keil P., Jossen A., Charging protocols for lithium-ion batteries and their impact on cycle life—An experimental study with different 18650 high-power cells, Journal of Energy Storage, 6, 125-141, 2016.

[21] Savoye F., Venet P., Millet M., Groot J., Impact of Periodic Current Pulses on Li-Ion Battery Performance, IEEE Transactions on Industrial Electronics, 59 (9), 3481-3488, 2012.

[22] Abdel-Monem M., Trad K., Omar N., Hegazy O., Van den Bossche P., Van Mierlo J., Influence analysis of static and dynamic fast-charging current profiles on ageing performance of commercial lithium-ion batteries, Energy, 120, 179-191, 2017.

[23] Tremblay O., Dessaint L. A., Dekkiche A. I., A Generic Battery Model for the Dynamic Simulation of Hybrid Electric Vehicles, 2007 IEEE Vehicle Power and Propulsion Conference, 284-289, 9-12 Sept. 2007.

[24] Omar N., Monem M. A., Firouz Y., Salminen J., Smekens J., Hegazy O., Gaulous H., Mulder G., Van den Bossche P., Coosemans T., Van Mierlo

J., Lithium iron phosphate based battery – Assessment of the aging parameters and development of cycle life model, Applied Energy, 113, 1575-1585, 2014.

[25] Yang F., Wang D., Zhao Y., Tsui K.-L., Bae S. J., A study of the relationship between coulombic efficiency and capacity degradation of commercial lithium-ion batteries, Energy, 145, 486-495, 2018.

[26] Dubarry M., Liaw B. Y., Identify capacity fading mechanism in a commercial LiFePO4 cell, Journal of Power Sources, 194 (1), 541-549, 2009.

[27] Rajagopalan Kannan D. R., Weatherspoon M. H., The effect of pulse charging on commercial lithium nickel cobalt oxide (NMC) cathode lithium-ion batteries, Journal of Power Sources, 479, 229085, 2020.

[28] Li Q., Tan S., Li L., Lu Y., He Y., Understanding the molecular mechanism of pulse current charging for stable lithium-metal batteries, Science Advances, 3 (7), e1701246, 2017.

[29] Kopczyński A., Liu Z., Krawczyk P., Parametric analysis of Li-ion battery based on laboratory tests, E3S Web Conf., 44, 00074, 2018.

[30] 12.8 V, 40 Ah, Lithium-Ion (LiFePO4) Battery Aging Model (1000 h Simulation). https://www.mathworks.com/help/sps/ug/12-8-v-40-ah-lithium-ion-lifepo4-battery-aging-model-1000-h-simulation.html. 17.03.2024.

J Inno Sci Eng, 2024, 9(1):118-133

DOI:https://doi.org/ 10.38088/jise.1617193

Research Article

Damage Assessment of Urban Interface Masonry Buildings after a Severe Wildfire along with a Comparison of NRC-2018

Aslan Soyer [1], Hamid Farrokh Ghatte [1*]

[1] *Department of Civil Engineering, Antalya Bilim University, Antalya, Türkiye*

ARTICLE INFO

Received Date: 14/01/2025
Accepted Date: 18/02/2025

Cite this paper as:
Soyer, A. and Ghatte, H.F. (2025). *Damage Assessment of Urban Interface Masonry Buildings after a Severe Wildfire along with a Comparison of NRC-2018.* Journal of Innovative Science and Engineering. 9(1): 118-133

*Corresponding author: Hamid Farrokh Ghatte
E-mail:ghatte@itu.edu.tr

Keywords:
Buildings
Damage
Failure mechanism
Masonry
Wildfire

ABSTRACT

The wildland-urban interface (WUI) has emerged as a focal point of wildfire management and community resilience efforts worldwide. The WUI, defined as areas where settlement reaches natural landscapes, presents a unique set of challenges for wildfire mitigation. On the other hand, the performance of the buildings throughout the fire and the provision of proper fire safety measures for structural members is one of the essential aspects of the design of buildings and infrastructures. This study attempts to emphasize the seriousness of the wildfire effects on the WUI in the Mediterranean neighborhood, especially in Turkey. For this purpose, the efficiency of the extreme heat throughout the wildfire on masonry buildings in Manavgat, Turkey (July-August 2021) was investigated in terms of performance and structural damages. Failure mechanisms and the damages that occurred during the wildfire are reported for masonry buildings as the main structural system in this neighborhood. Commonly used technical documents of a national guide for WUI fires presented by the National Research Council Of Canada (NRC- 2018) were employed to compare the condition of the buildings. Turkish standards do not cover wildfire conditions in terms of the WUI buildings. The influences of the materials, the type of cladding, and various types of roofs were investigated in masonry buildings. For this purpose, 121 masonry buildings in Manavgat, Turkey were examined in terms of performance and damage. Furthermore, a comparison of the data with WUI-NRC (2018) is represented to investigate some serviceable recommendations based on the investigation to reduce damages in buildings subjected to wildfire. Finally, an introduction to have detailed written local WUI regulations for masonry buildings to have enough safety in terms of life and economy.

1. Introduction

During the dry seasons, worldwide is subjected to combustible vegetation which can destroy everything. Minimizing the risk to human lives as well as improving the engineering measures of resistance of buildings to the effects of intense radiant heat, burning embers, and flame contact is a vital topic. The outcomes are reducing future property repair, reconstruction costs, and other costs of residential displacement. Furthermore, improving public health, especially those related to deaths, non-fatal injuries, and posttraumatic stress disorder, fewer job losses, and some job creation. Generally, the measures that are recommended to improve the wildfire resistance of buildings typically focus on the materials, design features, and fuel sources close to the building. A series of factors influence wildfire that it is not easy to keep under control, such as weather conditions (wind in terms of speed and direction; humidity; temperature) [1]. Wildfires can destroy the buildings and infrastructure of a subject community. On the other hand, several factors can influence building through wildfires, including its location, the material's flammability, and the design and building materials [2].

In the wildland areas, fire protection of the buildings is one of the main issues. So many design codes consider the safety of the buildings in case of fire, however, the current design codes and investigations in the field of construction and structural systems are mainly based on dead load, live load, wind, and snow as well as seismic actions to improve their performance for these purposes [3-5]. Another main issue is the consideration of fire since the ability of the construction materials to maintain their strength and the structures to preserve their stability throughout the fire have the same importance as well. Not only the investigations related to building damage in wildfires are superficial and extremely limited but also there are no recommendations based on the current design regulations [6]. The main focus in literature in the field of the performance of buildings during a fire is the use of models of buildings as well as the examination of conditions exposed to the fire [7-9]. Improving the performance of structural panel core materials against fire has been investigated by Li et al. [7] and the results showed the use of flame-retardant adhesives can lead to a proper safety level of fire. The effect of geometry and dimensions on the upward fire spread in U-shaped structures has been investigated by Chen et al. [9] and the study provides a guideline for the fire protection design. In another investigation, the performance of a steel structural system has been evaluated by Bailey et al. [10] in terms of structural stability. The tests showed that existing fire codes are not addressing the proper building behavior during a fire and, consequently, are highly conservative. Similarly, an investigation has been conducted by Wald et al. [11] based on the distribution of forces within different structural members of a steel-concrete composite frame construction through the fire test. The results demonstrate the performance of the structures subject to real fires is generally better than that predicted by standard tests. Foster et al. [12] investigate the thermal and structural performance of a full-scale composite building subject to a severe compartment fire. The output of the extended sensitivity studies showed the influence of extra protection on the connection areas of the beams, and the efficiency of different types of supports. As mentioned before the damage assessment of the buildings mainly focused on earthquakes in the literature [13-15]. However, the detailed damage assessment studies provide examples of deficiencies observed in various buildings not only in structural elements but also in nonstructural elements. On the other hand, the countries are updating their codes and standards by introducing performance-based fire safety design provisions. Considering the fire protection and materials as well as the modeling by using different methods, a series of studies have been done to estimate or understand their performance throughout the fire [16- 19]. A group of investigations has been done on the structural performance and behavior of the structural elements tested in terms of flexural and shear responses of prestressed concrete elements under fire conditions, as well as the fire behavior of hollow-core concrete slabs [20 and 21]. As an output of the parametric study, the authors proposed a simplified approach for evaluating the shear capacity of slabs under fire conditions. Furthermore, the numerical and experimental results demonstrate the fire performance of HPLWC hollow core slabs influenced dry curing conditions in reducing the spalling as well as growing the fire resistance capacity [21]. In the case of the high-temperature effects on masonry and stone building materials, Gomez-Heras et.al. [22] tried to show the need for the immediate effects and the long-term management issues of natural stone buildings that have experienced a fire. Similarly, Vasanelli et.al. [23] investigate the efficiency of the high temperature on stone building materials. The outputs were mainly in terms of compromising the aesthetic features of the tested stones, through the color changes.

Considering the density distribution of fire loads, Barnett et.al. [24] conducted a study in school buildings and statistical modeling. The results suggest that fire load selection for design should be better based on local data and a careful review of the unified approach in the international fire engineering guidelines is warranted.

As a result of the increase in urbanization and development in the wildlands, the risk of wildfire and associated hazards will increase as well. Therefore the Wildland-Urban Interface (WUI) regulations and guidelines are indispensable subject matter where developed lands meet or intermingle wildland vegetation. Otherwise, the constructions and structures will be subjected to a higher risk of wildfire and associated hazards. Various regulations have been developed and implemented to mitigate these risks to manage WUI areas. The main objectives of the National WUI guide considering construction are not only to prevent ignition but also to reduce the risk of wildfire in WUI areas by promoting fire-resistant building practices and managing development [25 and 26]. Satisfying the National WUI Guide's recommendations appears to offer benefits that greatly exceed its costs. The benefits come from avoiding future property and life-safety losses. Among the documents for approaching the various aspects of wildfires, one of the common guidelines for the wildland-urban interface areas is presented by the National Research Council Of Canada (NRC) in 2018 [25]. NRC 2018 represented a national guide for WUI fires; a document for use by qualified experts. In addition, standard test methods for resistance to wildfire penetration of door assemblies, and exterior windows are represented [27-30]. The Turkish standard (regulation on fire protection of buildings-2007) presents documents for fire prevention and extinguishing measures to be taken in all kinds of structures, buildings, facilities, and indoor or outdoor establishments in Turkey without any recommendation related to the wildfire condition [31]. Among the effective factors for ignition in Turkey, and all over the world population density, distance from the roads, close to residential areas, elevation, and intensive human activity are the main reasons. Furthermore, the weather conditions and strong winds during the dry seasons are the main reasons for the spreading of wildfires [32 and 33].

In light of the above-mentioned literature review, it is crystal clear that understanding the effect of fire on existing buildings and materials nowadays is one of the most critical topics considering climate change and wildfires all over the world. Furthermore, a deficiency in better understanding and characterizing the effectiveness of different mitigation actions related to individual building features and community layout on the resilience of a WUI community to fire is another issue. In this paper, the results of 121 masonry buildings in Manavgat, Turkey were examined in terms of the performance and building damage conditions exposure to the wildfire. Furthermore, the behavior of different construction materials is investigated based on the deadliest wildfires that occurred in Turkey in July-August 2021. On the other hand, another vital topic after a wildfire is the seismic performance of the existing buildings considering the efficiency of fire on the material and different elements of the buildings. View the fact that the behavior of the building's structural systems will not be the same before and after wildfire if they are subject to seismic actions and the structural systems should carefully control and check after a wildfire. The differences in construction practices between Canada and North America and Turkey reflect different cultural, economic, and historical parameters. Although both regions consider a high priority on building safe and sustainable structures, materials and design codes can vary depending on local conditions and practices. The technical documents of a national guide of WUI were employed in this study to clarify more details of the condition of the buildings. The local recipes had a great impact on relief during the last wildfire in Manavgat, Turkey in terms of general rules and limitations for the access lines and keeping the fire under control. However, the lack of detailed written regulations for WUI buildings and infrastructures in Turkey is a necessity to have enough safety in terms of life and economy. Therefore, it seems establishing a basic guideline for wildfire and protection methods, especially in Turkey will prevent or reduce the efficiency of wildfires on buildings.

2. Buildings and Construction Materials in Fires

Lightning, damaged power cables, and people's activities are the main reasons for a wildfire that can spread uncontrollably, destroying a large residential area. The performance of a building subjected to fire relies on different parameters, including materials, temperature improvement, and the continuance of fire. A nominal fire is represented as a curve of gas temperature with time (e.g., ISO 834-1). A simplified method can be employed for the prediction of the gas temperatures, such as one or two-zone models. Nominative fires are usually used for design purposes. In structural design, fire is treated differently all over the world, where the material is so talented to burn the efficiency is considered higher than in other places where this capacity is not that high. Buildings exposed to fire loads mainly are examined in the ultimate conditions, and it is sufficient to only analyze parts of the building without the need to examine the whole generally without consideration of wildfire. The above-mentioned analysis and the studies related to the analysis of characteristics of the WUI area could help managers to figure out the specific fuel treatment and thinning prescription development [34].

In the case of construction materials, any standards have a summary of the properties, behavior, and strategies represented to improve the resistance of fire for any construction materials composing the structural systems of the buildings. The efficiency of a fire on the performance of materials can also be identified as the effects of fire actions directly and indirectly. In the following section, the behavior of concrete, steel, timber, and masonry materials was discussed mainly in terms of building materials. On the other hand, the main difference between the structural damage caused by normal fires and wildfires is in terms of intensity heat and duration. The wildfire duration, heat, and intensity are generally more than normal fire and mainly can be kept easily under control.

2.1. Concrete and Reinforced Concrete Expose to the Fire

The behavior of concrete is directly related to aggregates, cement, and water. For reinforced concrete, the behavior of rebars will be another issue. The low thermal conductivity caused it to be considered to be non-combustible. Below 500 ◦C the temperature of concrete is not affecting on concrete strength while above 500 ◦C, the compressive strength of concrete begins to reduce based on the direct fire effect. This reduction of strength is higher in the case of high-strength concrete. In terms of modulus of elasticity the same condition is happening and it will reduce with an increase in temperature, mainly at temperatures lower than 200 ◦C. By cooling down the temperatures of concrete, it starts to regain the main part of its strength. Rebars are protected by the cover concrete if it is still in place. The critical consideration is by spalling the cover this efficiency cannot be available anymore. When they are exposed to fire, their yield strength is reduced dramatically above 400 ◦C. When rebars cool down, they regain the main part of their strength [24]. The color of the concrete after exposure to the fire can give a good estimation of the temperature of the surfaces. Although there is no real color change below 300 ◦C, above 300 ◦C, and below 600 ◦C, the color can be almost pink; between 600 and 900 ◦C, the color can change to gray; and above 900 ◦C it is buff-yellow. Smutting of the concrete can appear even below 300 ◦C. By increasing the temperature if thermal expansion is restrained the probability of the large axial forces will increase. Spalling of the cover concrete is the main damage type that can occur in reinforced structures and cause the corrosion of rebars. The pore pressure in the cement paste is the main reason for this phenomenon. Diagonal cracking in continuous beams, sagging of beams and slabs, and cracking of columns are other kinds of damage. It should be noted that by increasing the cover thickness the protection capacity of the rebars increases. Additionally, using fire-resistant materials can increase the capacity and safety of the buildings exposed to fire.

2.2. Masonry Buildings Expose to the Fire

Generally, masonry buildings had better performance than reinforced concrete, steel structures, or timber structures while exposed to fire. This leads to flaking and discoloration of the layers especially the outer layer generally happening in the masonry building exposed to high temperatures. The material that has low porosity experiences more disruption than the material with is porous. Bricks above 400 ◦C experience decreasing strength as well as the modulus of elasticity. The direct fire action is based on both shoot deposition and thermal oxidation of iron-containing minerals [26]. The starting of thermal oxidation can happen at temperatures around 250-300 ◦C. In masonry buildings, various minerals produce different types of colors. Although this kind of action does not destroy the stability of the building, it may change its appearance.

2.3. Timber Structures Expose to the Fire

Although the sustainability of timber building is one of the main reasons for increasing global demands in recent decades due to the combustible capacity of wood, timber structures, and timber materials are vulnerable to fire. When a timber structure is exposed to fire, behaves differently based on the heavy and light conditions of timbers. The large-dimension members (heavy timber structures) have better performance compared to the light ones in fires. When the cross-section of a timber element is big the surfaces start to burn and for a long time, it protects the inner wood from burning. The inner moisture of the wood below evaporates above 100 ◦C and at 200 ◦C, the wood starts to thermally decompose. The estimated charring temperature is considered about 300 ◦C [3]. In the case of direct fire action, the modulus of elasticity and strength of wood in timber structures are reduced by increasing the temperature. For increasing the resistance of smaller-dimension members against fire, protective materials such as gypsum boards and fiber cement panels can be employed. All of the wooden plates have poor performance in a fire if they are not protected properly.

2.4. Steel Structures Expose to the Fire

Generally, steel elements are relatively thin with high thermal conductivity compared to other building materials. The steel members mainly perform poorly if they are subjected to fire. The yield strength and modulus of elasticity of steel drop dramatically at 300 ◦C. In the case of direct fire action, stiffness, as well as strength, decrease almost to half the values. Furthermore, the restriction of thermal expansion causes large deformation and buckling of the steel elements. The mechanical properties like strength and modulus of elasticity return to their initial conditions after cooling down when the temperature does not exceed 700 ◦C. When the steel elements are subjected to temperatures above 700 ◦C for more than 20 min, the process of oxidation will start on the surfaces, as well as loss of the cross-sectional thickness. At temperatures more than 870 ◦C, the features cannot return to the initial conditions. Moreover, the steel elements will have less ductility high strength, and hardness. For aiming the protect steel elements from a fire so many methods are available; the application of certain coatings, encasement with concrete, and enclosure with boards.

3. Wildfire in Manavgat, Turkey

The case study consists of the effects of wildfire in Manavgat-Turkey (July-August 2021) on masonry buildings in terms of structural systems. In the case of the effective factors for ignition in Turkey, as stand before population density, residential areas that were located close to wildlands, elevation, and intensive human activity are the main factors. Additionally, the weather conditions and strong winds during the dry seasons are other main parameters of fire spreading in Turkey.

3.1. Location of the Occurrence of the Wildfire

Manavgat is located in the Antalya region, 75 km away from the city center of Antalya in the southern Mediterranean region (see Figure 1). Manavgat included of 2.283 km² area with a population of 241011 people according to the 2019 datasets. One of the important tourism centers with a 64 km coastline and many ancient and historical places (see Figures 1-3). The wildfire of Manavgat happened in 2021 at four different points on July 28 at 11.30 and spread to some neighborhoods of Akseki, Gundogmus, Ibradi, and Alanya districts. The high temperature (37 centigrade degrees), and low humidity (14%) increased the spreading of the fire immediately. In addition, strong wind blowing (50 km/h) allowed the fire to spread and grow rapidly. The fire spread to 21 different locations just in a day and 59 neighborhoods were severely damaged. After 220 hours of struggling and trying to keep under control it with different methods, it was brought under control at 15.30 on 6 August and the cooling works continued to have a sustainable condition for a few days. Based on the governmental information, 8 aircraft, 2 UAVs, 19 helicopters, 2 management helicopters, 1 unmanned helicopter, 1915 vehicles, and 8,155 personnel took part in the fight against the wildfire. Additionally, a large number of volunteer citizens came to the area to help the people subjected to the wildfire. As a result of the wildfire; 7 people lost their lives, 821 people were affected by smoke, thousands of hectares of forest and agricultural land areas were damaged, as well as many animals lost their lives. Generally, the vegetation cover is Red Pine forests. In low-lying areas (0-800 m) maquis was formed by the destruction of these forests. Maquis is a collection of plants consisting of short stunted trees such as Myrtle, Laurel, Kocayemiş, Olive, Oleander, and Carob that can withstand the summer drought.

Figure 1: Satellite photo of Turkey and the wildfire-affected areas (from Google Maps).

Figure 2: The three-dimensional position of the wildfire-affected areas (from Google Maps)

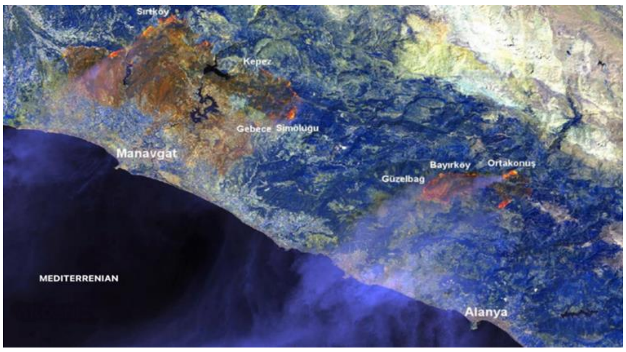

Figure 3: Real-time satellite image of Manavgat wildfire (Landsat-8 OLI satellite, July 31, 2021)

The image processing techniques on Landsat-8 OLI satellite images dated July 31, 2021, served by the US Geological Research Center (USGS) were employed to determine the changes that occurred in Manavgat, where the fire had the greatest impact. As a result of the analysis of the Landsat-8 thermal image, the observations demonstrate that the surface temperature reached 95 °C in the areas where active fires were observed in the region where the fire incident occurred, while the seawater temperature was around 27 °C. Based on the analysis, it was determined that a total of 83 thousand 810 hectares of land were burned, including 56 thousand 663 in Manavgat, 12 thousand 935 in Marmaris, 11 thousand 898 in Bodrum, 1629 in Koycegiz, and 685 in Gundogmus. During the last two decades, the big wildfires in the Antalya regions are Manavgat and Taşağıl region in 2008 with approximately 16 thousand hectares burned area. Considering this data, the 2021 Manavgat wildfire, which caused the burning of approximately 57 thousand hectares, has been recorded as the biggest fire disaster in Turkey [35]. Many strategies and methods have been employed to keep under control the wildfire and one of them was using the roads (Figure 4).

Figure 4: The road separates the forest area to better control fire.

A significant part of Manavgat is covered with red pine trees, which are common in the Mediterranean climate and are highly flammable. Strong winds (between 40 km/h and 60 km/h) carried the fire to the area uncontrollably. The roads separating settlements prevented the fire from spreading in some places, but most could not prevent the fires due to the pine cones blown by the wind.

3.2. The Specifications of the Study

The local buildings in Manavaret are generally masonry and stone structures with wooden beams. During the last three decades, this style has been modernized and changed to the proper buildings like RC frames and steel structures. Building types in terms of structural systems generally are; concrete frames with brick infill walls, masonry with wood/concrete roofs, light steel structural system, and mixed structures.

A total of 57 neighborhoods affected by the "Manavgat wildfire" were combined with a line on Google Maps and the affected areas were represented in Figure 2. To investigate the damage caused by the wildfire in the buildings, 18 neighborhoods in 4 districts (Manavgat, Alanya, Akseki, Gundogmus) were considered affected by the Manavgat wildfire. As stood before, a total, of 121 masonry buildings in various areas heavily damaged in the wildfire were examined in terms of the damage types and failure mechanisms. Most of the masonry buildings affected by the wildfire were 1-2 story buildings based on the situation in forested areas and settlements close to the forest. Near the city center, the number of the story in buildings increased but just two buildings were 3 stories (see Figure 5). Figure 5 shows the distribution of story numbers of the 121 examined buildings. One of the most important points observed during the investigation indicates that the buildings were mostly without any design project and engineering control during the construction process. Furthermore, by the time people have made an addition to the existing buildings based on their needs and possibilities. In the buildings examined in this study, it has been observed that the roof systems have great importance on fire in the buildings. Based on the observations, the fires reached the building mainly from outside, such as forest fires, starting from the most vulnerable part of the building and spreading. The stability of the building and its exposure to fire is closely related to the starting point of the fire in buildings. The observations demonstrate that the fire mostly reached the residential areas through the trees. Therefore, in buildings with wooden roofs, the fire mainly started from the roofs and in buildings without RC slabs under the roof, the fire could penetrate easily enter the building. Consequently, by burning the inside items in the building, the exposure time of the structure system to fire and their efficiency increased. The majority of masonry buildings have timber roofs or RC roofs at the same time which has a great effect on spreading the fire. While RC slab and wooden roof simultaneously could control the spreading better than wooden roof by itself.

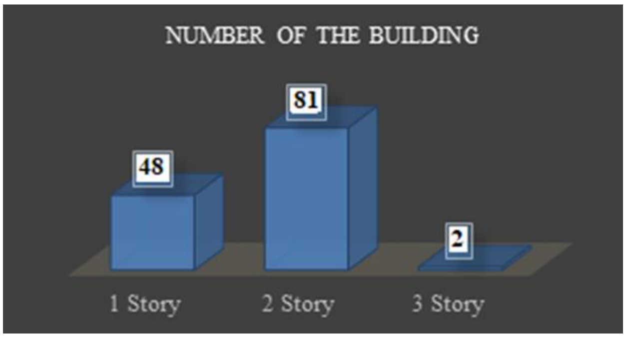

Figure 5: Number of stories and number of buildings.

3.3. Damages and Failure Mechanisms

In the following section, damage mechanisms of buildings in terms of the structural and nonstructural elements with all of the observed details have been investigated in the Manavgat wildfire.

In masonry buildings, fire primarily destroyed roofs, wooden beams, and floors. The burning of the timber structural elements that used to have a balanced condition of the walls mainly caused deformation and several kinds of cracks (see Figure 6). Furthermore, the unbalanced situation causes the disconnection of the joints and local failures. In many cases, reinforced concrete floors lost their capacity and collapsed or had deformation based on the instability conditions of the masonry walls absence of any kind of connections was not considered. Due to the low heat resistance of reinforcing bars, it deforms in fires at high temperatures. Although it was protected because of the cover of concrete, its deformation becomes inevitable as the exposure time increases.

The local structural system of masonry buildings in Manavgat is mainly based on masonry stone walls with wooden beams located inside of the wall (see Figures 7-9). Unfortunately, when the beams were subjected to fire, the stability of the masonry walls dramatically led to different kinds of failures. In some cases, the slabs (reinforced concrete slabs) could control the rate of fire in a safe direction where the wooden roof and beams were quickly subjected to fire and failure.

The observation of the cases showed that the separations and deep cracks in wall-to-wall connections, slab to slab-to-wall joints happened severally in masonry buildings. Furthermore, high temperatures destroy the properties of the mortar and bonding materials causing the separation of the walls, especially in terms of vertical and horizontal separation in wall joints (see Figures 8 and 9). Another observation expressed that the plaster, which was made to obtain a flat surface on walls, was separated from the walls based on the effect of high temperature. It shows that in masonry buildings high temperatures destroyed the cohesion between the wall and plaster not only on the inside of the building but also on the facades. Generally, all of the buildings with different kinds of structural systems are subjected to spalling of plasters in the facade as well as inside of the buildings based on the different temperatures and materials (see Figures 10).

3.4. Evaluation of the Roofs

As a main component of the building during the wildfire, the roof has been investigated separately based on the different types of roofs and their performance throughout the fire action. In buildings without reinforced concrete slabs under the wooden roof, the fire destroyed the roof, and, the elements inside of the roofs filed throughout the buildings and timber slabs. In buildings with reinforced concrete slabs under the wooden roof, it has been observed that although the wooden roof was destroyed, less destruction occurred compared to the buildings that do not have any reinforced concrete slabs under the wooden roofs. In addition, in reinforced concrete slabs with low-quality concrete and low reinforcement ratio collapse and failure happened severally. It has been observed that timber roofs on steel decks were burned and the tiles were collapsed or deformed severally. By increasing the fire exposure time, deformations increase in steel elements with an insufficient cross-sectional area. Generally, as the cross-sectional area decreases in light steel roofs, the resistance to heat decreases and visible deformations occur in the steel bars that are mainly not designed properly based on the updated design codes.

(a) (b)

Figure 6: The collapse of the reinforced concrete slabs based on the failure in the walls (a and b).

(a) (b)

Figure 7: Timber beams, slabs, and roofs have been destroyed by fire (a and b)

(a) (b)

Figure 8: The materials lost their qualities (a and b- deep cracks and separations)

Figure 9: Spalling of plasters in the facade

Figure 10: Inside spalling of plaster

(a) (b)

Figure 11: Timber roof without reinforced concrete slab (a and b-totally destroyed).

(a) (b)

Figure 12: Timber roof with RC slab (a and b-less destruction)

Figure 13: Reinforced concrete slab roofs (a and b)

Figure 14: The timber on steel roofs- totally destroyed (a and b)

Figure 15: Light steel roofs-totally destroyed (a and b)

In the mixed system consisting of masonry walls and steel, the plasters on the walls were separated from the steel section and steel elements had big deformation when exposed to the fire. As seen in the photos (Figures 16 and 17), different types of structural materials presented different systems.

Figure 16: Damages in the mixed materials (four types of materials)

Figure 17: Damages in the mixed materials (two types of material)

4. National Guide for Wildland-Urban Interface-NRC

The National Research Council of Canada (NRC) 2018 developed a National Guide for Wildland-Urban Interface (WUI) fires, referred to hereafter as the National WUI Guide [25]. In NRC the wildfire has been defined as an unplanned natural-caused or human-caused fire in live or dead combustible vegetation, as contrasted with prescribed fire. Additionally, the WUI fire is a wildfire that has spread into the wildland-urban interface. This Guide provides guidance not only for the development of a new community but also for the extending the old buildings. Furthermore, the WUI fire is a wildfire that has spread into the wildland-urban interface. This Guide provides guidance not only for the development of a new community but also for the expansion or modification of an existing community (e.g., adding new properties).

A chapter of this guideline represents the construction classes were classified into thirteen categories in terms of existing applicable, structural, and nonstructural elements, liquefied and gas tanks, and access route design for better firefighting capabilities. Since the study deals with the elements of the buildings, the investigation was limited to the construction elements measured in this study. Additionally, the evaluation of the case study of Manavgat, Turkey is represented in any subsection of NRC-2018.

4.1. Exterior Walls and Foundation Walls

The chapter implements all exterior walls, components, and gaps subject to WUI fire exposure. All joints in the exterior wall cladding or related wall components, openings, foundation walls, and penetrations should be covered with no unprotected gaps greater than 3 mm. In the case of the exterior surfaces that are less than 200 mm from the ground or a deck and roof. In this study as mentioned before the exterior plasters which were made to obtain a flat surface on facades were separated from the structural elements when subjected to high temperature. Therefore, high temperature disrupts the continuity between concrete and plaster since the recommendations based on NRC-2018 were not supported accurately.

4.2. Raised or Elevated Buildings

All of the supporting elements for the buildings should be made of non-combustible construction material. The heavy timber construction with a minimum nominal dimension of not less than 150 mm. In this study as already represented in diagrams, just a few buildings were subjected to this condition in NRC-2018 based on the number of stories, and the buildings were not constructed with non-combustible materials properly.

4.3. Roofing Materials

All kinds of roofs that could be exposed to accumulated embers should be non-combustible. Drip edges should be non-combustible, and extend at least 75 mm upslope from the edge of the roof. Roof penetrations, such as pipes, should be non-combustible. Any larger gaps more than 3 mm on the roof, should be sealed with non-combustible material. In this study, as stood before, the roof has been investigated separately as a main component of the building during the wildfire, based on the different types of roofs and their performance throughout the fire action. As pointed out previously, in buildings without reinforced concrete slabs under the wooden roof, the fire destroyed the roof, and, the elements inside of the roofs filled throughout the buildings and timber slabs since the roofs material generally do not support NRC-2018 specifications and material was not non-combustible. Additionally, drip edges mainly were not non-combustible, and did not extend upslope from the edge of the roof and the roof penetrations, such as pipes, were non-combustible considering NRC-2018.

4.4. Doors and Windows

Exterior doors on buildings should be non-combustible and have a fire-protection rating of not less than 20 min when tested using CAN/ULC-S104 [29]. Window glazing and skylights should be tested using SFM Standard 12-7A-2 [30]. The windows should be protected from corrosion, and non-combustible wire meshes with a maximum mesh aperture of 3 mm. The observations demonstrate that, in this study, exterior doors on buildings were not non-combustible with a fire-protection rating based on NRC-2018.

4.5. Decks, Balconies, and Other Building Attachments

All decks, balconies, porches, and similar building elements within 10 m of the main building structure should be prepared using non-combustible materials. Therefore, non-combustible materials should be used for all kinds of decks, balconies, and porches, as well as other similar structural and non-structural elements. Based on the observations in this study, decks, balconies, porches, and other similar building elements as well as graded surfaces were not properly constructed of non-combustible materials based on NRC-2018. As discussed previously, in the case of the buildings with reinforced concrete slabs under the wooden roof although the wooden roof was not non-combustible or appropriately protected and destroyed, less destruction occurred compared to the buildings with any reinforced concrete slabs under the wooden roof. It shows that the reinforced concrete slabs worked as lightly fire-protected elements in this investigation.

4.6. Liquefied Petroleum Gas Tanks and Access Routes

In the case of Liquefied Petroleum Gas (LPG) tanks within 100 m distance of any building should rest upon a non-combustible surface that extends not less than 1.5 m outward in all directions from the perimeter of the tank. The vegetation and combustible components within a zone of not less than 3 m should be removed. Furthermore, all directions from the perimeter of LPG tanks located within 100 m of any building should be removed. The observations in this study, clearly demonstrate that not only most of the items in NRC-2018 covered but also the access routes and primary aid supports were remarkable.

4.7. Comparison of the Current Study Results with Wildland-Urban Interface-NRC 2018

Generally, in the observations, the reinforced concrete slabs under the wooden roof, the wooden roof were destroyed. Furthermore, the percentage of the covered conditions is represented in terms of walls, raised or elevated buildings, roofing materials, gutters and downspouts, service openings and vents, doors and windows decks, balconies tanks, and access routes. Based on the NRC 2018 and observations, just a few items have been covered mainly in terms of the gutters and downspouts fitted with corrosion-resistant, access routes, and primary aid supports. Additionally, the plasters were mainly split up, separating of structural and nonstructural elements occurred, and reinforced concrete floors lost their capacity and collapsed or had deformation. The results of the case study are compared with the NRC 2018 in Table 1 where the covered percentage of the items is represented for all of the structural systems.

As represented in Table 1 the different structural systems such as masonry buildings, RC, steel, and mixed structures could not cover the specifications properly. Therefore, the percentage of the covered conditions is represented in terms of walls, raised or elevated buildings, roofing materials, gutters and downspouts, service openings and vents, doors and windows decks, balconies tanks, and access routes. Based on the NRC 2018 and observations, just a few items have been covered mainly in terms of the gutters and downspouts fitted with corrosion-resistant, access routes, and primary aid supports. The material of the roofs, balconies, porches, and other structural elements of the buildings were not non-combustible regarding NRC-2018.

Table1: Table 1. The results of masonry buildings and WUI-NRC 2018

NRC 1	NRC 2	NRC 3	NRC 4	NRC 5	NRC 6
Wall s (%)	Raised or Elevated Buildings (%)	Roofing Materials (%)	Doors and Windows (%)	Decks, Balconie s (%)	Tanks and Access Routes (%)
5	0	10	10 <	10	20

As stood before, the seismic performance of the buildings which subjected to a wildfire needs another demand considering the efficiency of fire on the material and structural elements. However, the structural systems will not be the same as before in terms of stiffness and capacity. Therefore, after a wildfire, if they are subject to seismic actions the structural systems will not have the same performance, particularly in terms of ductility and energy dissipation of the structural systems and materials.

5. Conclusions

In light of the observations, the effects of extreme temperatures on masonry buildings and materials were reported during the wildfire in Manavgat, Turkey (July-August 2021). A group of 121 masonry buildings was examined in terms of the performance and building damage mechanisms that occurred in the buildings exposed to the above-mentioned wildfire.

1. The main failure mechanisms in masonry structures; fire primarily destroyed roofs, wooden beams, and floors then disconnection of the joints and local failures, separation at wall-to-wall joints, and structural irregularity the stability of the masonry walls had dramatically led to failure, high temperature destroyed the cohesion between the wall and plaster.

2. In buildings with reinforced concrete slabs under the wooden roof, although the wooden roof was destroyed, less destruction occurred compared to the buildings that had no reinforced concrete slab under the wooden roof.

3. Generally, a main separation of structural and nonstructural elements has been reported.

4. Spalling of plasters in the facade as well as inside of the buildings is observed based on the different temperatures and materials.

5. Based on the NRC 2018 and observations, just a few items have been covered mainly in terms of the gutters and downspouts fitted with corrosion-resistant, access routes, and primary aid supports but the material of the roofs, balconies, porches, and other structural elements were not non-combustible regarding NRC-2018.

6. Because the behavior of the structural systems is not the same before and after wildfires if they are subject to seismic actions. The seismic performance of the existing buildings after a wildfire is another vital topic considering the efficiency of fire on the material and structural elements. Therefore, it seems that presenting a basic guideline and evaluation of the structural systems after a wildfire will prevent or reduce the efficiency of wildfires on buildings

Article Information

Funding

The author (s) has no received any financial support for the research, authorship or publication of this study.

Authors' Contrtibution

Conception or design of the work:
Hamid Farrokh Ghatte and Aslan Soyer
Data collection: Aslan Soyer

Data analysis and interpretation:
Hamid Farrokh Ghatte and Aslan Soyer
Drafting the article:
Hamid Farrokh Ghatte and Aslan Soyer
Critical revision of the article:
Hamid Farrokh Ghatte and Aslan Soyer
Final approval of the version to be published: Hamid Farrokh Ghatte and Aslan Soyer

The Declaration of Conflict of Interest/Common Interest

No conflict of interest or common interest has been declared by the authors.

The Declaration of Ethics Committee Approval

This study does not require ethics committee permission or any special permission.

The Declaration of Research and Publication Ethics

The authors of the paper declare that they comply with the scientific, ethical and quotation rules of Journal of Innovative Science and Engineering. in all processes of the paper and that they do not make any falsification on the data collected. In addition, they declare that Journal of Innovative Science and Engineering and its editorial board have no responsibility for any ethical violations that may be encountered, and that this study has not been evaluated in any academic publication environment other than Journal of Innovative Science and Engineering.

References

[1] Dimitrakopoulos, A., Gogi, C., Stamatelos, G., & Mitsopoulos, I. (2011). Statistical analysis of the fire environment of large forest fires (> 1000 ha) in Greece. Polish Journal of Environmental Studies, 20(2), 327-332.

[2] Xanthopoulos, G. (2003, May). Factors affecting the vulnerability of houses to wildland fire in the Mediterranean region. In Proceedings of the international workshop forest fires in the wildland-urban interface and rural areas in Europe (pp. 15-16).

[3] Buchanan, A. H., & Abu, A. K. (2017). Structural design for fire safety. John Wiley & Sons.

[4] Farrokh Ghatte, H., Comert, M., Demir, C., Akbaba, M., & Ilki, A. (2019). Seismic retrofit of full-scale substandard extended rectangular RC columns through CFRP jacketing: test results and design recommendations. Journal of Composites for Construction, 23(1), 04018071. 10.1061/(ASCE)CC.1943-5614.0000907

[5] Ghatte, H. F. (2020). External steel ties and CFRP jacketing effects on seismic performance and failure mechanisms of substandard rectangular RC columns. Composite Structures, 248, 112542. 10.1016/j.compstruct.2020.112542.

[6] Papalou, A., & Baros, D. K. (2019). Assessing Structural Damage after a Severe Wildfire: A Case Study. Buildings, 9(7), 171. 10.3390/buildings9070171.

[7] Li, K., Li, Y., Zou, Y., Yuan, B., Walsh, A., & Carradine, D. (2022). Improving the Fire Performance of Structural Insulated Panel Core Materials with Intumescent Flame-Retardant Epoxy Resin Adhesive. Fire Technology, 1-23. 10.1007/s10694-021-01203-0.

[8] Shahmansouri, A. A., Yazdani, M., Ghanbari, S., Bengar, H. A., Jafari, A., & Ghatte, H. F. (2021). Artificial neural network model to predict the compressive strength of eco-friendly geopolymer concrete incorporating silica fume and natural zeolite. Journal of Cleaner Production, 279, 123697. 10.1016/j.jclepro.2020.123697.

[9] Shahmansouri, A. A., Yazdani, M., Hosseini, M., Bengar, H. A., & Ghatte, H. F. (2022). The prediction analysis of compressive strength and electrical resistivity of environmentally friendly concrete incorporating natural zeolite using artificial neural network. Construction and Building Materials, 317, 125876.

[10] Lennon, T., Moore, D. B., & Bailey, C. (1999). The behaviour of full-scale steel-framed buildings subjected to compartment fires. The Structural Engineer, 77(8), 15-21.

[11] Wald, F., Da Silva, L. S., Moore, D. B., Lennon, T., Chladna, M., Santiago, A., ... & Borges, L. (2006). Experimental behaviour of a steel structure under natural fire. Fire Safety Journal, 41(7),509-522.

[12] https://doi.org/10.1016/j.firesaf.2006.05.006.

[13] Foster, S., Chladná, M., Hsieh, C., Burgess, I., & Plank, R. (2007). Thermal and structural behaviour of a full-scale composite building subject to a severe compartment fire. Fire Safety Journal, 42(3), 183-199. https://doi.org/10.1016/j.firesaf.2006.07.002.

[14] Adibi, M., Talebkhah, R., & Ghatte, H. F. (2023). Seismic reliability of precast concrete frame with masonry infill wall. Earthquakes and Structures, 24(2), 141.

[15] Ghatte, H. F. (2020, December). Failure mechanisms and cracking performance of T-shaped SCC beam-column connections at top floor: Test results and FE modeling. In Structures (Vol. 28, pp. 1009-1018). Elsevier.

[16] Bayraktar, A., Altunışık, A. C., & Muvafık, M. (2016). Field investigation of the performance of masonry buildings during the October 23 and November 9, 2011, Van Earthquakes in Turkey. Journal of Performance of Constructed Facilities, 30(2), 04014209. https://doi.org/10.1061/(ASCE)CF.1943-5509.0000383.

[17] Vahabi, H., Naser, M. Z., & Saeb, M. R. (2022). Fire Protection and Materials Flammability Control by Artificial Intelligence. Fire Technology, 1-3. https://doi.org/10.1007/s10694-021-01200-3.

[18] Lovreglio, R., Thompson, P., & Feng, Z. (2022). Automation in Fire Safety Engineering Using BIM and Generative Design. Fire Technology, 58(1), 1-5. https://doi.org/10.1007/s10694-021-01153-7.

[19] Hou, W., Zhang, G., & He, S. (2021). Fire Resistance Tests on Prestressed Concrete Box Girder with Intumescent Fire-Retardant Coatings. Fire Technology, 1-25. https://doi.org/10.1007/s10694-021-01145-7.

[20] Barnett, A., Cheng, C., Horasan, M., He, Y., & Park, L. (2022). Fire Load Density Distribution in School Buildings and Statistical Modelling. Fire Technology, 58(1), 503-521. https://doi.org/10.1007/s10694-021-01150-w.

[21] Kodur, V. K. R., & Shakya, A. M. (2017). Factors governing the shear response of prestressed concrete hollowcore slabs under fire conditions. Fire Safety Journal, 88, 67-88. 10.1016/j.firesaf.2017.01.003.

[22] Venanzi, I., Breccolotti, M., D'Alessandro, A., & Materazzi, A. L. (2014). Fire performance assessment of HPLWC hollow core slabs through full-scale furnace testing. Fire Safety Journal, 69, 12-22. 10.1016/j.firesaf.2014.07.004.

[23] Gomez-Heras, M., McCabe, S., Smith, B. J., & Fort, R. (2009). Impacts of fire on stone-built heritage: an overview. Journal of Architectural Conservation, 15(2), 47-58. 10.1080/13556207.2009.10785047.

[24] Vasanelli, E., Quarta, G., Masieri, M., & Calia, A. (2021). High temperature effects on the properties of a high porosity calcareous stone building material. European Journal of Environmental and Civil Engineering, 1-13. https://doi.org/10.1080/19648189.2021.196089.

[25] Barnett, A., Cheng, C., Horasan, M., He, Y., & Park, L. (2022). Fire Load Density Distribution in School Buildings and Statistical Modelling. Fire Technology, 58(1), 503-521. 10.1007/s10694-021-01150-w.

[26] Bénichou, N., Adelzadeh, M., Singh, J., Gomaa, I., Elsagan, N., Kinateder, M., ... & Sultan, M. National guide for wildland-urban-interface fires: guidance on hazard and exposure assessment, property protection, community resilience and emergency planning to minimize the impact of wildland-urban interface fires. 2021. National Research Council of Canada.

[27] Porter, K. A., Scawthorn, C., & Sandink, D. (2021). An Impact Analysis for the National Guide for Wildland-Urban Interface Fires.

[28] ASTM, E. 2957-Standard Test Method for Resistance to Wildfire Penetration of Eaves. Soffits and Other Projections.

[29] ASTM E2886/E2886M-20, "Standard Test Method for Evaluating the Ability of Exterior Vents to Resist the Entry of Embers and Direct Flame Impingement

[30] CAN/ULC-S104-15, "Standard Method for Fire Tests of Door Assemblies." http://bit.ly/WUI-075.

[31] State of California Office of the State Fire Marshal. 2011. SFM Standard 12-7A-2: Exterior Windows. In: California Code of Regulations. Sacramento, CA. http://bit.ly/WUI- 081.

[32] T.C. Çevre ve Şehircilik Bakanlığı, Binaların Yangından Korunması Hakkında Yönetmelikte Değişiklik Yapılmasına Dair Yönetmelik, Temmuz 2007.

[33] Guglietta, D., Conedera, M., Mazzoleni, S., & Ricotta, C. (2011). Mapping fire ignition risk in a complex anthropogenic landscape. Remote Sensing Letters, 2(3), 213-219. https://doi.org/10.1080/01431161.2010.512927.

[34] Gülçin, D., & Deniz, B. (2020). Remote sensing and GIS-based forest fire risk zone mapping: The case of Manisa, Turkey. Turkish Journal of Forestry, 21(1), 15-24. https://doi.org/10.18182/tjf.649747.

[35] Ganatsas, P., Oikonomakis, N., & Tsakaldimi, M. (2022). Small-Scale Analysis of Characteristics of the Wildland-Urban Interface Area of Thessaloniki, Northern Greece. Fire, 5(5), 159. https://doi.org/10.3390/fire5050159.

[36] Gebze Technical University Report Summer 2021:https://www.gtu.edu.tr/icerik/8/12549/display.aspx.

J Inno Sci Eng, 2025, 9(1):134-153

DOI:https://doi.org/ 10.38088/jise.1614320

Wave Actions and Responses for Large-Diameter Monopod Platform Structures

Ali Ete [1*]

[1] *Istanbul Esenyurt University, Department of Civil Engineering*, 34517, *Istanbul, Turkey*

ARTICLE INFO

Received Date: 6/01/2025
Accepted Date: 16/04/2025

Cite this paper as:
Ete Ali (2025). *Wave Actions and Responses for Large-Diameter Monopod Platform Structures.*Journal of Innovative Science and Engineering. 9(1): 134-153

*Corresponding author: Ete Ali
E-mail:alietemadi@esenyurt.edu.tr

Keywords:
Offshore Structure
Monopod Platform
Morison Equation
Linear Airy's wave theory
Sea-wave loads
Hydrodynamic module
Commercial offshore software

ABSTRACT

The sea-wave loads acting on the fixed offshore structures are estimated by using Airy's linear wave theory and Morison's equation, dissociating the total force into an inertia force component and a drag force component. The contribution of each component of the total force on tubular members can vary significantly based on size specification, from standard pipe members of fixed jacket structures to wide-ranging cylindrical Monopod towers. Inconclusive results can be seen in some published articles in estimating static wave loads using the hydrodynamic module of offshore platforms, indicating that this is still a subject of investigation. A demonstration of an example steel Monopod under Airy's type wave loading is presented. Several finite element offshore structure simulation packages use this simple monopod model for computationally efficient static wave load case simulations. The displacement pattern and the base shear force and bending moment of the Monopod model are calculated. The analytical solution is checked with numerical results of standard commercial FE software packages for verification and comparison purposes. The results show that the wave load calculation module of the finite element-based design programs considered in this study is underestimated, mainly when the contribution of the inertia coefficient to total instantaneous wave force is dominant, like in the monopod case with a large diameter. It can be thought that the differences here are due to the inertia coefficient weighting of the Morrison equation used in wave force calculations.

1. Introduction

Offshore platforms may have one, three, and so forth caisson-type legs. Offshore platforms with an individual caisson-type leg go by the Monopod tower [1]. Monopod steel towers may be applied for observatory, exploration, exploitation, and production aims. It may be appropriate in some offshore regions with shallow or medium seawater depths as a traditional structural concept. They are exposed to specific environmental loads throughout their service life. These loads are forced upon the Monopod tower through natural events such as ultimate wave loading, current, winds, and strong ground motions. For most towers, template, gravity, and caisson offshore structures, the hydrodynamic design load is mainly from sea waves, while wind loads and currents play a minor part [2]. Therefore, safe wave loading estimation is crucial for an economical and reliable design [3-4]. Figure 1 depicts the view of storm waves crashing against the steel Monopod tower.

Figure 1. Monopod tower under storm conditions [5]

While examining wave loads, the sea consists of periodic wave components with various wave heights, wave periods, and traveling ways co-occurring in a particular region. The superposition of these wave components and their distributive action causes a randomly changing sea level height, which can be refined with statistical operations. However, the use of regular wave theories to provide engineering solutions predominates because regular wave theories give well-mathematical models of long-crested periodic waves, which are components of irregular sea waves [6]. There are various regular sea wave theories, going back to the linear Airy's wave theory until the high-order solutions. The linear Airy's wave and Stokes second-order and Stokes fifth-order theories provided good compatibility for engineering applications [7-8].

The evaluation of wave loads on large-diameter vertical cylinders like Monopod is always of great interest to designers, especially now that this type of research is linked to the need to build stable offshore structures in conjunction with oil and gas production [7–18]. Wave kinematics are developed by using Airy's wave theory and Morison's equation. Linton and Evans [9] presented the method assuming linear wave theory for evaluating responses such as the forces on the cylinders, which is much simpler. Kriebel [10–11] developed a closed-form solution for the velocity potential due to the interactive relation of wave theories with a vertical cylindrical component with a large diameter and then compared the theoretical solutions with the results of laboratory experiments. To figure out the overall support size for an offshore platform, it is essential to quickly and accurately estimate the hydrodynamic forces and bending moments. Linear Airy's wave theory and Morison's Equation can be applied for this purpose [19]. Therefore, the wave loads on the large-diameter cylinder can be estimated analytically, and then the design parameters can be plotted in look-up graphs to speed up the design process [13]. Mendes [20] presented a numerical model to predict wave loading on jacket platforms subjected to an incident, regular sea waves. The linear wave theory has been applied to assessing water-particle kinematics. The hydrodynamic forces are enhanced with wave height and the combined effect of sea waves and current.

Furthermore, it was seen that at substantial current velocities, the wave loading is governed by the drag component in comparison with the inertia component. Lipsett [21] presented the impacts of nonlinear drag force on responses of the structure under random sea waves with a steady wave velocity component and a zero mean wave velocity. The wave load was supposed to be given by the relative velocity expression of Morison's equation which links the wave load to the structure's response. Gudmestad and Moe [22] checked the API's regulation and North Sea design practice methods relating to the excerpting convenient rates for the parameters used in the account of the hydrodynamic forces. Sunder and Connor [23] conducted a sensitivity analysis on offshore structures by taking into account different parameters, including alterations in wave height, ambiguities in wave period to be related to wave height; the selection of the hydrodynamic force coefficients, especially in connection with marine growth; modifications in characterizations of offshore structure as well as deck mass. The impacts of different wave patterns on offshore support structures become significant considerations in the hydrodynamic analysis process. The efficacy of hydrodynamic coefficients on response behaviour is connected with wave height and wave period [24-26].

Some studies on numerical modelling for the prediction of wave loading via commercial finite element offshore structure analysis software have been supplied in recent decades. Among them, the SAPOS (Spectral Analysis Program of Structures, [27]), CSI SAP2000 [28], Structural Analysis Computer System (SACS) [29], ABAQUS/AQUA [30], and ANSYS/AQWA [31] are commonly used for hydrodynamic analysis more than other commercial software packages. The hydrodynamic analysis of fixed offshore structure exposed to wave forces using CSI SAP2000 [3, 7, 18, 32-36]; SACS [37-38]; SAPOS [7, 27, 39]; ANSYS [36, 40] and ABAQUS AQUA [41-43] are some examples published by numerous researchers in the recent years. Some of these related studies are listed as follows:

Hydrodynamic analysis of jacket-type substructure for offshore wind turbines subjected to ultimate environmental loads was investigated by using CSI SAP 2000 [32, 34–35]. Environmental loads, such as wave and wind loads for Airy's and Stoke's laws, have been used to calculate offshore structures' deformation demands and bending moments. Cermelli [32] used SAP2000 software to figure out how much the structure of the wind float platform would be stressed when it was built. For the finite element model to work, the force results from the case studies, especially the base shear and overturning moments, had to be changed in a certain way. Raheem [3] showed a nonlinear response analysis for jacket structures under wave loading. The time-dependent wave load was considered through the drag component and the inertia component of Airy's wave theory. The drag force component is dependent upon 2nd-order water particle velocity, and the nonlinearity owing to the wave force has been subsumed in the calculations. Under both regular and extreme waves, the dynamic response of fixed offshore structures was studied, as well as the distribution of displacement demand, bending moment along the leg, and hydrodynamic loading on tubular members. Doman [34] performed a 3D static calculation and design process for a floating platform to support offshore wind turbines. The CSI SAP 2000 software was adopted for response behaviour when the structure was subjected to extreme environmental loads. Das and Janardhan [44] predicted the performance of a typical jacket-type structure at the Mumbai High Basin, using the CSI SAP2000 platform. Slake [18] investigated the effect of wave theories on the dynamic response of the fixed jacket platform. The modelling methods are initially indicated on a simple cantilever column, and then they are utilized for a complex offshore structure of interest (Martin Linge Jacket) on the Norwegian Continental Shelf (NCS).

The wave loading analysis was conducted on a simple beam in advance. Linear Airy's wave theory was employed, and implications were matched with analytical solutions. Airy's wave load on the member was acquired based on Morison's equation. Then, wave loading was developed automatically on the vertical cantilever column. It was conducted to examine the effects of wave loadings through different wave theories and also to verify the SAP2000 FE software results with analytical solutions for the linear Airy's wave theory. Only drag forces for the simple column were calculated manually and compared with the total wave load found from SAP 2000. It is known that the significant contribution comes from drag forces for slender members, such as members of jacket structures. The contribution of inertia forces should have been addressed in simple column calculations, which is not the case for vertical cylinders with a large diameter, such as monopod towers.

ANSYS/AQWA, ABAQUS/AQUA, and Structural Analysis Computer System (SACS) software have a workbench interface and direct use of the finite element analysis (FEA) solver dealing with offshore structures submitted to sea wave loads. Based on ABAQUS/AQUA environment, a steady current, Airy's wave load, and loads due to drag, buoyancy, and inertia forces for certain rigid elements can be defined easily [43]. Dagli et al. [45] investigated the bi-directional fluid-structure interaction analysis of monopod towers subjected to surface wave loads. Yaylacı [40] presented an offshore structure and its material properties in the examples using ANSYS software. Wave loads impacting a jacket structure were defined on the model and solved for multiple design scenarios. Kazemi Daliri [36] conducted time domain analysis on a gas/oil export riser subjected to wave loads using ANSYS/AQWA software. The risers have been assumed to be situated in a fixed jacket structure settled in the North Sea. The nodal displacements and reaction forces were compared by using different wave-loading theories. Noorzaei [37] presented the analytical solution and introduced an analysis platform to develop wave and current loads of slender offshore members. The developed program's results matched those of the Structural Analysis Computer System (SACS) software. Ishwarya [38] performed the nonlinear static and dynamic analyses on a three-dimensional model of a fixed jacket structure for North Sea environments, using the SACS platform.

In this research, commercial programs' static wave load calculation is examined through a simple benchmark monopod tower problem with a large diameter. The solution is compared with numerical results. The parameters used in the calculations are not real engineering design examples, and the structure size and wave load properties are hypothetical values for this study. The static sea wave forces applied on the Monopod tower are calculated through Morison's equation, which dissociates the overall wave force into an inertia force component that changes linearly with the water particle acceleration and a drag force component that changes quadratically with the water particle velocity. The Monopod tower under Airy's wave loads is solved manually by Morison's equation. Finite element models are formulated to designate the internal forces and displacements under similar wave loadings. The contribution of inertia and drag components on the total wave was calculated theoretically for comparison with the finite element method results. Commercial software packages, including SAPOS, SACS, SAP2000, and ABAQUS AQUA, are applied to calculate sea wave loads in the Monopod tower. The results of these examinations emphasize the stature of accurately simulating wave loading in cylindrical members with large diameters from the view of wave load prediction and safe design. Briefly, the primary aim of this research is to (i) compare the analytical results with the numerical solution of commercial finite element-based programs that can model wave forces on Monopod tower using Airy's wave theory and (ii) to demonstrate the applicability of the wave load module by analyzing a simple cylindrical Monopod tower instead of a complex offshore structure for the simplicity of comparison between the analytical solutions and numerical results.

2. Model design description and wave load data

The cylindrical monopod tower with a large diameter is adopted to compute static sea wave loads using Airy's linear wave theory and Morison's equation. The vertical steel Monopod tower with a diameter of 15.0 m is installed at a site where the water depth is 100 m. The height of the tower is 120.0 m. The monopod tubular section is made of welded plates with 0.08 m thickness. The steel material used for the construction of this platform is S355. Model design description, material properties, and Airy's wave load data are listed in Table 1. Considering the water-structure interaction, the added mass is assigned to the Monopod tower, concerning the added mass coefficients. A mass numerically equal to the mass of water displaced by the submerged monopod part is utilized to contain marine growth where practicable. Table 1 includes the added mass coefficients in dependence upon submergence, the thickness of marine growth, and the dry density of marine growth. D_h is the tower diameter containing marine growths, i.e., $(D_h = D + 2h)$ where h is the thickness of marine growths and D is the diameter of the member. The mean current defines a changing pressure distribution around the Monopod, producing a steady drag force on the cylindrical Monopod tower in line with the flow neglected in this study. The weight of the deck is not considered in the hydrodynamic analysis. The buoyancy force assigns to the Monopod tower water in the reverse direction of the gravitational loads. This force is ignored in the analysis. The soil-pile interaction effect is neglected. A regular periodic waveform is illustrated in Figure 2. The design wave has a height of 2.5 m and a wave period of 6.5 s. A schematic Monopod tower, geometry and material definition, and wave load data are summarized in the figure. The monopod tower was divided into 20-meter pieces starting from the seabed, then into elements 3-5 of 10 meters in length, 5-meter elements for the 30-meter piece at sea depth, and finally into 2 pieces 20 meters above the water level, thus obtaining a total of 14 elements. Detailed information on the number of elements and nodes for all models is presented in Figure 2. θ is the direction angle of the individual wave propagation and is defined between $(-\pi / 2 \leq \theta \leq \pi / 2)$ [7]. For regular waves, the wave amplitude $\hat{\eta}$ is to the halving of the wave height, $H/2$. Other dependent wave profile parameters can be calculated by using the data in Table 1. The wave number $m = 2\pi/\lambda$ and the other dependent parameters are angular wave frequency, $\omega = 2\pi/T$, and wave steepness, $\alpha = H/\lambda$ and wave celerity, $C = \lambda/T = \omega/m$.

Despite the dynamic nature of wave loads, they can be efficiently symbolized by their static equivalents to quasi-static loads. According to Morison's Equation, the force exerted by unbroken surface waves on a monopod tower has two components, inertia and drag forces [19]. Due to the wave forces, the members experienced stress depending on time, thus contributing to the cantilever impact as a deflection on the monopod towers. The solution to Morrison's equivalent forces for the Monopod tower example is presented in the following section.

Table 1: Model design description, material properties, and wave load data

Model Description		
Parameters	**Designation**	**Value (Unit)**
h_s	Height of the tower	120.0 (m)
D	Diameter of the tower	15.0 (m)
t	Wall thickness of the tower	0.08 (m)
Material properties		
ρ	Steel Mass Density	$7800.0\ (kg/m^3)$
ν	Poisson's ratio	0.30
f_y	Yield stress	$450.0 \times 10^6\ (P_a)$
E	Young's Modulus	$205.0 \times 10^9\ (P_a)$
Wave load		
ρ_w	Mass density of the water	$1024.0\ (kg/m^3)$
d_w	Water depth	100.0 (m)
	Still water surface	100.0 (m)
H_{max}	Maximum wave height	2.5 (m)
	wave period	6.5 (s)
C_d	Transverse Drag force Coefficient	1.3
	Tangential Drag force Coefficient	0.0
C_m	Transverse Inertia force Coefficient	2.0
Marine Growth		
	Marine Growth	0.25 (m)
	Dry density of marine growth	$1400\ (kg/m^3)$

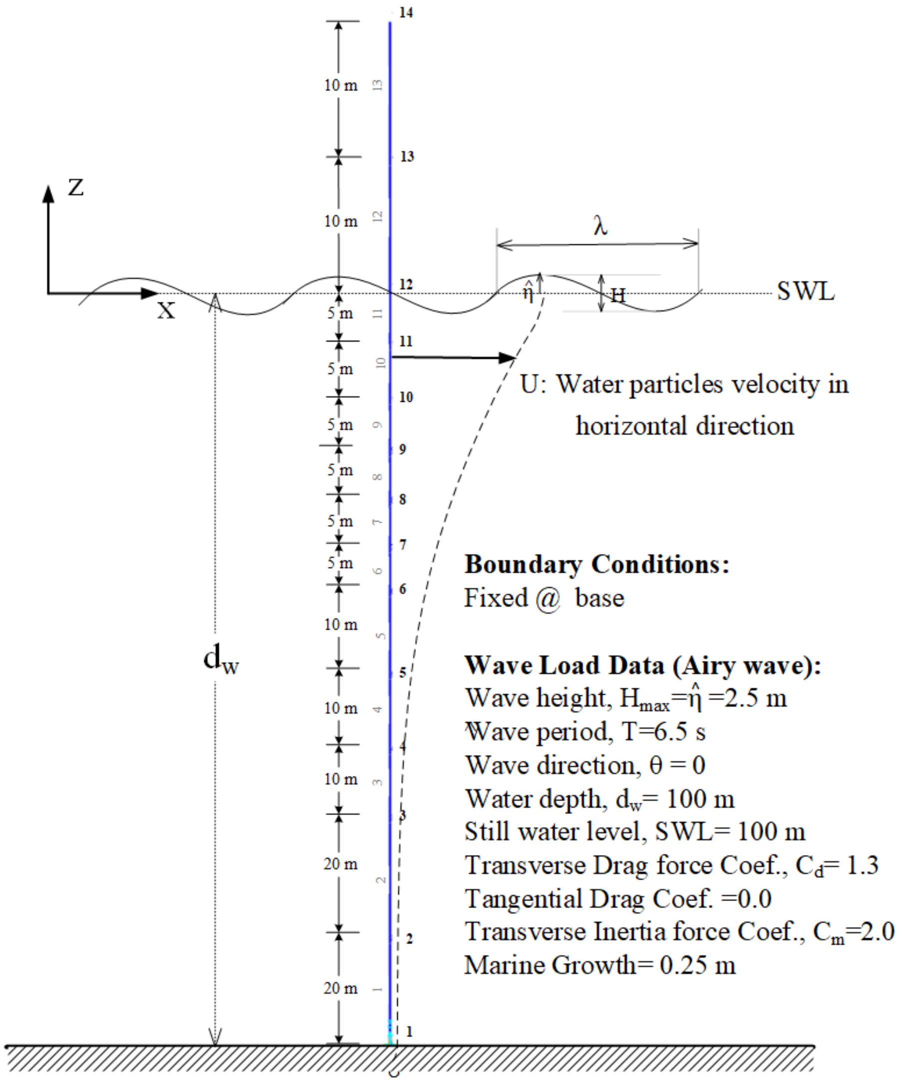

Figure 2. A schematic Monopod tower geometry, two-dimensional waveform, and description of some symbols

3. Analytical solution

Hydrodynamics principles are used to obtain water surface waves under certain boundary conditions from incompressible, irrotational, and inviscid flow [46]. The fundamental equations of water waves that fulfil various boundary conditions at the sea's bottom and on its free surface are continuity and irrotationality conditions of the flow. The linear Airy wave theory is the most straightforward and practical theory amongst wave theories. The assumption of low relative water depth and small wave steepness enables the linearization and satisfaction of the free surface boundary conditions at the still water level (mean water level). Airy's finite and infinite water depth theory calculates to provide an accurate depiction of the fundamental wave force. Then, one can determine Airy's wave force, using Morison's equation [19], which is provided for a rigid cylindrical monopod fixed at the bottom. The Morrison force expression depends on velocity, acceleration, and time, which on its own also depends on the depth considered. As a result, the force was reduced due to a combination of increased drag and added mass coefficients and the decreased absolute value of velocity and acceleration.

The computation of the force that sea waves apply to a cylindrical monopod tower changes depending on the wavelength, λ, and the member's diameter, D. The incident waves are dispersed or diffracted when the size of a cylindrical part is large enough to cover most of a wavelength. It may be in the diffraction regime based on the diameter of the Monopod tower. A solution to the linear diffraction issue for a cylindrical tower expanding from the seabed through the still water level can be found in [7-8, 47-48]. This ratio is not considered in this benchmark problem, and the pressure acting on the monopod due to the scattered wave is not incorporated. Instead, the wave forces have been obtained by using the Morrison equation and by calculating the pressure acting on the monopod tower from incident waves. Morison's equation disregards the convective acceleration component in the calculations of inertia force, slam forces, lift forces, and axial Froude-Krylov forces. According to Eq. 1 [49], Morison's equation, which is parallel to the planes of wave propagation direction and perpendicular to the monopod tower, defines a distributed wave force per unit length.

$$F = F_D + F_I = C_D \cdot |U| \cdot U + C_M \cdot \frac{\delta U}{\delta t} \qquad (1)$$

Where F is the whole instantaneous force, the magnitude and direction change during the wave's passage. The drag force contribution (F_D) is the first term, while the inertia force (F_I) is the second. The components of a water particle's velocity and acceleration, U and $\frac{\delta U}{\delta t}$, are normal to the tower axis. $|\cdot|$ designates an absolute value. Eq. 2 defines C_D and C_M, respectively, representing the drag and inertia force constants.

$$\begin{aligned} C_D &= \frac{1}{2} \cdot D_h \cdot \rho_w \cdot C_d \\ C_M &= \frac{1}{4} \cdot \pi \cdot D_h^2 \cdot \rho_w \cdot C_m \end{aligned} \qquad (2)$$

Where C_d and C_m are Morison's equation's coefficients for drag and inertia force, respectively and are listed in Table 1. These coefficients depend on the Keulegan-Carpenter number (K_c), which considers wave height and surface roughness, and the Reynolds number (R_e), a dimensionless parameter based on flow velocity. The cylinder's diameter, D_h, has an impact on the wave force regime as well.

By using the linear wave theory, a velocity potential function for two-dimensional waves can be obtained as,

$$\phi = -\hat{\eta} \cdot \frac{g}{\omega} \cdot \frac{\cosh(mz + md_w)}{\text{scosh}(md_w)} e^{i(\omega t - mx)} \qquad (3)$$

where,

d_w: Water depth

g : Acceleration of the gravity

m : Wave number ($m = 2\pi/L$ where L is the wavelength)

z : Vertical coordinate measured from the still water level

x : Horizontal coordinate in the wave propagation direction.

The wave number m is also dependent on the frequency ω by the relation,

$$\omega^2 = (mg) \cdot \tanh(m \cdot d_w) \qquad (4)$$

The water elevation η and velocities of water particles may be derived from the potential function as written by,

$$\eta = \frac{1}{g}\frac{\partial \phi}{\partial t}|z = 0 \quad \text{and} \quad \begin{aligned} U_x &= -\frac{\partial \phi}{\partial x} \\ U_z &= -\frac{\partial \phi}{\partial z} \end{aligned} \qquad (5)$$

Having used the statement of Φ given by Eq. (3) in Eq. (5), the real parts of these quantities will be,

$$\eta = \hat{\eta} \cdot \sin(\omega t - mx) \qquad (6)$$

$$U_x = \hat{\eta} \cdot \omega \cdot \frac{\cosh m(z + d_w)}{\sinh(md_w)} \sin(\omega t - mx)$$

$$U_z = \hat{\eta} \cdot \omega \cdot \frac{\sinh m(z + d_w)}{\sinh(md_w)} \cos(\omega t - mx) \qquad (7)$$

The accelerations of water particles are derived from Eq. (6) as,

$$\dot{U}_x = \hat{\eta} \cdot \omega^2 \cdot \frac{\cosh m(z + d_w)}{\sinh(md_w)} \cos(\omega t - mx)$$

$$\dot{U}_z = -\hat{\eta} \cdot \omega^2 \cdot \frac{\sinh m(z + d_w)}{\sinh(md_w)} \sin(\omega t - mx) \qquad (8)$$

or using Eq. (4) in Eq. (8), it can be obtained as,

$$\dot{U}_x = \hat{\eta} \cdot mg \cdot \frac{\cosh m(z + d_w)}{\cosh(md_w)} \cos(\omega t - mx)$$

$$\dot{U}_z = -\hat{\eta} \cdot mg \cdot \frac{\sinh m(z + d_w)}{\cosh(md_w)} \sin(\omega t - mx) \qquad (9)$$

where $m = 2\pi/\lambda$, (λ is the wavelength). Eqs. (7) and (9) will be used in calculation of wave forces from the Morison’s equation. The Morison's equation is used to figure out the wave load on a monopod tower when the wave profile is assumed to be harmonic, as shown in Eq. 10. Also, because the tower response is static, the contribution of the dynamic response is not considered. Under harmonic wave loads, the shear force and bending moment of the monopod tower example at the bottom are determined. The maximum wave-induced horizontal drag force F_D and an inertia force F_I are computed analytically for the values in Table 1 [7]. To calculate the extreme shear force and bending moment of the tower in practice, wave velocity and acceleration, which are based on a finite amplitude wave theory, must be used. For a progressive wave moving in the direction of $+x$, the horizontal velocity vector U of water particles is found using the Eq. 10. For the static analysis, the wave elevation is calculated by using a complex exponential function $\exp(i(\omega t - mx))$ with constant amplitude.

$$U = \hat{\eta} \cdot \omega \cdot \frac{\cosh m(z + d_w)}{\sinh md_w} \tag{10}$$

in which m is a constant (wave number), $\hat{\eta}$ is the wave amplitude and equal to the halving of the wave height $(H/2)$ for regular waves, x_w is the horizontal coordinate in the wave propagation direction, and U is the water velocity in the x_w direction. With velocity data, the Morrison equation [19] can be used to figure out the wave forces on the monopod tower. As shown in Eq. 11, in the first term of Morison's equation, $F_D(z)$ is the drag force per unit length acting on the axis of the monopod tower in the plane of the member axis.

$$F_D(z) = C_D \left(\hat{\eta} \cdot \omega \cdot \frac{\cosh m\,(z + d_w)}{\sinh md_w} \right)^2 \tag{11}$$

The following integration yields the total shear force at the bottom, V_D,

$$V_D = \int_{Z=-d_w}^{0} F_D(z) \cdot dz \tag{12}$$

$F_D(z)$ from Eq. 11 is then substituted into Eq. (12). Giving the derivation from both sides of the $m(z + d) = x$ expression to get $mdz = dx \rightarrow dz = \frac{dx}{m}$ and carrying out the integration for boundary conditions as $= -d \rightarrow x = 0$, $z = 0 \rightarrow x = md$ and substituting them into Eq. 13, the shear force at the bottom is calculated as Eq. 14.

$$V_D = \int_{0}^{md} C_D \cdot \left(\hat{\eta} \cdot \frac{\omega}{\sinh md} \right)^2 \cdot \frac{1}{m} \cdot \cosh^2 x \, dx \tag{13}$$

$$V_D = \frac{1}{4} \cdot \frac{C_D}{m} \cdot \hat{\eta}^2 \cdot \frac{\omega^2}{\sinh^2 md} \cdot \sinh 2md \cdot \left(1 + \frac{2md}{\sinh 2md} \right) \tag{14}$$

where the frequency of the wave, ω, that fulfils the dispersion relationship is $\omega^2 = mg \cdot \tanh md_w = mg \cdot \frac{\sinh md_w}{\cosh md_w}$ and replacing of $\sinh md_w \cdot \cosh md_w = \frac{1}{2} \cdot \sinh 2md_w$ expression into Eq.14, the shear force at the bottom due to drag force is simplified as Eq. 15.

$$V_D = \frac{1}{2} \cdot C_D \cdot g \cdot \hat{\eta}^2 \cdot \left(1 + \frac{2md}{\sinh 2md} \right) \tag{15}$$

The deep-sea wave condition is effectively employed in ocean conditions distant from the shoreline. Waves are divided into the categories of deep, moderate, and shallow water waves based on the connection between water depth and wavelength, d_w/λ, [50]. The deep-water condition is established when $(d_w/\lambda > 1/2)$. The alternative form of this condition is $(md > \pi)$. For the deep-water situation, instead of using Eq. 10, the velocity vector component in Eq. 16 is used. The drag force is formed as in Eq. 17.

$$U = \hat{\eta} \cdot \omega \cdot e^{mz} \tag{16}$$

$$F_D(z) = C_D \cdot \hat{\eta}^2 \cdot \omega^2 \cdot e^{2mz} \tag{17}$$

Eq. 18 is employed to determine the tower's shear force at the base due to drag and deep-water conditions,

$$V_D = C_D \cdot \hat{\eta}^2 \cdot \frac{\omega^2}{2m} \cdot \left(1 - e^{-2md} \right) \tag{18}$$

The following integration yields the bending moment of monopod at the bottom,

$$M_D = \int_{Z=-d}^{0} (d + z) \cdot F_D(z) \cdot dz \tag{19}$$

The bending moment is expressed after $F_D(z)$ in Eq. 17 was added to Eq. 19.

$$M_D = V_D \cdot d + C_D \cdot \hat{\eta}^2 \cdot \omega^2 \cdot \int_{-d}^{0} z \cdot e^{2mz} \cdot dz \tag{20}$$

Moreover, after integration is completed, it is possible to ascertain,

$$M_D = V_D \cdot d + C_D \cdot \hat{\eta}^2 \cdot \frac{g}{m} \cdot [(2md + 1) \cdot e^{-2md} - 1] \tag{21}$$

The constants for the bending moment's drag and inertia terms, B_D and B_M can be expressed more simply as follow,

$$M_D = \frac{g}{m} \cdot \hat{\eta}^2 \cdot B_D \tag{22}$$

where Eq. 23 is used to obtain the constants B_D of the drag force terms,

$$B_D = \frac{1}{4} \cdot C_D \cdot \left[2md - \left(1 - e^{-2md}\right)\right] \tag{23}$$

It is also possible to ignore the term in Eq. 23 for deep water conditions, and the constants for the drag terms of the bending moment at the bottom can be simplified as shown below,

$$B_D = \frac{1}{4} \cdot C_D \cdot (2md - 1) \tag{24}$$

$$\rightarrow \text{for deep water condition}$$

Also, the bending moment is only caused by the inertia force part of the Morison equation forces, M_M, which is found in Eq. 25.

$$M_M = \hat{\eta} \cdot \frac{g}{m} \cdot B_M \tag{25}$$

And the following formula is used to determine the inertia terms' constants B_M,

$$B_M = C_M \cdot \left[md \cdot \tanh(md) + \frac{1}{\cosh(md)} - 1\right] \tag{26}$$

In addition, the constant B_M for the inertia term in the case of deep-water situation is derived as follows,

$$B_M = C_M \cdot (md - 1) \tag{27}$$

$$\rightarrow \text{for deep water condition}$$

Finally, Eq. 28 is used to figure out the shear force that the force of inertia will have on the base of the monopod tower. This is determined in a way like how Eq. 15 describes the shear force brought on by the drag force.

$$V_M = \hat{\eta} \cdot g \cdot (C_M \cdot \tanh(md)) \tag{28}$$

Eqs. (19) and (23) enable us to find the maximum static total shear force and bending moment under the monopod tower for a given wave. Eq. 2 defines C_D and C_M, the drag and inertia force constants, respectively. By substituting the design parameters of the monopod tower according to Table 1, the drag force coefficient is calculated as $C_D = 807.1875$, and the shear force and the bending moment due to the drag force at the bottom of the monopod are calculated as $V_D = 961.036\ kN$, $M_D = 0.6849 \times 10^8\ N \cdot m$, respectively. Moreover, the bending moment due to the inertia force term is obtained as $M_M = 0.20430253 \times 10^8\ N \cdot m$, and the coefficients of the inertia forces are computed as $C_M = 2173.589$ and $B_M = 2408$, respectively.

In deep water, the maximum static bending moment depends on both the number and size of the waves, but the maximum static shear force depends only on the size of the waves [7]. The shear force is obtained as $V_D = 799.209\ kN$ for the tower in question in deep water conditions. The B_D coefficient and the moment forces are found to be equal to $B_D = 530.6148$ and $M_D = 0.6781 \times 10^8\ N \cdot m$, respectively. Furthermore, the moment force due to inertia force and related the B_M coefficient are calculated as $M_M = 0.17323179 \times 10^8\ N \cdot m$ and $B_M = 1952.1$, respectively.

4. Numerical model development

This section generates the finite element (FE) models of the cylindrical steel monopod model. The global FE model is developed through the commercial FE offshore analysis software packages: SAPOS (Spectral Analysis Program of Structures) [27], SAP2000 V.20 [28], Structural Analysis Computer System (SACS) V.12 [29], and ABAQUS V.6.14 [30]. The hydrodynamic analysis of the cylindrical monopod tower under Airy's wave loads is conducted. The shear forces and bending moments at the bottoms are computed numerically, and the results are compared with analytical solutions.

4.1. SAPOS Software

The stochastic analysis program for offshore structures is known as SAPOS [7]. Because the wave amplitude and profile are random, the shear force and static bending moment are calculated and expressed in terms of the random water level. For this reason, the real and imaginary components of the water elevation η have been introduced [7]. Design parameters for monopod tower cases are adopted as per Table 1. The input file for wave loading in the SAPOS program is shown in Table 2. Under Airy's theory of waves and conditions of deep water, the SAPOS reported the forces and displacement demands of the members. The moment at the basement due to inertia and drag forces is computed in Table 3. Based on analytical results, the maximum resultant moment forces at the midline are estimated to be off by 1.5%. The results show that the moment forces from SAPOS and the analytical solutions (see

Table 3) are the same. Figure 3 shows the member forces and nodal displacements calculated from SAPOS for the monopod tower as well as the results for both the imaginary and real parts. The weight of the imaginary part is the most important factor when estimating displacement patterns and the forces at the nodes. It is seen that the results of the analysis using SAPOS are consistent with the analytical solution for the same problem.

Table 2: Input file for wave loading in the SAPOS program

```
WAVe DATA
WAVe HEIght 2.5
WAVe PERiod 6.5
WAVe DIRection 0.0
WATer depth 100.0
STIll water surface 100.0
UNI-directional
MAin wave number 1
INErtia force coefficient cm 2.0 ALL
DRAg force coefficient cd 1.3 ALL
MARine growth thickness 0.25 ALL
DENsity of water ro 1024.0
    END of wave data
```

Table 3: The moment force at the basement

Software	$M_M\ (N \cdot m)$		$M_D(N \cdot m)$	
	Normal condition	Deep water condition	Normal condition	Deep water condition
Analytical solution	0.1732×10^8	0.1732×10^8	-	0.6780×10^8
SAPOS	-	-	-	0.6675×10^8
SAP2000	-	-	-	0.1024×10^8
SACS	-	-	-	0.497×10^7

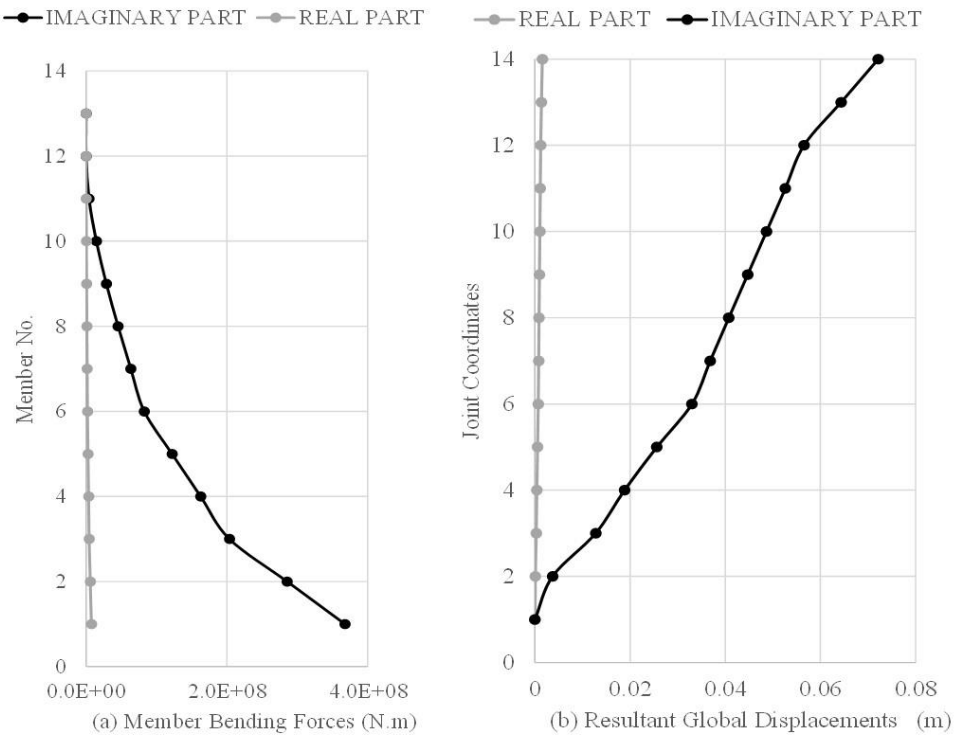

Figure 3. (a) Resultant moment forces (N.m) and (b) Resultant global displacement (m)

4.2. CSI SAP2000 Software

The CSI SAP2000 Ultimate Version 20.1.0 analysis software, which is based on finite elements, is used to perform a first-order elastic analysis on the Monopod tower model [28]. As suggested by [2], the displacement response of the hull structure is found by analysing wave loading cases that take the environmental condition into account. The wave loading results from the water pressure integrated over the submerged part of the monopod tower [51]. The automatic wave loads are based on the requirements for designing fixed offshore platforms given by APR RP 2A-WSD [2]. CSI SAP2000 represents the application of static wave load patterns by a significant wave height, a specified wave return period, and a direction (Figures 4 and 5). Wave velocities and acceleration fields are developed through linear Airy's wave theory, and the wave force is computed through Morison's equation (see Figure 4). The CSI SAP2000 automatically defines load cases for the defined wave load patterns. The program provides the option to look at multiple wave crests, but since the waves being looked at have long periods, user only need to look at one wavelength for static loading. Figure 4 shows the wave load pattern definition with an aligned wave. The magnitude of wave load is assigned based on the surface area exposed to a member's wave loading and volume. The wave loads are calculated and applied to the model manually. Once a wave load case is defined, there is no need to assign the wave loads to a member separately, only to provide the Monopod tower with appropriately representative surface areas and volumes. Figure 5 shows the load pattern displaying the resultant velocity of the wave. The wave load distribution over both load cases is compared in Figure 6. Figure 6 (a) wave loads are calculated by CSI SAP2000 module processes automatically, and Figure 6 (b) demonstrates wave load distribution calculated manually by using Morison's equation and applied to members with alternative static load cases. Base Reactions under both wave loading modules and equivalent static wave loads are listed in Table 3. There is a significant difference between both wave loading methods with equal parameters that truly illustrate the difficulties of simulation. A simulation model always abstracts away from the accurate values calculated via Morison's equation, which can affect the member stress rates and internal forces for further dynamic analysis. For the given monopod problem, the wave load distribution can be calculated manually according to Morison's equation, which is seen as Eq. 10. The design parameters could be obtained as $m = 0.095$ and $F_D(z) = 394267.3 \cdot e^{2mz}$, respectively.

Height-wise distribution of joint displacement and moment M3 for a monopod tower under both manual and automatic program-defined wave loads is illustrated in Figure 7. Compared to the manual wave load distribution, the results show that the wave loads calculated by the CSI SAP2000 module processes are too low. Figure 8 depicts the monopod displacement from CSI SAP2000 vs. the real part of SAPOS. The real part of SAPOS, which is related to the drag coefficient, has a minor contribution to wave loading, and in this case, the results are similar to those of CSI SAP2000 in both the displacement pattern and the response ranges (see Figure 8). The contribution of the inertia force component is of major importance here and needs to be reflected in the results. It is known that the contribution of the inertia force component is more dominant, particularly for cylindrical monopod towers with large diameters. The drag and inertia coefficients are defined automatically by default. The drag and inertia force coefficients were taken as per API by the CSI SAP2000 platform [28]. Different results are obtained manually by defining similar input values, implying some problems in the wave load definition module. In addition, changing the inertia coefficient along the Monopod tower does not affect the total wave load pattern, which in turn raises doubts about the correctness of the results.

Table 4: The moment force at the basement

Output Case	**Global FX**	**Global FZ**	**Global MX**	**Global MY**
Unit	N	N	N-m	N-m
Wave	-106903.59	-191853157	0	-10243336.2
Static Load	-4164332.05	0	0	-372546018

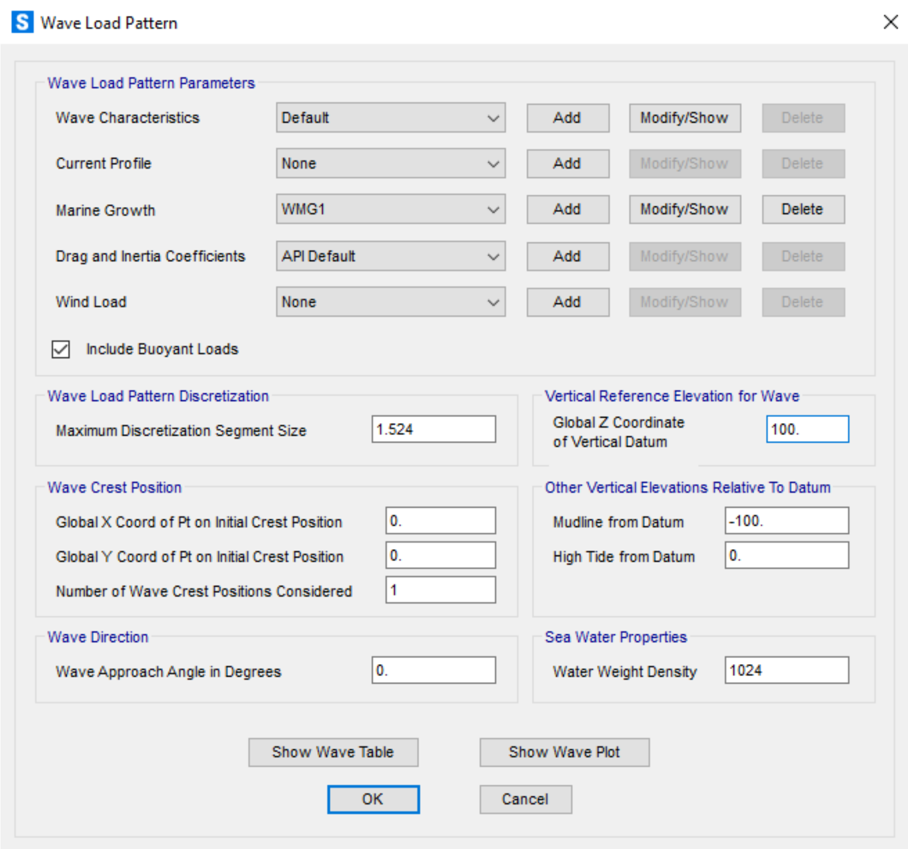

Figure 4. Wave load pattern definition in CSI SAP2000 V.20 for the aligned heading case of wave loading (units in meters) [28].

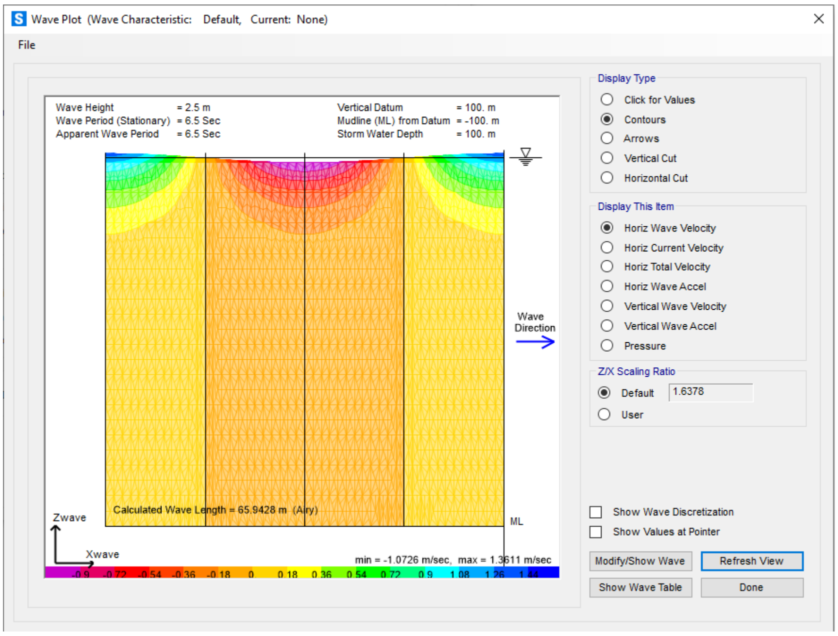

Figure 5. Wave load pattern plot displaying the resultant velocity of the wave in CSI SAP2000 [28].

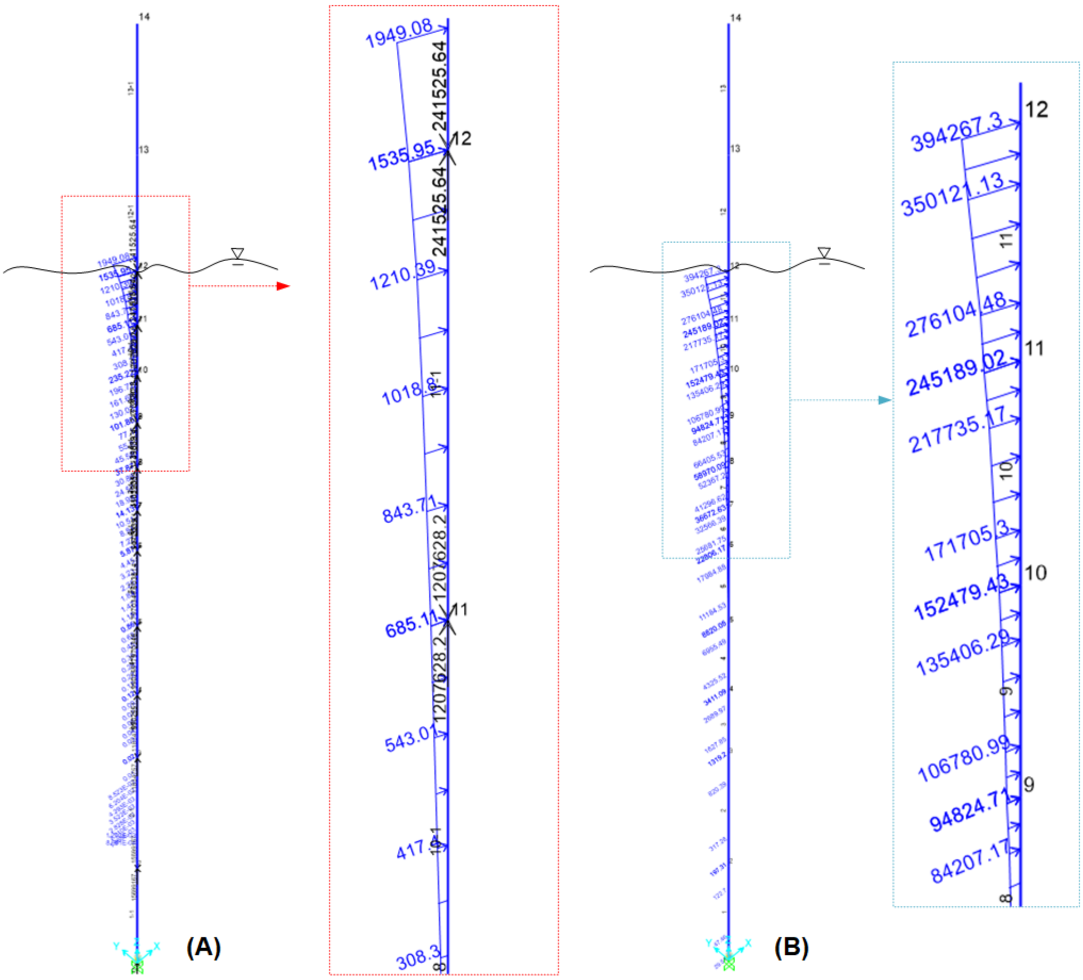

Figure 6. Wave load case applied to a monopod tower: (a) wave loads calculated by CSI SAP2000 module processes; (b) wave load distribution calculated manually using Morison's equation. (Units are kN).

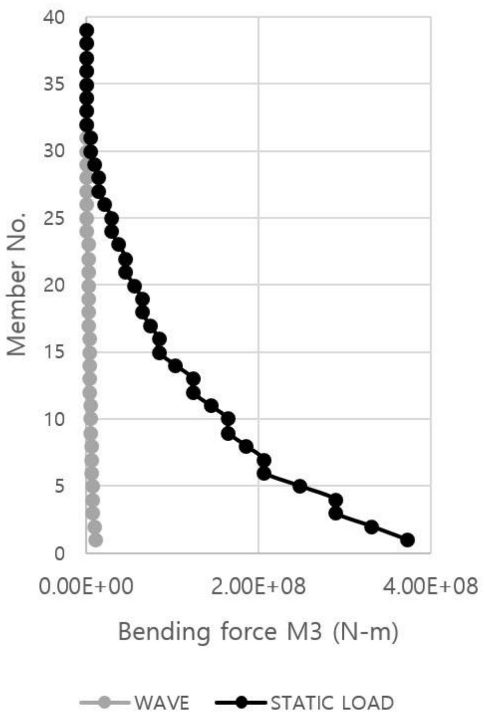

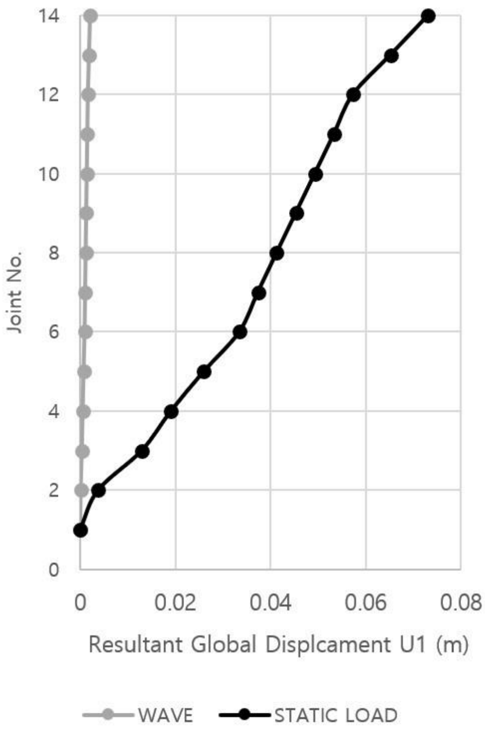

Figure 7. Member bending force M3 and displacement pattern of Monopod tower under program-defined wave loading and static load case calculated manually

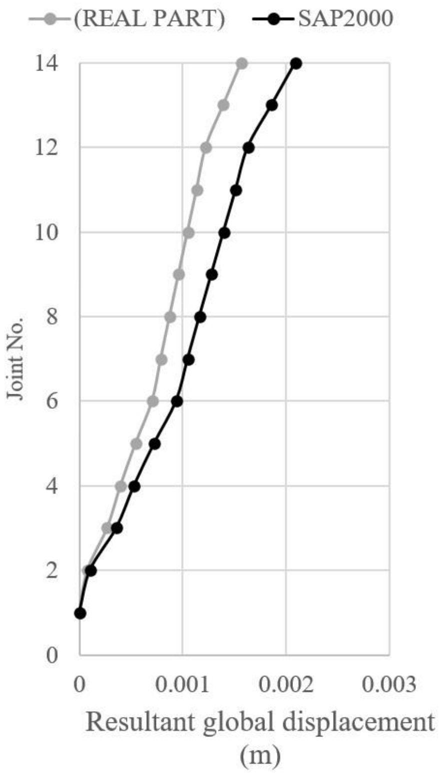

Figure 8. Monopod resultant displacement pattern from SAP2000 vs. SAPOS real part

4.3. Structural Analysis Computer System (SACS) Software

A comprehensive software package called SACS V.12 supports offshore structure analysis, design, and installation (Bentley Systems, 2018) [29]. The monopod tower model refinement phase employs the interactive full-screen graphical user Modeller (PRECEDE) program for hydrodynamic evaluation. The monopod characterizations and primary loads remain constant throughout the evaluation. The environmental loads on a fixed offshore structure are created and computed by SEA STATE using the API 20th edition [2] and several wave loading theories. This module computes the static and dynamic forces within and upon each part of the offshore structure using computer-based operations on environmental and design data provided by the user. The resultant moment forces under Airy's wave loading are plotted in Figure 9. There is a significant difference between the analytical solution and numerical calculated results with equal design parameters that truly demonstrate the simulation's difficulties; a simulation model always abstracts away from the actual conditions. This is one of the essential benefits of simulation, but it also means that the results may only sometimes match the real values.

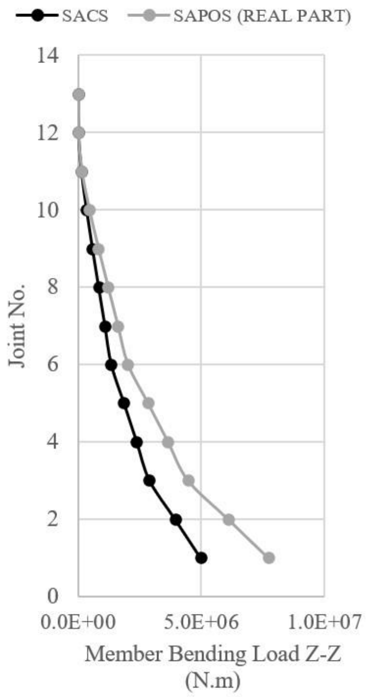

Figure 9. Member bending load under Airy's wave loading from SACS program and SAPOS (Real part)

4.4. ABAQUS Software

Another tool used to investigate wave loading on underwater or partially submerged offshore structures is the ABAQUS/AQUA V.6.14 [30] software, which is used in problems such as the analysis of marine risers and the modelling of offshore piping systems and monopod towers. This module calculates certain rigid elements' drag, buoyancy, and inertia forces. The monopod tower model is generated, and an Airy linear wave load is described, as shown in Table 5. To neglect the wind load, the coefficient value of the wind velocity components is entered as zero. The joint displacement, U1, over the monopod height is illustrated in Figure 10. However, the displacement pattern is similar, but the maximum displacement at the tower tip is obtained as 1.36 m, which is overestimated when compared to the analytical solution and the results of other analysis programs. The displacement pattern is identical, but the displacement demands are overestimated compared to the analytical results.

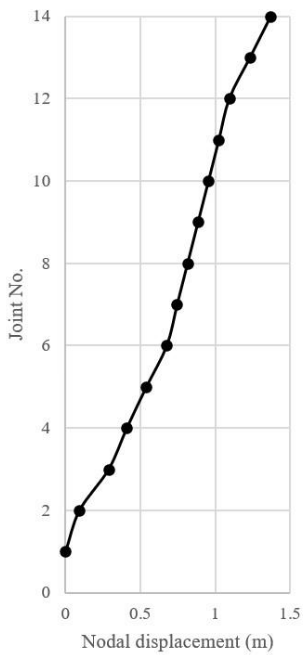

Figure 10. Monopod tower joint displacement distribution, U1, using ABAQUS/Aqua programs [30]

Table 5: Monopod wave loading input file for Abaqus/Aqua

```
*aqua
0,100,9.81,1024
0,0,0,0
0,0,0,100
*wave,type=airy, wave period
1.25,6.5,0,1
*wind
1.225,0.0,0,0,-1
*restart,write,frequency=1
*step
corrent flow
*static
1,1,1e-05, 1
```

5. Results and Discussions

Wave loads dominate the design and performance assessment processes of offshore structures. The finite element-based method is generally adopted for predicting marginal structural response and external loads such as wave loads. However, the results are considered realistic by the users even without an identification process in some cases. This study uses common FE offshore structure analysis platforms to figure out how a simple cylindrical monopod tower will react to a linear Airy's wave. The results are compared with analytical solutions. Because the node displacement generated in a structure is caused by its internal forces and stresses, it is fixed to use the node displacement as the index to evaluate the response of the monopod tower under a static wave load. Another response indicator used to compare findings was bending forces. Utilizing nodal displacement amounts and several numerical approaches of different commercial programs, the author defines the sensitivity of wave forces for default values and various input variables when defining wave load automatically through the wave loading interface module of offshore analysis platforms. The analytical solutions indicate that the maximum shear forces and moments at the bottom for wave number m=0.095 are calculated as V_Max=0.4738732×10^7 N and M_Max=42.3991878×10^7 N·m. Besides, the drag and inertia force coefficients are C_D=10316 and C_M=386.441, respectively. The SOPOS program provides the wave load for the deep-water condition and it has been found that the program can estimate the internal loads with acceptable accuracy. However, in the case of other software (SAPOS, SAP2000, SACS, and ABAQUS), the results do not match very well for the case study. For a more detailed examination of the problem, the wave load is defined automatically via the wave load module in CSI SAP2000 (see Figures 4 and 5). The results are surprisingly underestimated the ranges expected. When one calculated the wave loads manually and performed the static analysis, the displacement demands came out as expected. There is an error in the calculation of the forces resulting from the wave load calculation (see Figure 6). No significant changes in wave loading were seen when the drag and inertia coefficients were changed. The reason for this seems to be that the contribution of the drag coefficient is not taken into consideration. As stated earlier, the inertia coefficient contributes to the wave loading of the cylindrical member with a large diameter. In the following steps, it was shown that the result of CSI SAP2000 is similar in pattern and varies according to the real part response of the SAPOS software regarding the drag coefficient. This supported the view that only the drag coefficient is considered in the calculations (Figure 8). For further investigation, two other commercial FE software products are adopted for wave loading problems. The bending loads show that the load ranges are also around the Real part of the SAPOS results (Figure 9). In solving the problem, the ABAQUS/AQUA module calculates the drag, buoyancy, and inertia forces for certain rigid members. The nodal at the monopod tip reaches 1.36 m, which is very high when compared to analytical solutions.

6. Conclusions

This study presents a wide-ranging analysis of the main contributing factor in the definition of static wave load for cylindrical monopod tower systems. Wave loads significantly impact the design life of offshore structures, such that a realistic estimation of wave loading can affect the overall performance of offshore substructures and the stress level at critical zones. Wave velocity fields are developed through linear Airy's wave theory, and the wave forces are computed through Morison's equation, where the wave load is composed of the drag force and the inertial forces. It is known that the contribution of inertial forces increases with the tabular member's increasing diameter. This is not the case for large-sized cylindrical elements such as monopod towers, as the weight of inertia forces in Morison's equation is negligible for pipe-type components of jacket structures. The simple vertical cylindrical monopod tower with a large diameter is adopted as a case study to compare the static Airy's wave loads of numerical methods with identical analytical solutions. Therefore, only static Airy's wave loads were used to analyze the monopod tower. Other environmental loads, like wind and current loads, were not considered. In this way, it was possible to compare numerical results with analytical solutions. The extreme shear force and maximum static bending moment to which the tower is exposed in deep water conditions are calculated analytically. Commercial FE platforms have been adopted for analyzing monopods under Airy's wave loading. The number of elements and meshing details are the same for all software models. The main results of this study can be listed below:

- Estimating wave loading on offshore structures using FE methods is a contentious issue. And using wave load results without validating them for further analysis could lead to unsafe outcomes. A realistic estimation of internal forces and stress levels can highly affect the performance of offshore structures.

- The wave loading based on Airy's wave theory and Morison's equation is composed of both drag and inertia components. Each contribution of each may also vary with element cross section size. For large-diameter cylindrical members, the contribution of inertia force is dominant. Evaluation of the monopod case shows that the current numerical models may not be able to predict wave loading, mainly when the contribution of the coefficient of inertia to the total instantaneous wave force is dominant.

- As a result of the study, inconsistencies were observed in calculating the inertia load of commercial programs. The shear forces and moment reactions are compared. The difference arises from the inclusion of the inertia force component contribution to the wave loads. The results of the SAPOS program demonstrated good agreement with the analytical solution among the examined FE software packages.

Article Information Form

Funding

The author (s) has no received any financial support for the research, authorship or publication of this study.

Authors' Contrtibution

The authors contributed equally to the study.

The Declaration of Conflict of Interest/Common Interest

No conflict of interest or common interest has been declared by the authors.

The Declaration of Ethics Committee Approval

This study does not require ethics committee permission or any special permission.

The Declaration of Research and Publication Ethics

The authors of the paper declare that they comply with the scientific, ethical and quotation rules of SAUJS in all processes of the paper and that they do not make any falsification on the data collected. In addition, they declare that Sakarya University Journal of Science and its editorial board have no responsibility for any ethical violations that may be encountered, and that this study has not been evaluated in any academic publication environment other than Journal of Innovative Science and Engineering.

References

[1] Chakrabarti, S. (2005). Handbook of offshore engineering. 1st ed.1-2, *Oxford: El-Sevier Applied Science.*

[2] API RP 2A-WSD. (2007) Recommended Practice for Planning, Designing and Constructing Fixed Offshore Platforms - Working Stress Design - Twenty-First Edition, Errata and Supplement 3.

[3] Abdel Raheem Sh, E., Abdel Aal E, M. A., Abdel Shafy A. G. A. and Abdel Seed, F. K. (2012). Nonlinear analysis of offshore structures under wave loadings, *Proceedings of the 15th World Conference on Earthquake Engineering*-15WCEE, 24–28.

[4] Raheem, A. E. S. (2013). Nonlinear response of fixed jacket offshore platform under structural and wave loads, Coupled Systems Mechanics, 2: 111–126. DOI: 10.12989/csm.2013.2.1.111

[5] A storm at sea from the view of an oil rig, URL: https://www.reddit.com/r/pics/comments/13q5u9/a_storm_at_sea_from_the_view_of_an_oil_rig/

[6] Witz, J. Lyons, G. Patel, M.H. and Brown, D. (1994). Advanced Offshore Engineering, Offshore Engineering Handbook Series. *Bentham Press*, London, UK.

[7] Karadeniz, H. (2013). Stochastic Analysis of Offshore Steel Structures. *An Analytical Appraisal*, *Springer Series in Reliability Engineering*. DOI:10.1007/978-1-84996-190-5

[8] Boccotti, P. (2015). Wave mechanics and wave loads on marine structures, in: Butterworth-Heinemann publication, Waltham, MA 02451, USA, ISBN: 978-0-12-800343-5, 978–978.

[9] Linton, C.M. and Evans, D.V. (1990). The interaction of waves with arrays of vertical circular cylinders, J. Fluid Mech, 215: 549-569. DOI: https://doi.org/10.1017/S0022112090002750

[10] Kriebel, D.L. (1990). Nonlinear wave interaction with a vertical circular cylinder. Part I: *Diffraction Theory*, *Ocean Engineering*, 17(4): 345–377. https://doi.org/10.1016/0029-8018(90)90029-6

[11] Kriebel, D.L. (1992). Nonlinear wave interaction with a vertical circular cylinder. part II: *Wave Run-Up*, *Ocean Engineering*, 19(1):75-99. https://doi.org/10.1016/0029-8018(92)90048-9

[12] Zhu, S. (1993). Diffraction of short-crested waves around a circular cylinder, *Ocean Engineering*, 20: 389–407, https://doi.org/10.1016/0029-8018(93)90003-Z

[13] Vugts, J.H. Tempel, J.V.D. and Schrama, E.A. (2001). Hydro-dynamic loading on Monotower support structures for preliminary design. *Interfaculty Offshore Technology, Faculty of Civil Engineering and Geosciences*, Delft University of Technology.

[14] Wilson, J.F. (2003). Dynamics of Offshore Structures, *John Wiley & Sons, Inc*, United States of America. ISBN: 978-0-471-26467-5.

[15] Harish, N. Sukomal, M. Shanthala, B. and Subba, R. (2010). Analysis of offshore jacket platform, Natl. Conf. on Sustainable Water Resources Management - SWARM, 7–9.

[16] Karadeniz, H. Togan, V. and Vrouwenvelder, T. (2008a). Optimization of steel monopod offshore-towers under probabilistic constraints, *Proceedings of the International Mechanical Engineering Congress and Exposition*, Boston, USA.

[17] Karadeniz, H. Togan, V. and Vrouwenvelder, T. (2008b). Reliability based optimization of steel monopod offshore towers, *Proceedings of the 27th International Conference on Offshore Mechanics and Arctic Engineering*, Estoril, Portugal.

[18] Slåke, T. (2016). Analysis of Jacket type fixed platforms- Effect of various mass modelling approaches for Topsides on structural response, MASTER Thesis, University of Stavanger, Stavanger, Stavanger, Norway.

[19] Morison, J.R. Brien, M.P. WJohnson, J. and Schaaf, S.A. (1950). The force exerted by surface wave on piles, *Petroleum Transactions, American Institute of Mining Engineers*, 189:149-154. DOI:10.2118/950149-G

[20] Mendes, A.C. Kolodziej, J.A. and Correia, H.J.D. (2004). Numerical modelling of wave-current loading on offshore jacket structures, *Transactions on the Built Environment*, 71. DOI: 10.2495/FSI030091

[21] Lipsett, A.W. (1986). A perturbation solution for nonlinear structural response to oscillatory flow, *Applied Ocean Research*, 8(4):183-189. https://doi.org/10.1016/S0141-1187(86)80035-9

[22] Gudmestad, O.T. and Moe, G. (1996). Hydrodynamic Coefficients for Calculation of Hydrodynamic Loads on Offshore Truss Structures, Marine Structures, 9:23. 0951-8339(95)00023-23-2

[23] Sunder, S. and Connor, J. (1981). Sensitivity analyses for steel jacket offshore platforms, *Applied Ocean Research*, 3(1):19-28. DOI:10.1016/0141-1187(81)90081-X

[24] Chandrasekaran, S. Jain, A.K. and Chandak, N.R. (2004). Technical note: Influence of hydrodynamic coefficients in the response behavior of triangular TLPs in regular waves, Ocean Engineering, 31:2319-2342. https://doi.org/10.1016/j.oceaneng.2004.06.005

[25] Gücüyen, E. Erdem, R.T. and Gökkuş, Ü. (2012). Irregular wave effects on dynamic behavior of piles, *Arabian J. Sci. Eng. King Fahd University of Petroleum and Minerals*. DOI 10.1007/s13369-012-0428-6.

[26] Edvardsen, K. (2015). Forces on simplified offshore structures according to different wave models, Norway.

[27] Karadeniz, H. (1989). Advanced stochastic analysis program for offshore structures - Theoretical outline and the user's manual of SAPOS, Report, *Dept. of Civil Engineering, Delft University of Technology*, Delft, Netherland.

[28] CSI Analysis Reference Manual. (2014). CSI analysis reference manual for SAP2000 *Version 16; Computers & Structures Inc*. (CSI): Walnut Creek, CA, USA.

[29] SACS (2009). Version 12, EDI, Soft-ware Manual Version 7.

[30] Abaqus theory manual. (2004). Version 6.14-1 Hibbitt. *Karlsson and Sorensen, Inc*. Pawtucket, RI.

[31] ANSYS (2016). AQWA user's manual release 17.0. ANSYS Inc.: Canonsburg, PA, USA.

[32] Cermelli, C. Aubault, A. Roddier, D. and Mccoy, T. (2010). Qualification of a Semi-Submersible Floating Foundation for Multi-Megawatt Wind Turbines, *Offshore Technology Conference, Offshore Technology Conference*, 1–15.

[33] Computers, Structures, Inc, (2011). Automatic Wave Loads Technical Note Wave Load Overview. *Computers and Structures*, Inc, Berkeley, CA.

[34] Doman, A.C. (2014). Three-Dimensional equivalent static analysis and design methodology of a reinforced concrete floating offshore wind turbine platform, *California State University, Sacramento*.

[35] Lai, W.J. Lin, Ch.Y. Huang, Ch.Ch. and Lee, R.M. (2016). Dynamic Analysis of Jacket Substructure for Offshore Wind Turbine Generators under Extreme Environmental Conditions, *Appl. Sci*, 6:307. doi:10.3390/app6100307

[36] Kazemi Daliri, A. (2017). Evaluation of using new materials in offshore jacket structures and risers, PhD. *Dissertation, İstanbul Aydin University*, Istanbul, Turkey.

[37] Noorzaei, J. Bahrom, S. I. Jaafar, M.S. Abdul, W. Thanoon, M. and Mohammad, Sh. (2005). Simulation of Wave and Current Forces on Template Offshore Structures, *Suranaree J. Sci. Technol*, 12(3):193-210.

[38] Ishwarya, S. (2016). Nonlinear static and dynamic analyses of jacket-type offshore platform, *Anna University*, Chennai.

[39] Karadeniz, H. (1996). Spectral Analysis Program for Offshore Structures (SAPOS), Response calculation and fatigue damage estimates, *Proc. of the 2nd Int. Conference in Civil Engineering on Computer Applications*, Research and Practice, ICCE-96, 1:339-349.

[40] Yaylacı, M. (2007). Applications of offshore Structure and Explicated of Design Parameters, *Karadeniz Technical University*, Trabzon, Turkey.

[41] Mc Namara, J.F. Gilroy, J.P. Sorensen, E.P. and Hibbitt, H.D. (1985). ABAQUS/AQUA application to offshore risers and pipelines, *Maritime Simulation, Proceedings of the First Intercontinental Symposium*, Springer.

[42] Kuntiyawichai, K. and Chucheepsakul, S. (2004). Analysis of offshore structures subjected to various types of sea wave, *Proceedings of OMAE04, 23rd International Conference on Offshore Mechanics and Arctic Engineering, Vancouver*, Canada.

[43] Huizer, C.O. (2017). Modelling loads of steady current and waves with Abaqus, Aqua. URL: Url-2<https://info.simuleon.com/blog/modelling-loads-of-steady-current-and-waves-with-abaqus-aqua

[44] Das, B. and Janardhan, P. (2017). Model Development and Load Analysis of Offshore Jacket Structure using SAP2000, *International Journal for Research in Applied Science and Engineering Technology (IJRASET)*, 5:1482-1493. doi:10.22214/ijraset.2017.4263

[45] Dağlı, B. Y. Yiğit, M.E. and Gökkuş, U. (2017). Behaviour of large cylindrical offshore structures subjected to wave loads, *TEM Journal*, 6(3):550-557. DOI:10.18421/TEM63-16

[46] Lamb H. (1993) Hydrodynamics. *Cambridge University Press*, Cambridge.

[47] Maccamy, R.C. and Fuchs, R.A. (1954). Wave Forces on Piles: A Diffraction Theory, Army Corps of Engineers, *Beach Erosion Board. U.S. Beach Erosion Board*, ech. Memo No. 69.

[48] Sarpkaya, T. and Isaacson, M. (1981). Diffraction theory is reviewed in Mechanics of Wave Forces on Offshore Structures, Van Nostrand Reinhold Co.

[49] Det Norske Veritas - DNV (1977). Result for the Design, *Construction and Inspection of Offshore Structures*, Oslo, (Reprint with correction 1981). http://www.dnv.com

[50] Sawaragi, T. (1995). Coastal engineering- waves, beaches, wave-structure interaction. *Elsevier, Amsterdam.*

[51] Butterfield, S. Musial, W. Jonkman, J. Sclavounos, P. and Wayman, L. (2007). Engineering Challenges for Floating Offshore Wind Turbines, Golden, Colorado: National Renewable Energy Laboratory